

# UC Berkeley

## UC Berkeley Electronic Theses and Dissertations

### Title

Investigating Sperm-Specific Proteins and Physiology to Inform Development of Non-hormonal, Unisex Contraception.

### Permalink

<https://escholarship.org/uc/item/3dj1w9mc>

### Author

Skinner, Will M.

### Publication Date

2022

Peer reviewed|Thesis/dissertation

Investigating Sperm-Specific Proteins and Physiology  
to Inform Development of Non-hormonal, Unisex Contraception.

By

William M. Skinner

A dissertation submitted in partial satisfaction of the

requirements for the degree of

Doctor of Philosophy

in

Endocrinology

in the

Graduate Division

of the

University of California, Berkeley

Committee in charge:

Professor Polina V. Lishko, PhD, Chair

Professor Tyrone Hayes, PhD

Julia Schaletzky, PhD

Fall 2022





## Abstract

### Investigating Sperm-Specific Proteins and Physiology to Inform Development of Non-hormonal, Unisex Contraception

By William M. Skinner

Doctor of Philosophy in Endocrinology

University of California, Berkeley

Professor Polina V. Lishko, Chair

Pharmaceutical contraception is still nonexistent for half the world's population – people with testes – and nearly half of all pregnancies are still unintended, even in the United States. These unintended pregnancy rates remain stubbornly high despite increasing access to existing contraception, which suggests that new contraceptives are needed to give every person the tools to make independent, voluntary decisions about their own fertility. Spermatozoa are the only human cells that are created in one body and fulfill their function in another, so with proper pharmaceutical properties, the same sperm-impairing drug could be delivered either in bodies that produce or receive sperm, thereby creating the world's first non-hormonal, unisex contraceptive. To enable this goal, we need a better biological understanding of these unique and understudied cells, to identify which sperm physiological processes and sperm-specific proteins are the most targetable for pharmaceutical inhibition.

The studies in this dissertation improve the foundational biological understanding of multiple processes necessary for a spermatozoon to fertilize an egg, from energy metabolism and motility to sperm-egg fusion, using diverse approaches such as *in vitro* cell physiology, molecular biology, electrophysiology, and structural biology. The first of these studies found that human sperm can maintain their ATP content in the presence of small-molecule uncouplers, even though uncouplers can depolarize the mitochondrial and plasma membranes and impair sperm motility; these results also suggest that the FDA-approved uncoupler niclosamide might be a useful ingredient in spermicide gels. Another study described here revealed that the human sperm-specific protein TMEM95 has a binding partner on the egg membrane and that this interaction is involved in sperm-egg fusion but not binding. The final project produced extremely high-resolution cryo-electron tomography structures of the human and mouse sperm flagellar axonemes, which revealed several species-specific and asymmetrically distributed protein structures connecting various microtubule pairs, with likely significance in the creation of flagellar motility. Together, these findings set the stage for future investigations which may identify new ways to target sperm-specific proteins for the production of novel non-hormonal unisex contraceptives.



Dedicated to Katie Kelly-Hankin, my wife and partner.

Our shared interest in reproductive justice, science, and nature has inspired and sustained me throughout this PhD, and the ideas expressed here are much deeper because of your thoughtful contributions.

My world is infinitely richer and more beautiful because you are in it.

## Table of Contents

ACKNOWLEDGEMENTS .....	III
CHAPTER 1: INTRODUCTION .....	1
CHAPTER 2: SINGLE-CELL MOTILITY ANALYSIS OF TETHERED HUMAN SPERMATOZOA .....	5
CHAPTER 3: MITOCHONDRIAL UNCOUPLERS IMPAIR HUMAN SPERM MOTILITY WITHOUT ALTERING ATP CONTENT .....	21
CHAPTER 4: HUMAN SPERM TMEM95 BINDS EGGS AND FACILITATES MEMBRANE FUSION .....	46
CHAPTER 5: <i>IN SITU</i> CRYO-ELECTRON TOMOGRAPHY REVEALS THE ASYMMETRIC ARCHITECTURE OF MAMMALIAN SPERM AXONEMES.....	82
CHAPTER 6: CONCLUSION .....	123
REFERENCES.....	125

## Acknowledgements

Science is a team sport, and my success in this program would have been impossible without the support, belief, and contributions of a wide group of amazing people.

First and foremost, my advisor, Polina Lishko – thank you for your unflagging trust, encouragement, and generosity. Your work has made immense contributions to this field and blazed a trail that allowed me to work on contraceptive research without uprooting my family and life. For this I will be forever grateful, and I will always fondly remember our multi-hour end-of-the-day discussions about sperm physiology.

Deb Levine (my “fairy career-mother”), Logan Nickels, and the rest of the team at the Male Contraceptive Initiative – thank you for believing in me from the very beginning and making it possible for me to do this work that we all care about so deeply.

Monika Haoui and Liliya Gabelev Khasin – thank you for helping me chart a path through the complicated UC Berkeley landscape. I doubt I would have found my way without you.

All the other members of the Lishko Lab – I have learned so much from each of you and have been privileged to work alongside such smart and dedicated scientists.

To the undergraduates who assisted with this work: Emiliano Tabarsi, Natalie Petersen, and Jules Lamm – thank you for your dedicated work on our project, and for trusting me to guide you. I hope that our work together was equally rewarding for you, and I can’t wait to hear what you are all up to in the next phases of your lives.

My key collaborators, Shaogeng “Steven” Tang and Zhen Chen – I feel honored to have gotten a chance to work with both of you. I am consistently awed by your intelligence, skill sets, and dedication, and I doubt I will ever be half as accomplished a scientist as each of you already are. I look forward to watching your research groups flourish in the near future.

My dissertation committee, Tyrone Hayes and Julia Schaletzky – thank you for understanding the value of what I am working on even though it is different from most of the projects that come across your desks. Tyrone, your class was the most useful and fun class I took at Berkeley!

My qualifying exam committee: Tyrone Hayes, Gary Firestone, Niren Murthy, and Tom Carlson – thanks for the guidance and the thoughtful questions!

The staff, professors, and students of MBL’s Frontiers in Reproduction 2022 – I will forever be grateful to be a FIRbee and to have gotten a chance to learn and laugh with all of you for six beautiful weeks.

Liza Jalalian and the staff at the UCSF Center for Reproductive Health – Thank you for welcoming me into the Andrology Lab for so many days with such good humor!

The organizers, mentors, and students of the CTI Exchange Emerging Leaders in Contraceptive Technology Innovation mentorship program, and especially my mentor Kevin Peine – thank you for the amazing opportunity. It has been immeasurably valuable to get to know so many people who have found a way to make a career in this somewhat niche and underfunded field.

Monica Albe – your guidance through the consistently bewildering bureaucracy at UC Berkeley has been an absolute lifesaver so many times. Thank you!

Jennifer Garrison – thank you for steadfastly believing in my potential from the first time we met, and for consistently helping me achieve my goals.

The many excellent and accomplished scientists that I have had the privilege of consulting throughout this program: Erv Goldberg, Donner Babcock, Sharon Mortimer, Yuriy Kirichok, Ambre Bertholet, Jean-Ju Chung, and so many others – thank for your time, generosity, and openness.

My bandmates, Ryder, Clem, Isaac, Jamie, Jack, Jay, Derek, Matt, Jason, and Kevin – the exuberant art and magical moments we've made together are some of the most treasured memories of my life. Thanks for helping me balance all the rigorous scientific thinking of graduate school with lots of creativity and lighthearted fun.

My chosen family, David, Monica, Ava, Angie, and Chris – thank you for bringing so much meaning and joy to my life, and for supporting me and helping keep a smile on my face on even the hardest days. I feel incredibly proud of the community we have built together.

My parents, Bonnie Cook and Peter Skinner – no amount of thanks can ever be enough. Your dedication and unwavering belief in me are the foundation that makes all other things possible. Mom, thank you for teaching me to find beauty and wonder in even the smallest things in nature.

Dad, thank you for showing me that any problem is solvable through persistence, and encouraging me to fix things myself.

## Chapter 1: Introduction

The spermatozoon is a unique and highly specialized cell – for example, sperm are the only flagellated, motile cell type in mammals<sup>1</sup>, the only cell type that uses protamines instead of histones to package DNA<sup>2</sup>, and the only cell type that is produced in one body and then fulfills its function in another body<sup>3,4</sup>. This morphological and functional uniqueness means that there are an abundance of proteins that are expressed only in sperm<sup>5-11</sup>. Specific pharmacological inhibition of one of these proteins could block sperm functions necessary for fertilization, and therefore lead to development of a non-hormonal contraceptive<sup>12</sup>. Excitingly, because mature sperm cells spend time in the bodies of both sexual partners, inhibiting the action of a sperm-specific protein could also be a way to develop a *unisex* contraceptive, meaning a contraceptive that could be delivered either in the sperm-producing body, or in the body that produces eggs and receives sperm<sup>13</sup>.

Forty percent of all pregnancies worldwide are still unplanned<sup>14</sup>, and while birth rates are lower in developed countries than developing ones, the percentage of pregnancies that are unintended is actually higher in developed countries<sup>14,15</sup>. Although there are some complications to the measurement and use of this metric<sup>16,17</sup>, its stubbornly high rate suggests that the existing suite of contraceptive methods are insufficient for individuals and couples to freely and reliably choose the number and timing of their pregnancies. Some unintended pregnancies occur through contraceptive failure, which can occur even with perfect use of a method, while others arise because many contraceptive methods are difficult to use correctly and reliably in real-world settings<sup>18</sup>. Still other unintended pregnancies occur when users either discontinue or decline to use highly-effective methods due to unacceptable side effects or other undesirable product characteristics<sup>19</sup>. Since progestogens and estrogens have actions on tissues throughout the body, hormonal contraceptives for people with ovaries sometimes have systemic side effects that can drive users to decline or discontinue these products<sup>20</sup>. Non-hormonal contraceptives that specifically inhibit sperm after its arrival in the vagina or uterus could, in theory, avoid these kinds of systemic side effects and be administered only when needed, just before intercourse. These contraceptives could therefore have a higher user acceptability, increasing the worldwide uptake of modern contraceptive methods and decreasing the side-effect burden that hundreds of millions of women and people with ovaries endure today.

In addition, pharmaceutical contraception of any type is still nonexistent for half the world's population – people with testes. The only highly-effective methods available for this population are condoms and vasectomy; condoms are widely disliked and have a relatively high real-world failure rate<sup>12,18</sup>, and vasectomies cannot be considered a reversible form of contraception due to the risk of degenerative changes in the testes and epididymides and the development of antibodies against one's own sperm<sup>21-24</sup>. A contraceptive that reversibly interferes with sperm production or function and is administered in the sperm-producing body could give billions of people a significantly improved ability to make their own reproductive decisions separately from their sexual partner or partners. Additionally, in trusting relationships, these contraceptives could relieve the partner with ovaries from the burden of choosing and



managing contraception and enduring whatever side effects it may entail. Importantly, self-identified men report high acceptability of new forms of contraceptives, both in clinical trials of potential hormonal contraceptives and in surveys about hypothetical products, and self-identified women also report high enthusiasm for such products and high trust in their partners to adequately manage contraception<sup>25</sup>. By filling an unmet contraceptive need for a very large population of people, reversible contraceptives administered to men and people with testes have been projected to make a significant dent in unintended pregnancy rates across many diverse countries<sup>26</sup>.

Decreasing the global unintended pregnancy rate has the potential to improve many aspects of human wellbeing across the globe, since unintended pregnancies are associated with adverse physical health outcomes<sup>17,27</sup> (though this relationship is somewhat unclear and understudied), adverse mental health outcomes<sup>28</sup>, and significant economic costs<sup>29,30</sup>. Critically, unintended pregnancies can be fatal to pregnant people, since every year tens of thousands of women and people with ovaries die from unsafe abortions<sup>31</sup> and hundreds of thousands die yearly as a result of giving birth<sup>32-34</sup>. These problems are not restricted to underdeveloped countries – the rates of unsafe abortion may soon increase in the United States as medical abortion access becomes restricted in some states, and the rate of death as a result of childbirth in the US is unacceptably high and rising yearly, ranking as one of the worst among developed countries<sup>35-37</sup>. Importantly, the risk of death as a result of childbirth is nearly three times higher in the US in the Black population than it is in the white population<sup>35,36</sup>. Unintended pregnancy rates are also higher in socially disadvantaged and economically under-resourced communities<sup>15,38</sup>, and though studies are sparse on the effects of these pregnancies on individual economic and educational attainment<sup>39</sup>, it is reasonable to assume that they may have detrimental effects on these life metrics as well. Therefore, improved methods of contraception may serve as a tool for ameliorating existing social and gender inequalities and saving lives.

Despite the clear benefits of new or improved contraception and the wide potential market, development has proceeded slowly – most new contraceptive options for people with ovaries are incremental improvements of the same fundamental hormonal mechanism of action underpinning the original oral contraceptive pill<sup>20,40</sup>, and despite the prolonged efforts of many people, no pharmaceutical option for people with testes is yet approved. The reasons for this failure could fill many dissertations, and so will not be discussed at length here, but they include regulatory hurdles<sup>12,41-43</sup>, a lack of research and development investment from major governmental funders and large pharmaceutical companies<sup>44,45</sup>, and many technical and biological challenges<sup>46-49</sup>. In the absence of significant investment from deep-pocketed players, for the past two decades the mission of developing novel contraceptives has largely been carried by academic groups, small nonprofits, and startup pharmaceutical companies<sup>45,50-53</sup>. For more than a decade, the Lishko Lab has been one of these academic groups, committed to better understanding the fundamentals of sperm physiology and sperm ion channel biology, and in the process has helped identify or characterize several key proteins that have gone on to become targets for the development of sperm-based contraception<sup>54-62</sup>.

The sperm proteins that the Lishko Lab studies are present and functional in mature human spermatozoa, which is a key requirement for any target that could lead to development of

a unisex contraceptive able to be applied in either sperm- or egg-producing bodies, since only mature sperm are ejaculated and enter the egg-producing body. While this requirement narrows the potential repertoire of contraceptive targets by excluding proteins that are only involved in the process of spermatogenesis, potential contraceptive products acting on mature sperm would have several key advantages. Unisex contraceptives could simplify the contraceptive product landscape, with all people eligible to take the same drug, and since these products could act immediately on already-existing mature sperm cells, they would likely only need to be taken before intercourse. Additionally, mature spermatozoa are transcriptionally silent and therefore lack functional nuclear steroid hormone receptors, so contraceptives targeting these cells would necessarily act through a non-hormonal mechanism of action, which offers the potential for greater specificity. Although hormonal contraception for people with testes, which is currently in phase I and II clinical trials, is highly effective and well-accepted by study participants, it requires consistent daily administration, has a two- to three-month lag before sperm counts drop to contraceptive levels, requires semen analysis to confirm the decrease in sperm count, and works through a similar mechanism of action to traditional hormonal birth control, and so may cause similar side effects<sup>48,63–72</sup>. These hurdles may prove to be challenges for both regulatory approval and user uptake, though great efforts are being made to manage and mitigate each of these issues.<sup>73</sup> While non-hormonal contraceptives for men and people with testes are at least a few years behind in the drug development pipeline, their potential for shorter onset or even immediate efficacy and the possibility of fewer clinical side-effects may make them more palatable to regulators and users.

Despite their significance, sperm remain an understudied cell type, in part because of the aforementioned lack of investment in reproductive biology and contraceptive development, and in part because their specialized biology makes many standard cellular assays impossible – mature spermatozoa are terminally developed cells that are not yet possible to culture *in vitro*, they are transcriptionally silent so gene regulation or knockdown assays are impossible and irrelevant, and the extreme evolutionary selection pressure they face renders sperm from even closely related species different enough that the use of standard model organisms is of limited value<sup>74</sup>. Importantly, sperm are robust cells with many redundant physiological and structural features, and so it is important to fully investigate the physiological, structural, and pharmacological underpinning of a potential contraceptive development avenue before investing resources into drug development. For example, many sperm-specific proteins have been found to be dispensable for proper sperm development or fertility in knockout mouse studies<sup>75,76</sup>, and other promising targets have led only to subfertility when inhibited<sup>77</sup>. Additionally, as in all areas of contraceptive development, the majority of promising targets and leads will fail to reach the market due to insurmountable problems with specificity, toxicity, formulation, delivery, or any of the other key characteristics of a marketable drug<sup>78</sup>. Therefore, despite the many hormonal and nonhormonal targets and leads currently at various stages of the development pipeline<sup>11,12,47,48,53,63,64,64,79–82</sup>, it is critical to continue identifying new possible contraceptive targets and investigating their role in the functions of sperm physiology that are necessary for fertilization.

The projects described in this dissertation aim to contribute to this broader effort by investigating aspects of sperm physiology that remain poorly understood, revealing the structure

and function of previously identified potential contraceptive targets on sperm, and looking more closely at the structure of human sperm in the hopes of discovering new targets. These projects use a variety of approaches from the fields of cellular physiology, molecular biology, electrophysiology, and structural biology to cross-validate the significance of the findings.

Chapter two is a methods paper, originally published in the journal *Bio-protocol*, detailing our lab's methods of human sperm isolation, preparation, and high-speed video micrography, which we hope will help accelerate this field by making it easier for other researchers to work with human sperm. The techniques described in that chapter were used to prepare human sperm for all the studies in the following chapters.

Chapter three is an investigation of the physiological significance of the mitochondrial and plasma membrane potentials in human sperm fertilization capacity, with the aim of investigating whether small-molecule uncouplers, which can specifically depolarize these potentials, might be usable as an ingredient in sperm-inhibiting contraceptives. This study is currently in review and has been released as a preprint on *bioRxiv*.

Chapter four is a study recently published in *Proceedings of the National Academy of Sciences of the United States of America* which investigates the structural and functional significance of a sperm-specific protein called TMEM95 in fertilization. Despite its clear biological significance, the molecular mechanisms of sperm-egg binding and fusion remain poorly understood in humans, with many sperm-specific proteins known to be necessary for the process, but with few of their interactions or binding partners identified. This study aims to play a role in unraveling this complex mystery.

Chapter five is a study accepted to *Nature Structural and Molecular Biology* which used cryo-electron tomography to create the highest resolution model ever made of the human and mouse sperm flagellar axonemes in their native cellular state. In doing so, this work found radial asymmetries at multiple levels of flagellar organization and identified the presence of several previously unknown protein densities within the flagellum. Once these proteins and their functions are fully identified, they may prove to be contraceptive targets.

We hope these studies advance the fundamental field of sperm biology and attract other investigators to help answer the many remaining questions about these fascinating and unique cells. We also hope this work will accelerate the development of novel sperm-targeting non-hormonal unisex contraceptives, which could be useful or even potentially lifesaving for billions of people.

## Chapter 2: Single-cell Motility Analysis of Tethered Human Spermatozoa

William M. Skinner<sup>1</sup>, Nadja Mannowetz<sup>1</sup>, Polina V. Lishko<sup>1,\*</sup> and Nadia R. Roan<sup>2,3,\*</sup>

<sup>1</sup>Department of Molecular and Cell Biology, University of California, Berkeley, CA, USA;

<sup>2</sup>Department of Urology, University of California, San Francisco, CA, USA;

<sup>3</sup>Gladstone Institute of Virology and Immunology, San Francisco, CA, USA

\*For correspondence: lishko@berkeley.edu, nadia.roan@ucsf.edu

### Abstract

Vigorous sperm flagellar motility is essential for fertilization, and so the quantitative measurement of motility is a useful tool to assess the intrinsic fertility potential of sperm cells and explore how various factors can alter sperm's ability to reach the egg and penetrate its protective layers. Human sperm beat their flagella many times each second, and so recording and accurately quantifying this movement requires a high-speed camera. The aim of this protocol is to provide a detailed description of the tools required for quantitative beat frequency measurement of tethered human sperm at the single-cell level and to describe methods for investigating the effects of intracellular or extracellular factors on flagellar motion. This assay complements bulk measurements of sperm parameters using commercially-available systems for computer-assisted sperm analysis (CASA).

**Keywords:** Human spermatozoa, Sperm motility, High-speed imaging, Single-cell motility analysis, Sperm Swim-up, Sperm flagellum, Seminal plasma, Amyloid fibrils, Flagellar beat frequency

## Background

Sperm motility assessment using beat frequency analysis with the help of high-speed cinemicrography has historically been an important tool to analyze sperm well-being. The basal beat frequency (BF) of mammalian spermatozoa varies greatly, with human sperm having one of the highest frequencies – sometimes exceeding 20 Hz<sup>54,83</sup> – and many factors are known to affect the BF. These factors can be extracellular, such as the composition of oviductal fluid and seminal plasma, hormones, drugs or environmental toxins, and temperature; or intracellular, like sperm pHi, calcium concentration ( $[Ca^{2+}]_i$ ), and plasma membrane potential<sup>84,85</sup>. Additionally, as mammalian spermatozoa acquire their full fertilizing potential during their final maturation in the female reproductive tract – a process called capacitation<sup>86,87</sup> – they increase the amplitude and asymmetry of their flagellar waveform, while decreasing their BF. This motility pattern is known as “hyperactivation”<sup>88</sup>. Both flagellar wave shape and BF can serve as an important indicator of sperm fertility<sup>88-90</sup>. While CASA (Computer-Assisted Sperm Analysis) is an excellent and reliable tool widely used in clinics and research laboratories<sup>91,92</sup>, it is designed to specifically track the motion of the sperm head only and is not reliable to analyze the shape of flagellar motion. In order to accurately count BF and fully resolve the shape of the flagellar motion of human sperm cells, high-speed camera recordings with a frame rate of approximately 1,000 frames per second are required. Here we will describe a method to perform frame-by-frame analysis using high-speed camera recordings which can help detect motility defects, assess capacitation state, and evaluate the effects of different treatments on human sperm cells. We describe how the system is set up and use exposure of sperm cells to SEM1(86-107) fibrils (semen-derived amyloid fibrils previously shown to enhance HIV infection and participate in excess/defective sperm removal)<sup>93,94</sup> as an example of how an exogenous agent can affect sperm motility at the single-cell level.

As with many other human-derived cells, human sperm samples constitute a biosafety hazard. Therefore, all work with such materials should be performed in BSL-2 approved spaces. Moreover, all personnel should be properly trained, including undergoing annual bloodborne pathogen training per institutional guidelines. Lab personnel are also advised to undergo immunization against Hepatitis B.

Each human spermatozoon has a head of about 5  $\mu\text{m}$  connected to a 45  $\mu\text{m}$  tail (flagellum) which is about 0.5  $\mu\text{m}$  in diameter<sup>56</sup>. To observe such a small object, specialized high-resolution optics are required. Using a microscope equipped with Differential Interference Contrast (DIC) or Hoffman Modulation Contrast (HMC) optics is highly recommended over phase-contrast optics since DIC/HMC makes it easier to track the precise motion of the tiny flagellum<sup>95</sup>. The measurement rig is composed of an inverted microscope (such as the Olympus IX71 or Nikon Ti series) positioned on a vibration-damping air table and connected to a high-speed camera that can acquire 1,000 frames per second (Figure 1).

It is highly recommended to use an Olympus UPlanSApo 60x water immersion objective or similar lens, with numerical aperture of 1.20. Such an objective features a long working distance (0.28 mm) and an adjustment collar which can compensate for the thickness of coverslips between 0.13 and 0.21 mm. This combination of long working distance and adjustable

collar allows for observations through two 0.13 mm thickness coverslips: one coverslip serving as a glass bottom of the recording chamber, plus an additional round 5 mm diameter coverslip placed into the recording chamber, with sperm cells deposited on top. This objective can also allow for observation of free-swimming sperm cells in solution. As will be discussed below, depositing sperm cells on easily exchangeable round 5 mm diameter coverslips (rather than on the bottom of the recording chamber directly) is a convenient way to load fresh sperm cells into the recording chamber and quickly exchange samples of cells that have been exposed to different conditions. In addition to the 60x objective, inverted microscopes are equipped with 10x eyepieces and an optional 1.6x internal magnification. The regular internal magnification of the microscope (a total of 600x) is used to locate the appropriate sperm cell to record. If higher magnification is needed, the 1.6x internal magnification is engaged for a total of 960x.

The assembled rig is positioned on a vibration-damping air table (*e.g.*, Newport or TMC). The absence of any vibration is an essential part of a successful video recording since even a slight vibration will ultimately compromise the recording (Figure 1).

Finally, it is suggested to use a Warner Instruments RC-24E perfusion chamber connected via a manifold to a gravity-fed perfusion system (Figure 2). The RC-24E is a low-volume diamond-shaped chamber with laminar flow and relatively fast solution exchange rates. A round 5 mm diameter coverslip fits perfectly into the diamond-shape opening of this chamber. To perfuse a solution through the recording chamber, a simple self-made gravity-fed perfusion system with a Teflon manifold (Figure 3) allows one to connect the recording chamber to up to 8 separate perfusion lines. It is important to ensure that the tubing used for perfusion of bath solution with human sperm does not leach plasticizers or phthalates into the solutions since such chemicals can significantly alter sperm motility<sup>96</sup>. A small diameter polytetrafluoroethylene (PTFE, commonly known as Teflon) tubing is highly recommended as the main perfusion tubing. As this tubing is rather stiff, flexible connections are made using high purity silicon tubing that fits over the PTFE tubing<sup>95</sup>. In addition, syringes that lack any lubricant (*e.g.*, Air Tite Norm-Ject brand) are strongly recommended for injection of perfusion materials, since mineral oil or other lubricating additives can interfere with sperm ion channels, and hence impair flagellar motility.

## Materials and Reagents

1. Polypropylene sterile sample collection containers (SARSTEDT, catalog number: 75.9922.745)
2. Centrifuge Tubes, 50 ml and 15 ml (Olympus Plastics, catalog numbers: 28-106 and 28-101)
3. Positive Displacement Pipettes and Tips (Gilson, MICROMAN)
4. Micropipettes and Tips (Gilson, Pipetman)
5. 5 mm round coverslips (WPI, catalog number: 502040)
6. 0.22  $\mu\text{m}$  Polyethersulfone (PES) Vacuum-Driven Filter System, 500 ml and 1 L (Olympus Plastics, catalog numbers: 25-227 and 25-229)
7. MLA Pipette Tips, 200  $\mu\text{l}$  (Vista Labs, catalog number: 9025)
8. Osmolarity Calibration Standard (ELITech, OPTIMOLE, catalog number: OA-029)
9. Osmometer Paper Sample Disks (Wescor, VAPRO Sample Disks, catalog number: SS-033)
10. Sodium Chloride (NaCl) (Sigma-Aldrich, catalog number: S7653)
11. Potassium Chloride (KCl) (Fisher Scientific, catalog number: P217)
12. Magnesium Sulfate Heptahydrate ( $\text{MgSO}_4 \cdot 7\text{H}_2\text{O}$ ) (Sigma-Aldrich, catalog number: 63140)
13. Monopotassium Phosphate ( $\text{KH}_2\text{PO}_4$ ) (Sigma-Aldrich, catalog number: 60216)
14. Calcium Chloride Dihydrate ( $\text{CaCl}_2 \cdot 2\text{H}_2\text{O}$ ) (Sigma-Aldrich, catalog number: 21097)
15. HEPES (Fisher Scientific, catalog number: BP310)
16. D-(+)-Glucose ( $\text{C}_6\text{H}_{12}\text{O}_6$ ) (Sigma-Aldrich, catalog number: G8270)
17. Sodium Lactate ( $\text{C}_3\text{H}_5\text{NaO}_3$ ) (Sigma-Aldrich, catalog number: L7900)
18. Sodium Pyruvate ( $\text{C}_3\text{H}_3\text{NaO}_3$ ) (Sigma-Aldrich, catalog number: P2256)
19. Sodium Hydroxide (NaOH) (Sigma-Aldrich, catalog number: 221465)
20. Sodium Bicarbonate ( $\text{NaHCO}_3$ ) (Sigma-Aldrich, catalog number: S5761)
21. Fetal Bovine Serum (FBS) (Gibco, catalog number: 16000036)
22. Hydrochloric Acid (HCl) (Fisher Scientific, catalog number: A144S)
23. Human fibrillogenic peptide SEM1(86-107) (Celtek and CPC Scientific, sequence: DLNALHKTTKSQRHLGGSQQLL)
24. pH 4.0 Standard, Red (EMD Chemicals, catalog number: BX1628-1)
25. pH 7.00 Standard, Yellow (Fisher Scientific, catalog number: SB107-500)
26. pH 10.00 Standard, Blue (Fisher Scientific, catalog number: SB115-500)
27. Phosphate-Buffered Saline (PBS) (Fisher Scientific, catalog number: BP665-1)
28. 70% Ethanol (Decon Labs, catalog number: V1001)
29. Human Tubal Fluid (HTF) Solution (see Recipes)
30. High-Saline solution (HS) (see Recipes)
31. Capacitation media (see Recipes)
32. Motility disrupting reagents and control reagents (see Recipes)

## Equipment

### A. General

1. Incubator (Fischer Scientific, Isotemp Incubator)
2. CO<sub>2</sub> Incubator (for capacitation) (Eppendorf, Galaxy 170S, catalog number: CO17101001)
3. Water Filter (Millipore, Milli-Q, Advantage, catalog number: A10-TOC)
4. Balances (Mettler Toledo, models: XS2002S and XS105)
5. pH Meter (Denver Instruments, Ultra Basic UB-10)
6. Vapor Pressure Osmometer (Wescor, model 5600)
7. 10 µl Fixed volume MLA pipette (Vista Labs, catalog number: 1051C)
8. Forceps (Excelta, catalog number: 5-S-SE)
9. Thermomixer (Eppendorf) for generation of semen amyloid fibrils
10. 4 °C refrigerator
11. Hemacytometer (Hausser Scientific, Reichert Bright-Line, catalog number: 1483)
12. Slanted Tube Rack for 50 ml Tubes (Bel-Art, catalog number: F18794-0028)

### B. Microscopy (Figure 1)

1. Inverted microscope (Olympus, model: IX-71)
2. Water immersion objective (Olympus, UPlanSApo, 60x, 1.20 W,  $\infty/0.13-0.21$ /FN26.5, catalog number: UPLSAPO 60XW)
3. Digital high-speed camera (NAC Image Technology, Memrecam GX-1 or similar type of high-speed camera)
4. Light source (Olympus, 100 W halogen lamp housing U-LH100L-3 with lamp 12V100WHAL)
5. Light source power supply (Olympus, catalog number: TH4-100)
6. Vibration Isolation Table (Newport, Vision IsoStation)
7. Recording chamber (Warner Instruments, RC-24E); A rectangular coverslip (Corning, 24x40 mm Rectangular #1 Cover Glass, thickness .13 mm, catalog number: 2975-244) is glued to the bottom of the chamber with SYLGARD 184 (Dow Corning, Midland, MI) according to the manufacturer's instructions. Grease is not recommended since it can leach into the chamber and alter the physiological properties of sperm cells.

### C. Perfusion and Suction (Figures 2 and 3)

1. Teflon 8-position perfusion manifold (Warner Instruments, MP-8, catalog number: 64-0211)
2. Suction control (B. Braun, Exadrop, Germany)
3. Suction tube (Warner Instruments, ST-QE1, catalog number: 64-1403)
4. Magnetic clamps for suction tube (Warner Instruments, MAG-1, catalog number: 64-0358; and MAG-7, catalog number: 64-1554)
5. Polytetrafluoroethylene (PTFE) perfusion tubing (Microbore PTFE Tubing, 0.022" ID x 0.042" OD) (Cole-Parmer, catalog number: EW-06417-21)
6. Silicone Connector Tubing (Platinum-Cured Silicone Tubing, 1/32" ID x 3/32" OD) (Cole-Parmer, catalog number: EW-95802-01)



7. Manifold Connector Tubing (PTFE Tubing, 1/32" ID x 1/16" OD) (Cole-Parmer, catalog number: EW-06407-41)
8. Stopcock with Luer Connections; 4-way; Male Lock (Cole-Parmer, catalog number: EW-30600-09)
9. Female Luer Hose Barb Adapter, 1/16" (Cole-Parmer, catalog number: EW-45508-00)
10. Syringes (Air-Tite, Norm-Ject Luer Lock Syringe, catalog number: AL20 and AL3)

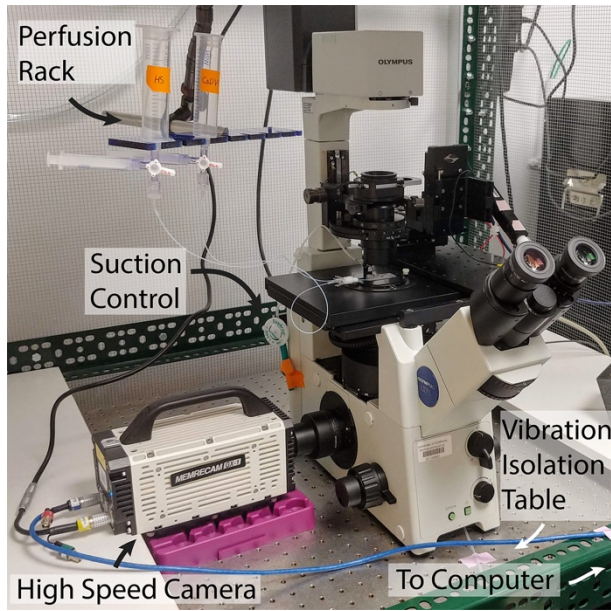


**Figure 1. Fully assembled high-speed video microscopy rig with perfusion setup, on a vibration-isolation table**

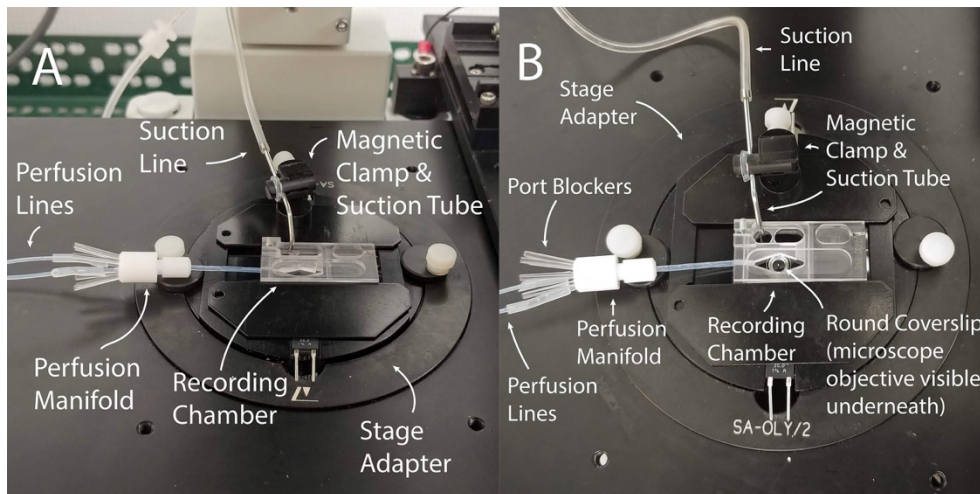


**Figure 2. Assembled perfusion chamber for recording.** A. The recording chamber is placed inside the stage adapter and connected to perfusion lines via a perfusion manifold. The suction line is attached to a metal suction tube, which is positioned on the stage adapter with a magnetic clamp. B. Top view of the same setup.

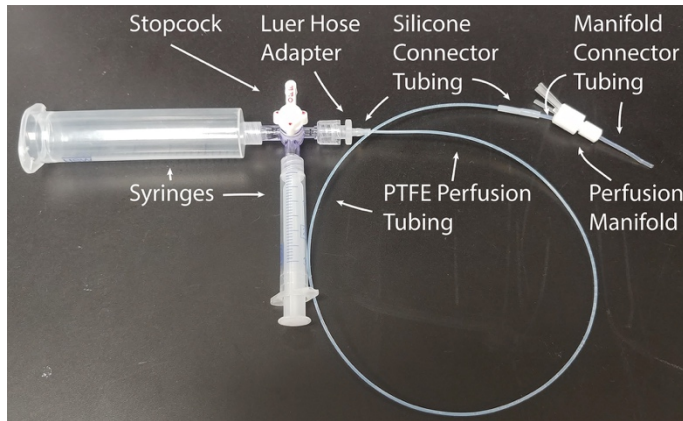


**Figure 3. Homemade perfusion line.** The large syringe is used to hold perfusion fluid, and the small syringe is used to purge air bubbles from the system. The Perfusion Manifold allows for up to 8 perfusion lines to be connected simultaneously. Extra manifold ports are blocked when not in use.

### Software

1. Memrecam GXLink software, version 3.20 (NAC Image Technology)
2. ImageJ version 1.44 (<http://rsb.info.nih.gov/ij/>)
3. Statistical Analysis Software (OriginLabs, Origin, or equivalent)

## Procedure

### A. Sperm collection and purification – “Swim-up”

1. Obtain approval from your organization’s Institutional Review Board to conduct studies involving human subjects. Recruit healthy male volunteers of reproductive age older than 21 years to provide semen samples. Freshly ejaculated semen samples should be collected by masturbation into sterile polypropylene sample containers. Ensure that the sample containers chosen are clear of plasticizers, which can negatively affect sperm quality. Advise donors to avoid sexual activity for 3 days before collecting a sample. Ask donors to record the time of collection, and to deliver the sample to the lab within 30 min of collection. (Figure 4)
2. The human ejaculate sample should be left at room temperature for 30-60 min from the time of collection to allow it to gradually become less viscous (through the action of seminal proteases). This eases pipetting of the semen and ensures complete release of sperm cells from the seminal plasma, which contains sperm-binding proteins such as semenogelins. However, it is essential to start the “swim-up” (Step A4 and Figure 4) within 1 h after collection to prevent the seminal proteases from damaging the sperm cells.

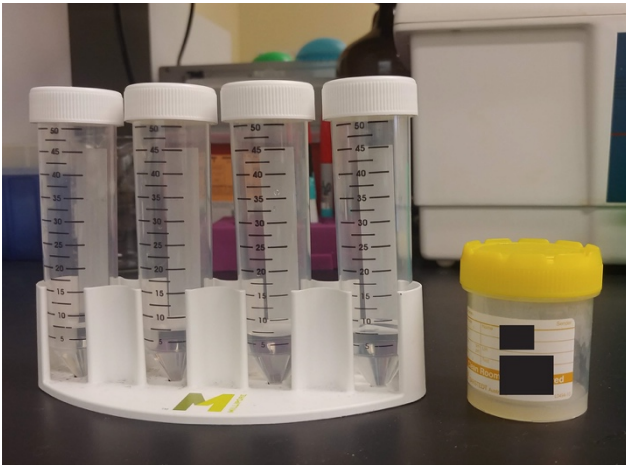


**Figure 4. Semen sample and tubes of HTF fluid.** The semen sample is in the collection container at right. The donor’s anonymized identity number and time of collection is labeled on the collection container (but redacted for publication). One ml of semen will be underlaid into each of the tubes of HTF on the left. In this case, only 3 tubes of HTF were used, as the ejaculate volume was roughly 3 ml.

3. Add 7 ml of HTF (Human Tubal Fluid) solution to a 50 ml centrifuge tube and warm it to approximately 37 °C in the incubator. Visually assess the volume of the ejaculate – if the volume is greater than 1 ml, prepare multiple tubes of HTF solution (Figure 4).
4. Once the HTF is warm, carefully underlay 1 ml of liquefied ejaculate to the bottom of each tube (Figure 5). Use of a positive displacement pipette greatly facilitates this process. Avoid agitating the semen, or introducing bubbles, which can lift strands of

semen to the surface of the HTF buffer. If strings of semen persist when removing the pipette from the semen sample, more liquification time is needed.

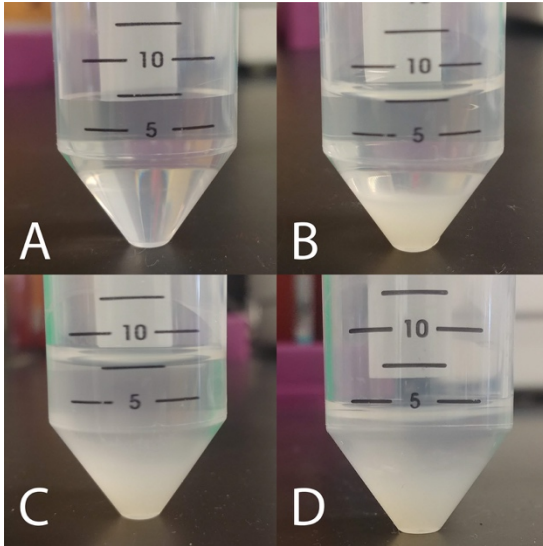


**Figure 5. Semen sample before and after swim-up.** A. HTF fluid in falcon tube before addition of semen. B. One ml of semen carefully underlaid at the bottom of the tube. C. The same tube after 1 h of incubation at 37 °C. Note the supernatant is cloudier, and the boundary between the semen and the HTF fluid less defined. This shows that sperm have swum up into the supernatant. D. The same tube after removing several milliliters of supernatant.

5. Place the tubes in a 37 °C incubator for 1 h, in a stand that holds them at a 45° angle, in order to increase the surface area for swim-up. If the incubator is a CO<sub>2</sub> incubator, close the cap tightly to prevent acidification of buffer – CO<sub>2</sub> is not required for this procedure. During this incubation, motile sperm will gradually swim out of the semen sample and up into the HTF supernatant, thereby cleansing themselves of most residual seminal proteins. Purifying human spermatozoa using this “swim-up” technique avoids sperm damage induced by the G-forces of the centrifugation used in other purification procedures (Figure 5).
6. After 1 h, the supernatant should contain only motile sperm. Carefully collect about 2-3 ml of the supernatant from each tube, merging the supernatant from all HTF tubes into a single separate 15 ml conical tube (Figures 5 and 6). The most motile sperm are found in the upper sections of the supernatant, so to gather only highly motile sperm, pipette from near the surface of the supernatant. To avoid gathering any seminal plasma, do not attempt to remove all of the supernatant – leave several milliliters of HTF remaining above the seminal plasma. Discard HTF and semen tubes after removal of supernatant.
7. Let the 15 ml tube stand vertically for about 30-60 min at RT. Spermatozoa will concentrate at the bottom (where a white cloud will form) as they gradually become less motile due to HTF solution’s relatively low sodium concentration. When submersed in HS solution (which has a higher sodium concentration) these sperm cells will resume their aggressive motility (Figure 6).

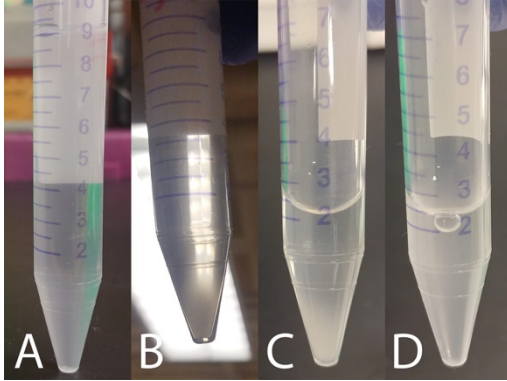


**Figure 6. Sperm settling and concentration.** A. Three ml of HTF supernatant was removed from each swim-up tube and pooled into one 15 ml conical tube. B. The cloud of sperm cells that have settled to the bottom of the tube after 30-60 min standing at RT. C. Several milliliters of supernatant removed to concentrate the sperm cells. D. Sperm cloud resuspended by gentle pipetting.

8. Remove the supernatant from the tube to concentrate the cells, and gently resuspend the cloud of cells in the remaining HTF solution (Figure 6). A normal ejaculate should contain at least  $15 \times 10^6$  sperm cells per ml<sup>97</sup>, but sperm counts vary widely between different samples, so technicians will need to develop an intuition of how much supernatant to leave in the tube, based on the size of the sperm cloud, in order to reach the desired concentration of cells. If cell concentration is outside of the desired range in downstream applications, the technician can use more or less of this sperm solution, or if needed, dilute it with more HTF or allow the cells to settle again and remove additional supernatant.
  9. Take an aliquot of the sperm suspension and determine the cell concentration using a hemacytometer.
- B. Recording high-speed video of sperm motility**
1. Place a 5 mm diameter coverslip in the main diamond-shaped well of the recording chamber. Then fill the recording chamber with  $\sim 300 \mu\text{l}$  of room temperature HS solution, making sure that all wells (including the main well and the suction wells) have liquid in them, and that no air bubbles are blocking the covered connection lane between the front and back wells. Ensure that the coverslip is fully submerged and flat on the bottom of the recording chamber, with no bubbles underneath it, by tapping it down with a pipette tip or forceps.
  2. Take 20-50  $\mu\text{l}$  of the concentrated sperm cell suspension from the storage tube, and gently add it to the HS solution above the coverslip. Although spermatozoa are motile, many will accumulate on the surface of the coverslip, where their heads will adhere electrostatically, while their flagella will vigorously beat in the solution just above the coverslip. Allow sperm cells to sediment onto the coverslip for 10-30 min at room temperature.
  3. If capacitated cells are needed, first allow cells to adhere to the coverslip, then perfuse the recording chamber with capacitation media and incubate cells at 37 °C for 4 h in a 5% CO<sub>2</sub> incubator<sup>59</sup>. It is essential to use a CO<sub>2</sub> incubator at this step as capacitation media



contains sodium bicarbonate, which together with atmospheric CO<sub>2</sub> maintains the required pH during the capacitation process. It is recommended to adhere the cells before adding capacitation media because the FBS in the capacitation media makes the sperm adhere less strongly to the coverslip.

4. With the microscope in Differential Interference Contrast mode, add a ~50 µl droplet of water directly onto the 60x objective, place the recording chamber into the stage adapter and mount the adapter on the microscope stage, then put the perfusion and suction lines into place, as shown in Figure 2. Then turn the light source on and find the correct focal plane for the upper surface of the coverslip. It is often helpful to do this by first finding an edge of the coverslip and then gradually adjusting the focal plane upwards – you will first encounter the glass bottom of the recording chamber, then the lower surface of the coverslip, then the upper surface of the coverslip.
5. At this point, it is often useful to turn on HS perfusion to remove debris and excess spermatozoa from the recording chamber. For capacitated sperm, one must avoid turning on perfusion immediately after a fresh coverslip is placed into the perfusion chamber to ensure that the largest number of capacitated spermatozoa are attached and available for analysis. In this case, after the appropriate cell is chosen and recorded, the perfusion can be turned on. Ensure that the HS solution in the syringe has reached room temperature (~24 °C) before starting perfusion. If incubation at a warmer temperature is required, you may place the recording chamber and stage adapter into the incubator, or use a built-in electrical heater in the stage adapter or incorporated into the perfusion line.
6. Assess the sperm cells for strict morphology, overall motility, and concentration using WHO guidelines<sup>97</sup>. Morphologically normal sperm cells<sup>98</sup> can then be sampled for movement analysis. Morphological abnormalities of sperm include vacuolated, round, amorphous, tapering, pyriform, megaloccephalic or microcephalic heads; asymmetrical, bent or thin midpiece; and various tail defects. Sperm motility should always be confirmed and recorded before any motility-altering drug/compound treatment is administered.
7. Once appropriate cells are identified, switch the optical routing to the camera mode, and activate the camera to record video. It is useful to find a field of view with enough sperm cells to allow for multiple measurements from the same video, but for accurate measurements, assess cells whose flagella do not overlap with other nearby cells. Gain, frame rate, and many other recording settings can be adjusted in the GXLink software. We use a frame rate of 1,000 frames per second to facilitate beat frequency calculations since 1 frame then corresponds to an interval of approximately 1 ms.
8. Once video has been captured of control cells, perfuse or pipette in treatment compounds (*e.g.*, 50 µg/ml SEM1(86-107) fibrils or the corresponding monomeric peptide control), wait 10 min, and then record additional videos. After all needed video has been recorded, carefully remove the coverslip from the recording chamber with forceps, and then discard it. If treatment with several different compounds is required, cells can also be seeded onto coverslips and incubated simultaneously in separate wells of a cell-culture dish, then each coverslip can be carefully transferred one at a time into the recording chamber for imaging. Ensure that the cells remain covered with liquid at all times.

Once all needed recordings have been made, remove the coverslip from the recording chamber, aspirate the remaining solution in the recording chamber, and clean

by rinsing it with water and 70% ethanol, followed by a triple rinse with deionized water (18 M $\Omega$ ). Avoid prolonged exposure of the chamber plastic to alcohols. The chamber can be reused indefinitely.

## Data analysis

1. Videos recorded in the GXLink software can be exported in a variety of formats. For quantitative analysis, export the movie as a series of images in 8-bit TIFF format.
2. Import these TIFF files as an image stack in ImageJ. Use the marker tool to mark a point touching the edge of a sperm's flagellum, near the midpiece, when it is at its maximum displacement from center. Then scroll through the images until the flagellum touches that marker again (Figure 7). The number of frames between the two touches of the marker point represents the Period (T), in milliseconds, which is the time required to complete one full flagellar stroke (if the frames were collected at 1,000 frames per second, where 1 frame equals 1 ms). Since Beat Frequency (BF) is measured in Hz, use the following equation to determine BF of the sperm tail:

$$BF = \frac{1000}{T}$$

Collect frequency measurements for a statistically appropriate number of cells, and evaluate the data with the statistical analysis software of your choice.

3. To quantitate the effects of SEM1(86-107) fibrils or other agents on motility, BFs are calculated twice: first prior to perfusion of the agent, and then 10 min after the perfusion.

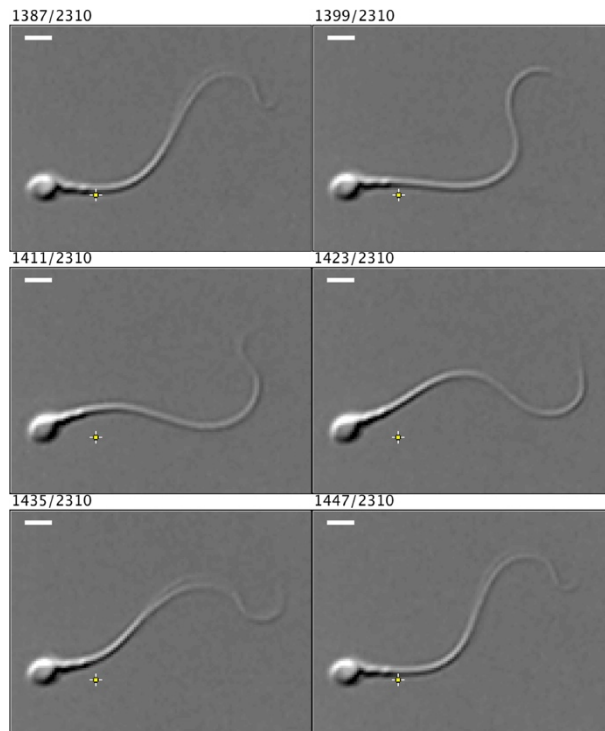


**Figure 7. Example frames illustrating the measurement of one full beat cycle of a human spermatozoa.** The numbers above each frame indicate specific frame position out of 2,310 frames collected. There is a 12-frame gap between each image displayed here, and the scale bars represent approximately 5  $\mu\text{m}$ . The image was contrast enhanced



in ImageJ for visual clarity. This spermatozoon has a period of 60 ms, and therefore a frequency of approximately 17 Hz. Video (.avi) and TIFF files are included as [supplemental materials](#).

## Notes

1. Once high-speed images have been captured, various methods exist to evaluate the beat frequency. In addition to the method described here, it is possible to choose a time window (*e.g.*, 0.5 s or 1 s) and measure how many full beats are completed in this time window, then mathematically scale that number to beats per second<sup>94</sup>. Others have used custom computer image analysis software to trace the pattern of flagellar motion and fit sinusoidal curves to it, or Fast Fourier Transform analysis to report beat frequency directly from the power spectrum of the intensity changes along a line scan perpendicular to the flagellar beat axis<sup>83,99–101</sup>.
2. Beat Frequency (BF) should not be confused with Beat Crossing Frequency (BCF) as reported by CASA systems, which is defined as the number of times the sperm head crosses the direction of movement of the free-swimming cell<sup>102</sup>. Due to the sinusoidal nature of tethered flagellar motion, the BCF will generally be twice as large as the BF.
3. When mammalian spermatozoa are free-swimming, rather than tethered, their flagella move in all three dimensions, resulting in a roughly helical path, which complicates beat frequency analysis<sup>101</sup>.

## Recipes

### 1. Human Tubal Fluid (HTF) Solution

Substance	Molar mass (g/mol)	Final concentration (mM)	Weight	
			For 500 ml	For 1,000 ml
NaCl	58.44	97.8	2.86 g	5.72 g
KCl	74.55	5	0.186 g	0.373 g
MgSO <sub>4</sub> ·7H <sub>2</sub> O	246.48	0.2	24.6 mg	49.3 mg
KH <sub>2</sub> PO <sub>4</sub>	136.09	0.37	25.2 mg	50.4 mg
CaCl <sub>2</sub> ·2H <sub>2</sub> O	147.02	2	0.147 g	0.294 g
HEPES	238.31	28	3.336 g	6.673 g
Sodium Lactate Solution (60% w/w)	112.06	20	1.5 ml	3 ml
Sodium Pyruvate	110	0.4	22 mg	44 mg
Glucose	180.2	3	0.270 g	0.540 g

- a. Adjust pH to 7.3-7.4 with NaOH. Osmolarity should be  $280 \pm 5$  mOsm, measured using a Vapor Pressure Osmometer.

- b. Filter through a sterile 0.2 µm PES filter and store the final solution at 4 °C for up to one month. Sodium lactate solution is used instead of lactic acid due to sodium lactate's greater stability and manufacturing consistency.

## 2. High-Saline (HS) Solution

Substance	Molar mass (g/mol)	Concentration (mM)	Weight (g)	
			For 500 ml	For 1,000 ml
NaCl	58.44	135	3.945 g	7.889 g
KCl	74.56	5	0.186 g	0.373 g
CaCl <sub>2</sub> ·2H <sub>2</sub> O	147.02	2	0.147 g	0.294 g
MgSO <sub>4</sub> ·7H <sub>2</sub> O	246.48	1	0.123 g	0.247 g
HEPES	238.3	20	2.383 g	4.766 g
Glucose	180.2	5	0.451 g	0.901 g
Sodium Lactate Solution (60% w/w)	112.06	10	0.75 ml	1.5 ml
Sodium Pyruvate	110	1	0.055 g	0.110 g

- a. Adjust pH to 7.3-7.4 with NaOH. Osmolarity should be  $320 \pm 5$  mOsm, measured using a Vapor Pressure Osmometer.
- b. Filter through a sterile 0.2 µm PES filter and store the final solution at 4 °C for up to one month. Sodium lactate solution is used instead of lactic acid due to sodium lactate's greater stability and manufacturing consistency.

## 3. Capacitation media<sup>59</sup>

In premade HS solution, add 20% Fetal Bovine Serum and 25 mM NaHCO<sub>3</sub>.

*Note: Capacitation media must be prepared freshly before each use and used within the same day.*

## 4. Motility disrupting reagents and control reagents

- a. Human fibrillogenic peptide SEM1(86-107) (Sequence: DLNALHKTTKSQRHLGGSQQLL) was custom-synthesized by a commercial vendor (Celtek and CPC Scientific) but can also be synthesized in-house. Peptide purity should be > 95%. The peptide can be dissolved at a concentration of 2.5 mg/ml in PBS (pH 7.0). This peptide serves as the monomeric peptide (negative) control and does not restrict sperm motility.
- b. To generate amyloid fibrils, the 2.5 mg/ml SEM1(86-107) peptide is agitated in 100 µl aliquots for 12 h at 37 °C at 1,400 rpm in an Eppendorf Thermomixer, after which the solution should look turbid as a result of fibril formation.
- c. Fibril formation can be confirmed by thioflavin T binding or electron microscopy<sup>93</sup>.
- d. We have previously found that cationic fibrils from semen [SEM1(86-107) fibrils, SEVI fibrils, and Galago repeat fibrils] entrapped sperm cells, while monomeric

peptides [unagitated SEM1(86-107), SEM1(68-85) and SEM1(108-159)] and non-cationic fibrils [A $\beta$ (1-42)] did not<sup>94</sup>.

### **Acknowledgments**

This work was supported by NIH grants R21AI116252 and R21AI122821 to N.R.R., and by R01GM111802, Pew Biomedical Scholars Award, and Packer Wentz Endowment Will to P.V.L. The authors would like to thank Dr. Donner F. Babcock for his valuable suggestions and comments, and to Emiliano Tabarsi for his technical assistance.

### **Competing interests**

We declare there are no competing interests.

### **Ethics**

This study was conducted with the approval of the Committee on Human Research at the University of California, Berkeley (CPHS protocol #2013-06-5395; issued under University of California, Berkeley Federalwide Assurance #00006252).

## **Chapter 3: Mitochondrial uncouplers impair human sperm motility without altering ATP content**

Will M. Skinner<sup>1,2</sup>, Natalie T. Petersen<sup>2,3</sup>, Bret Unger<sup>4</sup>, Shaogeng Tang<sup>5,6</sup>, Emiliano Tabarsi<sup>2,7</sup>, Julianna Lamm<sup>2,8</sup>, Liza Jalalian<sup>9</sup>, James Smith<sup>10</sup>, Ambre M. Bertholet<sup>11,12</sup>, Ke Xu<sup>4,13,14</sup>, Yuriy Kirichok<sup>11</sup>, Polina V. Lishko<sup>1,2,\*</sup>.

<sup>1</sup> Endocrinology Graduate Group, University of California, Berkeley, Berkeley, California, United States of America

<sup>2</sup> Department of Molecular and Cell Biology, University of California, Berkeley, Berkeley, California, United States of America

<sup>3</sup> Department of Obstetrics and Gynecology, Stanford University School of Medicine, Palo Alto, California, United States of America

<sup>4</sup> Department of Chemistry, University of California, Berkeley, Berkeley, California, United States of America

<sup>5</sup> Department of Biochemistry, Stanford University School of Medicine, Stanford, California, United States of America

<sup>6</sup> Sarafan ChEM-H, Stanford University, Stanford, California, United States of America

<sup>7</sup> Keck School of Medicine, University of Southern California, Los Angeles, California, United States of America

<sup>8</sup> Dewpoint Therapeutics, Boston, Massachusetts, United States of America

<sup>9</sup> Department of Obstetrics and Gynecology, University of California, San Francisco Center for Reproductive Health, San Francisco, California, United States of America

<sup>10</sup> Department of Urology, University of California, San Francisco, San Francisco, California, United States of America

<sup>11</sup> Department of Physiology, University of California San Francisco, San Francisco, California, United States of America

<sup>12</sup> Department of Physiology, David Geffen School of Medicine, University of California Los Angeles, Los Angeles, California, United States of America

<sup>13</sup> California Institute for Quantitative Biosciences, University of California, Berkeley, California, United States of America

<sup>14</sup> Chan Zuckerberg Biohub, San Francisco, California, United States of America

\*Corresponding Author: Polina V. Lishko. Email: [lishko@berkeley.edu](mailto:lishko@berkeley.edu)

## Abstract

In human spermatozoa, the electrochemical potentials across the mitochondrial and plasma membranes are related to sperm functionality and fertility, but the exact role of each potential has yet to be clarified. Impairing sperm mitochondrial function has been considered as an approach to creating male or unisex contraceptives, but it has yet to be shown whether this approach would ultimately block the ability of sperm to reach or fertilize an egg. To investigate whether the mitochondrial and plasma membrane potentials are necessary for sperm fertility, human sperm were treated with two small-molecule mitochondrial uncouplers (Niclosamide Ethanolamine and BAM15) that depolarize membranes by inducing passive proton flow, and evaluated the effects on a variety of sperm physiological processes. BAM15 specifically uncoupled human sperm mitochondria while Niclosamide Ethanolamine induced proton current in the plasma membrane in addition to depolarizing the mitochondria. Additionally, both compounds significantly decreased sperm progressive motility with NEN having a more robust effect. However, these uncouplers did not reduce sperm ATP content or impair other physiological processes, suggesting that human sperm can rely on glycolysis for ATP production if mitochondria are impaired. Thus, systemically delivered contraceptives that target sperm mitochondria to reduce their ATP production would likely need to be paired with sperm-specific glycolysis inhibitors. However, since Niclosamide Ethanolamine impairs sperm motility through an ATP-independent mechanism, and Niclosamide is FDA-approved and not absorbed through mucosal membranes, it could be a useful ingredient in on-demand, vaginally-applied contraceptives.

**Author Contributions:** W.M.S. and P.V.L conceived the project and designed experiments. W.M.S. conducted most experiments and analyzed most data, except as noted below, and wrote the manuscript. N.T.P. and W.M.S. performed *in vitro* fertilization experiments. B.U. and W.M.S. conducted STORM and B.U. analyzed data, under supervision of K.X. S.T. produced Izumo1 antibodies used during acrosome reaction assays. E.T. and J.L. assisted with multiple experiments. L.J. and J.S. enabled access to and training on computer-aided sperm analysis machines for motility assays performed by W.M.S. A.M.B. performed mitochondrial patch-clamp experiments and analyzed that data, under supervision of Y.K. P.V.L and W.M.S. performed human sperm patch-clamp electrophysiology. All of the authors discussed the results and commented on the manuscript.

Conceptualization: W.M.S and P.V.L

Data Curation: W.M.S.

Formal Analysis: W.M.S. and A.M.B.

Funding Acquisition: P.V.L. and W.M.S.

Investigation: W.M.S., N.T.P., B.U., E.T., J.L., A.M.B., P.V.L

Methodology: W.M.S., B.U., A.M.B, P.V.L

Project Administration: W.M.S.

Resources: W.M.S., S.T., L.J., J.S., K.X., Y.K., P.V.L.

Supervision: J.S., K.X., Y.K., P.V.L.

Validation: W.M.S.

Visualization: W.M.S., B.U., A.M.B

Writing – Original Draft Preparation: W.M.S.

Writing – Review & Editing: All Authors

**Competing Interest Statement:** W.M.S., P.V.L, E.T., A.M.B., and Y.K are co-inventors on a patent related to this work, which UC Berkeley has licensed to YourChoice Therapeutics, for which P.V.L is a co-founder, and Y.K. is a shareholder. The other authors declare no competing interests.

## Introduction

Human sperm are vigorously motile cells that require a well-regulated electrochemical potential across both the plasma membrane<sup>103–105</sup> and the mitochondrial membrane<sup>106–109</sup>. However, much is still unknown about the physiological importance of each of these potentials, since it has been difficult to disentangle their roles.

Small molecule uncouplers are a class of compounds that depolarize electrochemically charged membranes by passively shuttling protons down their concentration gradient. The name comes from the fact that they are able to ‘uncouple’ the mitochondrial electron transport chain from the ATP synthase machinery, thus causing cells to consume more oxygen and chemical energy substrates while producing less ATP<sup>110</sup>. These uncouplers were previously assumed to non-specifically pass through any phospholipid bilayer<sup>111</sup>, but in 2014, Kenwood *et al* developed BAM15, an uncoupler that specifically depolarizes the mitochondrial membrane potential without affecting the plasma membrane<sup>112</sup>, and in 2022 Bertholet *et al* showed that BAM15 and several other uncouplers actually perform a majority of their uncoupling activity through binding with the Adenine Nucleotide Translocase (ANT) family of proteins<sup>113</sup>.

The fourth isoform of the ANT family (ANT4) is specifically expressed in gametes<sup>114,115</sup>, and required for spermatogenesis<sup>116</sup>, but has an unclear role in mature sperm cells. Since its discovery, ANT4 has been seen as an attractive candidate for the development of a male contraceptive<sup>116–119</sup>, and efforts have been made to develop specific ANT4 inhibitors<sup>118,119</sup>. These inhibitors would theoretically block sperm mitochondrial ATP production, but no one has yet proved that human sperm cells would be unable to function without mitochondrially-produced ATP. In fact, there has been persistent debate about the role of mitochondrial oxidative phosphorylation in sperm physiology, with metabolic studies showing that glycolysis is sufficient for human sperm ATP production<sup>120</sup>, but physiological and clinical studies showing that proper mitochondrial functionality is correlated with high fertility in humans<sup>107,108,121,122</sup>.

Therefore, in this work we utilized a pair of small molecule uncouplers with different levels of mitochondrial specificity to investigate the physiological importance of the mitochondrial membrane potential (which is required for mitochondrial ATP production) and the plasma membrane potential to various human sperm functions necessary for fertilization, including motility, hyperactivation, and the acrosome reaction.

## Results

### **NEN and BAM15 both decrease human sperm mitochondrial membrane potential, but only NEN induces H<sup>+</sup> current across the plasma membrane.**

After a preliminary screening process, two small molecules uncouplers were chosen as representative uncouplers: BAM 15 (N5,N6-bis(2-Fluorophenyl)-[1,2,5]oxadiazolo[3,4-b]pyrazine-5,6-diamine); and Niclosamide Ethanolamine (NEN) (Fig. 1A). These two compounds were chosen because, in somatic cell types, BAM15 is known to be a protein-mediated<sup>113</sup>, mitochondrial-specific<sup>112,123</sup> uncoupler, and Niclosamide is known to uncouple both

mitochondria<sup>110,124</sup> and late endosomes<sup>125</sup>. Figure 1B shows a schematic of both protein-mediated mitochondrial uncoupling and protein-independent membrane uncoupling. Given the uniqueness of sperm and their mitochondria, we began by confirming that the two compounds work as expected in human sperm.

Live human sperm cells were treated with varying concentrations of each compound for 30 minutes at 37°C in noncapacitating media at pH 7.4, after which cells were stained with MitoTracker Red CMX-Ros and mitochondrial membrane potential (MMP) was qualitatively assessed using flow cytometry (Fig. 1C & D, Fig. S1A-C) and fluorescence microscopy (Fig. 1E). BAM15 and NEN were both able to dose-dependently reduce midpiece fluorescence and therefore MMP, with IC<sub>50</sub> values below 10 μM (Fig. 1C). The DMSO vehicle with which compounds were delivered did not have a dose-dependent effect on mitochondrial fluorescence (Fig. S1D) and none of the compounds decreased sperm viability as measured by propidium iodide permeability (Fig. S1E) in either non-capacitated (Fig. S1F) or capacitated (Fig. S1G) sperm.

To assess whether these two uncouplers were in fact acting through different mechanisms in human sperm, the effects of each compound on sperm plasma membrane H<sup>+</sup>-ion current were measured using whole-cell patch clamp electrophysiology. In this assay, 10 μM NEN induced a significant inward transmembrane H<sup>+</sup>-ion current at negative voltages while 10 μM BAM15 had no effect (Fig. 1F, G). The DMSO vehicle also induced no discernable H<sup>+</sup> current (Fig. 1F, S1H).

### **NEN-induced mitochondrial H<sup>+</sup> current is partially protein-mediated but more non-specific than BAM15-induced current.**

In somatic, non-thermogenic tissues of the body, Adenine Nucleotide Translocase (ANT) proteins are known to mediate mild mitochondrial uncoupling under physiological conditions and in the presence of exogenous uncouplers by allowing H<sup>+</sup> influx across the inner mitochondrial membrane<sup>113,126</sup>. Around 80% of BAM15's uncoupling effect has been shown to be mediated by these ANT proteins<sup>113</sup>. Therefore, we investigated whether NEN-induced uncoupling is also mediated by the ANT family of proteins. To do this, we performed mitochondrial patch-clamp electrophysiology, through which it is possible to directly measure current across the inner mitochondrial membrane (Fig. 1H). Indeed, in mouse heart mitochondria, which abundantly express ANT1<sup>127</sup>, 500 nM NEN induced a strong inward H<sup>+</sup> current at physiological pH and negative voltage (Fig. 1I). This H<sup>+</sup> current was reduced by approximately 25% in the presence of 1 μM Carboxyatractyloside (CATR), a known ANT inhibitor, and by approximately 40% in heart mitochondria from ANT1-knockout mice (Fig. 1I, J). This indicates that the NEN-induced current is partially mediated by ANT proteins, but that its activity is relatively more non-specific than BAM15's.

### **ANT4 is localized to the human sperm mitochondria.**

Given that NEN induces robust plasma membrane H<sup>+</sup> current in human sperm (Fig. 1F,G), that part of NEN's uncoupling in mitochondria is mediated by ANT proteins (Fig. 1I, J), and that the sperm-specific ANT4 protein has been reported to be present in the sperm flagellum<sup>128</sup>, it was necessary to confirm ANT4's cellular localization to see if any of NEN's observed



plasma membrane current might be ANT-mediated. Using a rabbit polyclonal antibody specific for human ANT4, which was validated both by the manufacturer and in-house (Fig. S2A-D), non-permeabilized human sperm cells showed no ANT4 signal (Fig. S2E), suggesting that ANT4 is not embedded in the plasma membrane. In permeabilized sperm cells, when excess primary antibody is used, some ANT4 staining is seen throughout the flagellum (Fig. S2F), but when primary antibody concentration is titrated down to an optimal concentration, ANT4 staining is restricted to the midpiece in a similar distribution to that of the inner mitochondrial membrane protein Cytochrome c oxidase (COXIV) (Fig. 2A-C). This finding was confirmed using stochastic optical reconstruction microscopy (STORM) on human sperm cells similarly costained for COXIV and ANT4 (Fig. 2D-F, top). Upon virtual cross-sectioning of the midpiece, distributions of these two proteins formed rings of similar diameter and thickness (Fig. 2D-F, bottom), consistent with mitochondrial localization. Together, these data suggest that NEN is acting as a non-specific protonophore in the human sperm plasma membrane. They also validate the use of these two compounds to investigate the differential physiological effects of impairing only mitochondrial membrane potential (BAM15) or both mitochondrial and plasma membrane potential (NEN).

### **NEN and BAM15 both impair human sperm basal motility.**

To begin exploring the physiological impacts of uncouplers on human sperm physiology, the effects of NEN and BAM15 on sperm motility were observed using computer-aided sperm analysis (CASA). 30 minutes of incubation with either NEN or BAM15 reduced the percent of noncapacitated sperm showing progressive motility (Fig. 3A) and incubation with NEN reduced the average curvilinear velocity (Fig. S3A); NEN reduced sperm progressive motility percent below the 5<sup>th</sup> percentile of fertile men<sup>129</sup> and showed a sub-micromolar IC<sub>50</sub> (Fig. 3A).

The effect of compounds on sperm hyperactivated motility was also assessed. Sperm were capacitated in the presence of BAM15, NEN, or DMSO vehicle, and then their motility was measured by CASA. Interestingly, the DMSO vehicle, which did not impair basal motility or any other sperm parameters in our assays, interfered with human sperm hyperactivation at higher concentrations (IC<sub>50</sub> of .004% DMSO) (Fig. 3B), complicating interpretation of these results. However, NEN but not BAM15 significantly reduced curvilinear velocity beyond the deleterious effect of the DMSO vehicle (Fig. S3B).

### **Small molecule uncouplers do not reduce human sperm ATP content or interfere with acrosome reaction.**

To investigate NEN and BAM15's mechanism of action on sperm motility (Fig. 3, S3), their effects on sperm ATP concentrations were measured. Despite their impacts on the mitochondrial membrane potential, neither compound caused any change in ATP concentrations in noncapacitated (Fig. 4A) or capacitated (Fig. 4B) spermatozoa. Consistent with this finding, NEN and BAM15 had no effect beyond the DMSO vehicle on the ability of sperm to undergo either the spontaneous or ionophore-induced acrosome reaction (Fig. S4A, B). The acrosome reaction is a necessary pre-fertilization exocytotic event<sup>130,131</sup> that exposes key fertilization receptors<sup>132,133</sup>. Additionally, pretreatment of mouse sperm with 10  $\mu$ M NEN also did not impair *in vitro* fertilization between mouse sperm and eggs (Fig. S4C, D).

## Discussion

In this study, we utilized a pair of small molecule uncouplers with different mechanisms of action to investigate the physiological roles of the mitochondrial membrane potential and plasma membrane potential in human sperm. Our data agree with data generated in other cell types<sup>112,113,123</sup> in finding that BAM15 specifically induces mitochondrial membrane uncoupling without causing uncoupling of the plasma membrane; in contrast, here we found that NEN leads to depolarization of both the mitochondrial and plasma membranes (Fig. 1). Given that there are no known uncoupling compounds that robustly depolarize the plasma membrane while leaving the mitochondrial membrane potential intact, this pairing of compounds is the best available way to tease apart the physiological importance of voltage across each of these membranes. The physiological effects of BAM15 are attributable specifically to the breakdown of mitochondrial membrane potential or its downstream effects, while any additive physiological effects of NEN over BAM15 are likely to be a result of the breakdown of the plasma membrane potential. This pairing of compounds could be a useful experimental system in a variety of cell types, since it enables relatively quick interrogation of the relevance of these two membrane potentials to any measurable physiological property.

This study also investigated whether the gamete-specific Adenine Nucleotide Translocase isoform ANT4 was expressed in the sperm plasma membrane, to rule out any possible ANT-mediated of NEN's plasma membrane effects. No immunocytochemical signaling was seen in the nonpermeabilized plasma membrane, and with proper antibody titration, no ANT4 signal was visible in the principal piece of the flagellum. Although this is in contrast to one previous study<sup>128</sup>, the mitochondrial localization observed here is consistent with the known localization of ANT1-3, and makes logical sense given ANT4's likely role as an ATP/ATP transmembrane transporter, based on its structural homology (Palmieri and Monné, 2016).

After confirming the mechanisms of action of these uncouplers, their effects on human sperm physiology and energy production were examined; both compounds had a dose-dependent inhibitory effect on sperm progressive motility, with NEN having a more potent effect than BAM15 (Fig. 3A). Next, the uncouplers' effects on hyperactivity were tested (Fig. 3B), and although the DMSO vehicle had no negative effects in any other assays, it had a dose-dependent inhibitory effect on sperm hyperactivity which prevented meaningful interpretation of the effects of the uncouplers on hyperactivation. Other investigators should be wary of this issue when designing future analyses of hyperactivation.

To investigate the root of the uncouplers' inhibition of basal motility, we analyzed their effect on ATP content in human sperm. There has been an ongoing debate in the field about whether oxidative phosphorylation or glycolysis is the primary source of ATP for human spermatozoa<sup>134-136</sup>, with increasing evidence supporting the idea that glycolysis is sufficient to support many human sperm functions<sup>120</sup>. Our data support this conclusion, with both NEN and BAM15 failing to reduce human sperm's ATP content.

In addition to their role in ATP production, the mitochondria have also been suggested to regulate calcium homeostasis in the sperm<sup>107</sup>. Since the ability to sequester cations is dependent on a negative potential within the mitochondrial matrix, and the acrosome reaction is a calcium-

evoked exocytotic event, we investigated whether NEN and BAM15 could affect sperm's ability to undergo the acrosome reaction. Interestingly, neither compound had a marked effect on either the rate of spontaneous acrosome reaction or calcium ionophore-induced acrosome reaction. Since the ability to undergo the acrosome reaction is dependent on successful capacitation, this result also suggests that the uncouplers did not impair that process even though sperm were exposed to them throughout the *in vitro* capacitation period.

The fact that NEN had a robust inhibitory effect on sperm basal motility while having no effect on ATP levels is likely due to its uncoupling of the sperm plasma membrane (Fig. 1), which would affect many motility-related ion channels and intracellular signaling pathways that rely on a carefully moderated membrane potential for proper function<sup>103</sup>. Since BAM15 is known as a more mitochondria-specific uncoupler<sup>112,113,123,137</sup> and did not induce plasma membrane current in the sperm electrophysiology assays (Fig. 1) the mechanism of action of its more modest inhibition of basal progressive motility remains to be clarified.

Although this study found that ANT4 was indeed mitochondrially localized and that the ANT family of proteins can mediate NEN-induced uncoupling, the physiological data herein suggest that contraceptives that solely interfere with mature sperm oxidative phosphorylation will be unlikely to successfully inhibit key sperm functions. However, pairing an oxidative phosphorylation inhibitor with an inhibitor of a sperm-specific glycolytic enzyme, like lactate dehydrogenase C<sup>138</sup>, might produce an effective contraceptive product. Additionally, since niclosamide has been FDA approved for use in humans with a favorable safety profile<sup>124</sup>, and possesses low bioavailability<sup>139</sup>, a pK<sub>a</sub> close to 6<sup>125</sup> (close to the vaginal pH), and significant deleterious effects on sperm motility, it could be a useful ingredient in on-demand vaginal contraceptive products as an alternative to nonoxynol 9-based spermicides.

## Materials and Methods

All experiments were performed in accordance with NIH guidelines for animal research and approved by UC Berkeley Animal Care and Use Committee (AUP 2015-07-7742), with every effort made to minimize animal suffering. All described methods are consistent with the recommendations of the Panel on Euthanasia of the American Veterinary Medical Association and IACUC committee. All experimental procedures utilizing human derived samples were approved by the Committee on Human Research at the University of California, Berkeley, IRB protocol number 2013-06-5395.

### Reagents

- Niclosamide Ethanolamine was purchased from AdipoGen Life Sciences, #AG-CR1-3644
- BAM15 was purchased from Sigma, product number SML1760-5MG
- 2,4, dinitrophenol was purchased from TCI, product D0109-25G
- FCCP was purchased from abcam, product code ab120081.
- Mitotracker Red CMXRos was purchased from ThermoFisher, #M7512
- Polyclonal Antibody to human ANT4 – Novus Biologicals NBP1-89074 raised in Rabbits against human ANT4 peptide
- Mouse Monoclonal Antibody against human COX4I1 – Proteintech #66110-1-Ig
- Polyvinyl Alcohol was purchased from Fluka, #81366-100G
- A23187 was purchased from MilliporeSigma, #C7522-5MG.
- 10% Goat Serum from Invitrogen, #50-062Z
- Bovine Serum Albumin from Sigma, #A3059-500G

### Sperm and Reagent Preparation

Human sperm cells were collected by masturbation from healthy donors and visually inspected for normal morphology and motility before use. Spermatozoa were isolated by the swim-up procedure in HTF or HS solution as previously described<sup>140</sup> and then concentrated by 5 minute centrifugation at  $\leq 500g$  and supernatant removal.

For all dose-response assays, NEN and BAM15 stocks were prepared at 10mM in DMSO, then these stocks were added to the necessary aqueous media to each assay, such that 30  $\mu M$  solutions contained .3% DMSO, and 10  $\mu M$  solutions contained .1% DMSO. These solutions were then serially diluted to lower concentrations. All plots show DMSO on the same x axis as compound concentration, to indicate the amount of DMSO necessary to deliver that concentration of compound.

### Flow Cytometric Assessment of MMP

Human sperm cells were incubated with small molecule uncouplers or vehicles in HS solution for 30 minutes at 37°C, then treated with 50nM MitoTracker Red in the presence of either uncouplers or vehicles for an additional 30 minutes. Subsequently, cells were washed by centrifugation for 5 minutes at 500 g, supernatant was removed, and cells were resuspended in HS solution. Fluorescence was measured by flow cytometry on a BD LSR Fortessa Celeste or BD LSR Fortessa X20, using gates for size and density to exclude debris and aggregates, and a

PE-Texas Red Filter set (561nm laser excitation, 610/20 nm emission filter) to record fluorescence (Fig. 1, S1). Fluorescence midpiece location was confirmed by microphotography on an Olympus IX71 inverted microscope using a Hamamatsu Orca-ER digital camera, and a 60x Olympus UPlanSApo objective (Fig. 1). Fluorescence statistics were analyzed using Microsoft Excel version 16 and GraphPad Prism version 9. The subpopulation of cells with the highest gaussian distribution of fluorescence were manually gated and the mean fluorescence of this population was normalized to the average of the means of the same population in the relevant vehicle control samples of each run. Each data point represents the mean fluorescence of the highest normally peak in an individual flow cytometry run of 10,000 cells. Nonlinear least squares regression performed using an unweighted [inhibitor] vs. response three parameter model (Hill Slope = -1.0), identifying “unstable” fits. Outliers tested using a ROUT coefficient of 1%, with no outliers detected. Residuals were checked for normality using the D’Agostino-Pearson omnibus normality test, checked for clustering using the Replicates test, and checked for appropriate weighting using the homoscedasticity test.

### **Area Under the Curve Analysis**

For all dose-response plots, Area Under the Curve (AUC) analysis was performed using the trapezoid method ( $\Delta X \cdot (Y_1 + Y_2) / 2$ ) on the arithmetic means of the measured parameter at each compound concentration. Each data point represents the area under the curve of all concentrations tested in one biological replicate. Effects of each compound were then compared using Dunnett’s Multiple Comparison’s Test.

### **Sperm Motility Assessment**

Isolated human sperm were incubated with small molecule uncouplers and vehicles at 37°C for 30 minutes, after which they were mixed with 1% Polyvinyl Alcohol to prevent adherence to glass and loaded into a Leja Standard Count 2-chamber sperm analysis slide (depth 20 micron). Sperm motility was analyzed on a Hamilton-Thorne IVOS I computer-aided sperm analyzer, at 37°C. Motility was measured for least 500 cells in each condition. Progressive motility was defined using Hamilton-Thorne’s proprietary software module. Nonlinear least squares regression performed by GraphPad Prism version 9 using an unweighted [inhibitor] vs. response three parameter model (Hill Slope = -1.0), identifying “unstable” fits. Outliers were tested using a ROUT coefficient of 1% and none were identified. Residuals were checked for normality using the D’Agostino-Pearson omnibus normality test, checked for clustering using the Replicates test, and checked for appropriate weighting using the homoscedasticity test. Residuals for NEN and BAM15 passed all tests, except that BAM15 failed the test for homoscedasticity with a p-value of 0.0207.

To study the effect of uncouplers on human sperm hyperactivated motility, cells were incubated for  $\geq 3$  hours in capacitation media (20% Fetal Bovine Serum and 25 mM Sodium Bicarbonate in HS solution) at 37°C and 5% CO<sub>2</sub> in the presence of various concentrations of uncouplers or DMSO vehicle. Motility was then measured on a Hamilton-Thorne IVOS II computer-aided sperm analyzer as above (except without the addition of polyvinyl alcohol), with the definition for hyperactivated motility set as VCL >150  $\mu\text{m/s}$  AND LIN <50% AND ALH >7.0  $\mu\text{m}^{141}$ .

## **Flow Cytometric Assessment of Acrosome Status**

Human sperm cells were incubated for 3.5 hours in capacitation media (20% Fetal Bovine Serum and 25mM Sodium Bicarbonate in HS solution) at 37°C and 5% CO<sub>2</sub>. In the final hour of incubation, custom monoclonal antibodies raised in mouse hybridoma cells against the ectodomain of human Izumo1 were added, at a concentration of 10µg/mL. Subsequently 50µM A23187 was added, and cells were incubated at 37°C and 5% CO<sub>2</sub> for an additional 30 minutes, after which cells were washed by centrifugation 3x (500 g, 5 min) in HS solution, incubated 30 minutes at room temperature with a goat anti-mouse 647 secondary antibody (Invitrogen A32728, final concentration 4µg/mL) in 10% goat serum. After an additional 3 washes by centrifugation, propidium iodide (PI) was added to a final concentration of 1µg/mL, and cells were analyzed by flow cytometry using the same instrumentation as above, except that Izumo-647 was visualized using an APC filter set (bandpass 670/30 or 670/14nm) and Propidium Iodide was visualized using a PE-Texas Red filter set (bandpass 610/20nm). Izumo-647 positive cells were scored as acrosome reacted, and PI negative cells were scored as living.

## **Generation of IZUMO1 monoclonal antibody using mouse hybridoma**

The IZUMO1 monoclonal antibodies were generated from mouse hybridoma and characterized as previously described<sup>142</sup>. Briefly, IZUMO1 antibodies 4E04 and 6F02 belong to the murine IgG1 isotype with kappa light chain. For antibody production, hIZUMO1-positive hybridomas were cultured in medium containing 10% FBS and subsequently adapted to an FBS-free medium. The condition media were harvested, and the IgG antibody were purified by protein G affinity chromatography and by Superdex-200 gel filtration chromatography in a buffer of 150 mM NaCl, 20 mM HEPES pH 7.4. Purified IgG antibodies were concentrated to 1 mg/mL with the addition of 10% (v/v) glycerol for use.

## **ATP Assessment**

Human Sperm cells were incubated with uncoupler compounds or vehicle for 1 hour at 37°C in white 96-well Costar polystyrene assay plates, under sterile conditions. ATP content was assessed using a PerkinElmer ATPlite Luminescence Assay System Kit, according to manufacturer instructions, and luminescence was imaged on a Biotek Synergy H4 Hybrid plate reader, set to endpoint/kinetic setting (one measurement point per well), with 1 second of integration time and a manual gain setting of 135. ATP content was quantified by interpolating against a standard curve of ATP solutions, per manufacturer instructions. Nonlinear least squares regression performed by GraphPad Prism version 9 using an [inhibitor] vs. response three parameter model (Hill Slope = -1.0), weighted by 1/Y<sup>2</sup>, identifying “ambiguous” fits. Outliers tested using a ROUT coefficient of 1%, with no outliers detected. Residuals were checked for normality using the D’Agostino-Pearson omnibus normality test, checked for clustering using the Replicates test, and checked for appropriate weighting using the homoscedasticity test, and passed all tests.

## **Mouse *In Vitro* Fertilization**

All mice were kept in the Animal Facility of the University of California, Berkeley, fed standard chow diet (PicoLab Rodent diet 20, #5053, LabDiet), and hyper-chlorinated water *ad libitum* in a room with controlled light (14 hours light, 10 hours darkness) and temperature ( $23\pm 0.5^{\circ}\text{C}$ ). Animals were humanely killed by  $\text{CO}_2$  asphyxiation and cervical dislocation according to ACUC guidelines with every effort made to minimize suffering.

C57Bl/6N (Charles River) female mice between 4 and 16 weeks old were superovulated by intraperitoneal injection of 5 IU pregnant mare serum gonadotropin (PMSG, Sigma, G4877) and 48 hours later, 5 IU human chorionic gonadotropin (hCG, Millipore, 230734). 13 hours after hCG injection the females were euthanized and cumulus-oocyte complexes were collected from the oviduct ampulla in HTF medium (Embryomax, Specialty Media, Millipore) and incubated for 30 minutes at  $37^{\circ}\text{C}$  and 5%  $\text{CO}_2$  prior to insemination. Simultaneously, mouse sperm were isolated from the cauda epididymis as previously described<sup>36</sup> and allowed to capacitate at  $37^{\circ}\text{C}$  and 5%  $\text{CO}_2$  for 60-90 minutes in the presence of uncoupler compounds or control vehicle. Sperm and eggs were then mixed to a final concentration of 210,000 sperm/mL in  $600\mu\text{L}$  of HTF medium and incubated at  $37^{\circ}\text{C}$  and 5%  $\text{CO}_2$  for 4 hours. Afterwards, the eggs were washed by mouth pipetting in HTF media to remove excess sperm. A final wash in KSOM media (Zenith Biotech) supplemented with  $1\text{mg/mL}$  BSA was then done before dividing the eggs into  $10\mu\text{L}$  drops of KSOM/BSA media overlaid with embryo-tested light mineral oil (Millipore) for culture at  $37^{\circ}\text{C}$ , 5%  $\text{CO}_2$ . Best efforts were made to divide equal numbers of eggs from each mouse into control and uncoupler-treated conditions. 3.5 days following IVF, the number of fertilized eggs was determined visually by assessing the percentage of embryos that reached morula or blastula stage.

### **Sperm Whole-Cell Electrophysiology**

Whole-cell electrophysiology was performed on isolated human sperm cells as described previously<sup>143,144</sup>. Once sperm cell “break in” was achieved in HS solution, cells were subjected to a voltage ramp protocol in the presence of bath and pipette solutions designed to ensure that only  $\text{H}^+$  current across the membrane was measured. Intracellular (pipette) solution contained:  $150\text{mM}$  NMDG,  $5\text{mM}$  BAPTA,  $100\text{mM}$  HEPES,  $1\text{mM}$  Tris Chloride, pH 7.5 with  $\text{MeSO}_3$ . Extracellular (bath) solution contained:  $157\text{mM}$  NMDG,  $20\text{mM}$  MES,  $1\text{mM}$   $\text{MgCl}_2$ ,  $100\mu\text{M}$   $\text{ZnCl}_2$ , pH 6 with  $\text{MeSO}_3$ . Compounds and vehicles were applied by perfusion, and currents were recorded until they showed a minimal change between subsequent voltage ramps. Then, compounds were washed out, and subsequent compounds added once currents had returned to baseline values. Representative traces and time courses created in Origin Pro version 9.0.0 and statistical analysis performed in GraphPad Prism 9.

### **Mitochondrial Patch-Clamp Electrophysiology**

Mouse heart mitochondria were isolated from wildtype and  $\text{ANT1}^{-/-}$  C57BL/6J2z mice and mitoplasts prepared and patch-clamped as described previously<sup>126</sup>. Both the bath and pipette solutions were formulated to record  $\text{H}^+$  currents and contained only salts that dissociate into large anions and cations that are normally impermeant through ion channels or transporters. Pipettes were filled with  $130\text{mM}$  tetramethylammonium hydroxide (TMA),  $1.5\text{mM}$  EGTA,  $2\text{mM}$  Tris chloride, and  $100\text{mM}$  HEPES (or MES). pH was adjusted to 7.5 with d-gluconic acid, and

tonicity was adjusted to ~360 mmol/kg with sucrose. Bath solution contained 100 mM HEPES (or MES) and 1 mM EGTA (pH adjusted to 7.0 with Trizma base, and tonicity adjusted to ~300 mmol/kg with sucrose).

## Immunocytochemistry

Briefly, sperm were adhered onto poly-D-Lysine coated coverslips, and, in some experiments, incubated 15 minutes at 37°C with 50 nM MitoTracker Red CMXRos, then washed and fixed in 4% PFA for 10 minutes, and washed and additionally fixed in ice-cold methanol for 1 minute. Cells were permeabilized and blocked in 5% BSA and 0.1% Triton X-100 in PBS for 45 minutes, then incubated overnight at 4°C with rabbit polyclonal antibody against Human ANT4 (Novus #NBP1-89074, used at .08 µg/mL) and, in some experiments, a mouse monoclonal antibody against COXIV (COX4I1) (Proteintech #66110-1-Ig, used at 6.8 µg/mL). After washing, samples were incubated with secondary antibodies (Jackson Alexa Fluor 647 AffiniPure Donkey Anti-Rabbit IgG (H+L) (code 711-605-152) at a dilution of 1:1000, and Jackson ImmunoResearch anti-mouse Cy3 or Molecular Probes A10521 goat anti-mouse Cy3 at a dilution of 1:1000) for 45 minutes, then washed and mounted using ProLong Gold Antifade mountant with DAPI.

Cells were imaged on an Olympus FV3000 inverted laser scanning confocal microscope, using an Olympus UPLSAPO Super Apochromat 60x oil immersion objective (NA 1.35) and Olympus Z-81226 immersion oil. Laser Scanning was performed by galvanometer, unidirectionally at a rate of 2µs/pixel with no averaging, with pixel sizes of .207 µm/pixel in the x and y direction. Multiple colors were imaged in line-by-line sequential scanning mode, and multiple z-planes were acquired with a thickness of .47 µm, on a linear-encoded stage. Images displayed are maximum intensity z-stacks of all relevant z-planes. All colors were imaged with a pinhole diameter of 233 µM, and laser illumination was passed through a 10% neutral density filter. DAPI was illuminated by a 405 nm laser set to 3% power, and emitted light was passed through a 430-470 nm emission filter and detected with a photomultiplier tube (PMT) set to 500V. Cy3 was illuminated by a 561 nm laser set to 4% power, with a 570-620 nm emission filter and a PMT set to 500V. Alexa 674 was illuminated by a 642 nm laser set to 4% power, with a 650-750 nm emission filter and a PMT set to 550V.

## Super-resolution Microscopy

ICC slides made as described above were imaged using three-dimensional stochastic optical reconstruction microscopy (3D-STORM)<sup>145,146</sup> performed on a home-built set-up using a Nikon CFI Plan Apo λ 100× oil immersion objective (NA 1.45), as described previously<sup>147</sup>. In brief, the sample was mounted with an imaging buffer consisting of 5% (w/v) glucose, 100 mM cysteamine, 0.8 mg ml<sup>-1</sup> glucose oxidase and 40 µg ml<sup>-1</sup> catalase in a Tris HCl buffer (pH 7.5). For two-color imaging of COXIV and ANT4, the two targets were labeled by Alexa Fluor 647 and CF568, respectively, and were imaged sequentially using 647- and 560-nm excitation lasers. These lasers were passed through an acousto-optic tunable filter and illuminated a few micrometers into the sample at around 2 kW cm<sup>-2</sup>, thus photoswitching most of the labeled dye molecules in the sample into the dark state while allowing a small, random fraction of molecules to emit across the wide-field over different camera frames. Single-molecule emission was passed



through a cylindrical lens of focal length 1 m to introduce astigmatism<sup>146</sup>, and recorded with an Andor iXon Ultra 897 EM-CCD camera at a frame rate of 110 Hz, for a total of around 50,000 frames per image. Data acquisition used publicly available software (<https://github.com/ZhuangLab/storm-control>). The raw STORM data were analyzed using Insight3 software<sup>146</sup> according to previously described methods<sup>145,146</sup>. Secondary antibodies used: Alexa Fluor 647-labelled goat anti-mouse (Invitrogen, A21236, 1:400) and donkey anti-rabbit (Jackson ImmunoResearch, 711-005-152, 1:70) conjugated with CF568 succinimidyl ester (Biotium, 92131).

## Western Blotting

Human Sperm or HEK293 cells were lysed by addition of RIPA<sup>++</sup> Buffer (composition: 50mM Tris HCl, pH 7.4; 150mM NaCl; 1% Triton X-100; 0.5% Sodium Deoxycholate; 0.1% Sodium Dodecyl Sulfate; 1 mM EDTA; 10% glycerol; with Pierce Protease inhibitor tablet or solution added to manufacturer's instructions), then homogenized by 25 passes through a 21-gauge or smaller syringe, then shook on ice for 30 minutes, and centrifuged at 12000 rpm at 4°C for 20 minutes, after which the supernatant was collected and frozen at -80°C. After thawing, protein concentration was assessed using a Pierce Rapid Gold BCA Protein Assay Kit, per manufacturer instructions, and measured on a Biotek Synergy H4 Hybrid plate reader. A target of 30µg of protein was mixed with 4x Laemmli Buffer and Beta-Mercaptoethanol, heated for 10 minutes at 99°C, then loaded to each well of a precast 4-20% mini-Protean TGX gel (Bio-Rad), and run in an electrophoresis chamber until ladder bands were well-resolved. Transfer onto a PVDF membrane was accomplished with an Invitrogen iBlot Dry Blotting System, following manufacturer instructions, at 20V for 7 minutes. After washing 3x with PBS with 0.1% Tween (PBST), the membrane was blocked in 3% Bovine Serum Albumin for 15-30 minutes, then incubated rocking with primary antibody overnight at 4°C. The following day, the membrane was washed 3x with PBST, and incubated with a 1:15000 dilution of HRP-conjugated Abcam Ab6721 Goat pAb anti-Rabbit IgG secondary antibody for one hour at room temperature. After 3x PBST washes and 2x PBS washes, bands were visualized using a Promethues ProSignal Pico kit, per instructions, and imaged in a ProteinSimple FluorChem M. Afterwards, images were inverted, rotated, and cropped in ImageJ 1.52a.

## Data Availability:

All data used to support the conclusions in this study appears in the main and supplementary figures.

## Acknowledgments:

This work was furthered by the support and guidance of Dr. Denise Schichnes, using the equipment of the CNR Biological Imaging Facility at the University of California, Berkeley. Research reported in this publication was supported in part by the National Institutes of Health S10 program under award number 1S10OD018136-01. The content is solely the responsibility of the authors and does not necessarily represent the official views of the National Institute of Health. The authors also wish to thank Dr. Liliya Gabelev Khasin, Dr. Caroline Williams, and Dr. Lisa Treidel, and Dr. Erwin Goldberg for their assistance with this project.

This work was supported by an Irving H. Wiesenfeld Fellowship administered by the UC Berkeley Center for Emerging and Neglected Diseases to W.M.S., a Male Contraceptive Initiative Graduate Fellowship to P.V.L. and Liliya Gabelev Khasin, NIH NICHD grant K99HD104924 to S.T., NIGMS grant R35GM136415 to Y.K., Pew Biomedical Scholars Award to P.V.L. and K.X. and Bakar Fellow Spark Award to P.V.L. This material is based upon work supported by the National Science Foundation Graduate Research Fellowship Program, given to W.M.S. under grant numbers DGE 1752814 and DGE 2146752. Any opinions, findings, and conclusions or recommendations expressed in this material are those of the author(s) and do not necessarily reflect the views of the National Science Foundation.

### **Abbreviations:**

ANT: Adenine nucleotide translocase  
ALH: Amplitude of lateral head displacement  
ATP: Adenosine triphosphate  
AUC: Area under the curve  
BAM15: (N5,N6-bis(2-Fluorophenyl)-[1,2,5]oxadiazolo[3,4-b]pyrazine-5,6-diamine)  
BAPTA: (1,2-bis(o-aminophenoxy)ethane-N,N,N',N'-tetraacetic acid)  
BSA: Bovine serum albumin  
CATR: Carboxyatractyloside  
COXIV: Cytochrome c oxidase subunit 4 isoform 1, mitochondrial  
DNP: 2, 4, Dinitrophenol  
EGTA: (ethylene glycol-bis( $\beta$ -aminoethyl ether)-N,N,N',N'-tetraacetic acid)  
FCCP: Trifluoromethoxyphenylhydrazine  
FDA: Food and Drug Administration  
HEPES: (4-(2-hydroxyethyl)-1-piperazineethanesulfonic acid)  
HRP: Horseradish peroxidase  
HS: High Saline  
HTF: Human Tubal Fluid  
ICC: Immunocytochemistry  
IMM: Inner mitochondrial membrane  
KSOM: Potassium-supplemented simplex optimized medium  
LIN: Linearity  
MES: 2-(N-morpholino)ethanesulfonate.  
MMP: Mitochondrial membrane potential  
NEN: Niclosamide Ethanolamine  
NMDG: N-methyl-D-glucamine  
PI: propidium iodide  
PMT: Photomultiplier tube  
PVDF: polyvinylidene difluoride  
STORM: Stochastic optical reconstruction microscopy  
Tris: tris(hydroxymethyl)aminomethane  
VCL: Curvilinear velocity

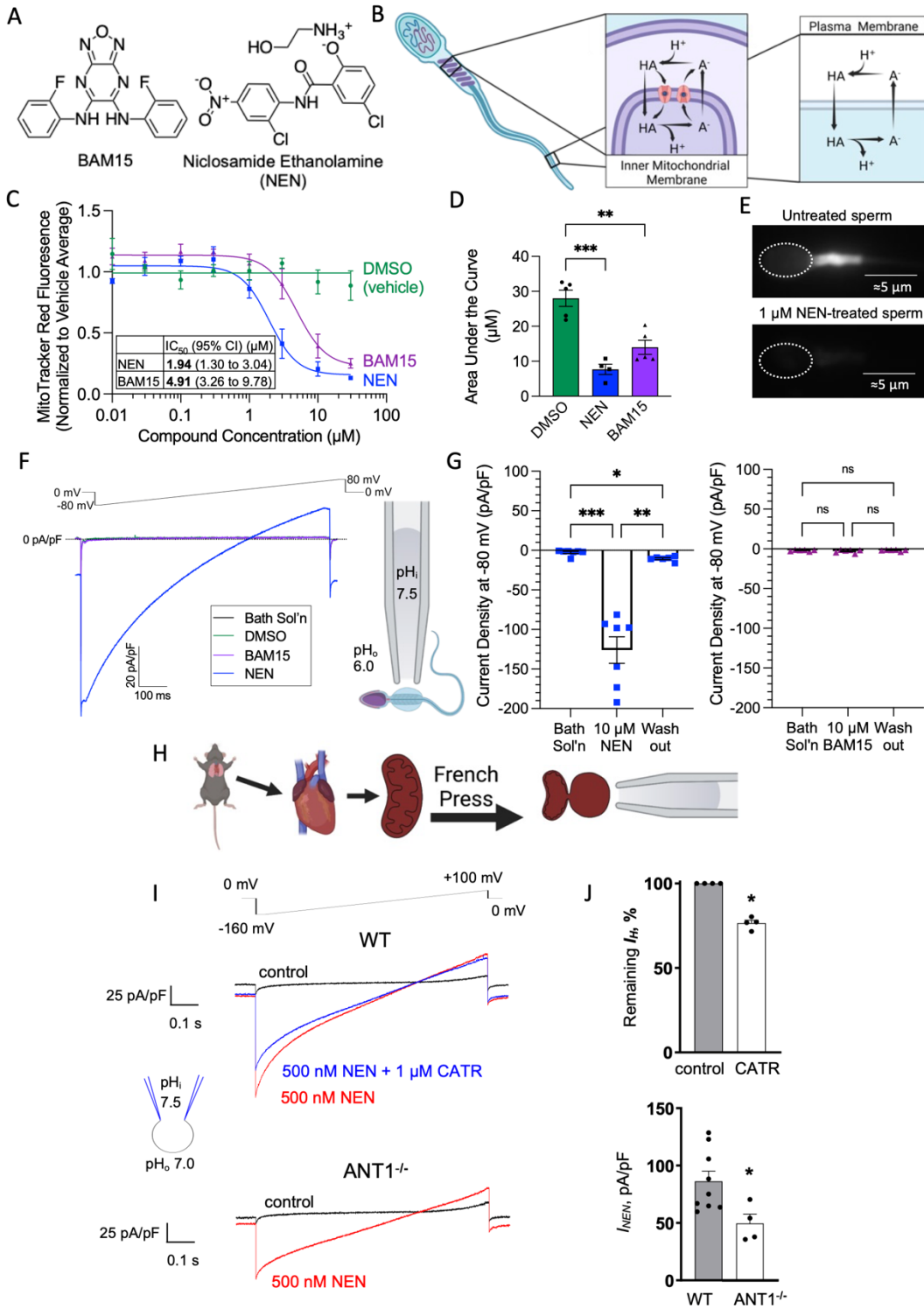


**Figure 1: BAM15 specifically uncouples human sperm mitochondria, while NEN uncouples both sperm mitochondria and plasma membrane.** **A)** Chemical structures of BAM15 and NEN. **B)** Model showing the possible mechanisms of action of small molecule uncouplers in the sperm mitochondria and plasma membrane. **C)** Effects of NEN and BAM15 on human sperm mitochondrial potential as measured by MitoTracker Red fluorescence, normalized to average fluorescence of the DMSO vehicle. Nonlinear least squares regression performed on NEN and BAM15 using an unweighted [inhibitor] vs. response four parameter model. DMSO data fitted to a horizontal line, based on the results of a regression model comparison using the Extra Sum-of-squares F Test. **D)** Area Under the Curve (AUC) analysis for data in C. Error bars represent SEM, and each data point represents the area under the curve for all concentrations of one biological replicate. Statistical significance calculated using Dunnett's multiple comparisons test. **E)** Representative fluorescence micrographs of sperm cells treated with MitoTracker Red CMX-Ros. **F) Left,** Representative electrophysiological traces showing the effect of vehicle and uncouplers on human sperm membrane  $H^+$  current density. **Right,** diagram of sperm electrophysiology setup. Cytoplasmic droplet is magnified for visibility. **G)** Quantification of maximal current densities in the presence of 10  $\mu$ M NEN (left) and BAM15 (right) at a voltage of -80 mV. Error bars represent SEM, and significance calculated using Tukey's Multiple Comparisons Test. **H)** Diagram of mouse heart mitoplast isolation and preparation for whole-organelle inner membrane electrophysiology. **I)** Representative whole-organelle electrophysiological traces of  $H^+$  current density in response to voltage ramp protocols performed on mouse heart mitoplasts. Top, Wildtype; Bottom, ANT1 knockout. **J)** Top, Quantification of NEN-induced  $H^+$  current across mitochondrial inner membrane before and after application of 1  $\mu$ M CATR, a known ANT inhibitor. Bottom, Quantification of  $H^+$  current density induced by 500 nM NEN in wildtype and ANT1-knockout mouse heart mitoplasts. Significances calculated by Student's unpaired t-test.

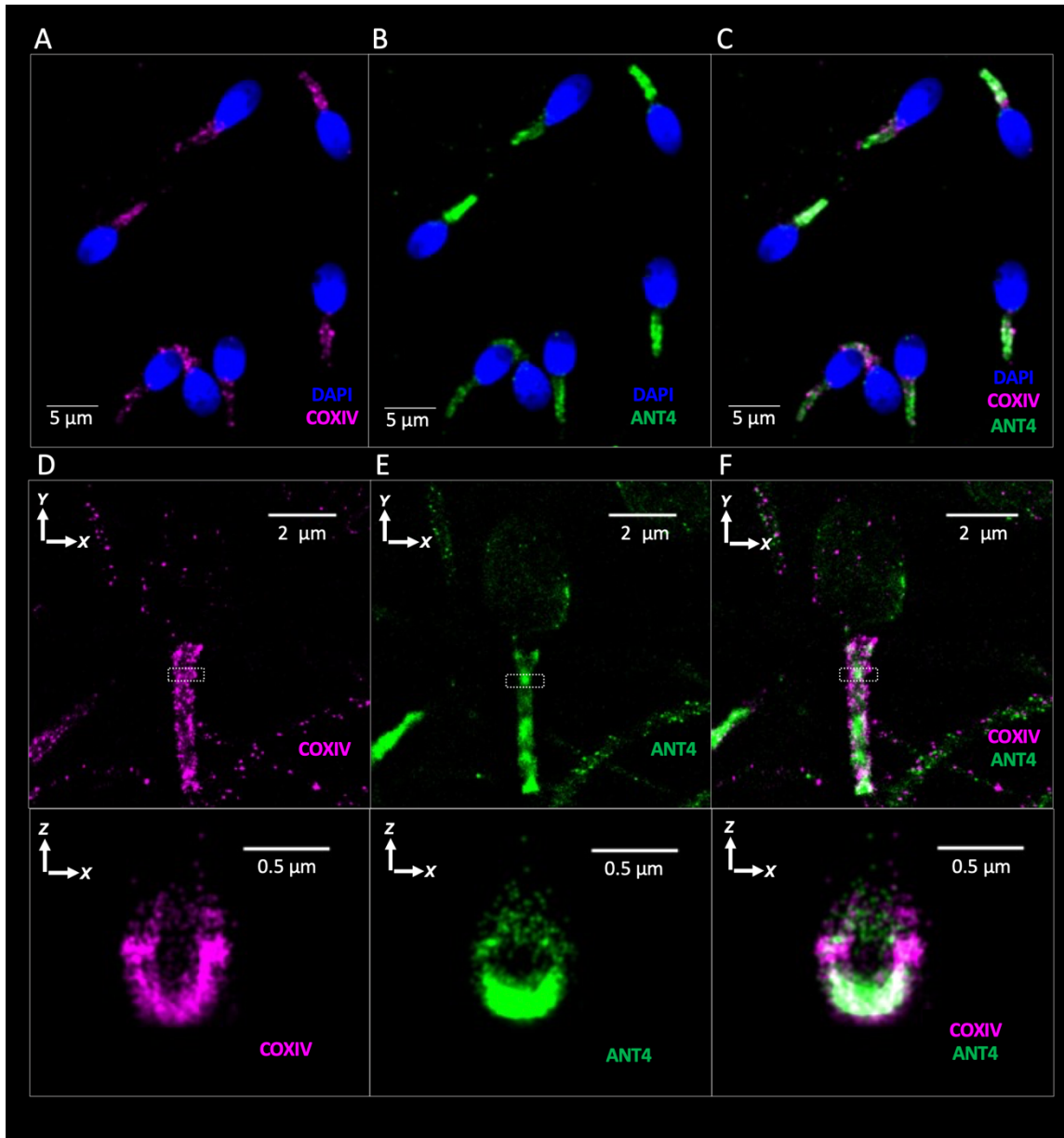


**Figure 2: ANT4 is located in the human sperm mitochondria.** A-C) Confocal microscopy of human sperm immunocytochemistry showing localization of COXIV (magenta), ANT4 (green), and DAPI (blue) D-E) STORM super-resolution microscopy of human sperm cells showing localization of COXIV (magenta) and ANT4 (green). Top panels: overhead view of sperm cells. Bottom panels: transverse plane of midpiece area indicated in top panels by white dotted box.

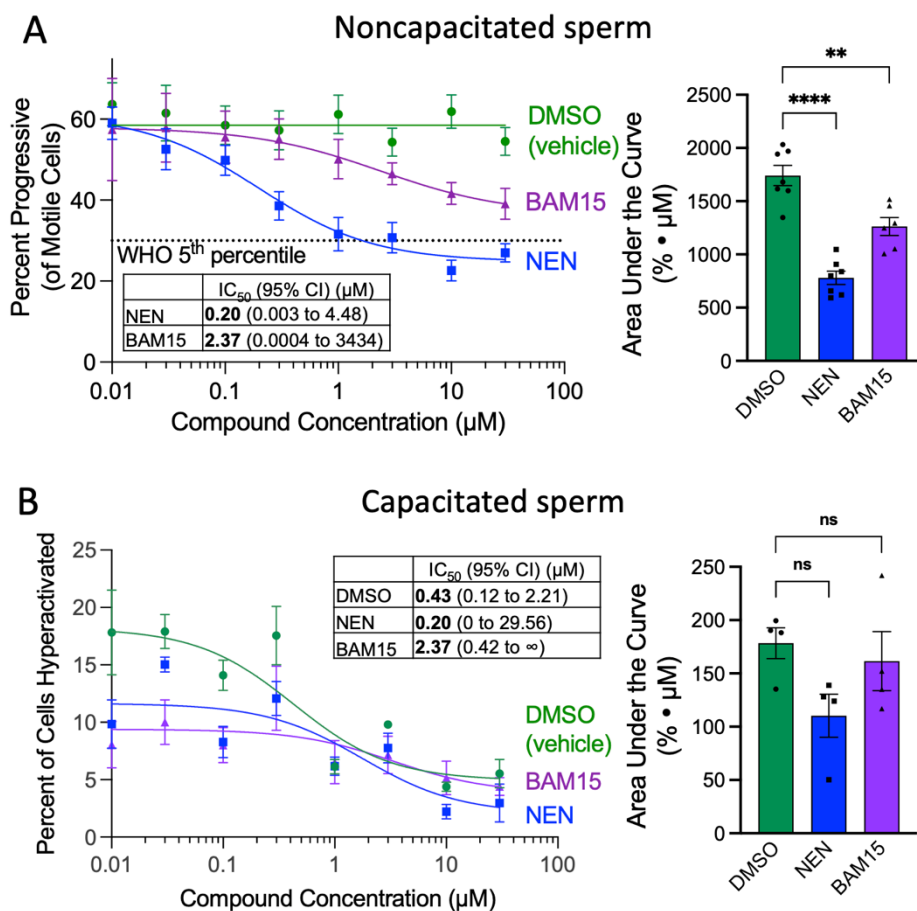


**Figure 3: Effects of NEN and BAM15 on human sperm motility and hyperactivity as measured by Computer-Aided Sperm Analysis. A) Left,** Effects of NEN and BAM15 on human sperm progressive motility. Data points represent the average of  $\geq 500$  sperm cells. Four-parameter nonlinear least squares regression performed, weighted by  $1/Y^2$ . Horizontal line fitted to DMSO data based on the results of a regression model comparison using the Extra Sum-of-squares F Test. **Right,** Area Under the Curve quantification for the graph at left. Each data point represents the area under the curve for all concentrations of one biological replicate. **B) Left,** Effects of compounds on human sperm hyperactivity. Three-parameter nonlinear least squares regression performed, weighted by  $1/Y^2$ . Data points represent the average of  $\geq 200$  sperm cells. To simplify the graph, the amount of DMSO vehicle is shown as the concentration of compound that would have been delivered by that amount of DMSO. Based on dilution procedures, the IC<sub>50</sub> shown corresponds to an actual DMSO concentration of .0043%. **Right,** Area Under the Curve quantification for the graph at left. Each data point represents the area under the curve for all concentrations of one biological replicate. Error bars in all plots represent SEM. Statistical significance in AUC analyses calculated using Dunnett's multiple comparisons test. Units in all AUC plots are the products of the x and y units in the relevant dose-response plot.

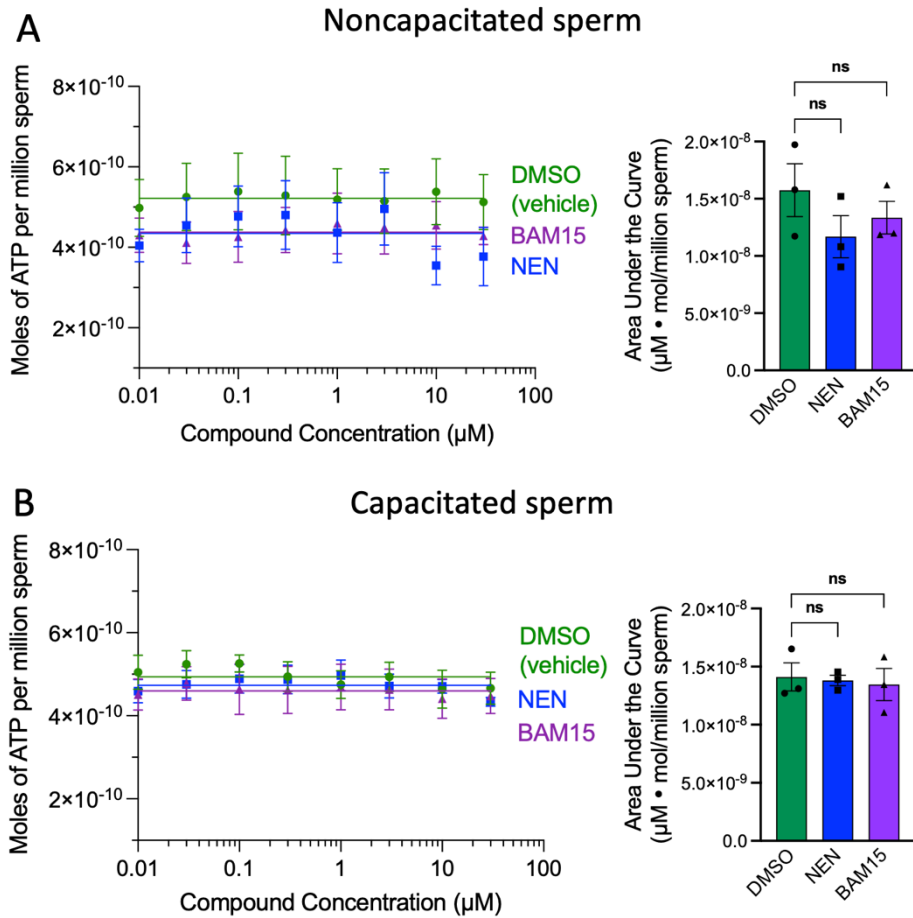


**Figure 4: Effects of small molecule uncouplers on human sperm ATP production. A) Left,** quantification of ATP content of non-capacitated human sperm treated with compounds for 30 minutes. **Right,** area under the curve analysis of the plot to the left. Each data point represents the area under the curve for all concentrations of one biological replicate. **B) Left,** quantification of ATP content of human sperm capacitated in the presence of compounds. **Right,** area under the curve analysis of the plot to the left. Each data point represents the area under the curve for all concentrations of one biological replicate. Error bars in all plots represent SEM. Statistical significance in AUC analyses calculated using Dunnett's multiple comparisons test. Units in all AUC plots are the products of the x and y units in the relevant dose-response plot.

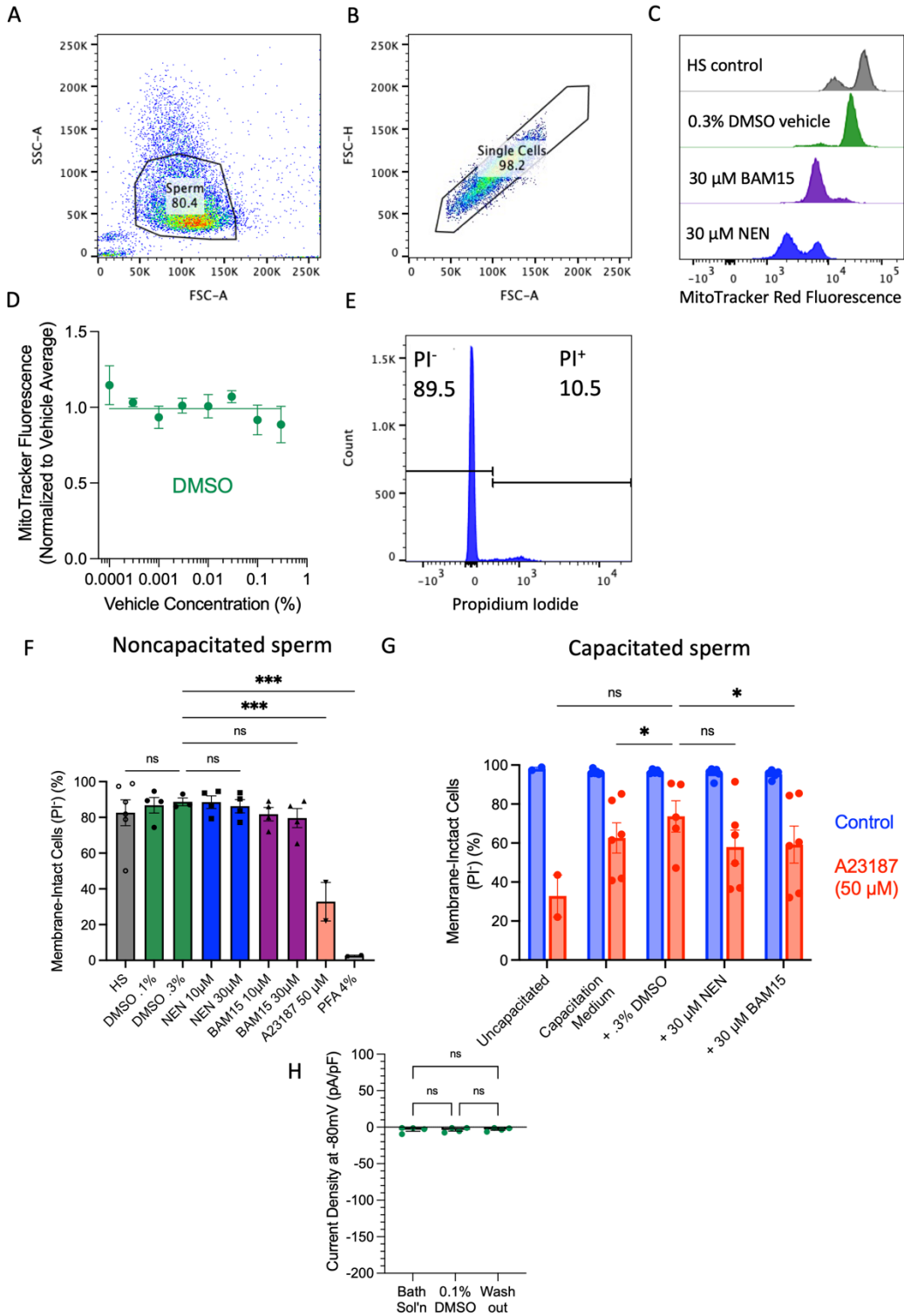
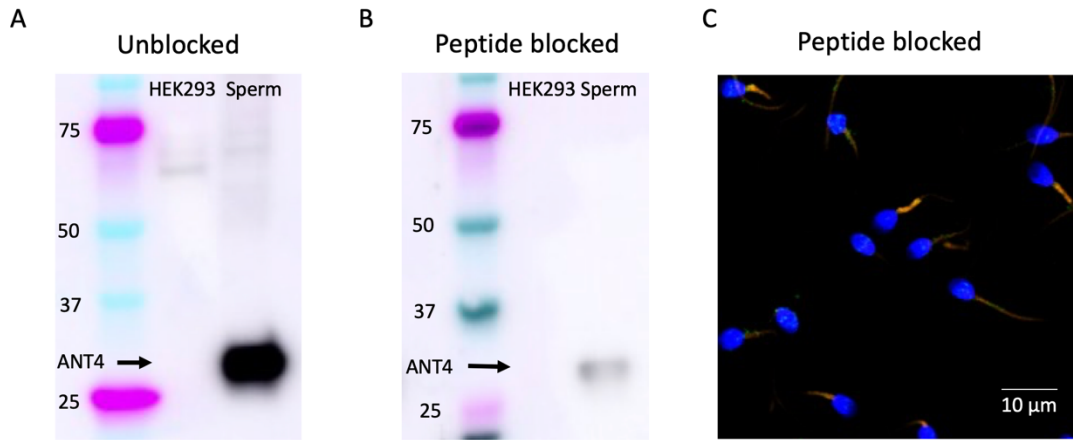


**Figure S1. Validation of flow cytometric assessment of human sperm mitochondrial membrane potential.** **A** and **B**) Representative gating logic for flow cytometry experiments, isolating individual sperm cells from debris (**A**) and aggregations (**B**). **C**) Representative flow cytometry histograms for MitoTracker Red CMX-Ros Mitochondrial Membrane Potential



Assays. **D)** Effect of DMSO vehicle on MitoTracker fluorescence. Horizontal line fitted to data. **E)** Representative flow cytometry result of propidium iodide vitality assay. **F)** Percent of propidium iodide-excluding noncapacitated sperm cells (membrane intact) after 30-minute incubation with compounds, as measured by flow cytometry. Each data point represents the average of 10,000 cells. All conditions were compared to DMSO .3% using a matched mixed-effect model and Dunnett's Multiple Comparisons Test. **G)** Percent of propidium iodide-excluding sperm cells after a  $\geq 3$  hour incubation with compounds in capacitating media, and a 30 minute incubation with control media (blue) or 50  $\mu$ M A23187 calcium ionophore (red). Each data point represents the average of 10,000 cells. All error bars represent SEM. **H)** 0.1% DMSO has no effect on sperm plasma membrane current densities. Significance calculated using Tukey's multiple comparisons test.



C-F) DAPI MitoTracker Red CMX-Ros ANT4

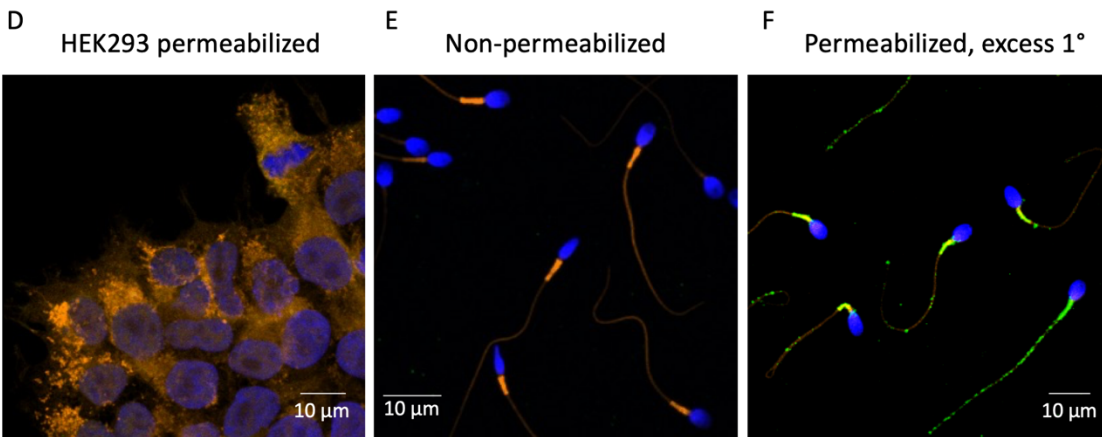


**Figure S2: Human ANT4 polyclonal antibody validation.** A,B) hANT4 Western blot of HEK293 cells and human sperm. A) unblocked; B) blocked with immunizing peptide. C) ICC of permeabilized human sperm incubated with hANT4 pAb preblocked with immunizing peptide and 50 nM Mitotracker Red CMX-Ros. D) ICC of permeabilized HEK293 cells labelled as in C. E) ICC of non-permeabilized human sperm labelled as in C. F) Permeabilized human sperm cells incubated with excess hANT4 pAb primary antibody (0.4 μg/mL) and 50 nM Mitotracker Red CMX-Ros. In C-F, Orange – Mitotracker Red CMX-Ros, Blue – Dapi, Green – hANT4. All images are maximum intensity projections of sequential confocal z-slices.

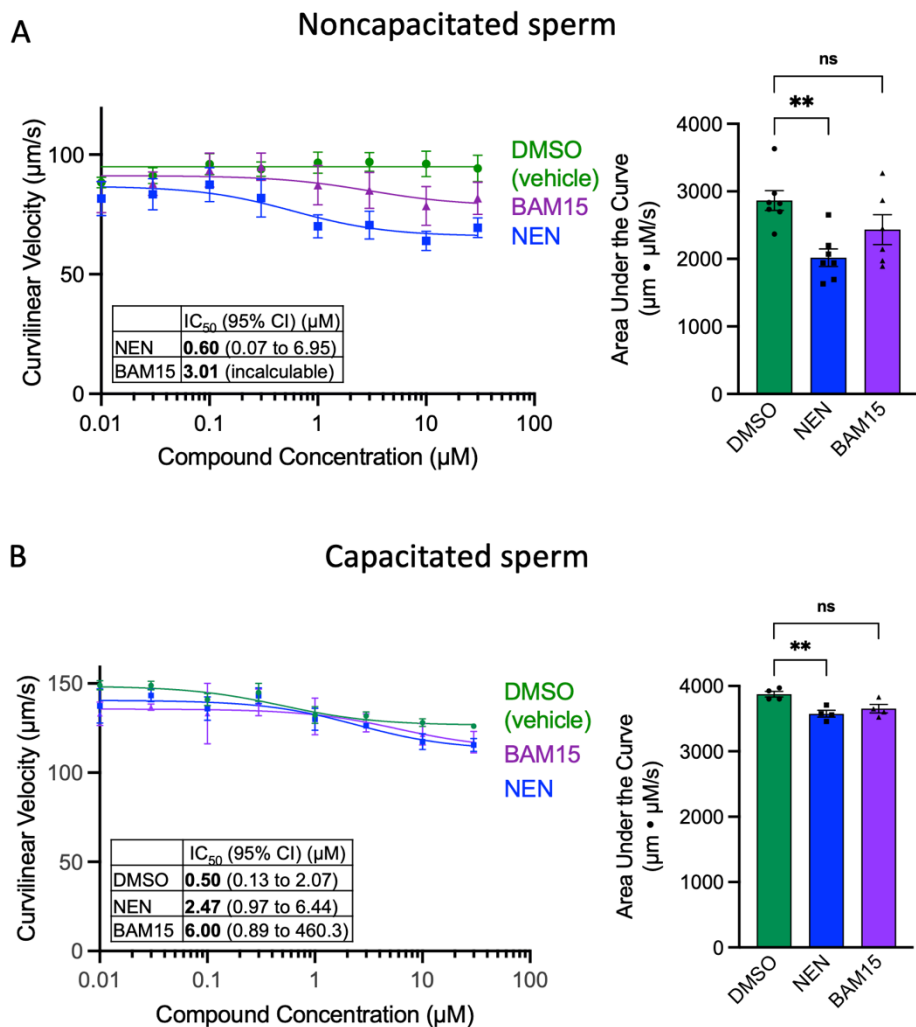


**Figure S3: Effects of compounds on human sperm curvilinear velocity as measured by computer-aided sperm analysis.** **A)** Curvilinear velocity analysis of noncapacitated human sperm cells. **Left,** Each data point represents the average curvilinear velocity of at least 500 sperm cells. Nonlinear least squares regression performed for NEN and BAM15 using an unweighted three-parameter model. Simple linear regression performed for DMSO. **Right,** Area Under the Curve analysis for data at left. Each data point represents the area under the curve of one biological replicate. Statistical significance calculated using Dunnett's multiple comparisons test. **B)** Curvilinear Velocity analysis of capacitated human sperm cells. **Left,** Nonlinear Regression performed for all three compounds using a three-parameter model weighted by  $1/Y^2$ . To simplify the graph, the amount of DMSO vehicle is shown as the concentration of compound that would have been delivered by that amount of DMSO. Based on dilution procedures, the IC<sub>50</sub> shown corresponds to an actual DMSO concentration of .005%. **Right,** Area Under the Curve analysis for data at left. Statistical significance calculated using Dunnett's multiple comparisons test. Units in all AUC plots are the products of the x and y units in the relevant dose-response plot.

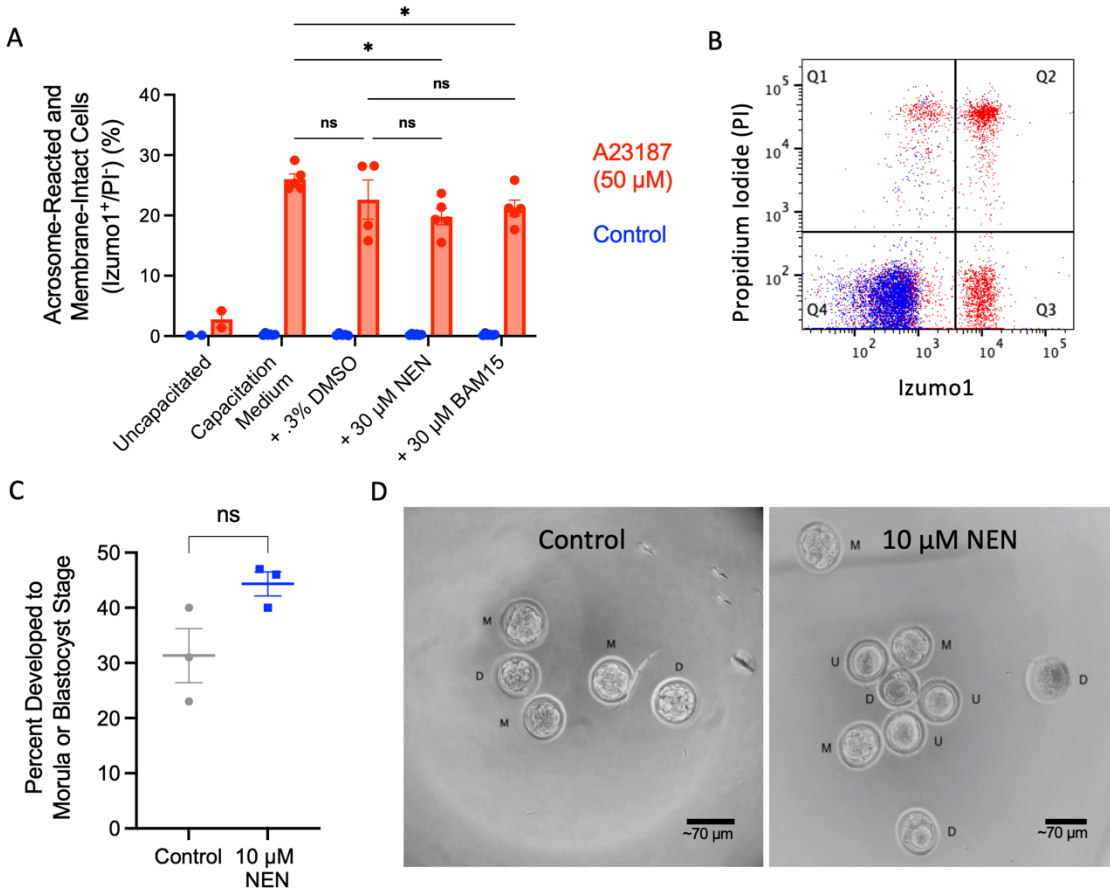


**Figure S4: NEN and BAM15 have no effect on human sperm acrosome reaction competence, and NEN has no effect on Mouse IVF success** **A**) Percentage of unfixed, capacitated human sperm cells that were acrosome-reacted and membrane-intact (Izumo1<sup>+</sup>/Propidium Iodide<sup>-</sup>) as measured by flow cytometry, after incubation with and without the calcium ionophore A23187. Each data point represents the percentage of 100,000 cells showing this fluorescence pattern. Error bars represent SEM, and significance was calculated by matched mixed-effect model Tukey's multiple comparisons test, with individual variances computed for each comparison. All combinations were compared, but for clarity, not all comparisons are shown. **B**) Representative data plots from one run of flow cytometry, comparing ionophore A23187-treated (red) and control cells (blue). **C**) Quantification of mouse eggs that developed to morula or blastocyst stage after *In vitro* fertilization (IVF) using SMU-treated sperm. Significance calculated using a one-tailed ratio paired t-test. **D**) Representative micrographs of mouse embryos 3.5 days after IVF. **Left**, oocytes exposed to control sperm; **Right**, oocytes exposed to 10  $\mu$ M NEN-treated sperm. M - Morula, D - Dead, U - Unfertilized.

# Chapter 4: Human sperm TMEM95 binds eggs and facilitates membrane fusion

## Authors and Affiliations

Shaogeng Tang<sup>a,b,1</sup>, Yonggang Lu<sup>d,e,1</sup>, Will M. Skinner<sup>h</sup>, Mrinmoy Sanyal<sup>a,b</sup>, Polina V. Lishko<sup>i,j</sup>, Masahito Ikawa<sup>d,e,f,g,\*</sup>, Peter S. Kim<sup>a,b,c,\*</sup>

<sup>a</sup> Department of Biochemistry, Stanford University School of Medicine, Stanford, CA 94305

<sup>b</sup> Sarafan ChEM-H, Stanford University, Stanford, CA 94305

<sup>c</sup> Chan Zuckerberg Biohub, San Francisco, CA 94158

<sup>d</sup> Immunology Frontier Research Center, Osaka University, Osaka 565-0871, Japan

<sup>e</sup> Department of Experimental Genome Research, Research Institute for Microbial Diseases, Osaka University, Osaka 565-0871, Japan

<sup>f</sup> Center for Infectious Disease Education and Research, Osaka University, Osaka 565-0871, Japan

<sup>g</sup> Laboratory of Reproductive Systems Biology, Institute of Medical Science, The University of Tokyo, Tokyo 108-8639, Japan

<sup>h</sup> Endocrinology Graduate Group, University of California, Berkeley, Berkeley, CA 94720

<sup>i</sup> Department of Molecular and Cell Biology, University of California, Berkeley, Berkeley, CA 94720

<sup>j</sup> Center for Reproductive Longevity and Equality, Buck Institute for Research on Aging, Novato, CA 94945

<sup>1</sup> S.T. and Y.L. contributed equally to this work

\* To whom correspondence may be addressed. Emails: P.S.K. [kimpeter@stanford.edu](mailto:kimpeter@stanford.edu), M.I. [ikawa@biken.osaka-u.ac.jp](mailto:ikawa@biken.osaka-u.ac.jp)

## Classification

BIOLOGICAL SCIENCES - Developmental Biology

PHYSICAL SCIENCES - Biophysics and Computational Biology

## Keywords

TMEM95, Membrane fusion, Sperm-egg fusion, Fertilization

## Abstract

*Tmem95* encodes a sperm acrosomal membrane protein, whose knockout has a male-specific sterility phenotype in mice. *Tmem95* knockout murine sperm can bind to, but do not fuse with eggs. How TMEM95 plays a role in membrane fusion of sperm and eggs has remained elusive. Here, we utilize a sperm penetration assay as a model system to investigate the function of human TMEM95. We show that human TMEM95 binds to hamster egg membranes, providing evidence for a TMEM95 receptor on eggs. Using X-ray crystallography, we reveal an evolutionarily conserved, positively charged region of TMEM95 as a putative receptor-binding surface. Amino-acid substitutions within this region of TMEM95 ablate egg-binding activity. We identify monoclonal antibodies against TMEM95 that reduce the number of human sperm fused with hamster eggs in sperm penetration assays. Strikingly, these antibodies do not block binding of sperm to eggs. Taken together, these results provide strong evidence for a specific, receptor-mediated interaction of sperm TMEM95 with eggs and suggest that this interaction may have a role in facilitating membrane fusion during fertilization.

## Significance statement

Membrane fusion of sperm and eggs is pivotal in sexual reproduction. *Tmem95* knockout mice produce sperm that can bind to, but do not fuse with eggs. How sperm TMEM95 facilitates membrane fusion with eggs was unknown. We show here that human TMEM95 binds eggs. Our crystal structure of TMEM95 suggests a region where this binding may occur. We develop monoclonal antibodies against TMEM95 that impair sperm-egg fusion but do not block sperm-egg binding. Thus, we propose that there is a receptor-mediated interaction of sperm TMEM95 with eggs, and that this interaction may have a direct role in membrane fusion. Our work suggests avenues for the identification of the TMEM95 egg receptor and may enable the development of infertility treatments and contraceptives for humans.

## Introduction

Fertilization is a central event of sexual reproduction, but how sperm and eggs bind to and fuse with one another has been largely undefined. Sperm IZUMO1<sup>148</sup> and egg JUNO<sup>149</sup> mediate the only known cell surface interaction between mammalian gametes. Recent reports suggested that *Tmem95* (encoding transmembrane protein 95) mutant cattle<sup>150,151</sup> and mice<sup>77</sup> exhibit impaired male fertility, and their sperm have defects in fusion with eggs; *Tmem95* knockout mice show male-specific sterility<sup>152,153</sup>. *Tmem95* knockout murine sperm, which have normal expression and localization of IZUMO1, can bind to, but do not fuse with eggs<sup>152,153</sup>. *Tmem95* encodes a sperm acrosomal membrane protein, which re-localizes to the equatorial segment of the sperm head<sup>150,153</sup> where membrane fusion with the egg takes place<sup>154,155</sup>. These observations shed light on a potential role of TMEM95 in sperm-egg membrane fusion.

Humans also express *TMEM95* transcripts<sup>57</sup>. In this study, we utilized the sperm penetration assay<sup>97</sup>, a clinical laboratory test that evaluates fusion of human sperm with eggs from Syrian golden hamsters (*Mesocricetus auratus*), as a model system. TMEM95 is a type-I single-pass transmembrane protein<sup>150,152,153</sup>. Motivated by a hypothesis that the ectodomain of TMEM95 binds to eggs through a specific, membrane-bound receptor on eggs, we found that a bivalent TMEM95 ectodomain protein binds hamster eggs, providing direct evidence for a TMEM95 receptor on eggs. The 1.5 Å-resolution X-ray crystal structure of TMEM95 we describe here reveals an evolutionarily conserved region of the protein with a positively charged surface. Amino-acid substitutions within this region of TMEM95 ablate egg binding. We speculate that this region serves as an egg-receptor binding site for TMEM95.

We also found that human TMEM95 plays a role in membrane fusion. After generating two monoclonal antibodies that bind to different epitopes of TMEM95, we observed that neither antibody blocks binding of human sperm to hamster eggs, but both could inhibit membrane fusion of sperm with eggs. Taken together, our results provide evidence for a specific, receptor-mediated interaction of human sperm TMEM95 with eggs and inform strategies for the identification of this receptor. We propose that the interaction of TMEM95 with eggs facilitates membrane fusion of human sperm and eggs.

## Results

### A bivalent TMEM95 protein binds hamster eggs

We hypothesized that the ectodomain of TMEM95 mediates a cell-surface interaction of sperm with eggs. To monitor the interaction between TMEM95 and eggs, we designed and produced TMEM95-Fc, a fusion protein of the ectodomain of human TMEM95 and the fragment crystallizable region of human immunoglobulin G1 (IgG1) (*SI Appendix*, Fig. S1A). TMEM95-Fc contains two copies of the TMEM95 ectodomain (Fig. 1B) and the Fc confers increased avidity for binding over monomeric TMEM95. Given that human sperm can fuse with eggs from Syrian golden hamsters<sup>97,156</sup>, we incubated the Fc or TMEM95-Fc proteins with hamster eggs, whose surrounding zona pellucida and cumulus cells were removed. Using a fluorescently labeled anti-Fc antibody, we detected binding to the hamster egg surface only with TMEM95-Fc, not Fc alone (Fig. 1A and B and *SI Appendix*, Fig. S1F). We did not observe binding of TMEM95-Fc to murine eggs (*SI Appendix*, Fig. S1B). To confirm that our labeling approach can also detect known protein-protein interactions of sperm with eggs, we next surveyed IZUMO1-Fc on hamster eggs<sup>157</sup>, a fusion protein of human sperm IZUMO1<sup>148</sup> ectodomain with Fc. While IZUMO1-Fc binds eggs, the IZUMO1<sup>W148A</sup>-Fc variant does not (Fig. 1C and D). The substitution of W148A ablates the interaction of IZUMO1 with JUNO<sup>158,159</sup> (*SI Appendix*, Fig. S1C-I), the egg receptor of IZUMO1<sup>149</sup>. Our results show that TMEM95 binds egg plasma membranes and suggest the presence of a receptor for TMEM95 on eggs.

### The structure of TMEM95 is homologous to that of the N-terminus of IZUMO1

To understand how TMEM95 binds eggs, we determined a crystal structure of the TMEM95 ectodomain to 1.5 Å resolution using multi-wavelength anomalous X-ray diffraction (Fig. 2A and *SI Appendix*, Fig. S2A and Table S1). TMEM95 adopts an elongated rod shape, comprised of an N-terminal  $\alpha$ -helical bundle (residues 17-110) and a C-terminal  $\beta$ -hairpin region (residues 111-135) (Fig. 2C). TMEM95 shows homology to the N-terminus of IZUMO1<sup>158,159</sup> with a C $\alpha$  root-mean-square deviation of 7.2 Å and to the N-terminus of SPACA6<sup>160</sup>. Unlike IZUMO1 and SPACA6, TMEM95 does not have an immunoglobulin-like domain at the C-terminus (Fig. 2D). The helical bundle of TMEM95 has three helices ( $\alpha$ 1,  $\alpha$ 3, and  $\alpha$ 4) and a coil (loop 2) that are arranged in an anti-parallel manner ( $\alpha$ 1-loop 2 and  $\alpha$ 3- $\alpha$ 4). TMEM95 has three unique disulfide bonds: C35-C45 between  $\alpha$ 1 and loop 2 (*SI Appendix*, Fig. S2B), and C105-C134 and C109-C128 adjacent to the  $\beta$ -hairpin (Fig. 2B-D).

JUNO does not act as an egg receptor for TMEM95<sup>152,153</sup>. A conserved N-linked glycan in the  $\beta$ -hairpin of TMEM95 (*SI Appendix*, Fig. S2E and J) could cause a clash if TMEM95 were to make a contact similar to that of IZUMO1 with JUNO (*SI Appendix*, Fig. S2C and D). However, even if this glycan is removed by the treatment with N-glycosidase PNGaseF, TMEM95-Fc binds egg plasma membranes but does not bind JUNO (*SI Appendix*, Fig. S2F-I).



## **A conserved surface of TMEM95 is a putative receptor-binding site**

To gain further insights into the TMEM95 interaction with eggs, we analyzed the protein sequences of TMEM95 orthologs and mapped the degree of conservation for each amino acid onto the structure of TMEM95. We found that the area surrounding the N-glycan is variable (Fig. 3A), while the opposite side harbors a conserved (Fig. 3B), positively charged surface (Fig. 3C).

To examine whether the conserved, charged surface is critical for binding of TMEM95 to eggs, we produced TMEM95-Fc proteins that carry amino-acid substitutions of arginine residues (Fig. 3D and *SI Appendix*, Fig. S3A and B). These TMEM95 variants have melting temperatures comparable to that of the wild-type TMEM95-Fc protein (*SI Appendix*, Fig. S3C). When incubated with hamster eggs, the R70A, R73A, and R70A R73A TMEM95-Fc variants showed drastically reduced egg-binding activities compared to the wild-type (Fig. 3E-H and *SI Appendix*, Fig. S3D). Our data suggest that the identified evolutionarily conserved, positively charged surface of TMEM95 may function as a receptor-binding site.

## **Monoclonal antibodies detect TMEM95 in human sperm**

To generate reagents to investigate the functions of TMEM95 in human sperm, we immunized mice with the TMEM95 ectodomain (*SI Appendix*, Fig. S4A-C) and generated hybridoma cell lines that produce TMEM95 ectodomain-specific monoclonal antibodies, 3A01 and 6B08 (*SI Appendix*, Table S2). We used biolayer interferometry to assess the binding of the antibodies to TMEM95 (Fig. 4A) and found that 3A01 and 6B08 bind TMEM95 via two non-competing epitopes (Fig. 4B) with association constants of 1.4 nM and 1.3 nM, respectively (*SI Appendix*, Fig. S4D and E). The binding of either 3A01 or 6B08 to TMEM95-Fc does not inhibit its binding to the eggs (*SI Appendix*, Fig. S4G). 3A01 and 6B08 bind similarly to TMEM95-Fc and the R70A and R73A TMEM95-Fc variants (*SI Appendix*, Fig. S4H). These results suggest that the 3A01 and 6B08 antibodies against TMEM95 do not compete for binding of TMEM95 with its egg receptor.

We next performed Western blotting using the TMEM95 antibodies to probe whole cell lysates of human sperm and each could detect a band of ~20 kDa (*SI Appendix*, Fig. S4F), the expected molecular weight of TMEM95. To investigate whether TMEM95 is N-linked glycosylated, we treated the human sperm lysate with PNGaseF and observed a shift in size to ~17.5 kDa (Fig. 4C), consistent with the loss of one glycan. Our results show that TMEM95 is expressed and N-linked glycosylated in human sperm.

Using a similar approach for IZUMO1 (*SI Appendix*, Fig. S5A-C), we generated hybridoma cell lines that produce IZUMO1-specific monoclonal antibodies, 4E04 and 6F02 (Fig. 4D and *SI Appendix*, Table S2). These antibodies both bind IZUMO1 (*SI Appendix*, Fig. S5F, S5J) via two non-competing epitopes (Fig. 4E and *SI Appendix*, Fig. S5D and E). Compared to 4E04-bound IZUMO1-Fc, 6F02-bound IZUMO1-Fc blocks binding of IZUMO1-Fc to eggs (*SI Appendix*, Fig. S5G) and JUNO (*SI Appendix*, Fig. S5H and I). These results suggest that 4E04

and 6F02 bind to different epitopes of IZUMO1, and that the 6F02 epitope overlaps with the IZUMO1-binding site for JUNO.

### **TMEM95 antibodies impair fusion of human sperm to hamster eggs**

To examine whether human TMEM95 plays a role in membrane fusion, we produced the fragments antigen-binding (Fab) of the TMEM95 and IZUMO1 antibodies and tested these in a sperm penetration assay. These Fab fragments bind antigens at nanomolar affinities (*SI Appendix*, Figs. S4E and S5E) and may have less steric effects in membrane fusion than their larger IgG counterparts. We inseminated hamster eggs with human sperm preincubated with the TMEM95 antibody Fab, 3A01 (Fig. 5C) or 6B08 (Fig. 5D). We used an untreated group as a negative control (Fig. 5A) and IZUMO1 antibody Fab 6F02-treatment as a positive control (Fig. 5B). Based on the numbers of bound (Fig. 5E) and fused (Fig. 5F) sperm per egg, we found that the TMEM95 antibody Fab fragments do not block binding of sperm to eggs (Fig. 5E).

However, the averaged numbers of fused sperm per egg significantly decreased from  $9.1 \pm 0.7$  (mean  $\pm$  standard error of the mean, SEM) in the untreated group to  $4.1 \pm 0.9$  ( $p = 0.0002$ ) and  $3.4 \pm 0.6$  ( $p < 0.0001$ ) in the TMEM95 Fab 3A01 and 6B08 groups, respectively (Fig. 5F and *SI Appendix*, Fig. S6A-D). Similarly, we observed that the TMEM95 antibody IgGs do not block sperm-egg binding (*SI Appendix*, Fig. S6E-G), but they decrease the average numbers of fused sperm per egg when compared with a control group treated with pre-immune IgG (*SI Appendix*, Fig. S6H-L). Therefore, the two non-competing TMEM95 monoclonal antibodies do not block sperm-egg binding but impair sperm-egg fusion, suggesting that TMEM95 plays a role in sperm-egg membrane fusion.

## Discussion

### Evidence for a receptor for TMEM95 on eggs

Our results provide strong evidence for the existence of a membrane-bound receptor for sperm TMEM95 on eggs. Although the receptor has yet to be identified, our structural and site-directed mutagenesis studies identify a putative receptor-binding site on TMEM95. This region has a solvent-accessible surface area of  $\sim 1,200 \text{ \AA}^2$ , comparable to protein surfaces that mediate many protein-protein interactions<sup>161,162</sup>. We envision that the TMEM95 receptor is a membrane protein with a negatively charged region on its ectodomain surface. Nevertheless, we cannot rule out potential non-protein receptor candidates with electrostatic negative properties on the egg surface, such as phospholipids and glycans.

The bivalent TMEM95-Fc protein introduced here may be a useful reagent to facilitate the identification of the egg receptor of TMEM95. As cell surface interactions between membrane-bound proteins are often transient and dynamic<sup>149,163</sup>, the avidity of a bivalent protein could serve to stabilize the potentially weak interaction of TMEM95 with its receptor. TMEM95-Fc could therefore be used as a bait for the egg receptor, for example, for co-immunoprecipitation of mammalian eggs (*e.g.* Ref<sup>164</sup>), or for screening cultured cells expressing an egg cDNA library (*e.g.* Ref<sup>149</sup>).

### Potential roles of TMEM95 in membrane fusion

The TMEM95 antibodies used in this study do not ablate binding of TMEM95 to hamster eggs. How would the non-blocking antibodies of TMEM95 inhibit sperm-egg fusion? One possibility is that TMEM95 undergoes structural changes that are important for membrane fusion. Should sperm-egg fusion be accompanied by changes of TMEM95 in protein conformation or oligomeric state, the antibodies raised here against a defined conformation of TMEM95 may trap TMEM95 in a pre-fusion, monomeric state. Notably, early studies have suggested essential structural changes for IZUMO1 (*e.g.*, rearrangement of disulfides, protein dimerization) during sperm-egg membrane fusion<sup>158,165,166</sup>.

Alternatively, or in addition, TMEM95 may assemble into a complex with other sperm proteins, such as a membrane fusogen. Antibody binding to TMEM95 could affect these events and explain the inhibitory results. Additionally, these antibodies might create steric hinderance which could interfere with membrane fusion (note, however, that an anti-IZUMO1 IgG, Mab125, does not block sperm-egg fusion<sup>167</sup>).

Taken together, we conceptualize that sperm-egg membrane fusion involves pairwise cell surface interactions. Sperm IZUMO1 binds egg JUNO, which mediates gamete adhesion, and a receptor-mediated interaction of sperm TMEM95 to the egg takes place; membrane fusion occurs thereafter. We anticipate additional analogous, yet to be identified, interactions between sperm proteins<sup>152,168-171</sup> and their specific egg receptors (Fig. 6).

In summary, our results suggest that human sperm TMEM95 likely plays a direct role in membrane fusion with eggs. Future work is needed to rule out indirect effects of TMEM95

antibodies that inhibit fusion while not blocking sperm-egg binding. More broadly, our work takes steps towards fully understanding the molecular interactions of the fertilization complex and has implications for the development of infertility treatments and contraceptives.

## Materials and methods

### Immunofluorescence microscopy of hamster eggs

Sexually mature female Syrian golden hamsters (Japan SLC Inc.) (approved by the Animal Care and Use Committee of the Research Institute for Microbial Diseases, Osaka University #28-4-2) were superovulated by peritoneal injection of pregnant mare serum gonadotropin and human coagulating gland (20 units for each; ASKA Pharmaceutical). Cumulus-oocyte complexes were extracted from the oviductal ampulla and treated with 1 mg/mL collagenase to remove the cumulus cells and zona pellucida, which yields zona-free eggs. These zona-free eggs were incubated with 200 nM Fc-fusion proteins in Biggers-Whitten-Whittingham medium<sup>97</sup> for 1 h and then stained with goat anti-human IgG Fc antibody DyLight 488 (Invitrogen) at a dilution of 1:50 for 1 h at 37 °C, 5% CO<sub>2</sub>. The eggs were imaged under a Keyence BZ-X810 microscope.

### Protein crystallization of TMEM95

Native TMEM95 proteins were crystallized at room temperature in a sitting-drop vapor diffusion system. 350 nL of 6.8 mg/mL protein was mixed with 350 nL of a reservoir solution of 150 mM NaCl, 20 mM HEPES pH 7.3, 30 mM CaCl<sub>2</sub>, 2% (w/v) PPG-P400, and 22% (w/v) PEG 3,350, over 80 µL of reservoir solution. Native crystals were supplemented with 20% (w/v) PEG 400 before cryo-cooling in liquid nitrogen. For multi-wavelength anomalous diffraction, crystals were grown in 150 mM NaCl, 20 mM HEPES pH 7.3, 10 mM CaCl<sub>2</sub>, 2% (w/v) PPG-P400, and 18% (w/v) PEG 3,350, and were transferred to a solution supplemented with 500 mM SmCl<sub>3</sub> and incubated for ~5 min. The Sm<sup>3+</sup>-bound crystals were washed in a SmCl<sub>3</sub>-free reservoir solution, cryo-protected with 20% PEG 400, and cooled in liquid nitrogen.

### Sperm penetration assay

Sperm penetration assays were performed as previously described<sup>97</sup> with minor changes. Briefly, human semen from healthy donors, who had informed consent, was liquefied for 30 min at room temperature. The sperm were purified by discontinuous Percoll gradients<sup>172</sup> and incubated in Biggers-Whitten-Whittingham medium containing 2.5 µM calcium ionophore for 3 h at 37 °C, 5% CO<sub>2</sub>. The sperm were washed in fresh Biggers-Whitten-Whittingham medium and treated with monoclonal antibodies at 40 µg/mL for 1 h at 37 °C, 5% CO<sub>2</sub>. Motile sperm were manually counted in a hemocytometer under an inverted microscope. Zona-free hamster eggs were inseminated in 100 µL medium drops by the antibody-treated sperm at a density of 3×10<sup>6</sup> motile sperm per mL for 3 h at 37 °C, 5% CO<sub>2</sub>. The eggs were washed in fresh medium, gently flattened by coverslips, and examined under a phase-contrast microscope.

### Expression and purification of the Fc-fusion proteins

The cDNAs encoding human TMEM95 (residues 1-145) or human IZUMO1 (residues 1-255) were subcloned into a pADD2 vector that carries a C-terminal fusion of a TEV protease cleavage site, a human IgG1 Fc, an Avi tag, and a hexa-histidine tag (*SI Appendix*, Table S3). The recombinant Fc-fusion proteins were overexpressed by transient transfection of HEK293F cells (ThermoFisher) cultured at 37 °C, 8% CO<sub>2</sub>. TMEM95-Fc was purified by Ni-NTA affinity purification (Invitrogen), followed by anion exchange using an AKTA pure system by a Mono Q 5/50 GL (Cytiva). IZUMO1-Fc was purified by Protein-A affinity purification using a MabSelect

Prism (Cytiva), followed by anion exchange using a Mono Q 5/50 GL. Purified proteins were stored in a buffer of 150 mM NaCl, 20 mM HEPES pH 7.4.

Tagless IZUMO1 proteins were obtained from IZUMO1-Fc through TEV (Sigma-Aldrich) cleavage overnight at 4 °C. Undigested proteins and the histidine tagged TEV proteases were removed by a MabSelect Prism followed by a HisTrap excel (Cytiva). Tagless IZUMO1 was further purified by gel filtration with a Superdex 200 Increase 10/300 GL (Cytiva) in a buffer of 150 mM NaCl, 20 mM HEPES pH 7.4.

### **Immunofluorescence microscopy of murine eggs**

Sexually mature female B6D2F1 mice (Japan SLC Inc.) (approved by the Animal Care and Use Committee of the Research Institute for Microbial Diseases, Osaka University #Biken-AP-H30-01) were superovulated by peritoneal injection of pregnant mare serum gonadotropin and human coagulating gland (20 units for each; ASKA Pharmaceutical).

Cumulus-oocyte complexes were extracted from the oviductal ampulla and treated with 1 mg/mL collagenase to remove the cumulus cells and zona pellucida, which yields zona-free eggs. These zona-free eggs were incubated with 200 nM TMEM95 in Toyoda-Yokoyama-Hoshi medium<sup>173</sup> for 1 h and then stained with goat anti-human IgG Fc antibody DyLight 488 (Invitrogen) at a dilution of 1:50 for 1 h at 37 °C, 5% CO<sub>2</sub>. The eggs were imaged under a Keyence BZ-X810 microscope.

### **Protein expression and purification of JUNO**

The cDNA encoding human JUNO (residues 20-227) was subcloned into a baculoviral vector pACgp67a that carries a signal sequence of MVSAIVLYVLLAAAHSFA and C-terminal hexa-histidine tag (*SI Appendix*, Table S3). Baculovirus was generated from Sf9 cells (ThermoFisher) by a co-transfection of pACgp67a and the BestBac Linearized Baculovirus DNA (Expression Systems). Passage one baculovirus was titered and used for infecting HighFive cells (ThermoFisher) cultured at 27 °C. ~3 days post infection, the conditioned media were harvested and mixed with NiCl<sub>2</sub>, CaCl<sub>2</sub>, and Tris pH 8.0 to a final concentration of 1 mM, 5 mM, and 100 mM, respectively. After centrifugation, the JUNO-His6 proteins was purified by Ni-NTA affinity purification from the resulting supernatant, followed by gel filtration with a Superdex 200 Increase 10/300 GL in a buffer of 150 mM NaCl, 20 mM HEPES pH 7.4.

### **Biolayer interferometry**

An Octet RED96 system (Pall ForteBio) was employed for protein-protein interaction assays in a buffer of 150 mM NaCl, 20 mM HEPES pH 7.4, 0.1% bovine serum albumin, and 0.05% Tween 20 at 29 °C under a shaking speed of 1,000 rpm. Biotinylated TMEM95-Fc or IZUMO1-Fc proteins were loaded onto Streptavidin biosensors (Sartorius). After loading the biosensors were baselined, associated in defined concentrations of analytes, and dissociated in the buffer with no analytes. Baseline-corrected binding traces were plotted and analyzed using GraphPad Prism 9.

### **Differential scanning fluorimetry**

A Prometheus NT.48 (NanoTemper) was employed for nanoscale differential scanning fluorimetry (NanoDSF). Protein samples were loaded into capillaries and subject to a temperature from 20 to 95 °C at a heating rate of 1 °C/min. Intrinsic fluorescence at 350 nm and 330 nm was recorded as a function of temperature. Thermal melting profiles were plotted using the first derivative of the ratio ( $F_{350\text{ nm}}/F_{330\text{ nm}}$ ). Melting temperatures were calculated by the instrument and represented peaks in the thermal melting curves.

### Protein purification of TMEM95

The cDNA encoding human TMEM95 (residues 17-138) was subcloned into a pADD2 vector. The N-terminus of TMEM95 was fused to a signal sequence of MRMQLLLIALSLALVTNS and the C-terminus to a C-tag of EPEA (*SI Appendix*, Table S3). Recombinant TMEM95 proteins were overexpressed in HEK293F cells by transient transfection. Affinity purification was performed using the CaptureSelect C-tagXL affinity matrix (ThermoFisher). The eluate was purified by cation exchange by a Mono S 5/50 GL (Cytiva), followed by gel filtration with a Superdex 200 Increase 10/300 GL in a buffer of 150 mM NaCl, 20 mM HEPES pH 7.4. Size exclusion with multiangle light scattering was performed on an Agilent 1260 Infinity II high performance liquid chromatography coupled with Wyatt detectors for light scattering (miniDAWN) and refractive index (Optilab) measurements.

### X-ray crystallography

X-ray diffraction data were collected at the Stanford Synchrotron Radiation Lightsource (SSRL) beam line 12-2 of SLAC National Accelerator Laboratory. For the  $\text{Sm}^{3+}$ -bound crystal, multi-wavelength anomalous diffraction data were collected at wavelengths 1.694 Å (peak), 1.137 Å (remote), and 1.695 Å (inflection). For the native crystal, the diffraction data were collected at 0.979 Å wavelength to 1.50 Å resolution. All diffraction data were processed using *autoPROC*<sup>174</sup>. The TMEM95 ectodomain structure was solved by experimental phasing using *AutoSol* in *Phenix*<sup>175</sup>. An initial model containing 110 amino acids and two  $\text{Sm}^{3+}$  ions were obtained using *AutoBuild* and was subsequently applied to the native X-ray dataset by molecular replacement using *Phaser*. Model refinement and density modification were performed in *Phenix*. Model building was performed using *Coot*<sup>176</sup>. Structural illustrations were generated with *PyMOL*.

### Evolutionary conservation by *CONSURF*

The protein sequence of human TMEM95 was input as a query sequence for a protein *BLAST* search using *blastp*. The top 150 results from were filtered manually and ortholog-unique sequences were subjected for alignment by *MAFFT*. The multiple sequence alignment and the TMEM95 structure were used as input in the *CONSURF* server<sup>177</sup>. The overall conservation scores from 1 to 9 were calculated using the Bayesian methods for each amino acid and were mapped onto the TMEM95 structure in a color-coordinated fashion as shown in Fig. 3.

### Generation of mouse hybridomas

Five female BALB/c mice (Jackson Laboratory) aged ~8 weeks (approved by Stanford University Administrative Panel on Laboratory Animal Care, APLAC 33984) were immunized with 10 µg purified protein of TMEM95 (residues 17-138) in 100 µL of 150 mM NaCl, 20 mM HEPES pH 7.4, adjuvanted with 10 µg Quil-A (InvivoGen) and 10 µg monophosphoryl lipid A (InvivoGen). Mice were boosted at days 21, 43, 64, and 86. At day 90, a spleen of one mouse was disaggregated into a single-cell suspension for hybridoma generation following the manufacturer's procedures (Stemcell technologies). Briefly, splenocytes were purified and fused with Sp2/0-Ag14 cells (ATCC) using polyethylene glycol. Hybridomas were cultured in 96-well plates with a selection medium containing hypoxanthine, aminopterin, and thymidine. ~14 days after recovery, the conditioned media were screened for binding to TMEM95 by ELISA. TMEM95-binding-positive cells were sorted as single cells in 96-well plates using a SONY SH800S. ~14 days after recovery, the conditioned media were screened, and the selected TMEM95-positive clones were expanded for antibody sequencing (Genscript Biotech) (*SI Appendix*, Table S2). Similarly, five mice were immunized with IZUMO1 (residues 22-255) and boosted at days 21, 43, 61, and 96. At day 100, a spleen from one mouse was used for hybridoma generation.

### **Antibody production and purification**

Hybridomas producing the TMEM95 and IZUMO1 antibodies were cultured in ClonaCell-HY Medium E (Stemcell technologies) and subsequently adapted to serum-free AOF Expansion Medium (Stemcell technologies) for 5-7 days at 37 °C, 5% CO<sub>2</sub>. The IgG in the conditioned AOF media was harvested from the supernatants and subjected for affinity purification by a HiTrap Protein G HP (Cytiva) and gel filtration with a Superdex 200 Increase 10/300 GL in a buffer of 150 mM NaCl, 20 mM HEPES pH 7.4.

The cDNAs encoding the heavy and light chains of the TMEM95 and IZUMO1 antibody Fab were subcloned into a pVRC vector (*SI Appendix*, Table S3). The Fabs were produced in HEK293F cells by transient transfection at 37 °C, 8% CO<sub>2</sub>, and purified from the supernatants of the conditioned media by a HiTrap Protein G HP, followed by gel filtration with a Superdex 200 Increase 10/300 GL in a buffer of 150 mM NaCl, 20 mM HEPES pH 7.4. All antibodies were concentrated to 1.0 mg/mL, supplemented with 10% glycerol, and aliquoted for long-term storage at -80 °C.

### **Human sperm isolation and western blotting**

The experimental procedures utilizing human derived samples in Fig. 4 and *SI Appendix* Figs. S4 and S5 were approved by the Committee on Human Research at the University of California, Berkeley, IRB protocol 2013-06-5395. Purified human sperm<sup>140</sup> were lysed in a buffer of 150 mM NaCl, 50 mM Tris pH 7.4, 1% Triton X-100, 0.5% Sodium deoxycholate, 0.1% SDS, 1 mM EDTA, 10% (v/v) glycerol, and Halt protease inhibitors (ThermoFisher). The protein concentrations of the whole cell lysates were estimated by a Bradford assay (BioRad) using bovine serum albumin as a standard. The lysates were stored at 4 °C in a non-reducing condition before loaded onto an SDS-PAGE gel for electrophoresis. 15 µg of lysates and 10 µg/mL of TMEM95 antibodies were used for the detection of TMEM95; 7 µg of lysates and 2 µg/mL of IZUMO1 antibodies were used for the detection of IZUMO1. A secondary antibody of HRP-conjugated goat anti-mouse IgG (BioLegend) was used for immunoblotting. PNGaseF



treatment was performed under non-reducing conditions following the manufacturer's instructions (NEB).

**Accession number**

The coordinate and structure factor of human sperm TMEM95 ectodomain has been deposited in the RCSB Protein Data Bank under PDB ID code 7UX0. The structure is available immediately at <https://peterkimlab.stanford.edu>.

## **Acknowledgement**

We thank members of the P.S.K., M.I., and P.V.L. laboratories, Dr. Jonathan Z. Long, and Dr. Masaru Okabe for discussion, Dr. Mirella Bucci for comments on the manuscript, Gita Abhiraman and the laboratory of Dr. K. Christopher Garcia for protocols of baculovirus protein production, Dr. Daniel Fernandez of the Sarafan ChEM-H Macromolecular Structure Knowledge Center, and Silvia Russi of the Stanford Synchrotron Radiation Lightsource (SSRL) beam line 12-2 for X-ray crystallographic data collection. Use of the SSRL, SLAC National Accelerator Laboratory, is supported by the US Department of Energy (DOE), Office of Science, Office of Basic Energy Sciences under Contract DE-AC02-76SF00515. The SSRL Structural Molecular Biology Program is supported by the DOE, Office of Biological and Environmental Research and by a National Institutes of Health (NIH) grant P30GM133894.

We are grateful to the late Dr. Stuart Moss of the National Institute of Child Health and Human Development (NICHD). This work was supported by a NIH NICHD grant K99HD104924 (S.T.), Damon Runyon Cancer Research Foundation DRG-2301-17 (S.T.), the Ministry of Education, Culture, Sports, Science, and Technology, Japan Society for the Promotion of Science grants JP22K15103 (Y.L.), JP19H05750 (M.I.), and JP21H05033 (M.I.), a National Science Foundation Graduate Research Fellowship DGE1752814 and DGE2146752 (W.M.S.), a Pew Biomedical Scholars Award (P.V.L.), the Global Consortium for Reproductive Longevity and Equality at the Buck Institute by the Bia-Echo Foundation (P.V.L.), the Virginia & D.K. Ludwig Fund for Cancer Research (P.S.K.), and Chan Zuckerberg Biohub (P.S.K.).

## **Conflict of Interests**

The authors declare that there are no competing interests

## Figures

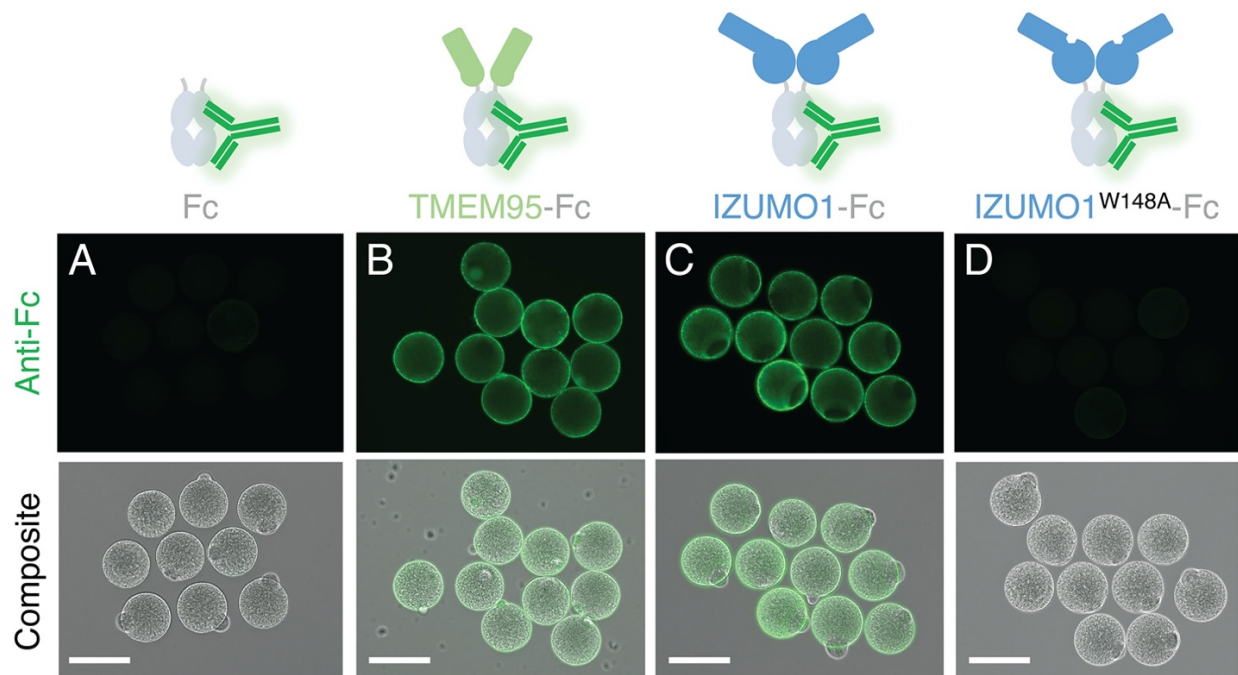


**Fig. 1 TMEM95-Fc binds eggs.** Schematics of the Fc-fusion protein with a fluorescence-conjugated anti-Fc antibody. Immuno-fluorescence (upper) and differential interference contrast composite images (lower) of zona-free hamster eggs with 200 nM of (A) Fc, (B) TMEM95-Fc, (C) IZUMO1-Fc, or (D) IZUMO1<sup>W148A</sup>-Fc. Green fluorescence was conferred by a DyLight 488-conjugated anti-Fc antibody. Scale bars, 100  $\mu$ m. TMEM95-Fc and IZUMO1-Fc bind zona-free hamster eggs. See also *SI Appendix*, Fig. S1.

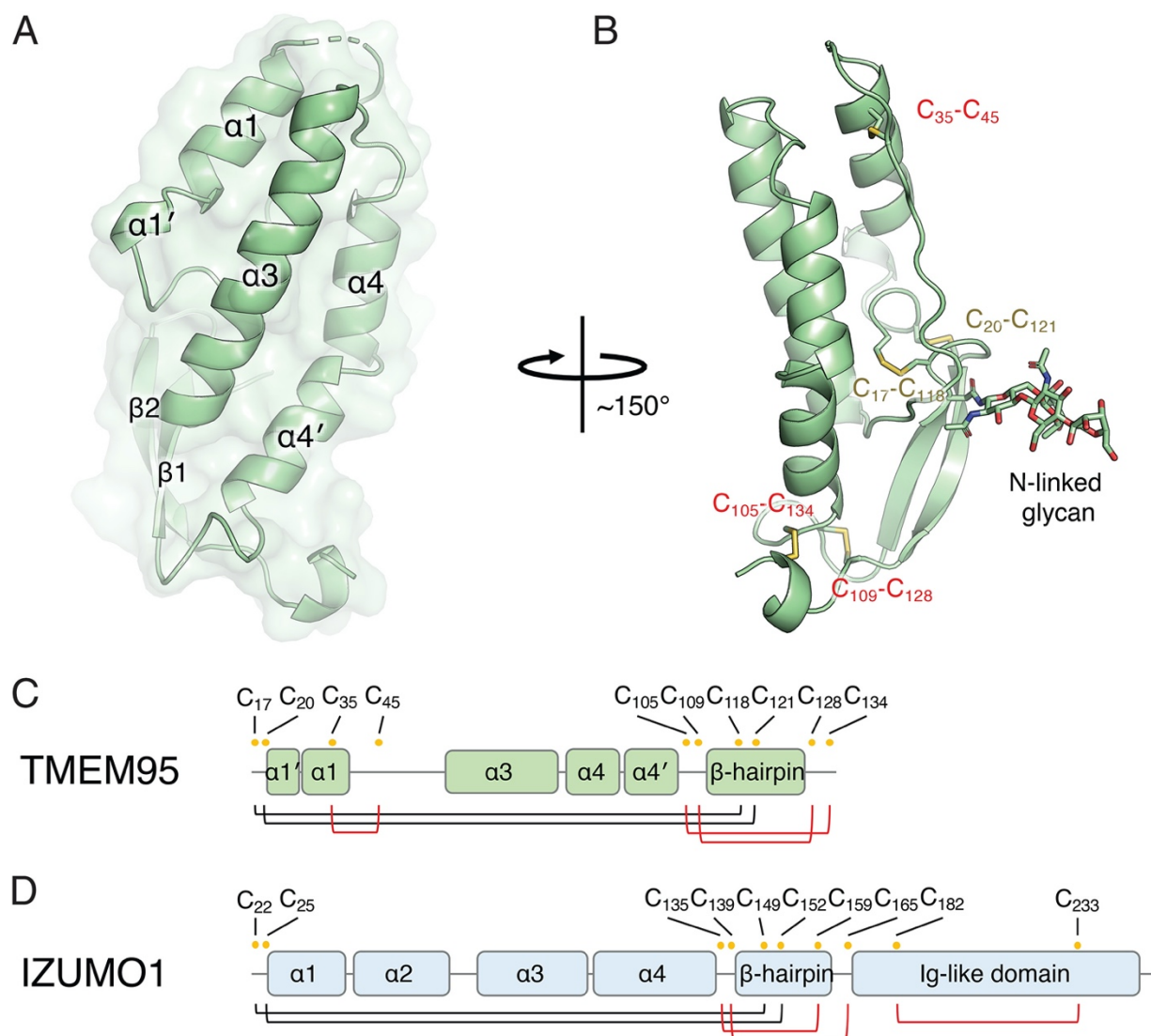


**Fig. 2 The structure of TMEM95 is homologous to IZUMO1.** (A) Overlay of ribbon and space-filling diagrams of TMEM95 with structural elements labeled. (B) Ribbon diagram of TMEM95 with disulfide linkages labeled in yellow texts (same in IZUMO1) or red texts (different in IZUMO1). Domain organizations of (C) TMEM95 and (D) IZUMO1 with cysteine positions labeled as yellow dots and disulfide linked in black (same in TMEM95 and IZUMO1) or red lines (different between TMEM95 and IZUMO1). TMEM95 shows homology to the N-terminus of IZUMO1. See also *SI Appendix*, Fig. S2.

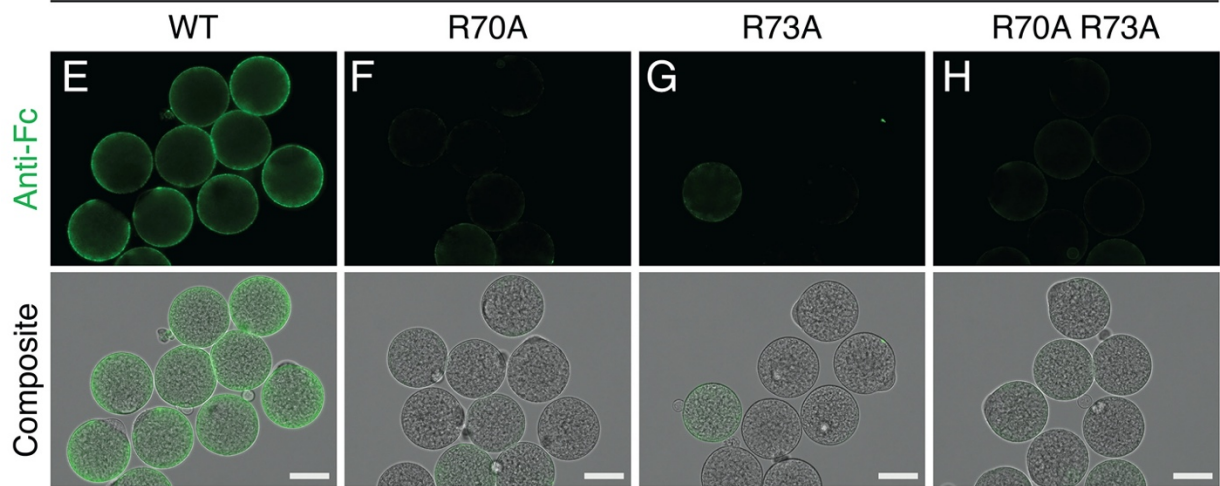
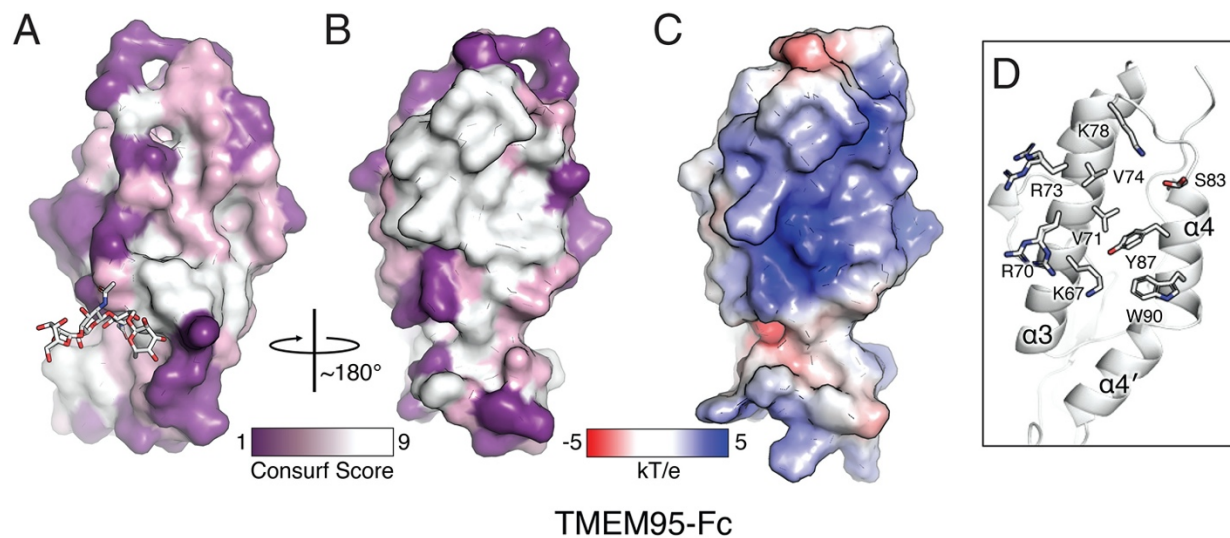


**Fig. 3 A conserved area of TMEM95 is a putative receptor binding site.** (A-B) Space-filling *CONSURF* models<sup>177</sup> of TMEM95 with  $\sim 180^\circ$  rotation with purple representing variable and white representing conserved in TMEM95 orthologs. (C) Space-filling model of electrostatic surface potential generated by APBS (Adaptive Poisson-Boltzmann Solver) with blue representing positively charged and red representing negatively charged. (D) Ribbon diagram of the conserved area of TMEM95 showing the side chains of surface-exposed residues. (E-H) Immuno-fluorescence (upper) and differential interference contrast composite images (lower) of zona-free hamster eggs with 200 nM of (E) TMEM95<sup>WT</sup>-Fc, (F) TMEM95<sup>R70A</sup>-Fc, (G) TMEM95<sup>R73A</sup>-Fc, and (H) TMEM95<sup>R70A R73A</sup>-Fc. WT, wild type. Green fluorescence by a DyLight 488-conjugated anti-Fc antibody. Scale bars, 50  $\mu\text{m}$ . Substitutions of the conserved arginine residues on the identified surface of TMEM95 ablate egg-binding activities. See also *SI Appendix*, Fig. S3.

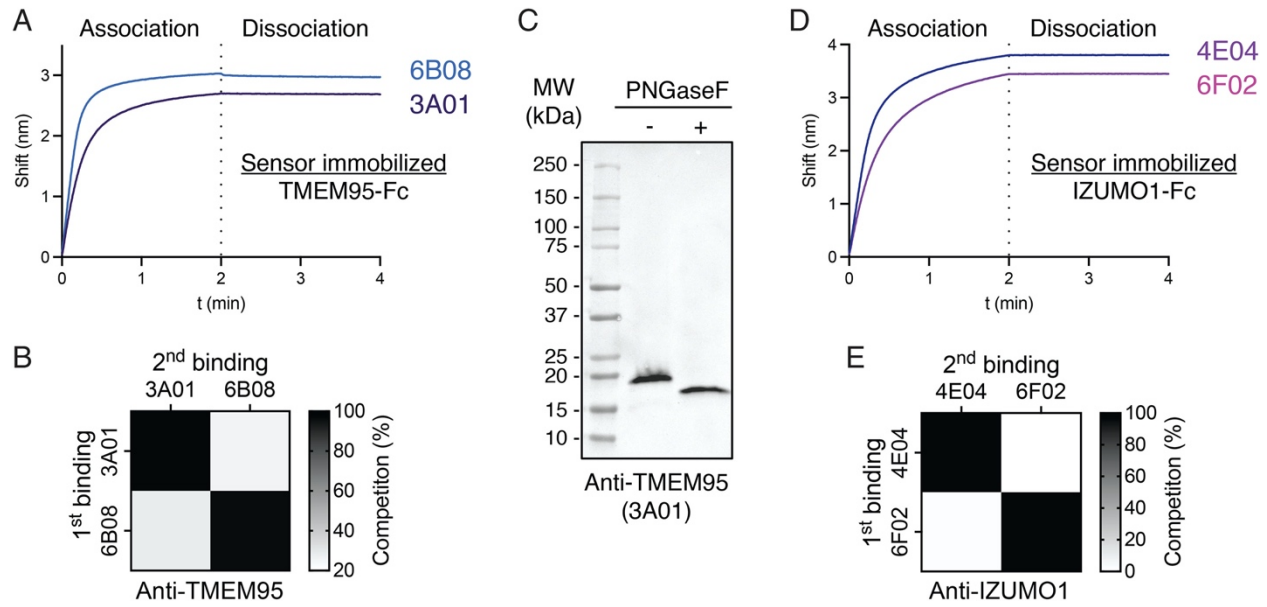


**Fig. 4 Antibodies detect the expression of TMEM95 in human sperm.** (A, D) Biolayer interferometric traces of sensor immobilized (A) TMEM95-Fc binding to 200 nM of TMEM95 antibodies 3A01 IgG and 6B08 IgG or (D) IZUMO1-Fc binding to IZUMO1 antibodies 4E04 IgG and 6F02 IgG, with association for 2 min and dissociation for 2 min. (B, E) Summary in a heat map of antibody competition (B) of 3A01 IgG and 6B08 IgG to sensor immobilized TMEM95-Fc and (E) of 4E04 IgG and 6F02 IgG to sensor immobilized IZUMO1-Fc. (C) Human sperm lysates without or with PNGaseF treatments. Western blots were performed using non-heat-denatured, non-reduced sperm lysates by a primary antibody of 10  $\mu\text{g}/\text{mL}$  anti-TMEM95 3A01 IgG, and a secondary HRP-conjugated anti-mouse antibody. TMEM95 is expressed and N-linked glycosylated in human sperm. See also *SI Appendix*, Figs. S4 and S5.

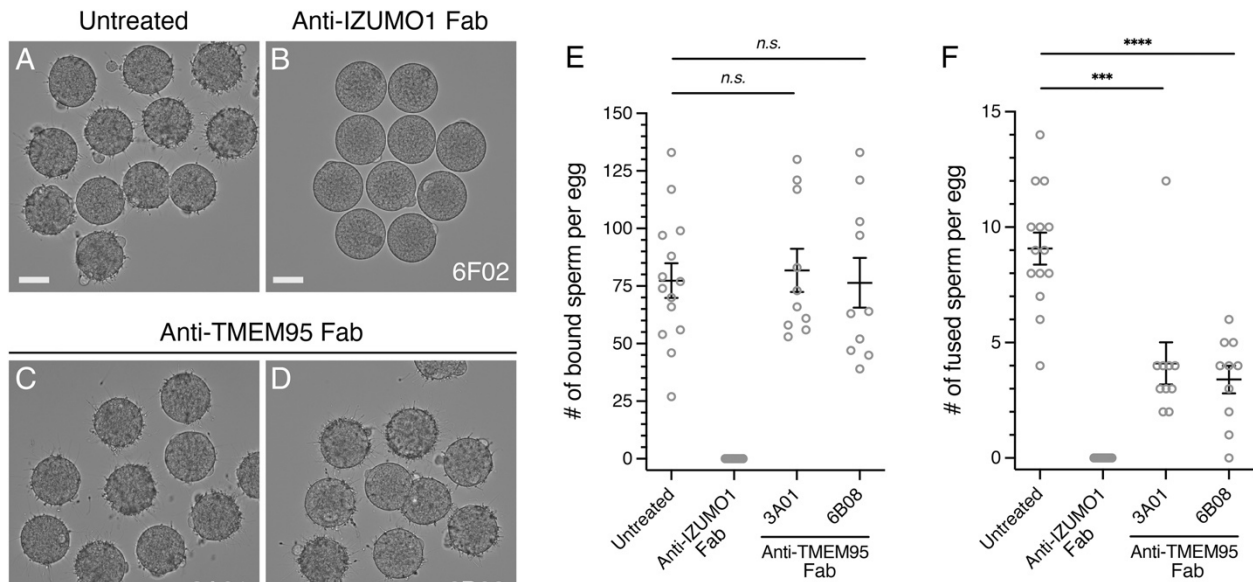


**Fig. 5 TMEM95 antibodies impair sperm-egg fusion.** (A-D) Representative images showing binding of human sperm to zona-free hamster eggs (A) untreated or treated with 40  $\mu\text{g}/\text{mL}$  of (B) anti-IZUMO1 Fab 6F02, (C) anti-TMEM95 Fab 3A01, or (D) anti-TMEM95 Fab 6B08. (E) Summary of the numbers of bound human sperm per zona-free hamster eggs (mean  $\pm$  SEM), untreated  $77.4 \pm 7.5$  ( $N = 14$ ), anti-IZUMO1 6F02 Fab  $0 \pm 0$  ( $N = 10$ ), anti-TMEM95 3A01 Fab  $81.8 \pm 9.4$  ( $N = 10$ , *n.s.*, not significant), and anti-TMEM95 6B08 Fab  $76.4 \pm 10.8$  ( $N = 10$ , *n.s.*, not significant). (F) Summary of the numbers of fused human sperm per zona-free hamster eggs (mean  $\pm$  SEM), untreated  $9.1 \pm 0.7$  ( $N = 14$ ), anti-IZUMO1 6F02 Fab  $0 \pm 0$  ( $N = 10$ ), anti-TMEM95 3A01 Fab  $4.1 \pm 0.9$  ( $N = 10$ ,  $p = 0.0002$ ), and anti-TMEM95 6B08 Fab  $3.4 \pm 0.6$  ( $N = 10$ ,  $p < 0.0001$ ). TMEM95 antibodies do not block sperm-egg binding but impair sperm-egg fusion. See also *SI Appendix*, Fig. S6.



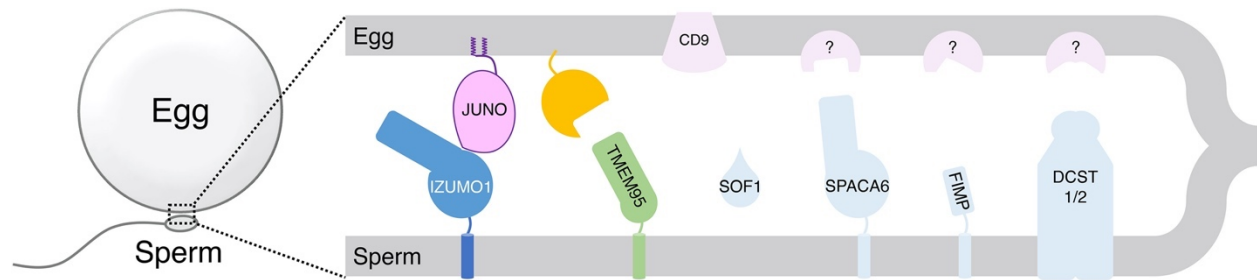


**Fig. 6 Model of sperm-egg binding and fusion.** Illustration of membrane fusion of sperm and an egg and pairwise protein-protein interactions: sperm IZUMO1 (blue) binds egg JUNO (pink) and a receptor (orange)-mediated interaction of sperm TMEM95 (green) to the egg takes place; membrane fusion occurs thereafter. CD9 of egg is essential for sperm-egg fusion<sup>178–180</sup>. Additional analogous, yet to be identified, interactions between sperm proteins (*e.g.*, SOF1, SPACA6, FIMP, and DCST1/2) and their specific egg receptors may play a role in sperm-egg binding and fusion.



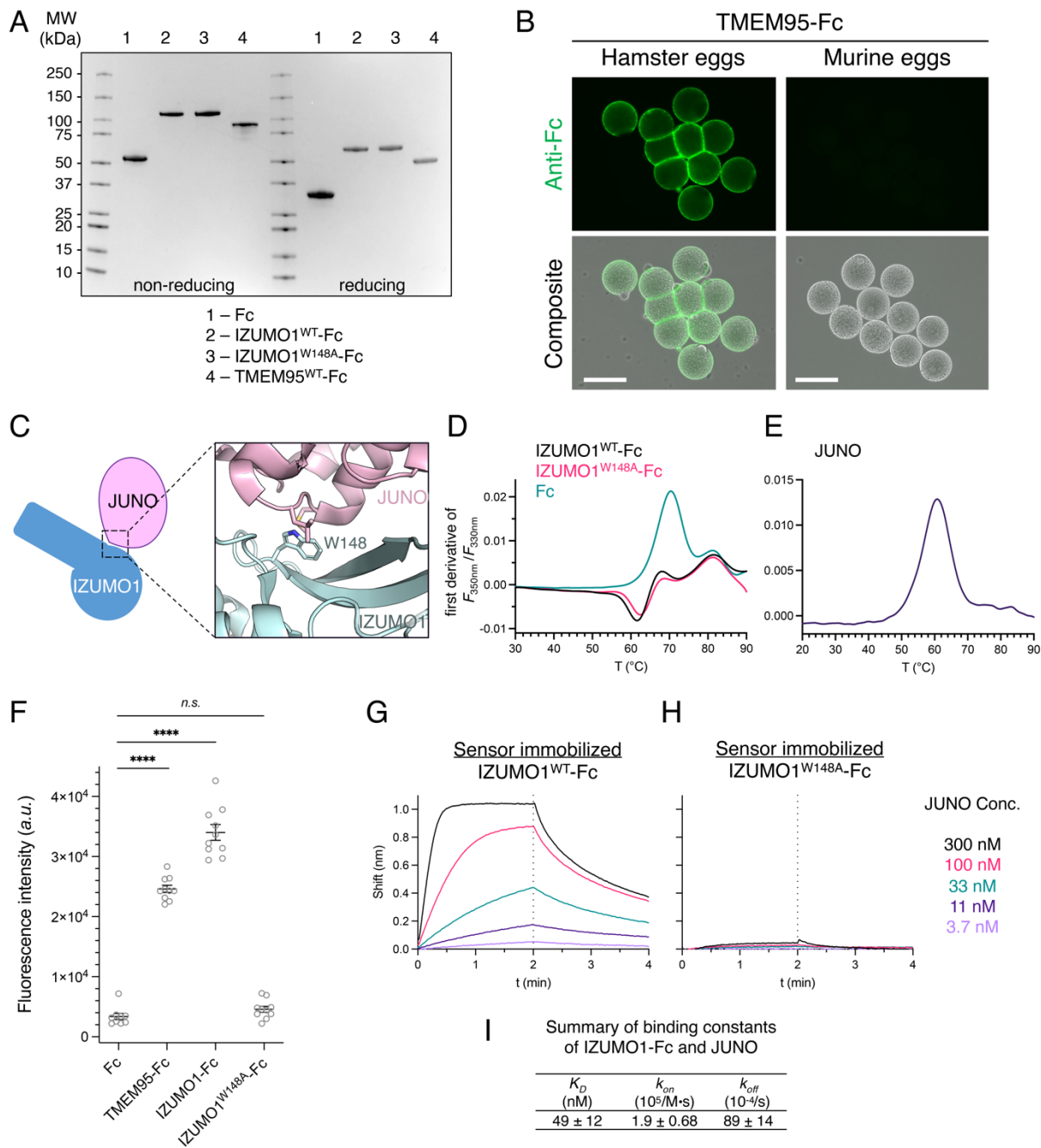


**Fig. S1**, related to Fig. 1, Characterization of TMEM95-Fc and IZUMO1-Fc. (A) Coomassie-blue stained SDS-PAGE gel of Fc, IZUMO1<sup>WT</sup>-Fc, IZUMO1<sup>W148A</sup>-Fc, and TMEM95-Fc proteins under non-reducing (left) or reducing conditions (right). (B) Immuno-fluorescence (upper) and differential interference contrast composite images (lower) of (left) zona-free hamster eggs and (right) zona-free mouse eggs were incubated with 200 nM TMEM95-Fc. Green fluorescence by a DyLight 488-conjugated anti-Fc antibody. Scale bars, 100  $\mu$ m. (C) Cartoon schematic and ribbon diagram (PDB ID: 5F4E) of the IZUMO1-JUNO complex showing the

side chain of W148 of IZUMO1 interacting with JUNO. (D-E) NanoDSF thermal melting profiles of (D) Fc, IZUMO1<sup>WT</sup>-Fc, IZUMO1<sup>W148A</sup>-Fc, and (E) JUNO proteins. (F) Quantification of fluorescence intensities (*a.u.*, arbitrary unit; \*\*\*\*,  $p < 0.0001$ ; *n.s.*, not significant) of Fc, TMEM95-Fc, IZUMO1<sup>WT</sup>-Fc, and IZUMO1<sup>W148A</sup>-Fc on eggs shown in Fig. 1. (G-H) Biolayer interferometric traces of sensor immobilized (G) IZUMO1<sup>WT</sup>-Fc or (H) IZUMO1<sup>W148A</sup>-Fc binding JUNO of 300 nM, 100 nM, 33 nM, 11 nM, and 3.7 nM, with association for 2 min and dissociation for 2 min. WT, wild type. (I) List of binding constants of IZUMO1-Fc with JUNO calculated from traces in (G).

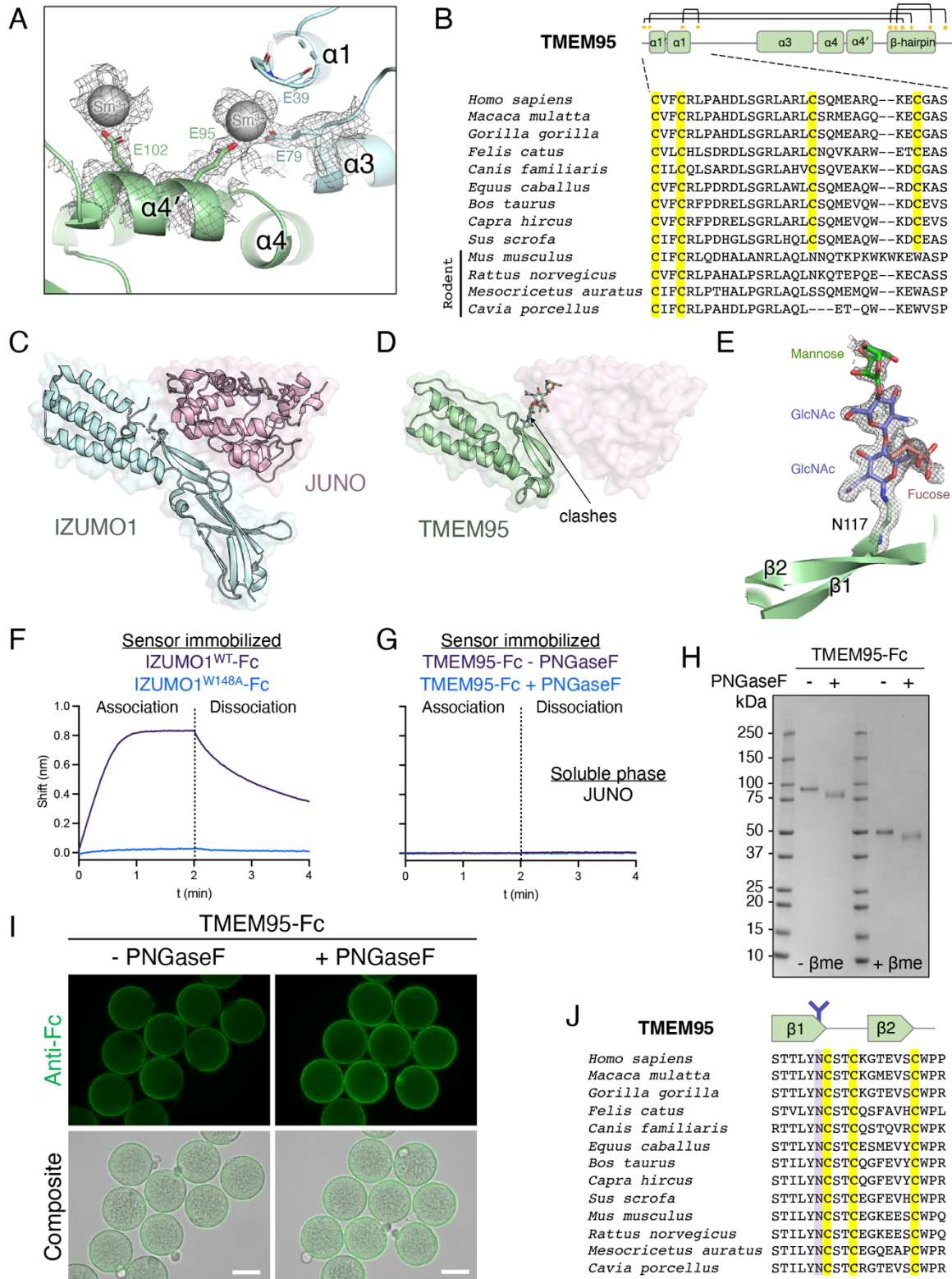


**Fig. S2**, related to Fig. 2, JUNO does not act as a receptor of TMEM95. (A) Ribbon diagram overlay with a  $2F_{\text{obs}}-F_{\text{calc}}$  electron density map surrounding the  $\text{Sm}^{3+}$  ions between two TMEM95 protomers (green and cyan) in the crystal lattice solved by multi-wavelength X-ray anomalous diffraction. (B) Multiple sequence alignment of the  $\alpha 1$  region of TMEM95 orthologs with conserved cysteines highlighted in yellow. (C-D) Ribbon diagrams overlay with a space-filling model of (C) the IZUMO1-JUNO complex (PDB ID: 5F4E), (D) the TMEM95-superimposed JUNO complex, where the N-glycan of TMEM95 causes a clash with JUNO. (E) Ribbon diagram overlay with a  $2F_{\text{obs}}-F_{\text{calc}}$  composite omit (10%) electron density map of the N117 side chain and its linked glycan. Biolayer interferometric traces of (F) sensor immobilized IZUMO1<sup>WT</sup>-Fc or IZUMO1<sup>W148A</sup>-Fc, and (G) sensor immobilized TMEM95-Fc treated without or with PNGaseF binding to JUNO of 300 nM, with association for 2 min and dissociation for 2 min. Data in (F) are also shown in *SI Appendix*, Fig. S1G-H. (H) Coomassie-blue stained SDS-PAGE gel of TMEM95-Fc treated without or with PNGaseF under non-reducing (left) or reducing (right) conditions. (I) Immuno-fluorescence (upper) and differential interference contrast composite images (lower) of zona-free hamster eggs incubated with TMEM95-Fc treated without PNGaseF (left) and with PNGaseF (right). Green fluorescence by a DyLight 488-conjugated anti-Fc antibody. Scale bars, 50  $\mu\text{m}$ . (J) Multiple sequence alignment of the  $\beta$ -hairpin of TMEM95 orthologs with conserved cysteines highlighted in yellow and the asparagine in purple.

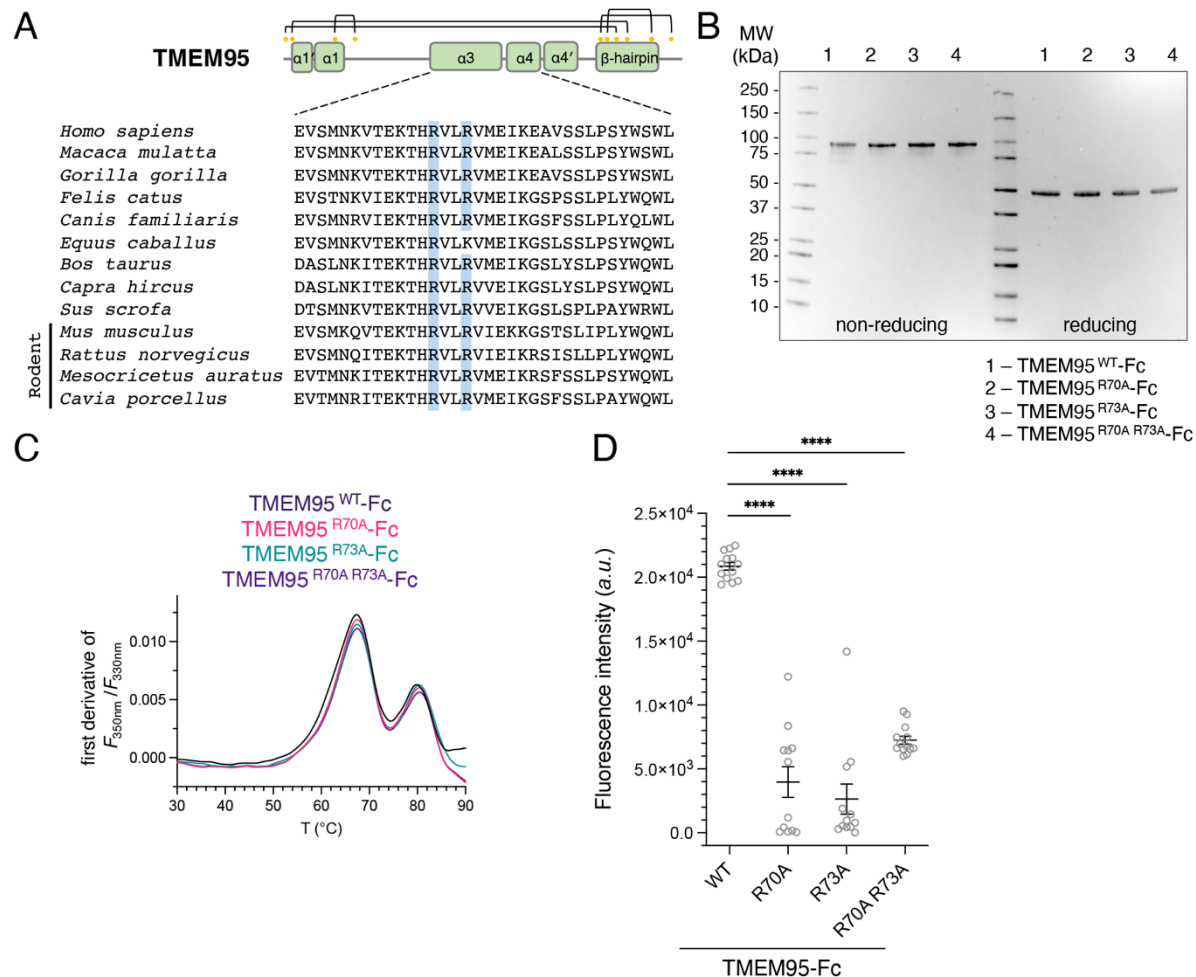


**Fig. S3**, related to Fig. 3, Characterization of TMEM95-Fc variants. (A) Multiple sequence alignment of the  $\alpha 3$ - $\alpha 4$  region of TMEM95 orthologs with conserved arginine highlighted in blue. (B) Coomassie-blue stained SDS-PAGE gel of TMEM95<sup>WT</sup>-Fc, TMEM95<sup>R70A</sup>-Fc, TMEM95<sup>R73A</sup>-Fc, and TMEM95<sup>R70A R73A</sup>-Fc proteins under non-reducing (left) or reducing (right) conditions. WT, wild type. (C) NanoDSF thermal melting profiles of TMEM95<sup>WT</sup>-Fc, TMEM95<sup>R70A</sup>-Fc, TMEM95<sup>R73A</sup>-Fc, and TMEM95<sup>R70A R73A</sup>-Fc proteins. (D) Quantified green fluorescence intensities (a.u., arbitrary unit; \*\*\*\*,  $p < 0.0001$ ) of TMEM95<sup>WT</sup>-Fc, TMEM95<sup>R70A</sup>-Fc, TMEM95<sup>R73A</sup>-Fc, and TMEM95<sup>R70A R73A</sup>-Fc proteins on eggs shown in Fig. 3.

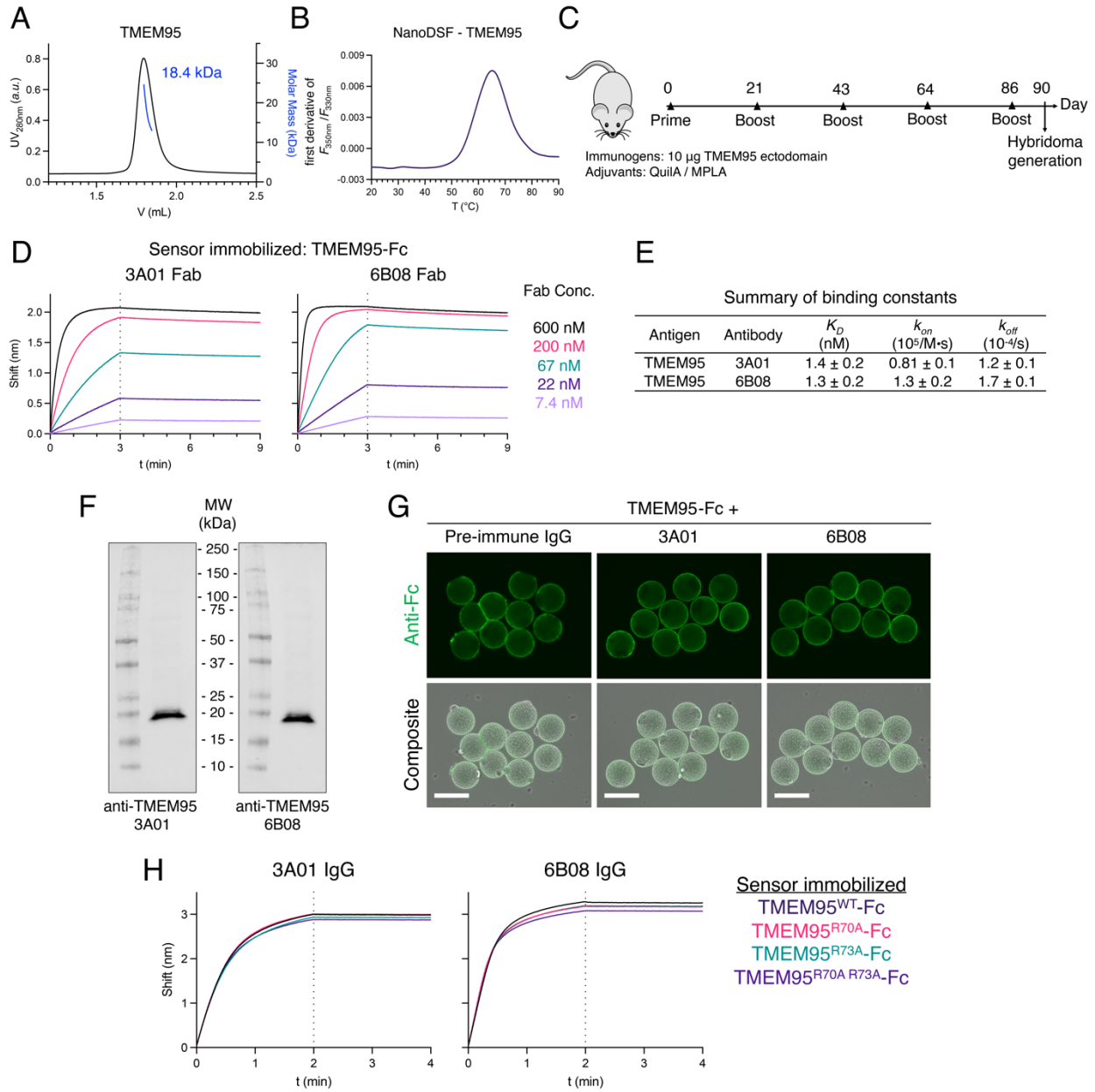


**Fig. S4**, related to Fig. 4, Characterization of the TMEM95 antibodies. (A) Size exclusion and multiangle light scattering of the TMEM95 protein showing a monodispersed peak with a calculated molecular weight of 18.4 kDa, as an expected monomer in solution. (B) NanoDSF thermal melting profile of the TMEM95 protein used for protein crystallization and mouse immunization. (C) Schedule of mouse immunization using the TMEM95 protein. (D) Biolayer interferometric traces of sensor immobilized TMEM95-Fc binding to 3A01 Fab or 6B08 Fab at concentrations of 600 nM, 200 nM, 67 nM, 22 nM, and 7.4 nM, with association for 3 min and dissociation for 6 min. (E) Summary of binding constants of TMEM95-Fc with anti-TMEM95 3A01 Fab and 6B08 Fab calculated from traces in (D). (F) Western blots of non-heat-denatured, non-reduced human sperm lysates by a primary antibody of 10  $\mu\text{g}/\text{mL}$  anti-TMEM95 3A01 IgG

or 6B08 IgG, and a secondary HRP-conjugated anti-mouse antibody. (G) Immuno-fluorescence (upper) and differential interference contrast composite images (lower) of zona-free hamster eggs incubated with TMEM95-Fc that has been pre-bound to protein G purified pre-immune mouse IgG, anti-TMEM95 3A01 IgG, or 6B08 IgG. 2.5  $\mu$ M TMEM95-Fc was mixed with 5  $\mu$ M (0.75 mg/mL) IgG for 1 hour to form a complex of TMEM95-Fc and the antibody, and the mixture was added to the eggs at a final concentration of 200 nM TMEM95-Fc. Green fluorescence by a DyLight 488-conjugated anti-Fc antibody. Scale bars, 100  $\mu$ m. (H) Biolayer interferometric traces of sensor-immobilized TMEM95<sup>WT</sup>-Fc, TMEM95<sup>R70A</sup>-Fc, TMEM95<sup>R73A</sup>-Fc, and TMEM95<sup>R70A R73A</sup>-Fc proteins binding to 200 nM of 3A01 IgG or 6B08 IgG, with association for 2 min and dissociation for 2 min. WT, wild type.

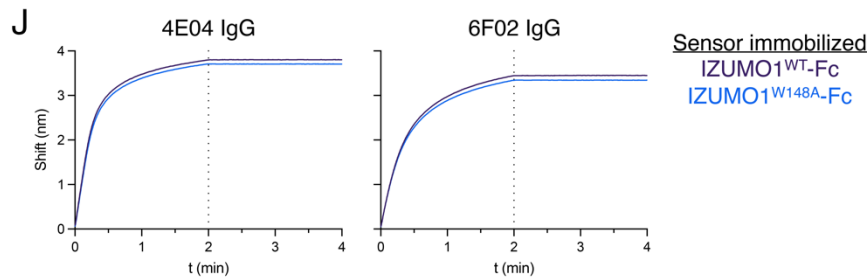
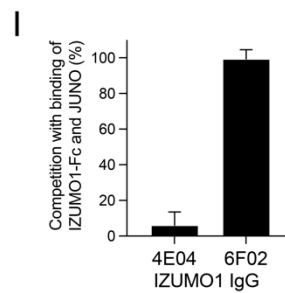
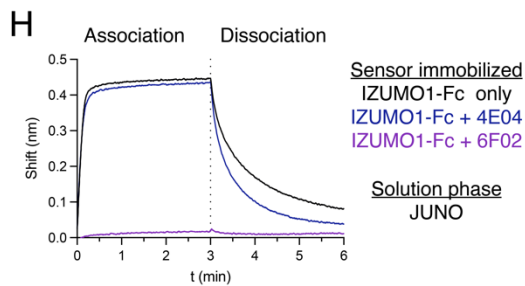
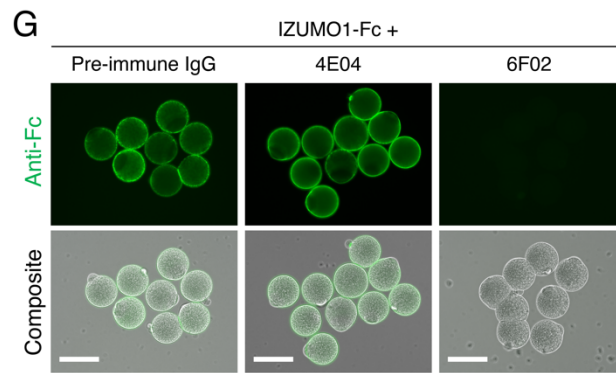
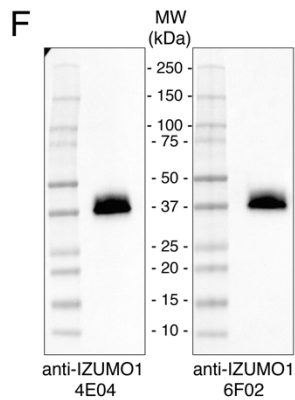
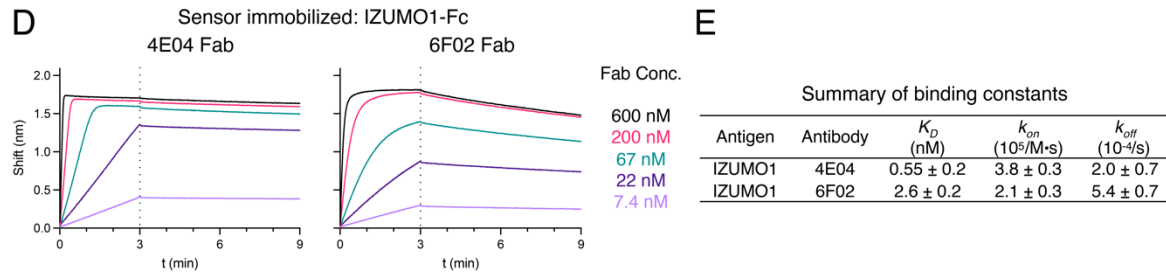
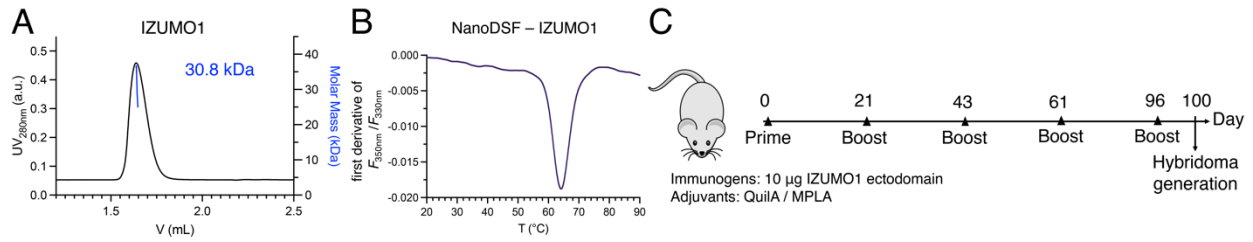




**Fig. S5**, related to Fig. 4, Characterization of the IZUMO1 antibodies. (A) Size exclusion and multiangle light scattering of the IZUMO1 protein showing a monodispersed peak with a calculated molecular weight of 30.8 kDa, as an expected monomer in solution. (B) NanoDSF thermal melting profile of the IZUMO1 protein used for mouse immunization. (C) Schedule of mouse immunization of the IZUMO1 protein. (D) Biolayer interferometric traces of sensor immobilized IZUMO1-Fc binding to 4E04 Fab or 6F02 Fab at concentrations of 600 nM, 200 nM, 67 nM, 22 nM, and 7.4 nM, with association for 3 min and dissociation for 6 min. (E) Summary of binding constants of IZUMO1-Fc with anti-IZUMO1 4E04 Fab and 6F02 Fab calculated from traces in (D). (F) Western blots of non-heat-denatured, non-reduced human sperm lysates by a primary antibody of 2  $\mu\text{g}/\text{mL}$  anti-IZUMO1 4E04 IgG or 6F02 IgG, and a secondary HRP-conjugated anti- mouse antibody. (G) Immuno-fluorescence (upper) and differential interference contrast composite images (lower) of zona-free hamster eggs incubated with IZUMO1-Fc that has been pre-bound to protein G purified pre-immune mouse IgG, anti-IZUMO1 4E04 IgG, or 6F02 IgG. 2.5  $\mu\text{M}$  IZUMO1-Fc was mixed with 5  $\mu\text{M}$  (0.75 mg/mL) IgG for 1 hour to form a complex of IZUMO1-Fc and the antibody, and the mixture was added to the eggs at a final concentration of 200 nM IZUMO1-Fc. Green fluorescence by a DyLight 488-conjugated anti-Fc antibody. Scale bars, 100  $\mu\text{m}$ . (H) Biolayer interferometric traces of sensor immobilized IZUMO1-Fc, or IZUMO1-Fc in complex with 4E04 IgG, 6F02 IgG binding to 300 nM JUNO, with association for 3 min and dissociation for 3 min. (I) Summary of antibody competition with the IZUMO1-Fc and JUNO interaction calculated from (H). (J) Biolayer interferometric traces of sensor-immobilized IZUMO1<sup>WT</sup>-Fc and IZUMO1<sup>W148A</sup>-Fc binding to 200 nM of 4E04 IgG or 6F02 IgG, with association for 2 min and dissociation for 2 min. WT, wild type.

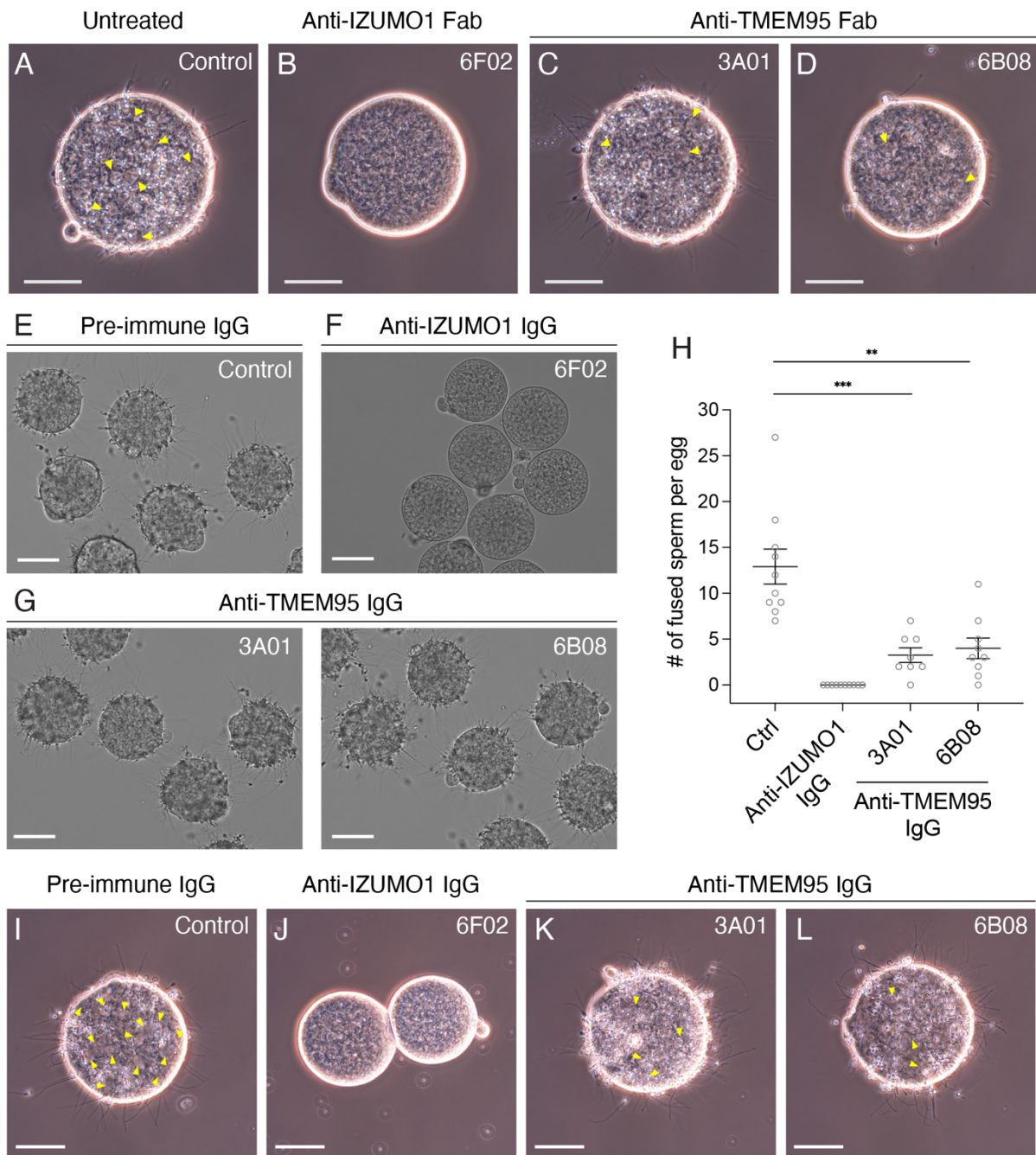


**Fig. S6**, related to Fig. 5, TMEM95 antibodies impair sperm-egg fusion. Representative images showing fusion of human sperm with zona-free hamster eggs (A) untreated or treated with 40  $\mu\text{g}/\text{mL}$  of (B) anti-IZUMO1 Fab 6F02, (C) anti-TMEM95 Fab 3A01, or (D) anti-TMEM95 Fab 6B08. Arrows indicating fused sperm with swollen sperm heads. Scale bars, 50  $\mu\text{m}$ . (E-G) Representative images showing binding of human sperm with zona-free hamster eggs in the

presence of 40  $\mu\text{g}/\text{mL}$  (E) pre-immune mouse IgG, (F) anti-IZUMO1 IgG 6F02, (G) anti-TMEM95 IgG 3A01 (left), or anti-TMEM95 IgG 6B08 (right) after 3 hours of insemination. Scale bars, 50  $\mu\text{m}$ . (H) Summary of the numbers of fused human sperm per zona-free hamster eggs in each group (mean  $\pm$  SEM), pre-immune mouse IgG control  $12.9 \pm 1.7$  ( $N = 10$ ), anti-IZUMO1 IgG 6F02  $0 \pm 0$  ( $N = 10$ ), anti-TMEM95 IgG 3A01  $3.3 \pm 0.8$  ( $N = 8$ ,  $p < 0.001$ ), and anti-TMEM95 IgG 6B08  $4.0 \pm 1.1$  ( $N = 9$ ,  $p < 0.01$ ). Representative images showing fusion of human sperm with zona-free hamster eggs in the presence of 40  $\mu\text{g}/\text{mL}$  (I) pre-immune mouse IgG, (J) anti-IZUMO1 IgG 6F02, (K) anti-TMEM95 IgG 3A01, and (L) anti-TMEM95 IgG 6B08. Arrows indicating fused sperm with swollen sperm heads. Scale bars, 50  $\mu\text{m}$ .

**Table S1 Crystallographic data collection and refinement statistics**

	Human TMEM95 ectodomain			
	Native	Multi-wavelength anomalous diffraction		
		Peak	Remote	Inflection
<b>PDB ID</b>	7UX0			
<b>Wavelength, Å</b>	0.97946	1.69457	1.13743	1.69515
<b>Resolution range, Å</b>	36.01 - 1.50 (1.52 - 1.50)	39.01 - 2.10 (2.14 - 2.10)	29.09 - 1.97 (2.00 - 1.97)	39.02 - 2.12 (2.15 - 2.12)
<b>Space group</b>	<i>P</i> 2 <sub>1</sub> 2 <sub>1</sub> 2 <sub>1</sub>	<i>P</i> 2 <sub>1</sub> 2 <sub>1</sub> 2 <sub>1</sub>	<i>P</i> 2 <sub>1</sub> 2 <sub>1</sub> 2 <sub>1</sub>	<i>P</i> 2 <sub>1</sub> 2 <sub>1</sub> 2 <sub>1</sub>
<b>Unit cell</b>	39.53 43.11 72.02 90 90 90	39.30 43.22 78.01 90 90 90	39.32 43.25 78.09 90 90 90	39.31 43.23 78.03 90 90 90
<b>Total reflections</b>	258299 (13130)	90875 (3275)	109780 (6269)	92437 (3364)
<b>Unique reflections</b>	20505 (1004)	7810 (370)	8952 (476)	7866 (365)
<b>Multiplicity</b>	12.6 (13.1)	11.6 (8.9)	12.3 (13.2)	11.8 (9.2)
<b>Completeness, %</b>	99.7 (100.0)	95.7 (92.7)	90.1 (100.0)	98.0 (93.8)
<b>Mean I/σ(I)</b>	12.3 (2.2)	14.20 (2.4)	12.10 (2.2)	14.1 (2.1)
<b><i>R</i><sub>merge</sub></b>	0.148 (1.803)	0.188 (0.922)	0.184 (1.641)	0.173 (1.137)
<b><i>CC</i><sub>1/2</sub></b>	0.997 (0.855)	0.998 (0.882)	0.998 (0.834)	0.998 (0.786)
<b><i>R</i><sub>work</sub></b>	0.223			
<b><i>R</i><sub>free</sub></b>	0.251			
<b>Number of non-hydrogen atoms</b>	1133			
macromolecules	985			
solvent	89			
<b>Protein residues</b>	115			
<b>RMS(bonds), Å</b>	0.007			
<b>RMS(angles), °</b>	1.03			
<b>Ramachandran favored, %</b>	98.20			
<b>Ramachandran outliers, %</b>	0.00			
<b>Clashscore</b>	3.90			
<b>Average B-factor</b>	29.95			
macromolecules	28.69			
solvent	36.35			

Statistics for the highest-resolution shell are shown in parentheses.

**Table S2 Summary of the TMEM95 and IZUMO1 monoclonal antibodies**

Antigen	Antibody	Isotype	V-gene	D-gene	J-gene	CDR1	CDR2	CDR3	
TMEM95	3A01	V <sub>H</sub>	IgG1	IGHV5-9-4*01	IGHD1-1*01	IGHJ4*01	NYVMS	EISTYGRYTFYPDSVTG	RDYYGSSSVMDY
		V <sub>L</sub>	Kappa	IGKV4-57-1*01		IGKJ1*01	RASSSVSSSLH	STSNLAS	QQYSGYPLT
	6B08	V <sub>H</sub>	IgG1	IGHV5-6*01 IGHV5-6-1*01	N/A	IGHJ4*01	TYGMS	TISFYGHTHTYYPDILKG	EDYDAMDY
		V <sub>L</sub>	Kappa	IGKV9-120*02		IGKJ2*01	RASQDIGSNLN	ATSSLDS	LQYAIFFYT
IZUMO1	4E04	V <sub>H</sub>	IgG1	IGHV2-6-5*01	IGHD2-1*01 IGHD2-10*01 IGHD2-10*02	IGHJ2*01	DFGIS	LIWGGGNTYYNSALKS	HGRFGNTPDY
		V <sub>L</sub>	Kappa	IGKV1-110*01		IGKJ1*01	TSGQSLVQSNGNTYLH	KVSNRFS	SQSTRFPWT
	6F02	V <sub>H</sub>	IgG1	IGHV3-1*02	IGHD2-4*01 IGHD2-9*02	IGHJ2*01	SAYVWH	YIQYSGSTNYNPSLTS	AMITRGYFDY
		V <sub>L</sub>	Kappa	IGKV14-111*01		IGKJ4*01	KASQDSNSYLS	GANRLVD	LQYDEFPFT

**Table S3 Plasmids and protein sequences used in this study**

Plasmids for protein expression from HEK293F transient transfection

Plasmid	Description & encoded protein sequence
pST980	pADD2 Fc MGWSCIIILFLVATATGVHSENLVFQGGSGGDKTHTCPPCPAPELLGGPSVFLFPPPKPDKTLMISRTPEVTCVVVDVSHEDPEVKFNWYVDGVEVHNAKTKPREEQYNSTYRVVSVLTVLHQDWLNGKEYKCKVSNKALPAPIEKTISKAKGQPREPQVYTLPPSRDELTKNQVSLTCLVKGFYPSDIAVEWESNGQPENNYKTTPPVLDSDGSFFLYSKLTVDKSRWQQGNVFSVMSVHEALHNHYTQKSLSLSPGK
pST1392	pADD2 Fc-Avi-His6 MGWSCIIILFLVATATGVHSENLVFQGGSGGDKTHTCPPCPAPELLGGPSVFLFPPPKPDKTLMISRTPEVTCVVVDVSHEDPEVKFNWYVDGVEVHNAKTKPREEQYNSTYRVVSVLTVLHQDWLNGKEYKCKVSNKALPAPIEKTISKAKGQPREPQVYTLPPSRDELTKNQVSLTCLVKGFYPSDIAVEWESNGQPENNYKTTPPVLDSDGSFFLYSKLTVDKSRWQQGNVFSVMSVHEALHNHYTQKSLSLSPGKSGSLNDIFEAQKIEWHEGGHHHHH
pST1359	pADD2 TMEM95-Fc-Avi-His6 MWRLLALGGVFLAAAQACVFCRLPAHDLSGRLARLCSQMEARQKECGASPDFSAFALDEVSMNKVTEKTHRVLRVMEIKEAVSSLPSYWSWLRKTKLPEYTREALCPPACRGSTTLVNCSTCKGTEVSCWPRKRCFPGSQDLWEAKENLYFQGGSGGDKTHTCPPCPAPELLGGPSVFLFPPPKPDKTLMISRTPEVTCVVVDVSHEDPEVKFNWYVDGVEVHNAKTKPREEQYNSTYRVVSVLTVLHQDWLNGKEYKCKVSNKALPAPIEKTISKAKGQPREPQVYTLPPSRDELTKNQVSLTCLVKGFYPSDIAVEWESNGQPENNYKTTPPVLDSDGSFFLYSKLTVDKSRWQQGNVFSVMSVHEALHNHYTQKSLSLSPGKSGSLNDIFEAQKIEWHEGGHHHHHH
pST1094	pADD2 IZUM01-Fc MGPHFTLLCAALAGCLLPAEGCVICDPSVVLALKSLEKDYLPGLDAKHHKAMMERVENAVKDFQELSLNEDAYMGVVDEATLQKGSWSLLKDLKRITDSVKGDLFVKELFWMLHLQKETFATYVARFQKEAYCPNKCGVMLQTLIWCKNCKKEVHACRKS YDCGERNVEVPQMEDMILDCELNWHQASEGLTDYSFYRVWGNNTETLVSKGKEATLTKPMVGPEDAGSYRCELGSVNSSPATIINFHVTVLPKENLYFQGGSGGDKTHTCPPCPAPELLGGPSVFLFPPPKPDKTLMISRTPEVTCVVVDVSHEDPEVKFNWYVDGVEVHNAKTKPREEQYNSTYRVVSVLTVLHQDWLNGKEYKCKVSNKALPAPIEKTISKAKGQPREPQVYTLPPSRDELTKNQVSLTCLVKGFYPSDIAVEWESNGQPENNYKTTPPVLDSDGSFFLYSKLTVDKSRWQQGNVFSVMSVHEALHNHYTQKSLSLSPGK
pST1373	pADD2 IZUM01-Fc-Avi-His6 MGPHFTLLCAALAGCLLPAEGCVICDPSVVLALKSLEKDYLPGLDAKHHKAMMERVENAVKDFQELSLNEDAYMGVVDEATLQKGSWSLLKDLKRITDSVKGDLFVKELFWMLHLQKETFATYVARFQKEAYCPNKCGVMLQTLIWCKNCKKEVHACRKS YDCGERNVEVPQMEDMILDCELNWHQASEGLTDYSFYRVWGNNTETLVSKGKEATLTKPMVGPEDAGSYRCELGSVNSSPATIINFHVTVLPKENLYFQGGSGGDKTHTCPPCPAPELLGGPSVFLFPPPKPDKTLMISRTPEVTCVVVDVSHEDPEVKFNWYVDGVEVHNAKTKPREEQYNSTYRVVSVLTVLHQDWLNGKEYKCKVSNKALPAPIEKTISKAKGQPREPQVYTLPPSRDELTKNQVSLTCLVKGFYPSDIAVEWESNGQPENNYKTTPPVLDSDGSFFLYSKLTVDKSRWQQGNVFSVMSVHEALHNHYTQKSLSLSPGKSGSLNDIFEAQKIEWHEGGHHHHHH
pST1710	pADD2 IZUM01-Fc-Avi-His6 W148A MGPHFTLLCAALAGCLLPAEGCVICDPSVVLALKSLEKDYLPGLDAKHHKAMMERVENAVKDFQELSLNEDAYMGVVDEATLQKGSWSLLKDLKRITDSVKGDLFVKELFWMLHLQKETFATYVARFQKEAYCPNKCGVMLQTLIACKNCKKEVHACRKS YDCGERNVEVPQMEDMILDCELNWHQASEGLTDYSFYRVWGNNTETLVSKGKEATLTKPMVGPEDAGSYRCELGSVNSSPATIINFHVTVLPKENLYFQGGSGGDKTHTCPPCPAPELLGGPSVFLFPPPKPDKTLMISRTPEVTCVVVDVSHEDPEVKFNWYVDGVEVHNAKTKPREEQYNSTYRVVSVLTVLHQDWLNGKEYKCKVSNKALPAPIEKTISKAKGQPREPQVYTLPPSRDELTKNQVSLTCLVKGFYPSDIAVEWESNGQPENNYKTTPPVLDSDGSFFLYSKLTVDKSRWQQGNVFSVMSVHEALHNHYTQKSLSLSPGKSGSLNDIFEAQKIEWHEGGHHHHHH
pST1557	pADD2 TMEM95-Ctag MRMQLLLLIALSLALVTNSCVFCRLPAHDLSGRLARLCSQMEARQKECGASPDFSAFALDEVSMNKVTEKTHRVLRVMEIKEAVSSLPSYWSWLRKTKLPEYTREALCPPACRGSTTLVNCSTCKGTEVSCWPRKRCFPGSEPEA

pST1704	pADD2 TMEM95-Fc-Avi-His6 R70A MWRLALGGVFLAAAQACVFCRLPAHDLSGRLARLCSQMEARQKECGASPDFSAFALDEVSMNKVTEKTHA VLRVMEIKEAVSSLPSYWSWLRKTKLPEYTREALCPPACRGSTTLNCSTCKGTEVSCWPRKRCFPGSQD LWEAKENLYFQGGSGGDKTHTCPPCPAPELLGGPSVFLFPPKPKDTLMI SRTPEVTCVVVDVSHEDPEVK FNWYVDGVEVHNAKTKPREEQYNSTYRVVSVLTVLHQDWLNGKEYKCKVSNKALPAPIEKTISKAKGQPR EPQVYTLPPSRDELTKNQVSLTCLVKGFYPSDIAVEWESNGQPENNYKTPPVLDSDGSFFLYSKLTVDK SRWQQGNVFCSCVMHEALHNHYTQKSLSLSPGKSGSLNDFEFAQKIEWHEGHHHHHH
pST1705	pADD2 TMEM95-Fc-Avi-His6 R73A MWRLALGGVFLAAAQACVFCRLPAHDLSGRLARLCSQMEARQKECGASPDFSAFALDEVSMNKVTEKTHR VLAVMEIKEAVSSLPSYWSWLRKTKLPEYTREALCPPACRGSTTLNCSTCKGTEVSCWPRKRCFPGSQD LWEAKENLYFQGGSGGDKTHTCPPCPAPELLGGPSVFLFPPKPKDTLMI SRTPEVTCVVVDVSHEDPEVK FNWYVDGVEVHNAKTKPREEQYNSTYRVVSVLTVLHQDWLNGKEYKCKVSNKALPAPIEKTISKAKGQPR EPQVYTLPPSRDELTKNQVSLTCLVKGFYPSDIAVEWESNGQPENNYKTPPVLDSDGSFFLYSKLTVDK SRWQQGNVFCSCVMHEALHNHYTQKSLSLSPGKSGSLNDFEFAQKIEWHEGHHHHHH
pST1761	pADD2 TMEM95-Fc-Avi-His6 R70A R73A MWRLALGGVFLAAAQACVFCRLPAHDLSGRLARLCSQMEARQKECGASPDFSAFALDEVSMNKVTEKTHA VLAVMEIKEAVSSLPSYWSWLRKTKLPEYTREALCPPACRGSTTLNCSTCKGTEVSCWPRKRCFPGSQD LWEAKENLYFQGGSGGDKTHTCPPCPAPELLGGPSVFLFPPKPKDTLMI SRTPEVTCVVVDVSHEDPEVK FNWYVDGVEVHNAKTKPREEQYNSTYRVVSVLTVLHQDWLNGKEYKCKVSNKALPAPIEKTISKAKGQPR EPQVYTLPPSRDELTKNQVSLTCLVKGFYPSDIAVEWESNGQPENNYKTPPVLDSDGSFFLYSKLTVDK SRWQQGNVFCSCVMHEALHNHYTQKSLSLSPGKSGSLNDFEFAQKIEWHEGHHHHHH
pST1720	pVRC anti-TMEM95 3A01 IgG1 heavy chain MGWSCIIILFLVATATGVHSEVQLVESGGDLVPRGGSLKLSKVSGFAFSNYVMSWVRQSPKRELVVAEI STYGRYTFYPDSVTGRFTISRDNAKNTLFLEMSLSRSEDSAMYCARRDYGGSSVMDYWGQGTSVIVSS AKTTPPSVYPLAPGSAQAQTNMVTLGCLVKGYFPEPVTVTVNSGSLSSGVHTFPAVLQSDLYTLSSSVTV PSSTWPSETVTCNVAHPASSTKVDKIVPRDCGCKPCICTVPEVSSVFI FPPKPKDVLTI TLPKVTVCV VDISKDDPEVQFSWFVDDVEVHTAQTQPREEQFNSTFRSVSELPIMHQDWLNGKEFKCRVNSAAFPAPIE KTISKTKGRPKAPQVYTI PPPKEQMAKDKVSLTCMITDFFPEDITVEWQWNGQPAENYKNTQPIMDTDGS YFVYSKLNQKSNWEAGNTFTCSVLHEGLHNHHTEKSLSHSPGK
pST1721	pVRC anti-TMEM95 3A01 Fab heavy chain MGWSCIIILFLVATATGVHSEVQLVESGGDLVPRGGSLKLSKVSGFAFSNYVMSWVRQSPKRELVVAEI STYGRYTFYPDSVTGRFTISRDNAKNTLFLEMSLSRSEDSAMYCARRDYGGSSVMDYWGQGTSVIVSS AKTTPPSVYPLAPGSAQAQTNMVTLGCLVKGYFPEPVTVTVNSGSLSSGVHTFPAVLQSDLYTLSSSVTV PSSTWPSETVTCNVAHPASSTKVDKIVPRDC
pST1722	pVRC anti-TMEM95 3A01 light chain MGWSCIIILFLVATATGVHSENVLTQSPAIMSASPGEKVTMPCRASSVSSSSLHWYQQKGSASPGLWIYS TSNLASGVPARFSGSGSSTYSLSLTSVEAEDAATYYCQQYSGYPLTFGGGKLEIKADAAPTIVSIFPPS SEQLTSGGASVVCFLNNFYPKDINVKWKIDGSRQNGVLNSWTDQSKDSTYSMSSTLTLTKDEYERHNS YTCEATHKTSTSPIVKSFNRNEC
pST1723	pVRC anti-TMEM95 6B08 IgG1 heavy chain MGWSCIIILFLVATATGVHSEVQLVESGGDLVPGGSLKLSAASGFTFSTYGMWSWVRQTPDKRLEWVATI SFYGTHTYYPDILKGRFTISRDNAKNTLYLQMSLSKSEDTAMYFCAREDYDAMDYWGQGTSVTVSSAKTT PPSVYPLAPGSAQAQTNMVTLGCLVKGYFPEPVTVTVNSGSLSSGVHTFPAVLQSDLYTLSSSVTVPSST WPSETVTCNVAHPASSTKVDKIVPRDCGCKPCICTVPEVSSVFI FPPKPKDVLTI TLPKVTVCVVDIS KDDPEVQFSWFVDDVEVHTAQTQPREEQFNSTFRSVSELPIMHQDWLNGKEFKCRVNSAAFPAPIEKTIS KTKGRPKAPQVYTI PPPKEQMAKDKVSLTCMITDFFPEDITVEWQWNGQPAENYKNTQPIMDTDGSYFVY SKLNVQKSNWEAGNTFTCSVLHEGLHNHHTEKSLSHSPGK
pST1724	pVRC anti-TMEM95 6B08 Fab heavy chain MGWSCIIILFLVATATGVHSEVQLVESGGDLVPGGSLKLSAASGFTFSTYGMWSWVRQTPDKRLEWVATI SFYGTHTYYPDILKGRFTISRDNAKNTLYLQMSLSKSEDTAMYFCAREDYDAMDYWGQGTSVTVSSAKTT PPSVYPLAPGSAQAQTNMVTLGCLVKGYFPEPVTVTVNSGSLSSGVHTFPAVLQSDLYTLSSSVTVPSST WPSETVTCNVAHPASSTKVDKIVPRDC
pST1725	pVRC anti-TMEM95 6B08 light chain MGWSCIIILFLVATATGVHSDIQMTPSSLSASLGERVSLTCRASQDIGSNLNLWQQEPPDGTIKRLIYAT SSLDGVPKRFSGSRSGSDYSLTISSELEDFVDYCYLOYAI FPHYFGGGTKLEIKADAAPTIVSIFPPSS

	EQLTSGGASVVCFLNMFYPKDINVKWKIDGSRQNGVLNSWTDQDSKDYSTYSMSSTLTLTKDEYERHNSY TCEATHKTSTSPIVKSFNRECE
pST1776	pVRC anti-IZUM01 4E04 IgG1 heavy chain MGWSCIIILFLVATATGVHSQVQLKESGPGLVAPSQSL SITCTVSGFSLTDFGISWIRQPPGKLEWLGLI WGGGNTYNSALKSRLSISKDNSKSOVFLKMNSLQTDDTAMYCAKHGRFGNTPDYWGQGTTLTVSSAKT TPPSVYPLAPGSAQAQTNMVTGCLVKGYFPEPVTVTWNSGSLSSGVHTFPAVLQSDLYTLSSSVTVPSS TWPSETVTCNVAHPASSTKVDKIVPRDCGCKPCICTVPEVSSVFI FPPKPKDVLTIITLTPKVTCVVVDI SKDDPEVQFSWFVDDVEVHTAQTPREEQFNSTFRSVSELPIMHQDWLNGKEFKCRVNSAAFPAPIEKT SKTKGRPKAPQVYTI PPPKEQMAKDKVSLTCMITDFFPEDITVEWQWNGQPAENYKNTQPIMDTDGSYFV YSKLVNQKSNWEAGNTFTCSVLHEGLHNNHTEKSLSHSPGK
pST1777	pVRC anti-IZUM01 4E04 Fab heavy chain MGWSCIIILFLVATATGVHSQVQLKESGPGLVAPSQSL SITCTVSGFSLTDFGISWIRQPPGKLEWLGLI WGGGNTYNSALKSRLSISKDNSKSOVFLKMNSLQTDDTAMYCAKHGRFGNTPDYWGQGTTLTVSSAKT TPPSVYPLAPGSAQAQTNMVTGCLVKGYFPEPVTVTWNSGSLSSGVHTFPAVLQSDLYTLSSSVTVPSS TWPSETVTCNVAHPASSTKVDKIVPRDC
pST1778	pVRC anti-IZUM01 4E04 light chain MGWSCIIILFLVATATGVHSDVVMQTPLSLPVS LGDQASFSCTSGQSLVQSNQNTYLHWYLQKPGQSPKL LIYKVS NRFSGVPDRFSGSGSDTDFTLKISRVEAEDLG VYFCSQSTRFPWTFGGGKLEIKADAAPT VSI FPPSSEQLTSGGASVVCFLNMFYPKDINVKWKIDGSRQNGVLNSWTDQDSKDYSTYSMSSTLTLTKDEYE RHNSYTCEATHKTSTSPIVKSFNRECE
pST1779	pVRC anti-IZUM01 6F02 IgG1 heavy chain MGWSCIIILFLVATATGVHSDVQLQESGPDLVKPSQSPSLTCTVTGYSITSAYVWHWIRQFPGNKLEWMGY IQYSGSTNYPNPSLTSRISITRDTSKNQFFLKLKSVTTADTATYYCARAMITRGYFDYWGQGTTLTVSSAK TTPPSVYPLAPGSAQAQTNMVTGCLVKGYFPEPVTVTWNSGSLSSGVHTFPAVLQSDLYTLSSSVTVPS STWPSETVTCNVAHPASSTKVDKIVPRDCGCKPCICTVPEVSSVFI FPPKPKDVLTIITLTPKVTCVVVD ISKDDPEVQFSWFVDDVEVHTAQTPREEQFNSTFRSVSELPIMHQDWLNGKEFKCRVNSAAFPAPIEKT ISKTKGRPKAPQVYTI PPPKEQMAKDKVSLTCMITDFFPEDITVEWQWNGQPAENYKNTQPIMDTDGSYF VYSKLVNQKSNWEAGNTFTCSVLHEGLHNNHTEKSLSHSPGK
pST1780	pVRC anti-IZUM01 6F02 Fab heavy chain MGWSCIIILFLVATATGVHSDVQLQESGPDLVKPSQSPSLTCTVTGYSITSAYVWHWIRQFPGNKLEWMGY IQYSGSTNYPNPSLTSRISITRDTSKNQFFLKLKSVTTADTATYYCARAMITRGYFDYWGQGTTLTVSSAK TTPPSVYPLAPGSAQAQTNMVTGCLVKGYFPEPVTVTWNSGSLSSGVHTFPAVLQSDLYTLSSSVTVPS STWPSETVTCNVAHPASSTKVDKIVPRDC
pST1783	pVRC anti-IZUM01 6F02 light chain MGWSCIIILFLVATATGVHSDIKMTQSPSSMYASLGERVTITCKASQDSNSYLSWIIQQKPKGSPKTLIYGA NRLVDGVPSPRFSGSGSDYSLTISSELEYEDMGFYCYLQYDEFPPFTFGSGTKLETKADAAPT VSI FPPSS EQLTSGGASVVCFLNMFYPKDINVKWKIDGSRQNGVLNSWTDQDSKDYSTYSMSSTLTLTKDEYERHNSY TCEATHKTSTSPIVKSFNRECE

Plasmid for protein expression from baculovirus infection

Plasmid	Description & encoded protein sequence
pST1618	pACgp67a JUNO-His6 MVSAIVLYVLLAAAHAFAAGDELLNICMNAKHHKRVSPEDKLYEECIPWKDNACCTLTTSWEAHL DVS PLYNFSLFHCGLLMPGCRKHFIQAICFYECSPNLGPWIQPVGSLGWEVAPSGQGERVVNVP LQEDCEEW WEDCRMSYTKSNWRGGWDSQGNRCPKGAQCLPFSHYFPTPADLCEKTWSNSFKASPERRNSGRCLQK WFEPAQGNPNVAVARLFAGGHHHHH



## Chapter 5: *In situ* cryo-electron tomography reveals the asymmetric architecture of mammalian sperm axonemes

Zhen Chen<sup>1,2</sup>, Garrett A. Greenan<sup>1,2</sup>, Momoko Shiozaki<sup>3</sup>, Yanxin Liu<sup>2</sup>, Will M. Skinner<sup>4</sup>, Xiaowei Zhao<sup>3</sup>, Shumei Zhao<sup>3</sup>, Rui Yan<sup>3</sup>, Zhiheng Yu<sup>3</sup>, Polina V. Lishko<sup>4,5</sup>, David A. Agard<sup>2,\*</sup>, and Ronald D. Vale<sup>1,3,\*</sup>

1. Department of Cellular and Molecular Pharmacology, University of California, San Francisco, San Francisco, CA, USA.
2. Department of Biochemistry and Biophysics, University of California, San Francisco, San Francisco, CA, USA.
3. Janelia Research Campus, Howard Hughes Medical Institute, Ashburn, VA, USA.
4. Department of Molecular and Cell Biology, University of California, Berkeley, CA, USA.
5. Center for Reproductive Longevity and Equality, Buck Institute for Research on Aging, Novato, CA, USA

Correspondence: [valer@janelia.hhmi.org](mailto:valer@janelia.hhmi.org); [agard@msg.ucsf.edu](mailto:agard@msg.ucsf.edu)

### Abstract

The flagella of mammalian sperm display non-planar, asymmetric beating, in contrast to the planar, symmetric beating of flagella from sea urchin sperm and unicellular organisms. The molecular basis of this difference is unclear. Here, we perform *in situ* cryo-electron tomography of mouse and human sperm, providing the highest-resolution structural information to date. Our subtomogram averages reveal mammalian sperm-specific protein complexes within the microtubules, the radial spokes and nexin-dynein regulatory complexes. The locations and structures of these complexes suggest potential roles in enhancing the mechanical strength of mammalian sperm axonemes and regulating dynein-based axonemal bending. Intriguingly, we find that each of the nine outer microtubule doublets is decorated with a distinct combination of sperm-specific complexes. We propose that this asymmetric distribution of proteins differentially regulates the sliding of each microtubule doublet and may underlie the asymmetric beating of mammalian sperm.

## Introduction

Eukaryotic flagella and motile cilia are whip-like organelles whose rhythmic beating propels single-cell eukaryotes through fluids, clear dust particles in respiratory tracts, and enable the swimming of sperm cells of various species<sup>74,181,182</sup>. Most flagella from protozoa to mammals share a conserved core structure, the axoneme, comprised of nine doublet microtubules (doublets) arranged in a circle around a central pair complex of two singlet microtubules (the 9+2 configuration, Fig. 1a)<sup>183,184</sup>. Dyneins, microtubule-based molecular motors anchored on the nine doublets, drive the relative sliding of neighboring doublets<sup>185,186</sup>. However, if all dyneins were active at once, forces around the circle of nine outer doublets would be canceled and the axoneme would not bend<sup>184,187</sup>. To produce rhythmic beating motions, non-motor protein complexes are needed to regulate dynein activities across the axoneme structure<sup>184,188–194</sup>. The largest and most critical of these regulatory complexes are the radial spokes that bridge the outer doublets to the central pair complex, and the nexin-dynein regulatory complexes (N-DRCs) that crosslink neighboring doublets and regulate dynein activities across the axoneme structure.

Flagella from different cells display a wide variety of beating patterns, from the planar and symmetric waveforms observed in flagella of unicellular organisms and sea urchin sperm, to the various non-planar and asymmetric waveforms displayed by different mammalian sperm<sup>187</sup>. The structural and regulatory mechanisms underlying these different waveforms are poorly understood. Much of our current structural understanding of axonemes is derived from studies of *Chlamydomonas* and sea urchin sperm flagella using advanced cryo-electron tomography (cryo-ET) and image processing<sup>195–197</sup>. Apart from minor variations of the dyneins on a subset of the nine doublets, most of the other motor and non-motor protein complexes were found to be the same across the nine outer doublets. A unique bridge-like structure that crosslinks two neighboring doublets is proposed to constrain the plane of bending<sup>195–198</sup>. The pseudo-ninefold symmetry and the bridge structure are thought to be important for generating equivalent beating amplitudes in the opposite directions, leading to planar and symmetric waveforms.

Comparable structural information for mammalian sperm, which display varied non-planar asymmetric waveforms<sup>101,199,200</sup>, has lagged behind. A technical challenge in using modern cryo-electron microscopy to investigate mammalian sperm flagella is their thickness (>500 nm), which is close to the upper limit for the widely used 300 kV transmission electron microscopes (TEM). Recently, cryogenic focused ion beam/scanning electron microscopy (cryo FIB-SEM) and cryo-ET have been applied to study *in situ* macromolecular structures in sperm axoneme from mammals<sup>201</sup>. However, the limited data obtained in the previous study precluded processing strategies to analyze individual microtubule structures within the axonemes and also their spatial relationships *in situ*.

Here, we combined cryo FIB-SEM and *in situ* cryo-ET with data processing strategies to study the contextual assembly of different microtubule-based structures within mouse and human sperm flagella. Our data provide the highest resolution information to date for the mammalian sperm axonemes. Furthermore, our data reveal non-motor protein complexes in mammalian sperm that are not found in axonemes of other mammalian cilia and non-mammalian sperm. We show that each of the nine outer doublets is unique with regard to the composition of regulatory

complexes including radial spokes and N-DRC. The distribution of regulators varies between mouse and human sperm. We propose that the asymmetric distribution of these regulatory complexes across the axoneme could contribute to the asymmetric and nonplanar beating waveforms of various mammalian sperm.

## Results

### Sperm-specific features revealed by subvolume averaging

Freshly extracted mouse sperm were vitrified on EM grids and loaded into a cryo FIB-SEM to generate lamellae of  $\sim 300$  nm-thickness (Extended Data Fig. 1a, b). The lamellae were then imaged using a Krios 300 kV TEM and dose-symmetric tomographic tilt series ( $\pm 48^\circ$ ) around the axoneme were then acquired (Extended Data Fig. 1c). Our images showed detailed molecular features including the double-bilayer membranes of the surrounding mitochondria and individual microtubule protofilaments (Extended Data Fig. 1e,f). 3D tomograms were reconstructed from the tilt series, which revealed repetitive axonemal dyneins and radial spokes along the outer doublets, as well as periodic protrusions from the singlet microtubules of the central pair complex (Extended Data Fig. 1h,i). The periodicities of the radial spokes and central pair protrusions are  $\sim 96$  nm and  $\sim 32$  nm, respectively (Extended Data Fig. 1i), consistent with those described in *Chlamydomonas* and sea urchin sperm<sup>202,203</sup>.

To overcome the low signal-noise ratio of raw cryoET data, subvolume averaging of 96 nm-repeating units was used to reconstruct consensus density maps (Extended Data Fig. 2a). Our consensus maps of periodic units from all nine doublets revealed robust signals for individual microtubule protofilaments and other associated protein complexes that repeat every 96 nm (24 Å at FSC = 0.143;  $n = 9055$  subvolumes;  $N = 69$  tomograms) (Fig. 1b-d and Supplementary Data 1 and 2).

Inside the A-tubule of the outer doublet, we observed a filamentous density of microtubule inner proteins (MIPs) that is very similar to, but more extensive than that recently assigned as Tektin filaments in bovine trachea cilia<sup>204</sup> (Fig. 1b and Extended Data Fig. 3). The densities of MIPs have a periodicity of 48 nm, consistent with previously studied *Chlamydomonas* flagella and bovine trachea cilia<sup>204,205</sup>. We thus calculated a subvolume average of the 48 nm-repeating doublets focusing on the microtubule only (18 Å at FSC = 0.143;  $n = 18153$  subvolumes;  $N = 70$  tomograms) (Extended Data Fig. 3). The filamentous components have connections to all thirteen protofilaments of the A-tubule in mouse sperm axonemes, in contrast to the more limited connections of the Tektin filaments to A9-A13 and A1 protofilaments observed in bovine trachea cilia (Fig. 1e and see comparisons in Extended Data Fig. 3b). We observed three different modes of interaction between the MIPs and the lumen of microtubules: 1) interaction with tubulins within a single protofilament, 2) connections to the inter-protofilament space across two neighboring protofilaments, and 3) connections spanning multiple protofilaments (Figure 1e and Extended Data Fig. 3a,b). Notably, the A9-A10 junction is where the microtubule seam of the A-tubule is located<sup>206</sup>, and we observed several sperm-specific densities spanning protofilaments A9-A10 that are absent in the map of bovine respiratory cilia (Extended Data Fig. 3b). In addition, we observed striated densities along the helical pitch of the microtubule inside the B-tubule (Extended Data Fig. 3b,c). These striations

are separated by 8 nm and cover the intradimeric interface between the  $\alpha$ - and  $\beta$ -tubulins. Together, our averages revealed sperm-specific MIPs that form an extensive interaction network inside the doublets.

Our consensus map of mouse sperm axoneme reveals similar outer and inner arm dynein structures to those observed in sea urchin sperm (Fig. 1b-d and Extended Data Fig. 4a,b). However, we observed several unique non-motor protein complexes in the mouse sperm axoneme that do not have equivalent counterparts in the reported structures from *Chlamydomonas*, *Tetrahymena* and human respiratory cilia (Figure 1f,g)<sup>196,202,207–209</sup>. While the N-DRC in human respiratory cilia has a “V” shape<sup>209</sup>, our consensus map reveals extra densities that extend to the microtubule surface, creating an “N”-shaped structure (Fig. 1f). The radial spokes are comprised of three tower-like densities with two adopting similar morphology (RS1 and RS2) and a third, distinct radial spoke 3 (RS3) (Fig. 1b,c,g). When viewed from the “head” of the towers, radial spoke 1 (RS1) and 2 (RS2) both exhibit a cleft and a C2 symmetry axis that extends through the “tower”, while the radial spoke 3 (RS3) has a distinctive S-shaped surface with two holes (Fig. 1c), similar to the ones observed in human respiratory cilia<sup>209</sup>. In contrast, the heads of RS1 and RS2 from *Chlamydomonas* and *Tetrahymena* do not have the deep cleft<sup>192–194,207,208</sup> and the RS3 stump from *Chlamydomonas* is much shorter and RS3 from *Tetrahymena* has a smaller surface area of the head<sup>194,207</sup> (Extended Data Fig. 4c). Multiple additional densities, not found in respiratory cilia or unicellular organisms, were observed between the three spokes in the mouse sperm axoneme (Fig. 1g). First, we observed an ~20 nm-sized barrel-shaped density between RS1 and RS2, consistent with extra densities in sperm axonemes reported recently<sup>201,210</sup>. Our higher-resolution map revealed that the barrel is comprised of ten rod-shaped strands arranged in a right-handed twist configuration (Supplementary Movie 1). Furthermore, densities were found to crosslink RS2 and RS3, hereafter named as “RS2-RS3 crosslinker” (Fig. 1g). Of note, all of these extra densities in the MIPs, N-DRC and radial spokes are apparent even when our maps were low-pass filtered to 50 Å, a resolution lower than the published map of human respiratory cilia axoneme that does not possess these features (Extended Data Fig. 4d-f). Therefore, the additional densities found in mouse sperm are not due to higher resolution in this work but most likely reflect the presence of additional sperm-specific proteins.

### **The outer doublets are arranged in fixed radial positions**

We next calculated a subvolume average for the 32 nm-repeating units of the central pair complex (26 Å at FSC = 0.143; n = 3062 subvolumes; N = 70 tomograms) (Fig.2a-c and Extended Data Fig. 2b, Supplementary Data 1 and 2). Individual protofilaments of the two singlet microtubules were clearly resolved (Fig. 2b). Various proteins protrude from both microtubules, giving rise to an asymmetric cross-section contour of the central pair complex (Fig. 2b). We observed two distinct sets of MIPs inside the two singlet microtubules, both of which repeat every 32 nm (Extended Data Fig. 5a). On the external surface of microtubules, we observed both 32 nm-repeating and 16 nm-repeating protrusions. Notably, compared to the central pair complex of sea urchin sperm, where MIPs were not observed, the overall shapes of the external protrusions are very similar (Extended Data Fig. 5b), while both are different compared to the central pair complex of *Chlamydomonas* flagella (Extended Data Fig. 5c)<sup>203,211–213</sup>. These comparisons suggest that the central pair complex is likely conserved from

invertebrate to vertebrate sperm (animal sperm), but different from the ones from unicellular protists.

To understand how the outer doublets are arranged relative to the asymmetric central pair complex, we expanded our aligned subvolumes of the central pair complex three times to include the region where the outer doublet microtubules reside and then calculated an average without further alignment (Fig. 2d,e). Although the alignment was only performed for the center of central pair complex in the expanded subvolumes, nine distinct doublet microtubule densities that are parallel to the singlet microtubules could be resolved, indicating a remarkably consistent radial arrangement of doublets in the axonemes. The A- and B-tubules of doublet microtubule were clearly distinguishable based on the stronger MIP signals in the former. In contrast, discrete external complexes such as dyneins, radial spokes and N-DRC were poorly resolved. The lack of alignment along the longitudinal direction could be caused by mismatch of the 32-nm periodicity of the central pair complex and the 96-nm periodicity of the doublet microtubules (Fig. 2d,e).

To better understand the spatial relationship between the central pair complex and the outer doublets, we performed multi-body refinement by treating the central pair protrusions and the doublet structure as two rigid bodies, refining them separately and remapping them back to each raw subvolume<sup>214</sup>. Their relative positions were then subjected to principal component analysis (See Methods section and Extended Data Fig. 2c). For all nine interfaces, we always observed that the first principal component, which explains most variations (40-50%), was parallel to the longitudinal axis of axonemes (Supplementary Movie 2), suggesting the doublets and the central pair complex from different tomograms meet at different longitudinal offsets.

The multi-body refinement also yielded a map with the two rigid bodies placed at their average positions, allowing us to examine how the nine doublets interact with different protrusions of the central pair complex (Fig. 3a). Interestingly, we observed that most radial spoke heads were separated by a short distance from the central pair protrusions, without any resolved densities between them (Extended Data Fig. 5d). However, at the central pair interface with doublet 8, we observed protrusions from the central pair complex fit into the “cleft” of radial spoke 1 and 2 and also the two holes of the “S-curve” of the head of radial spoke 3 (Fig. 3b-d). Such complementary shapes may limit the sideways movement of doublet 8 and stabilize its radial position.

### **Asymmetric distribution of sperm-specific regulators**

We then sought to investigate if the outer doublets themselves differ from each other. We grouped doublet subvolumes based on their radial positions relative to the central pair complex (numbered as 1 through 9 as in references<sup>1,215</sup>). The subvolumes were aligned and the averages were calculated for each of the nine doublets ( $n = 810-954$  subvolumes;  $N = 58-64$  tomograms). This processing strategy identified unique densities emerging from the inner arm dyneins of doublet 5 and connecting to the B-tubule of doublet 6 (Extended Data Fig. 6). These connecting densities are similar to the “5-6 bridge” observed in sea urchin at lower resolutions<sup>197</sup>, validating our assignment of doublets and processing strategies. Interestingly, the radial spokes and other 96-nm repeating features on both doublet 5 and 6 could be resolved concurrently after local refinement, indicating there is a relatively consistent longitudinal offset (~20 nm) between these

two doublet microtubules throughout different axonemes (Extended Data Fig. 6d). The correlation of the unique bridge densities and the consistent offset that is observed only between doublet 5 and 6 suggest that the bridge could limit the relative sliding between this outer doublet pair (in comparison to another doublet pair in Extended Data Fig. 6g,h).

Next, we systematically compared motor and non-motor/regulatory protein complexes across the nine doublets. Outer arm dyneins across all nine doublets were indistinguishable from our consensus average (as shown in Figure 1d). The densities of inner arm dyneins were also generally similar, with two exceptions. For doublet 5, densities corresponding to dynein e and g (nomenclature defined in *Chlamydomonas*<sup>196</sup>) were shifted compared to the other doublets (Extended Data Fig. 7a), while for doublet 9, densities for dynein b were not resolved (Extended Data Fig. 7b). These results indicate that the motor proteins are largely the same with only minor variations.

We next examined the radial spokes from each doublet. Strikingly, we observed that the sperm-specific features were asymmetrically distributed across the nine doublets (Fig. 4). The barrel density was not observed in doublet 1 and 9 and was present at a lower occupancy in doublet 3. In the remaining six doublets, the occupancy of the barrel was comparable to other repeating structures (e.g. radial spoke 1). The RS2-RS3 crosslinkers are absent in doublets 3 and 8, but present in the remaining doublets. In addition, for doublets 2 and 3, we resolved extra densities close to the base of RS3 (RS3 scaffold) that were not observed in our consensus averages or previously reported consensus averages, in which subvolumes from all nine doublets were averaged together<sup>201,210</sup>. This is likely because only one or two doublets out of the nine possess these features (11-22%) and averaging smeared the signals. Our processing strategy allowed us to isolate these subvolumes based on cellular contextual information and the high occupancies of these unique structures in the respective doublets suggest their consistent presence in these specific doublets.

We also examined the N-DRCs that crosslink neighboring doublets (Figure 5). All nine N-DRCs share the common “V” shape density, but the extra connections to the microtubule show heterogeneities. Interestingly, N-DRCs from doublets 2, 3, 4 share an arch-shaped density perpendicular to the microtubules while the ones from doublets 6, 7, 8 have 45°-tilted thin strands. Doublets 1, 5 and 9 all have distinct densities, leading to five different N-DRCs. Note all these features were observed at similar signal-to-noise levels and since they resulted from averaging of more than 800 subvolumes sampled in ~60 different axoneme tomograms, they represent the commonly shared features within each individual doublet.

In order to test if the bending states of the axonemes affect the features of radial spokes and N-DRC, we curated subvolumes from tomograms with and without apparent curvatures and calculated per-doublet averages. The same set of features of radial spokes and N-DRC were observed. In addition, we also collected a dataset of demembrated sperm axonemes (48 tomograms) that are not actively beating. The radial spokes and N-DRCs in these non-motile sperm have the same asymmetric features highlighted in Fig. 4 and Fig. 5, suggesting the asymmetric densities were not caused by bias in macroscopic curvatures, but likely reflect intrinsic compositional heterogeneities in the nine doublets.

Our *in situ* data also allowed us to separate axonemes of the midpiece and principal piece based on the presence of mitochondrial and fibrous sheaths, respectively. We averaged subvolumes from these two regions for each doublet and found only subtle differences in the base of RS3 of doublet 2 and also the RS1 of doublet 7 (Extended Data Fig. 8a). In these per-doublet averages, we did not resolve robust densities corresponding to the attachments between outer dense fibers and the respective doublets. Previous studies suggest averages of all nine doublets in the proximal principal region from a few tomograms have such attachments<sup>201</sup>. However, our raw tomograms of the proximal principal piece showed that some outer dense fibers are close to the corresponding doublets and some are further away (Extended Data Fig. 8b). Such variations require per-doublet averages to be considered. However, the subset of tomograms in the proximal principal region is small and per-doublet averaging resulted in anisotropic 3D reconstructions. An even larger dataset is required to resolve structures with such a specific and complex distribution pattern. We also calculated an average of subvolumes from the nine doublets near the beginning of axonemes (within 2  $\mu\text{m}$ ) and found no significant difference when compared to the overall consensus average, suggesting the sperm-specific features are established very close to the basal region of the flagella (Extended Data Fig. 8c,d). Together, these data highlighted the overall consistency of the axoneme structure along the flagella.

Overall, our per-doublet averages showed that the distributions of various sperm-specific features for both the radial spoke complexes and the N-DRC follow distinct patterns, such that every doublet is decorated by a unique combination of proteins.

### **A distinct asymmetric pattern in human sperm**

We next examined whether the unique outer doublet features observed in mouse sperm were also conserved in human sperm. We collected tilt series of intact human sperm without milling, focusing on the thinner principal piece of the flagella (Extended Data Fig. 9a,b; Supplementary Data 1 and 2). We then calculated consensus averages of doublet microtubules and the central pair complex (23  $\text{\AA}$  and 31  $\text{\AA}$  at FSC = 0.143;  $n = 6613$  and  $2365$  subvolumes,  $N = 56$  and  $59$  tomograms, respectively) (Fig. 6a,b). These consensus averages of human sperm were similar to the ones from mice, with the notable exception that the relative occupancy of the barrel between RS1 and RS2 was much lower in human sperm. Using the per-doublet processing approach described above, we then calculated averages for each of the nine doublets individually. Although the per-doublet averages from human sperm were noisier than those from mouse sperm due to larger sample thickness ( $\sim 330$  nm vs.  $>400$  nm as shown in Extended Data Fig. 9c-e), they were sufficient to identify the aforementioned unique features, including the 5-6 bridge, the barrel and RS3 scaffolds (Fig. 6c). In particular, the 5-6 bridge, RS2-RS3 crosslinkers and RS3 scaffolds show similar asymmetric distributions between human and mouse sperm. However, we observed that the barrel density only exists in four out of nine doublets, in contrast to seven out of nine doublets in mouse sperm axonemes (Fig. 6c). This is consistent with the lower occupancy of barrel densities in our consensus average (Fig. 6a). In particular, doublet 2-5 appear to be different in human and mouse axoneme in terms of the presence of the barrel, while the rest of the doublets are similar. We also examined the N-DRC from each doublet and found five distinct structures like those in mouse sperm (Extended Data Fig. 9f). In summary, our data

indicate the asymmetric architecture of axonemes is a general feature of mammalian sperm axonemes, although there are intriguing variations of distribution for the barrel in human and mouse sperm.

## Discussion

Our *in situ* tomography studies of mouse and human sperm revealed a large ensemble of macromolecular complexes in their native cellular environment. In particular, we observed various sperm-specific features in the MIPs, radial spokes and N-DRC that were not observed in mammalian respiratory cilia and non-mammalian sperm. Furthermore, we reconstructed the entire axoneme using the cellular contextual information and uncovered the asymmetric architecture of mammalian sperm axoneme, where every microtubule-based structure is decorated by a unique set of non-motor proteins (Fig. 7a,b). As these non-motor proteins regulate the dynein activity based on previous studies, we propose that the asymmetries of non-motor protein complexes could modulate the sliding of the nine doublets individually to shape the species-specific asymmetric waveforms observed for mammalian sperm, as discussed below.

### Sperm-specific structures added mechanical couplings

Mammalian sperm flagella are generally much longer and wider compared to flagella from unicellular organisms or respiratory cilia (lengths of  $>45\ \mu\text{m}$  vs.  $\sim 10\ \mu\text{m}$  and diameters of  $>0.5\text{-}1\ \mu\text{m}$  vs.  $\sim 0.3\ \mu\text{m}$ ). Sperm axonemes are also surrounded by additional subcellular structures, such as outer dense fibers, mitochondrial and fibrous sheaths, which likely present additional mechanical challenges during rhythmic beatings. Previous studies also suggested larger bending torques are associated with mammalian sperm compared to other cilia<sup>216</sup>, but it has remained unclear how sperm axonemes have evolved specific mechanisms to withstand the additional mechanical stress. Our averages of *in situ* cryoET revealed many additional non-motor proteins that crosslink the known axonemal components. We propose that these additional proteins function to strengthen the mechanical rigidity of the corresponding components to accommodate higher mechanical requirements of sperm axonemes.

The microtubules themselves must be able to withstand vigorous bending and the seam is the weakest point<sup>217,218</sup>. Our data revealed the most extensive MIPs interaction network in microtubules observed in axonemes to date. The proteins between the A9 and A10 protofilaments could stabilize the lateral interfaces within the seam. Also, the proteins that form the striations inside the B-tubule could crosslink the tubulins within B2-B6 protofilaments while also couple these protofilaments laterally along the helical pitch. We also observed extensive filamentous structures within the A tubule that likely provide additional mechanical stability. Tektin-1 to -4 have been known to assemble into three-helix bundles that pack along one another laterally inside the microtubule doublets of bovine trachea cilia<sup>204</sup>, and likely compose a part of the filamentous densities observed in sperm. Mammalian sperm also contain an additional tektin (Tektin-5; see Supplementary Table S1)<sup>219</sup>, which is a candidate for some of the additional sperm-specific densities (as shown in Extended Data Fig. 3b), although the assignment requires confirmation with higher-resolution reconstructions.



We also observed unique sperm-specific densities on the exterior of the microtubules, specifically the barrel and RS2-RS3 crosslinker between the three radial spokes, the RS3 scaffolds, and extra densities in N-DRC. The radial spokes were previously observed to tilt relative to the microtubule<sup>220</sup>. Additional connections between the three radial spokes and the scaffolds at the bases would integrate them together into a more rigid unit. Another possibility is that the coupling could lead to coordinated movement of the three radial spokes. The N-DRCs regulate the sliding between the neighboring doublets and prevent splaying of axonemes<sup>191</sup>. Extra densities linking to the microtubules could improve the stability of N-DRC under higher mechanical stress. Together, the additional protein complexes in mammalian sperm would help to maintain the geometric integrity of the (9+2)-microtubule configuration of the axoneme under mechanical stress during vigorous beating motions.

### **The arrangement of the doublets and the central pair complex**

Previous studies suggested that the central pair complex can twist radially relative to the nine outer doublets in *Chlamydomonas* flagella<sup>221</sup>. Our observation of densities corresponding to the nine doublet microtubules in the average of the entire (9+2) axoneme can exclude the possibility of such free twisting in mammalian sperm as the doublet densities would be smeared by averaging (Fig. 2d,e). Interestingly, we observed a cleft between the two halves of radial spokes 1 and 2 and holes in the radial spoke 3 in mammalian sperm axonemes (Fig. 1c), in contrast to the flatter surface of the radial spoke heads from *Chlamydomonas* flagella<sup>192-194</sup> (Extended Data Fig. 4c). While the flat surfaces may enable the twisting in *Chlamydomonas*<sup>221</sup>, the complementary shapes of radial spokes and protrusions from the central pair complex in mammalian sperm may restrict such radial movements (as shown in Fig. 3b-d). Fixation of radial positions of the nine doublets also orients each of the radial spoke complexes in proximity to unique stripes of densities of the central pair complex (Fig. 3a). This arrangement could allow functional specialization and divergent evolution of each doublet microtubule, such as the distinct sets of sperm-specific features in the nine doublets.

Our multi-body refinement suggests the existence of heterogeneities in the longitudinal offsets between doublets and the central pair complex in the randomly sampled axonemes that were combined in the averages (Supplementary Movie 2). This observation is consistent with the sliding hypothesis for axonemal bending, in which active dyneins generate displacement between the neighboring doublets<sup>185</sup>. Such movement would also lead to displacement of the doublets relative to the central pair complex along the longitudinal axis of axonemes, as if there are nine trains (doublets) move along nine tracks (central pair protrusions) (Fig. 7c).

The 5-6 bridge is a sperm-specific feature that appears to be conserved between sea urchin<sup>197</sup> and mammalian sperm. Previous studies pointed out for two parallel inelastic microtubule filaments, bending would lead to gradual accumulation of longitudinal offsets between if they are at different radii of the bend since the outer curve would be longer than the inner one (Fig. 7d)<sup>220</sup>. As an estimate based on the reported curvature of mouse sperm<sup>1</sup>, the offsets between neighboring doublets could differ as much as  $\Delta \sim 28$  nm within one tomogram (See details in the method section). More importantly, the initial offset of each tomogram varies depending on how much sliding has happened upstream or downstream of the imaged area of the flagella. On the other hand, the resolved periodic features in both doublet 5 and 6 at the same

time suggest there is a consistent offset between these two doublets (Extended Data Fig. 6), not just within each tomogram but also among the 63 tomograms that contribute to the average. Due to the nature of random sampling of our imaging areas of different cells (N = 63 tomograms), this could happen if there is generally limited bending along the direction parallel to the plane of these two filaments in mouse flagella (Fig. 7e). The bundling of these two doublets can create a stiffer filament compared to a single doublet, with distinct elastic properties or bending propensities in different directions. Such asymmetries of mechanical properties within the nine doublets could also contribute to complicated waveforms.

### **Asymmetries of regulators may lead to asymmetric beatings**

Our *in situ* data and processing strategies based on the contextual information revealed that the axoneme itself, which appeared to have “pseudo nine-fold symmetry” in the classical TEM images<sup>74</sup>, is highly asymmetric at the molecular level. As the axoneme is the underlying engine that drives the flagellar beating motion, such asymmetries in structure could lead to asymmetric beating waveforms.

Furthermore, the asymmetries lie mostly in the mammalian sperm-specific non-motor protein complexes, including the radial spokes and N-DRCs. These complexes are well-established regulators of dynein motor activities and defects in individual protein components can lead to irregular beating<sup>188,189,191,192</sup>. In mammalian sperm, we show here that each of the nine doublet microtubules is decorated by a unique composition of these regulators. We speculate that this distinct molecular composition could lead to differences in the sliding speeds, or bending forces for each of the doublet pairs (Fig. 7). The non-equivalent forces could lead to a deviation from the single plane of beating characteristic of more symmetric axonemes. Thus, we hypothesize that the non-uniform distribution of sperm-specific radial spoke and N-DRC regulators are important for asymmetric and non-planar beating. Additionally, previous studies showed that human and mouse sperm have different swimming waveforms (see movies in references<sup>200,222</sup>). Our studies suggest that although the radial spoke barrels are conserved in human and mouse, their distribution varies and this variation could create diversities in sperm swimming behavior.

This study has revealed mammalian sperm-specific structures within the microtubules, radial spokes and N-DRCs that are absent in sea urchin and zebrafish sperm<sup>223–225</sup>. The still unknown proteins likely arose to serve functions required by natural fertilization in mammals. Sperm from different species are cast into a foreign environment and selected for their ability to reach and fertilize an egg. Sea urchin and zebrafish sperm swim in water whereas mammalian sperm swim in a thin layer of viscous liquid on uneven surfaces of the female reproductive tracts<sup>4</sup>. The viscous environment brought more mechanical challenges to the axonemes, hence the microtubule filaments inside. In addition, asymmetric and non-planar waveforms of mammalian sperm could be beneficial to navigate around three-dimensional obstacles in the reproductive tracts. Furthermore, the dimensions and physical characteristics of reproductive tracts vary among different mammals, so fine-tuning the underlying molecular features to produce specialized waveforms, are likely under strong evolutionary selection. In the future, systematic genetic and proteomic analyses of mammalian sperm-specific proteins would be

valuable to connect sperm-specific axonemal structures with their functions in sperm motility and reproductions.

### **Acknowledgement**

We are grateful to members of the Vale and Agard laboratories for discussions and critical reading of the manuscript. We thank Shixin Yang from the CryoEM facility at Janelia Research Campus for his assistance with data collection. We thank Caiying Guo for generously sharing the resources required for the mouse experiments. We thank Zanlin Yu, Eric Tse and David Bulkley in the UCSF EM core facility for their assistance with data collection. We thank Sam Li and Shawn Zheng at UCSF for suggestions on EM data processing. We thank Tom Goddard at UCSF for providing a script to mark coordinates of subtomograms. EM data processing utilized computing resources at both the workstations at Janelia Research Campus and HPC Facility at UCSF. We are grateful to members of the Vale laboratory and Agard laboratory for discussions and critical reading of the manuscript. Z.C. was supported by the Helen Hay Whitney Foundation Postdoctoral Fellowship. This material is based upon work supported by the National Science Foundation Graduate Research Fellowship Program under grant numbers DGE 1752814 and DGE 2146752 (To W.M.S.). Any opinions, findings, and conclusions or recommendations expressed in this material are those of the author(s) and do not necessarily reflect the views of the National Science Foundation. P.V.L. received funding from Pew Biomedical Scholars Award and GCRLE grant from Global Consortium for Reproductive Longevity and Equality made possible by the Bia-Echo Foundation. D.A.A. received funding from NIH R35GM118099. R.D.V. received funding from NIH R35GM118106 and the Howard Hughes Medical Institute. The UCSF cryoEM facility has been supported NIH grants 1S10OD026881, 1S10OD020054, and 1S10OD021741.

### **Author Contributions Statement**

Z.C., G.A.G. D.A.A. and R.D.V. conceived the project and designed the experiments after discussions with other authors. S.Z. provided the mouse sperm sample. M.S. and Z.C. prepared mouse sperm lamellae grids. W.S. and P.V.L. provided human sperm samples. Z.C. and Y.L. prepared the human sperm grids. M.S., Z.C. and G.A.G. performed the FIB-SEM processing. Z.X. and Z.Y. optimized the data collection. Z.C. processed the data with help from M.S., X.Z and R.Y. and suggestions from G.A.G. and D.A.A.. Z.C. and R.D.V. wrote the manuscript draft with comments from all authors.

### **Competing Interests Statement**

The authors have no conflicts of interest to declare that are relevant to the content of this article.

## Figures Legends/Captions

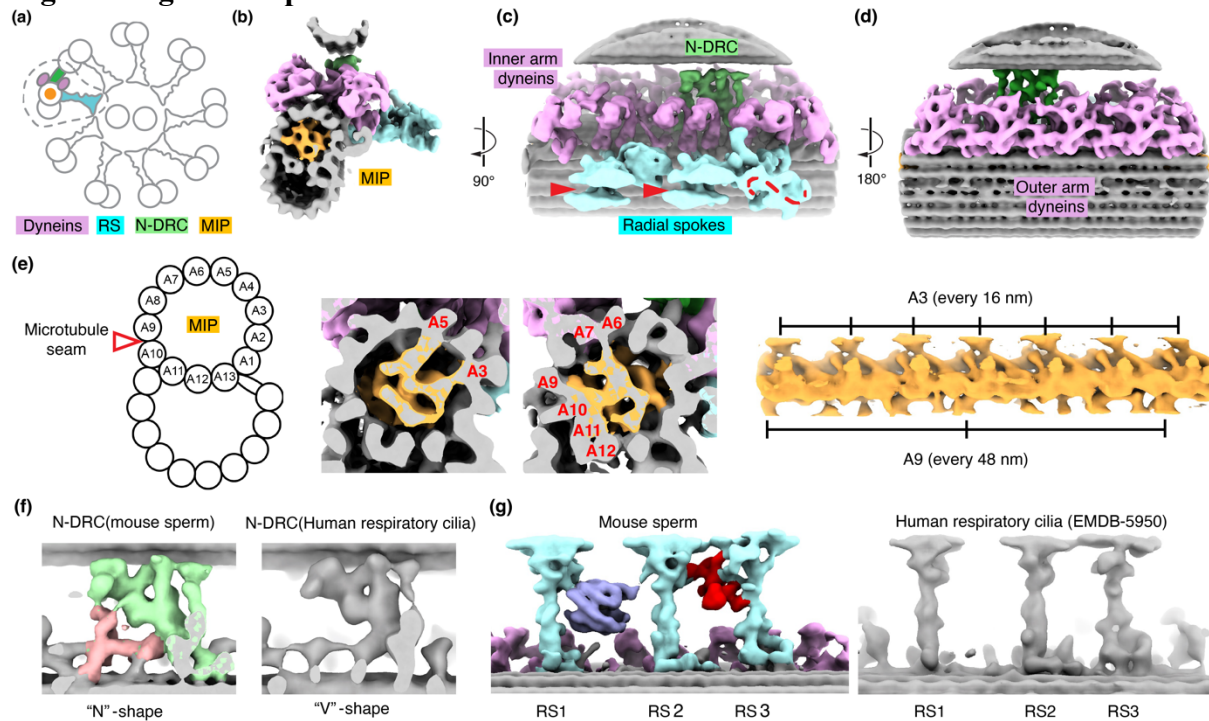


**Figure 1. The consensus average of nine doublets in mouse sperm possesses unique features in non-motor protein complexes including microtubule inner proteins (MIPs), nexin-dynein regulatory complex (N-DRC) and radial spokes (RS).** a, Schematic of a cross-section view of the conserved (9+2) configuration of axonemes in motile cilia. One doublet is highlighted, and its associated motor and non-motor protein complexes are labeled. The dyneins, N-DRC, MIPs and RS are colored in pink, green, orange and cyan, respectively. b-d, Three views of the consensus subvolume average of nine doublets in mouse sperm axonemes. Different protein complexes are highlighted as in a. The clefts in the top of radial spokes 1 and 2 and the “S”-shaped head of radial spoke 3 are indicated by the red arrowheads and dashed line, respectively in c. e, Schematic of the doublet microtubule with individual protofilaments labeled. Two cross-sections of the A-tubule and one longitudinal view of the isolated MIPs densities are shown. The MIPs are colored in orange. The protofilaments connecting to the MIPs and the periodicities for the connections are indicated. f, g, Comparison of densities of N-DRC and radial spokes from mouse sperm flagella (this study) and human respiratory cilia (EMD-5950)<sup>209</sup>. In f, Additional densities in the mouse sperm N-DRC are highlighted (light red). In g, the unique densities of a barrel and a RS2-RS3 crosslinker in the mouse sperm axoneme are highlighted in blue and red, respectively.

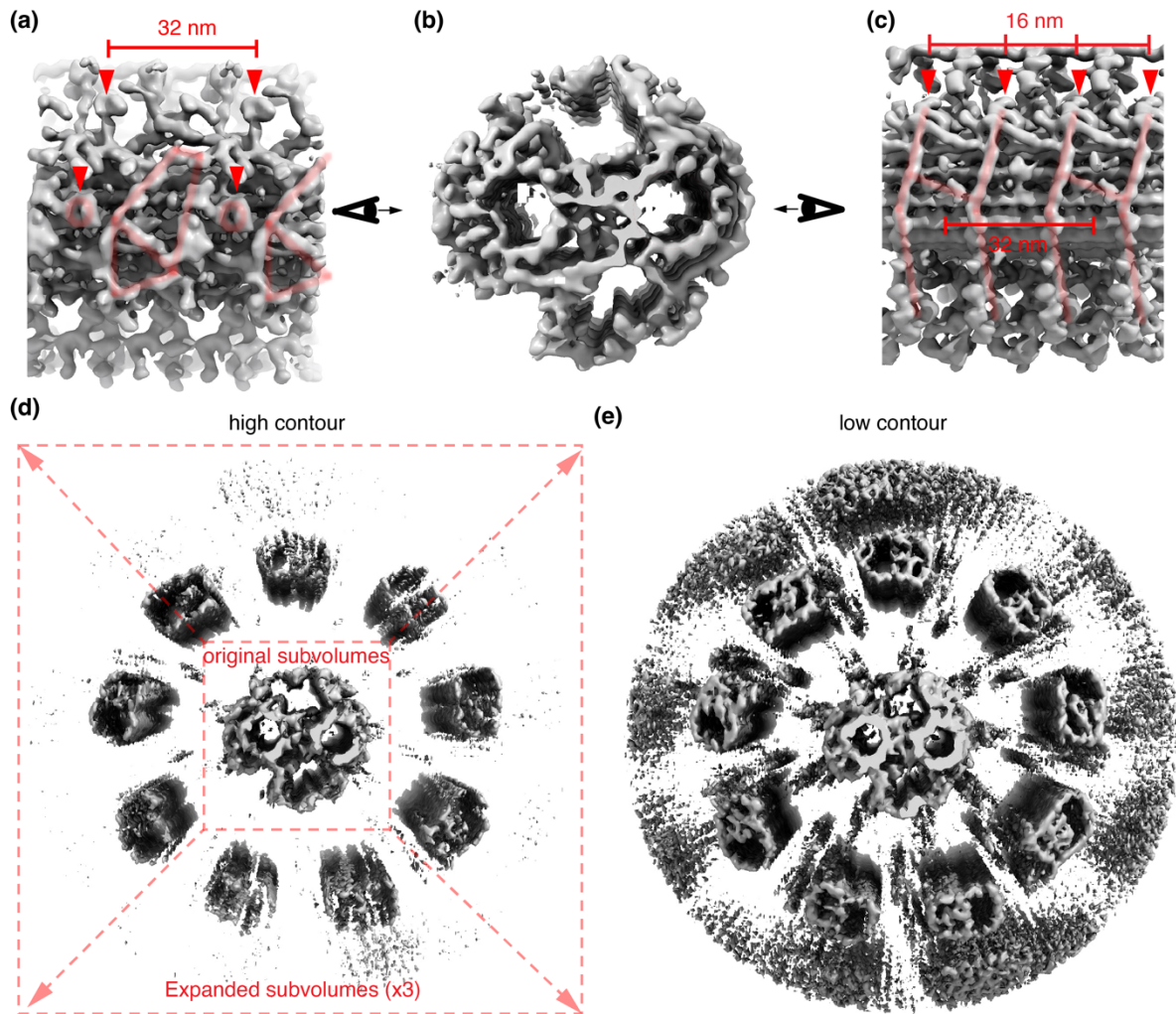


**Figure 2. The central pair complex presents asymmetric surfaces in different directions. a-c,** Three views of the central pair complex of the mouse sperm axoneme. In **a, c**, periodic densities are indicated by red arrowheads or highlighted by light red lines and their periodicities are labeled. **d**, An average of the entire axoneme calculated by expanding the original subvolumes for the central pair complex three folds, and averaging without further alignment. At high contour, densities of nine doublet microtubules are resolved at nine distinct radial positions. **e**, The same average as in **d** is shown at low contour. Note the A-tubules from doublet microtubules are distinguishable due to the presence of extensive MIPs densities. Smear densities corresponding to where dyneins, radial spokes and N-DRCs locate could be observed at lower occupancies than the doublet microtubules.

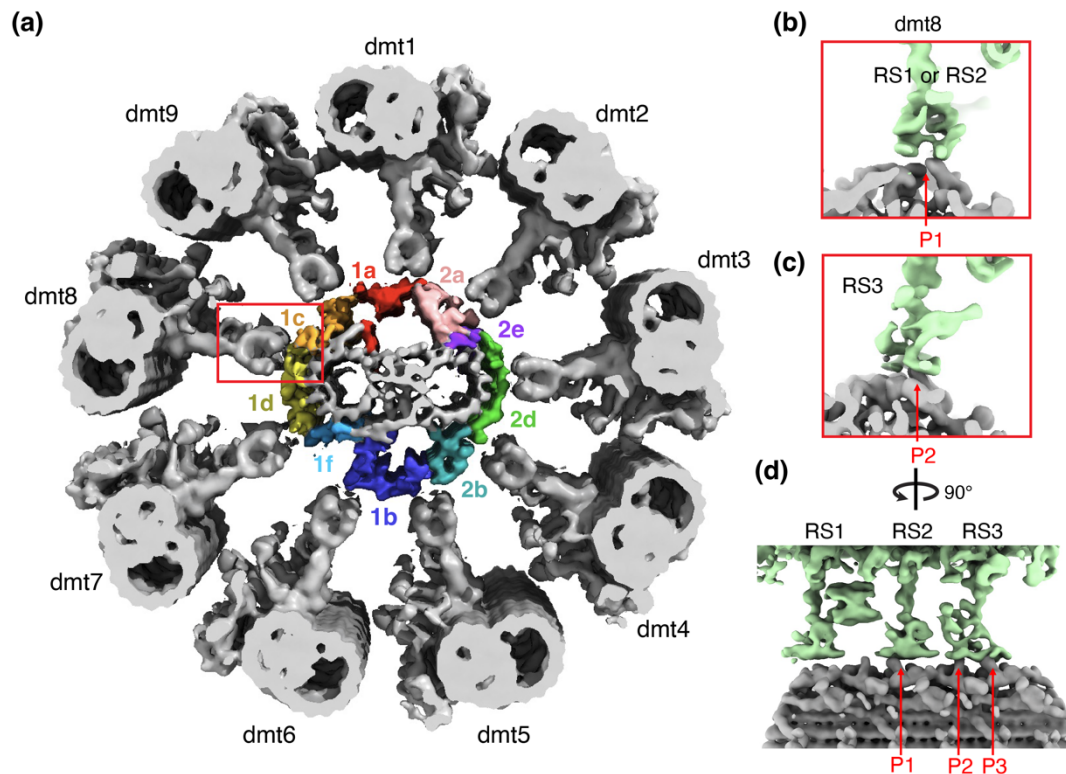


**Figure 3. The diverse interfaces between radial spokes and central pair.** **a**, The arrangement of central pair complex and nine doublets is mapped based on averaging relative positions deduced by the multi-body refinement. The different protrusions of the central pair complex are colored in accordance with Carbajal-Gonzalez et al. 2013. The interface between the radial spokes from doublet 8 and the central pair complex is indicated (red rectangle). **b-d**. Three different views of the interface between the radial spokes from doublet 8 and the protrusions from the central pair complexes (P1, P2 and P3). **b**, Longitudinal view of the interface. **c**, Two cross-sections views showing how the RS1/RS2 and RS3 from doublet 8 interact with the protrusions of central pair.



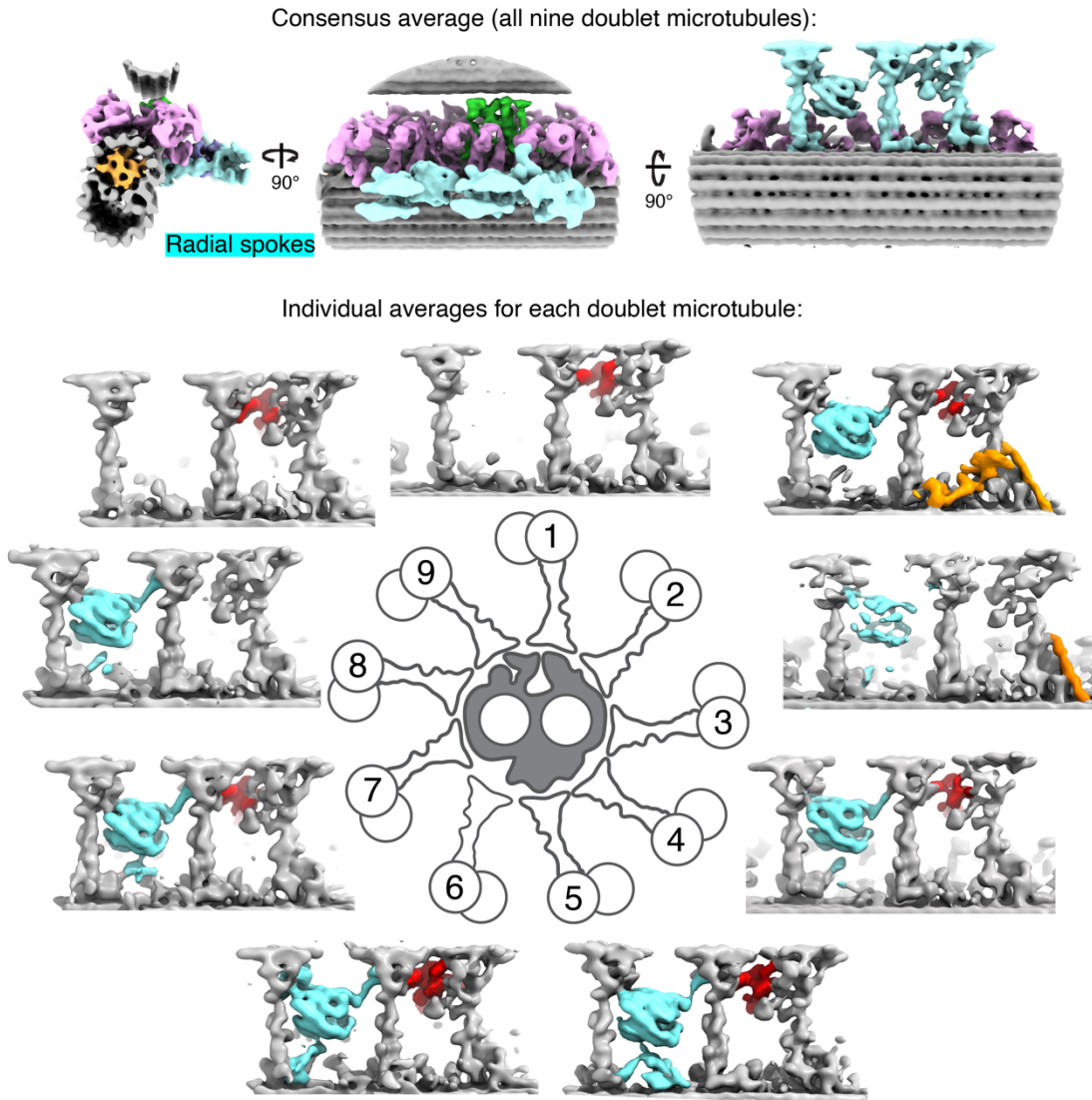


**Figure 4. Asymmetric distribution of sperm-specific features in radial spokes from the nine doublet microtubules in mouse sperm.** Three orthogonal views of the consensus average of doublets in mouse sperm are shown as in Fig. 1b-d. At the bottom panel, densities corresponding to radial spokes from the nine per-doublet averages are shown around a schematic of a cross-section view of the (9+2)-axoneme. Common features are colored in grey, while the barrel, RS2-RS3 crosslinker and RS3 scaffolds are highlighted in cyan, red and orange, respectively.

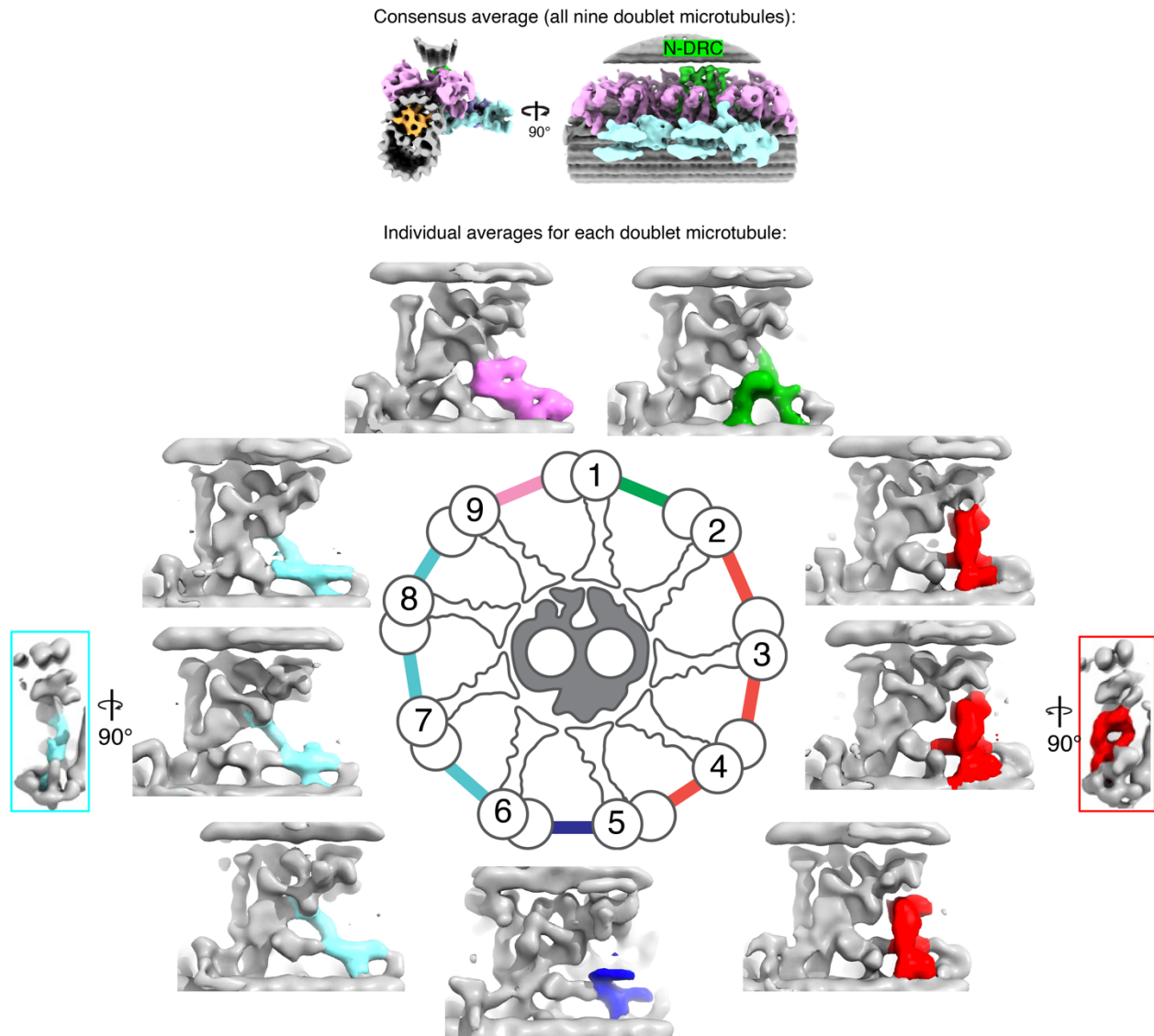


**Figure 5. Asymmetric distribution of sperm-specific features in N-DRCs from the nine doublet microtubules in mouse sperm.** Two orthogonal views of the consensus average of doublets in mouse sperm are shown at the top panel. At the bottom panel, densities corresponding to N-DRC from the nine per-doublet averages are shown around a schematic of a cross-section view of the (9+2)- axonemes. Common features among the N-DRC are colored in grey, while the unique features are highlighted.



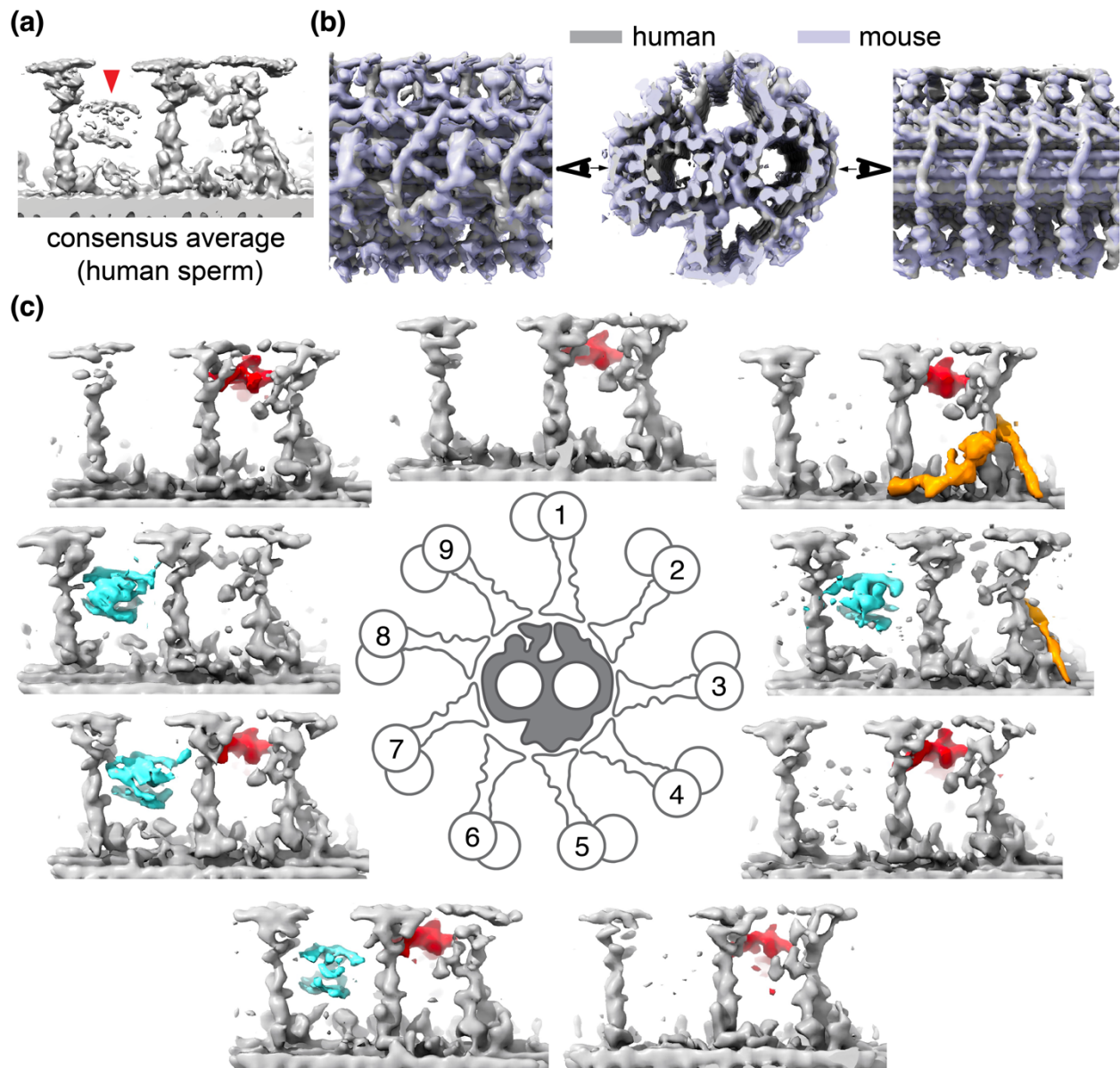


**Figure 6. Human sperm have the barrel structures differently distributed in the nine doublet microtubules compared to mouse sperm.** **a**, A consensus average map of the radial spoke for human sperm axonemes. The barrel density appears to have lower occupancy compared to the radial spokes (indicated by the red arrowhead), which is not the case in mouse sperm shown in Fig. 1g. **b**, The consensus average map of the central pair complex for human sperm axonemes (grey) is overlaid with the one from mouse sperm axonemes (blue). **c**, Densities corresponding to radial spokes from the per-doublet averages are shown around a schematic of the (9+2)-axonemes. Common features among the radial spokes are colored in grey, while the barrel, RS2-RS3 crosslinker and RS3 scaffold are highlighted in cyan, red and orange, respectively.

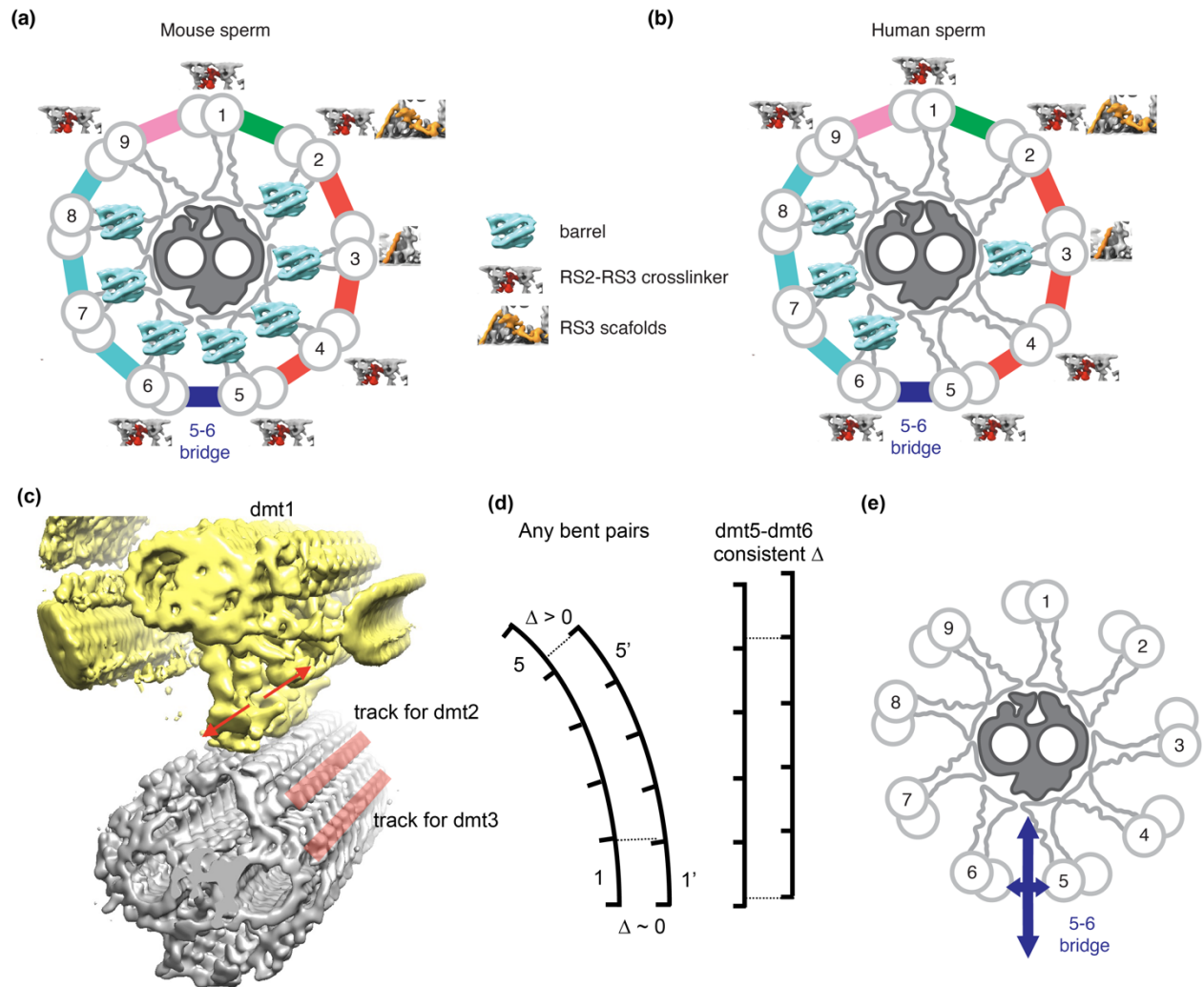
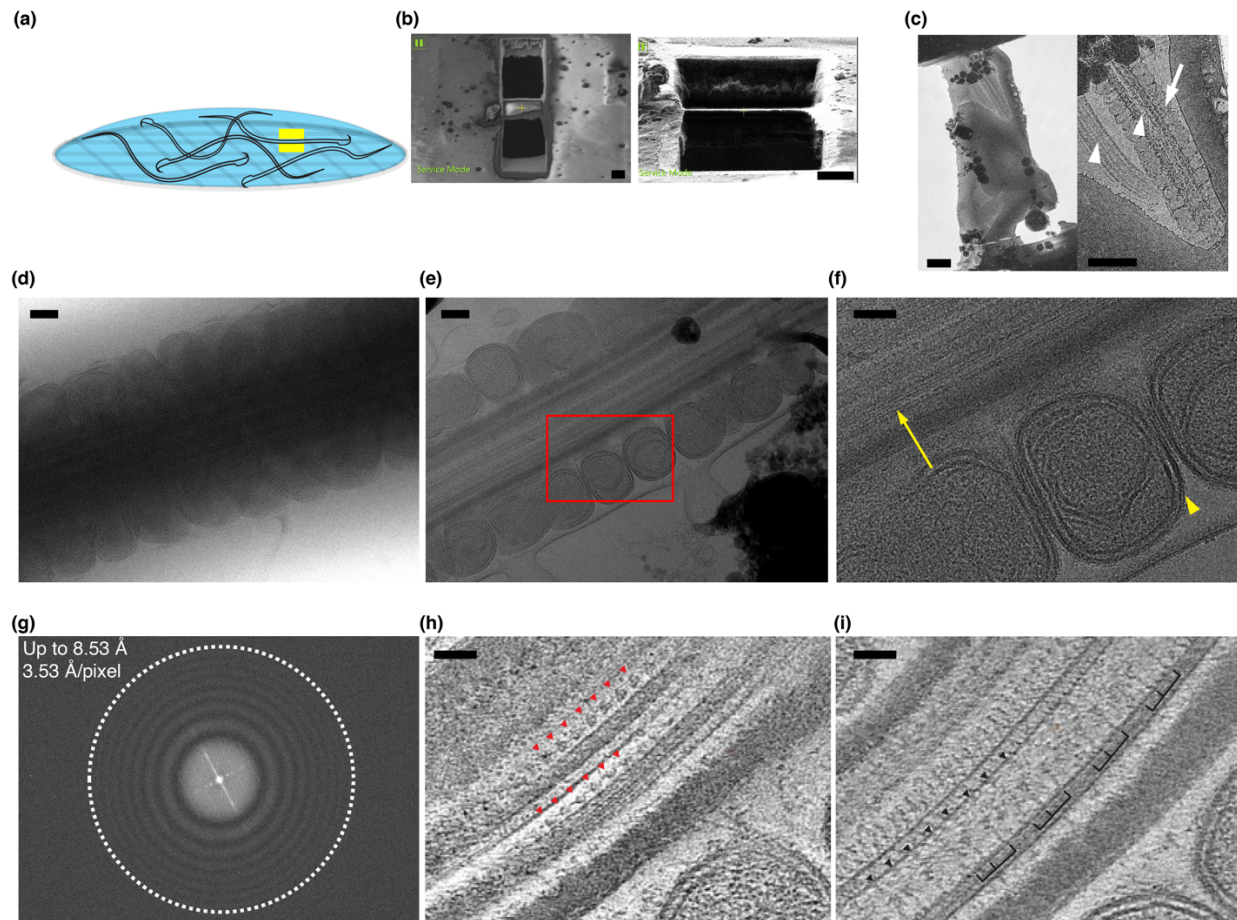


**Figure 7. Model: every outer doublet is surrounded by a different set of regulatory complexes in mammalian sperm.** Schematic of the (9+2) axonemes of mouse (a) and human sperm (b). The doublets are numbered and the sperm-specific regulatory complexes are labeled for each of the nine outer doublets. In particular, the components from the radial spokes are shown for each doublet and the N-DRCs are colored differently depending on the extra density (as in Fig. 4-6). Note the barrel distribution is different in mouse and human sperm axonemes. c, Radial spokes from different doublets interact with specific stripes of protrusions of the central pair complex. Our multi-body refinement is consistent with the sliding hypothesis and potential longitudinal movements of dmt1 are indicated by the two red arrows. The model is analogous to “a train moving on a track”. d, Schematics showing gradual accumulations of offsets between two filaments in a curved axoneme (left panel) and consistent offset between doublet 5-doublet 6 (right panel). e, The constant offset within tomograms and among tomograms (N = 63) would be consistent with limited horizontal bending in sperm flagella.

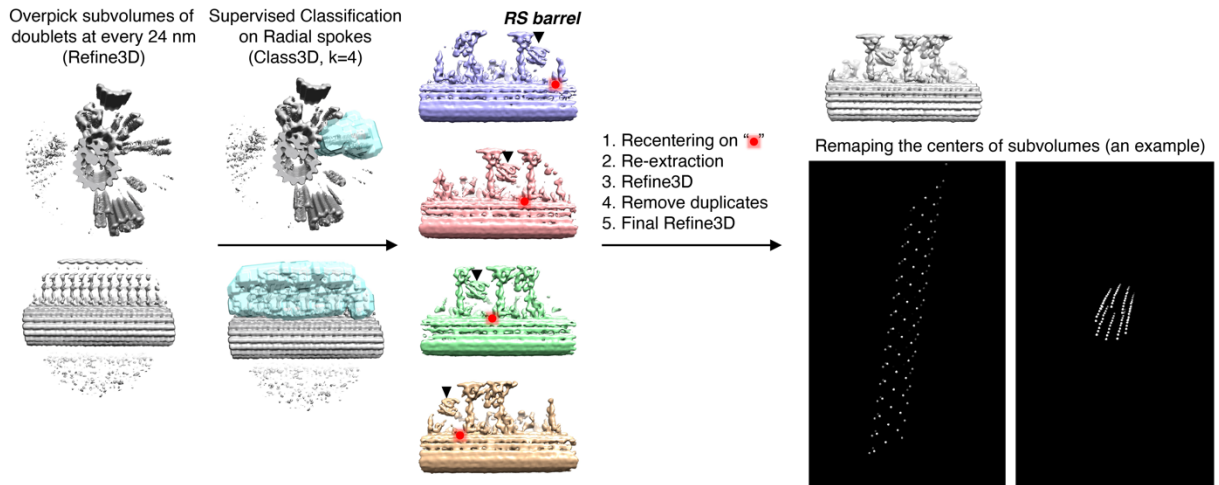


**Extended Data Fig. 1. The workflow of FIB-SEM/cryo-ET and representative images.** **a**, Schematic of EM grids with vitrified mouse sperm. An example for where the windows were milled by FIB-SEM is denoted by two yellow boxes. **b**, SEM (left panel) and FIB (right panel) images of a lamella are shown (scale bar: 5  $\mu\text{m}$ ,  $N = 200$  lamellae). **c**, A low-magnification montage and its zoom-in view of a lamella acquired in 300 kV Titan Krios TEM (scale bar: 1  $\mu\text{m}$ ,  $N = 200$  lamellae). Axonemes and mitochondria are indicated by white arrowheads and an arrow, respectively. Note there are two flagella, one with the mitochondrial sheath and the other with the fibrous sheath, corresponding to the midpiece and the principal piece of the flagella, respectively. **d**, A representative image of non-milled sperm axoneme recorded by 300 kV Titan Krios TEM at a total dose of  $3 \text{ e}^-/\text{\AA}^2$  (scale bar: 100 nm,  $N = 10$  tilt series, not processed further). **e**, A representative image of milled lamella (thickness  $\sim 300$  nm) is shown (scale bar: 50 nm,  $N = 69$  tilt series). The zoom-in view in **f** is outlined using the red rectangle. **f**, Individual protofilaments of microtubules and double-bilayer membranes of the mitochondria are indicated by yellow arrows and arrowheads. Fourier transform of the image is shown in **g** and the upper limit of ctf fitting when using CTFFIND4 is indicated. Note the limit is 8.53  $\text{\AA}$ , which is close to the Nyquist limit (7.06  $\text{\AA}$ ) at the pixel size of 3.53  $\text{\AA}$  ( $N = 69$  tilt series). **h**, **i**, Two sections of 3D tomograms are shown. Periodic outer arm dyneins (every 24 nm) anchored on doublet microtubules are indicated in **h** (red arrowheads). Periodic protrusions (every 32 nm) extending from the singlet microtubule are indicated in **i** (black arrowheads). Periodic patterns of three radial spokes on the doublet

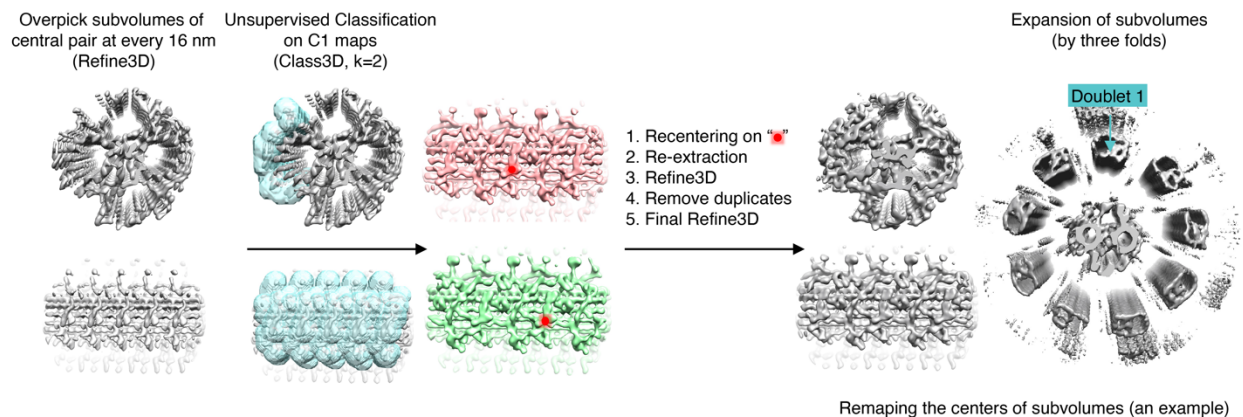
microtubules (every 96 nm) are grouped and indicated in **i** (black brackets) (scale bar: 50 nm, N = 69 tomograms).



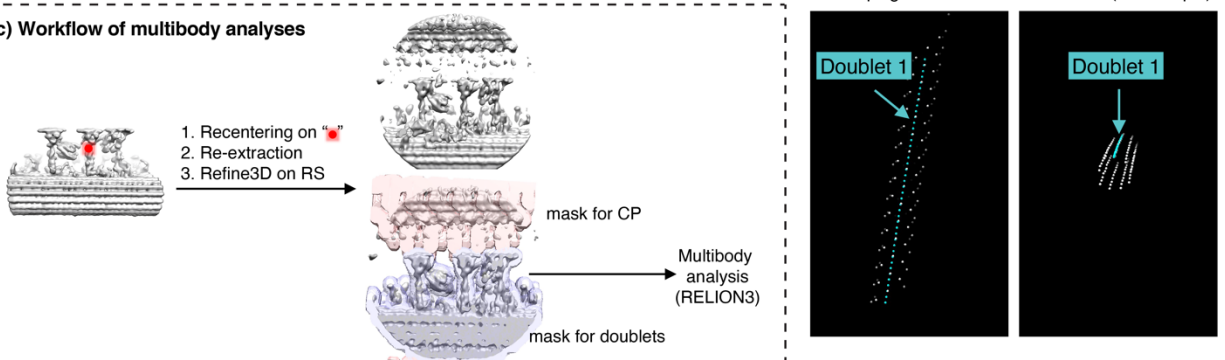
**(a) Processing workflow of 96-nm repeating units of doublets**



**(b) Processing workflow of 32-nm repeating units of central pair complex**

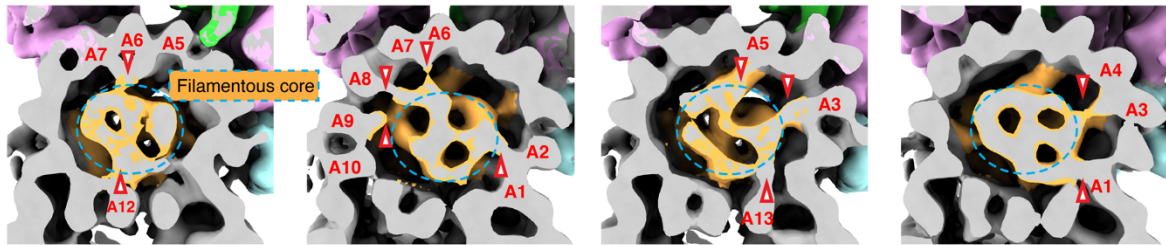


**(c) Workflow of multibody analyses**

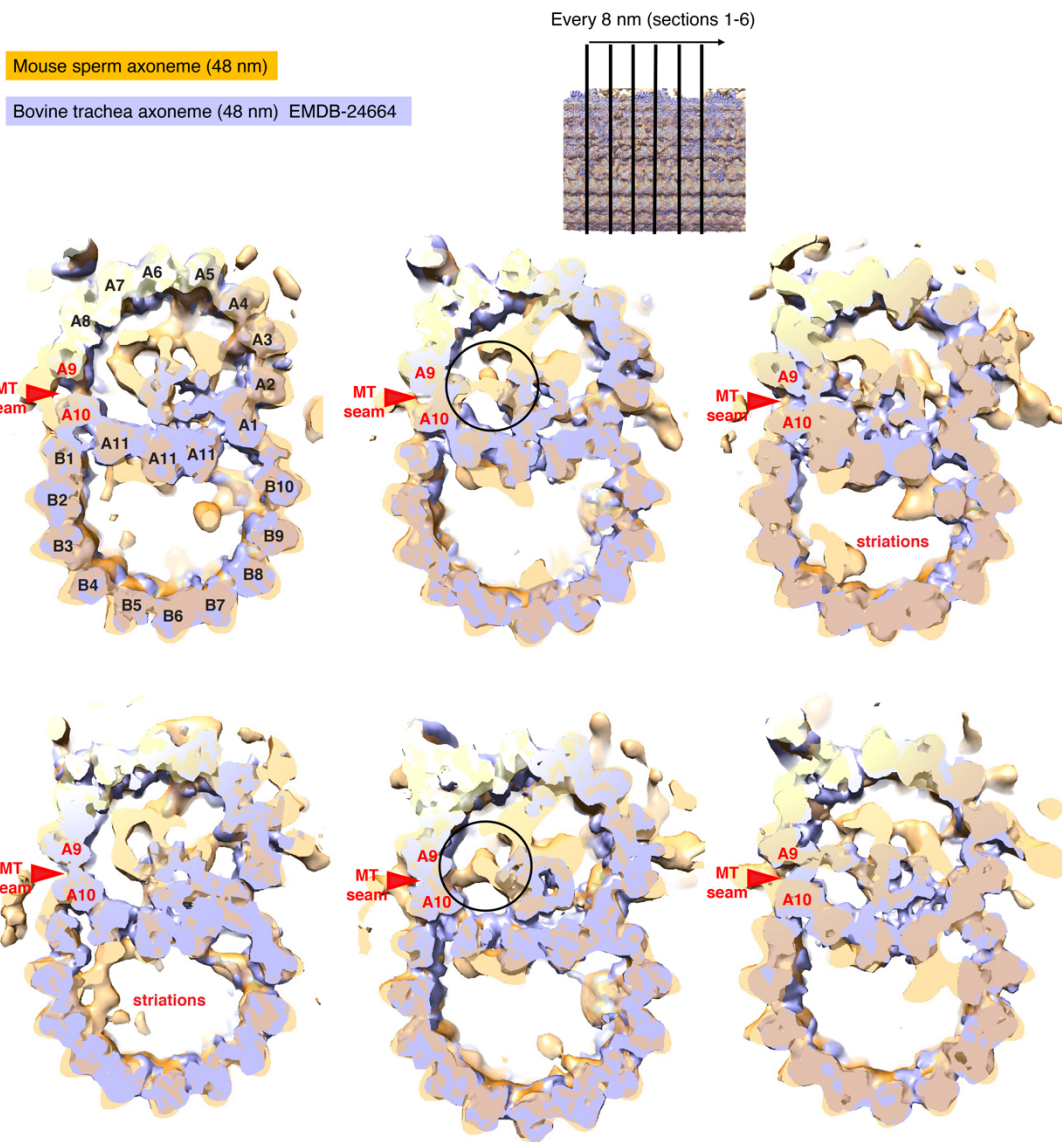


**Extended Data Fig. 2. Schematics of data processing.** **a**, A schematic of the processing workflow of 96 nm-repeating units of doublets to achieve the consensus average combining data from all nine doublets. An example of remapping of the centers of the final subvolumes in three dimensions is shown. **b**, A schematic of the processing workflow of 32 nm-repeating units of central complex to achieve the subvolume average. Recentering of subvolumes of the central pair complex (every 32 nm) on the doublet 1 is shown. Remapping of these subvolumes helps to trace the trajectory of doublet 1 in three dimensions. The centers of these doublet 1 subvolumes are shown in the same tomogram as in **a**. **c**, A schematic of the workflow of multi-body refinement.

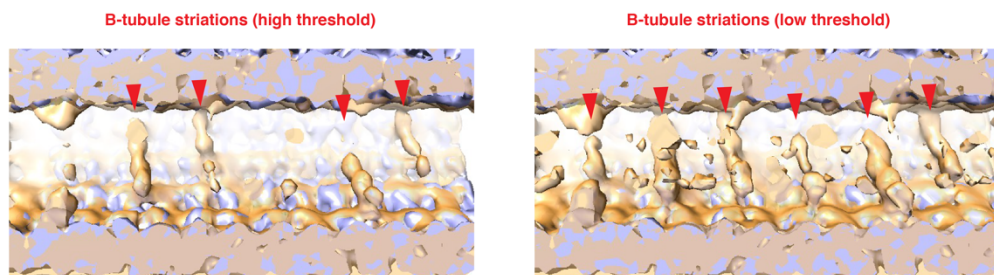
(a)



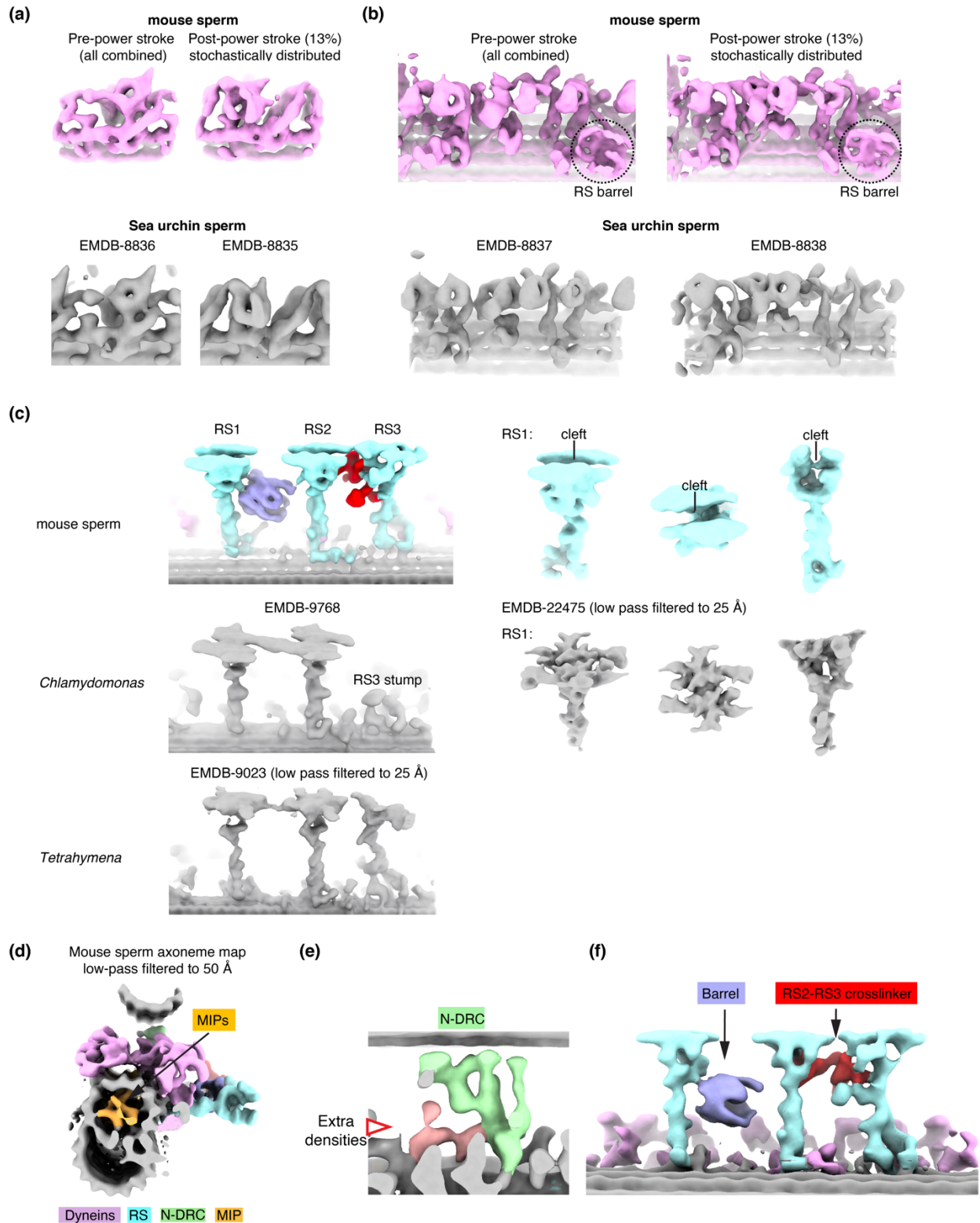
(b)



(c)



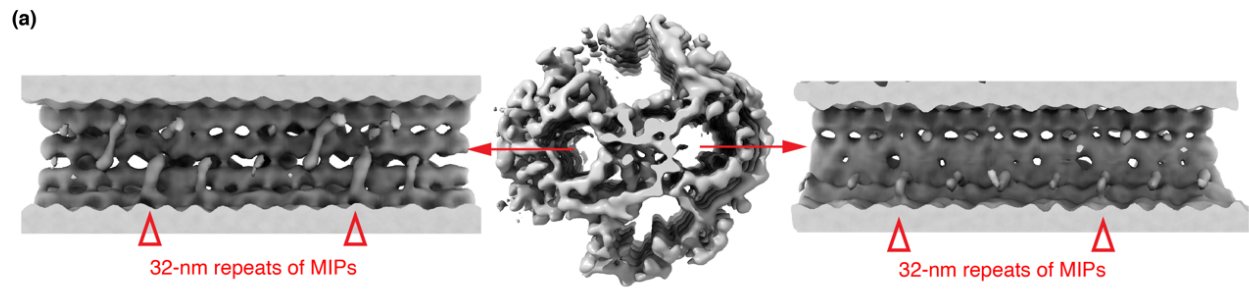
**Extended Data Fig. 3. MIPs network in A-tubule of doublet microtubules.** **a**, Four cross-section views of the A tubule in the doublet microtubule are shown. The MIPs network is colored in orange. Three modes of interactions between the MIPs and the protofilaments are observed (see text). The protrusions from the filamentous core are indicated by empty red arrowheads and dashed cyan ovals, respectively. **b**, Six cross-section views of the overlay of the average of the 48-nm repeat of doublets of mouse sperm (orange, this study) and the 48-nm repeat of doublets of bovine trachea cilia (blue, EMD-24664)<sup>204</sup>. The contour levels of the two maps are adjusted so that the densities of microtubules are matched. The microtubule seam, A9 and A10 protofilaments are labeled in all views. Note there are additional densities near A9-A10 region in the mouse sperm axoneme (black circles). We observed density striations in the B-tubule in some cross sections. **c**, An orthogonal view of the B-tubule striations along the helical pitch of the microtubule at a high and a low threshold, respectively. Note the striations are separated by 8 nm and they cover the intradimeric interface between the  $\alpha$ - and  $\beta$ -tubulins based on the model for the bovine doublet (PDB: 7tro)<sup>204</sup>.



**Extended Data Fig. 4. Comparisons of dyneins and radial spokes of mouse sperm axonemes to published equivalent structures from other motile cilia.** a, Comparison of outer arm dyneins in mouse sperm axoneme (this study) and published maps for those from sea urchin sperm (EMD-

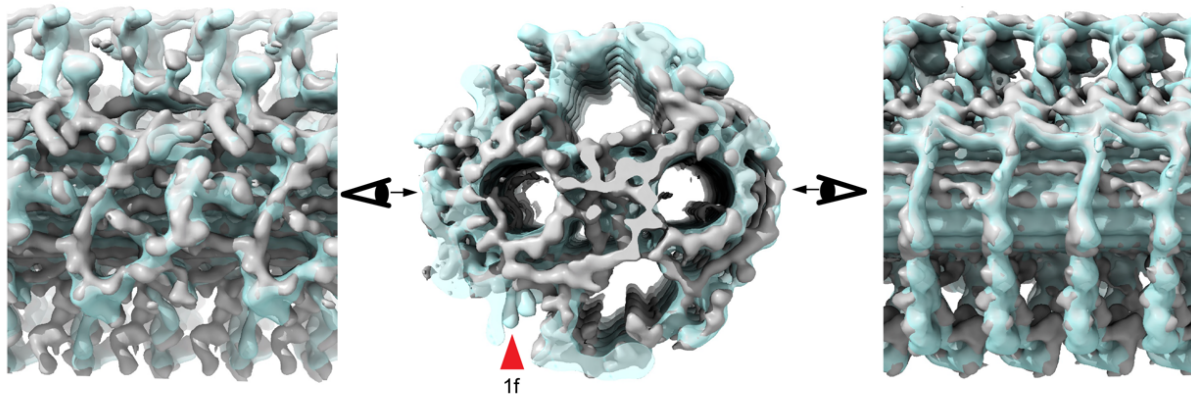


8835 and EMD-8836)<sup>223</sup>. **b**, Comparison of inner arm dyneins in mouse sperm axoneme (this study) and published maps for those from sea urchin sperm (EMD-8837 and EMD-8838)<sup>223</sup>. Note the barrel densities between RS1 and RS2 only exist in the mouse sperm are indicated (dashed ovals). **c**, Comparison of radial spokes of mouse sperm axoneme (this study) and the ones from motile cilia of *Chlamydomonas* (EMD-9768<sup>208</sup> and EMD-22475<sup>193</sup>) and *Tetrahymena* (EMD-9023)<sup>207</sup>. Note the RS3 stump in *Chlamydomonas* is much shorter than the others and the head of RS3 from *Tetrahymena* has a smaller surface area. **d-f**, The doublet average of mouse sperm axoneme is low-pass filtered to 50 Å and viewed from different angles. Note this resolution is lower than published axoneme maps (e.g. 34 Å for EMD-5950 shown in Fig. 1 for comparison)<sup>209</sup>. The extensive network of MIPs (**d**), extra densities at N-DRC (**e**) and radial spokes (**f**) remain apparent while comparing to human respiratory cilia, suggesting the presence of novel densities in our maps are not due to higher resolutions, but most likely the presence of additional proteins.



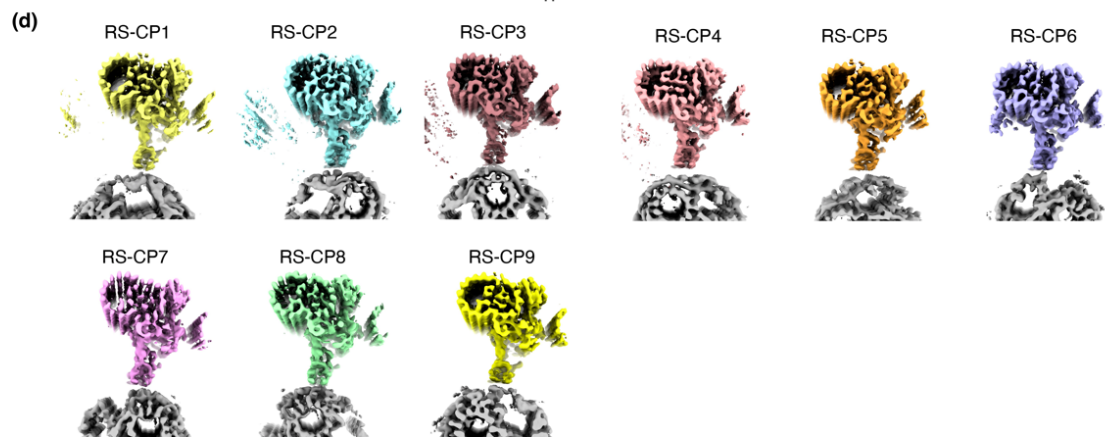
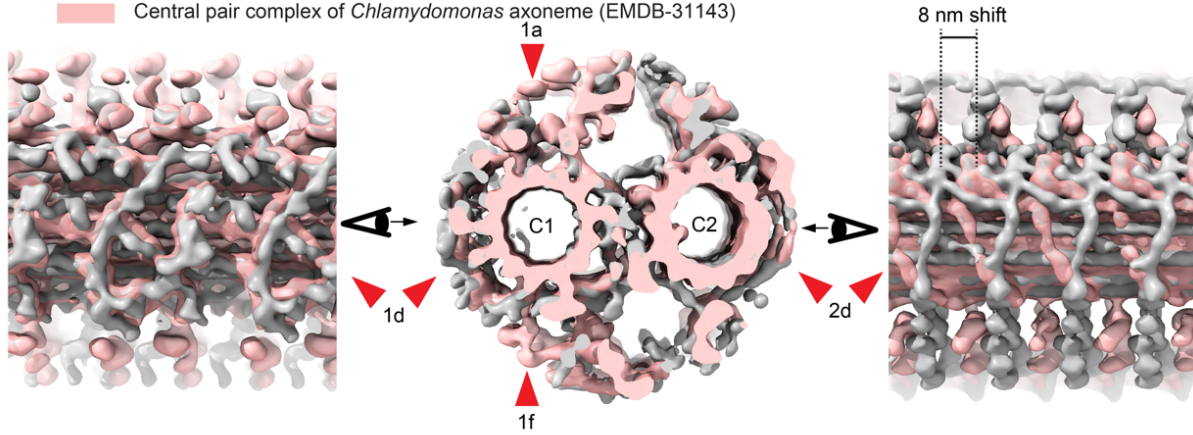
(b)

- Central pair complex of mouse sperm axoneme
- Central pair complex of sea urchin sperm axoneme (EMDB-9385)

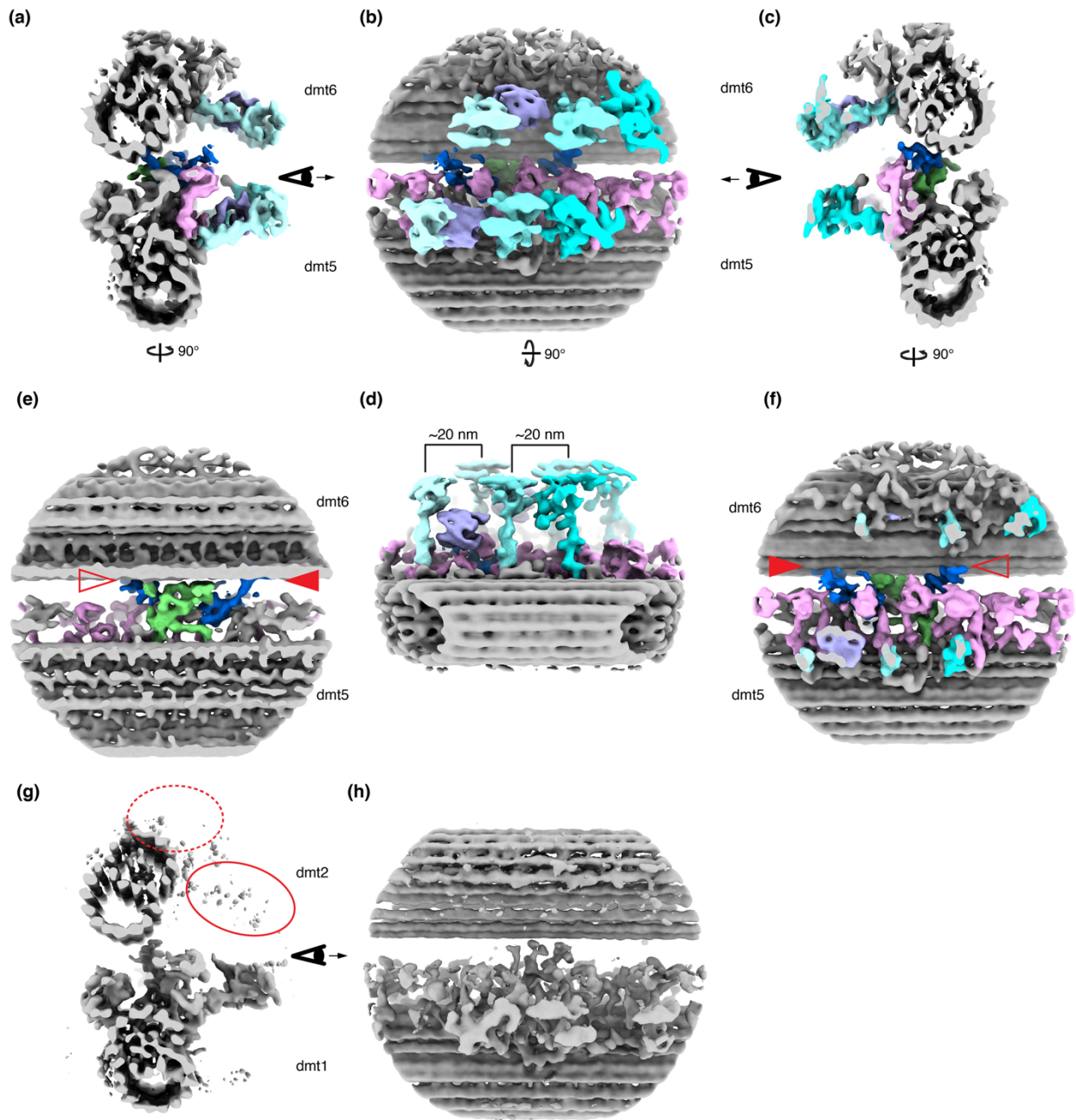


(c)

- Central pair complex of mouse sperm axoneme
- Central pair complex of *Chlamydomonas* axoneme (EMDB-31143)

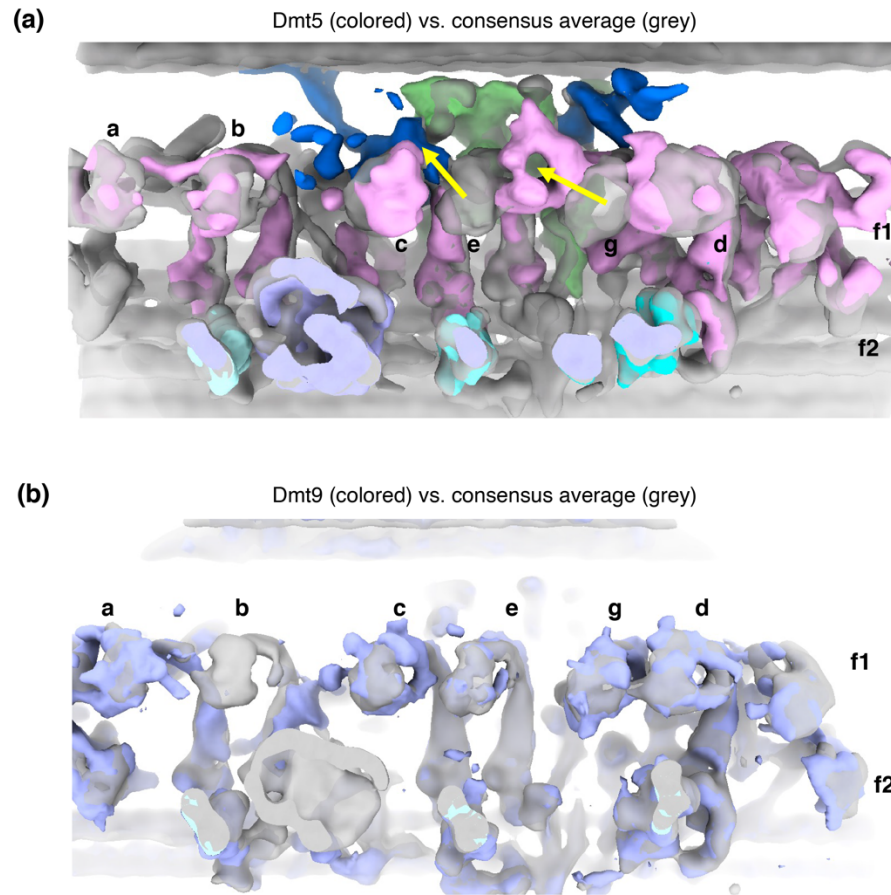


**Extended Data Fig. 5. The central pair complex in mouse axoneme possesses more MIPs but the overall shape is similar to the one from sea urchin sperm.** **a**, Two longitudinal views of the MIPs inside the two singlet microtubules are shown. Periodic features (every 32 nm) are indicated (red empty arrowheads). **b**, The average of the central pair complex in mouse sperm axonemes is overlaid on the published map for the central pair complex from sea urchin sperm (EMD-9385) and they are colored in grey and cyan, respectively<sup>203</sup>. Note most of the protrusions are very similar and one difference in the protrusion 1f is indicated in the middle panel (red arrowhead). **c**, The average of the central pair complex in mouse sperm axonemes is overlaid on the published map for the central pair complex from *Chlamydomonas* (EMD-31143)<sup>213</sup>. Note the maps are aligned based on the similar C1 protrusions 1d. Other protrusions are generally less similar (1a, 1f and 2d) and there appears to be an 8-nm shift for the C2 protrusions. The *Chlamydomonas* C2 microtubule was recently shown to possess two possible registers with 8-nm longitudinal differences<sup>211</sup>. **d**, The spatial relationship between the nine radial spokes and the central pair complex are determined by multibody refinement and the “average positioning” of these two rigid bodies are shown (RS-CP1 denotes the interface between radial spokes from doublet 1 and the central pair).



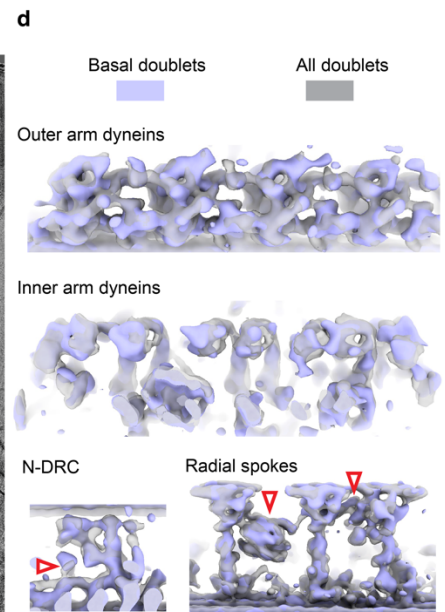
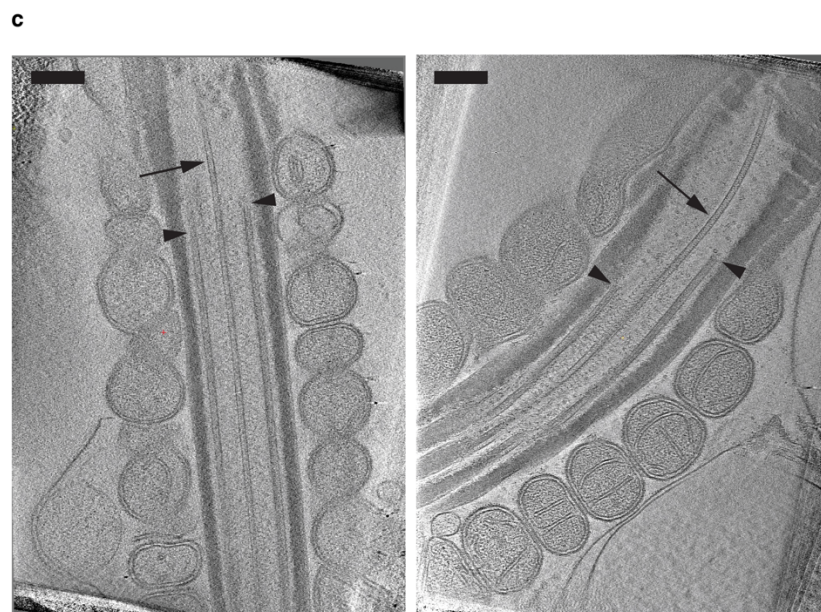
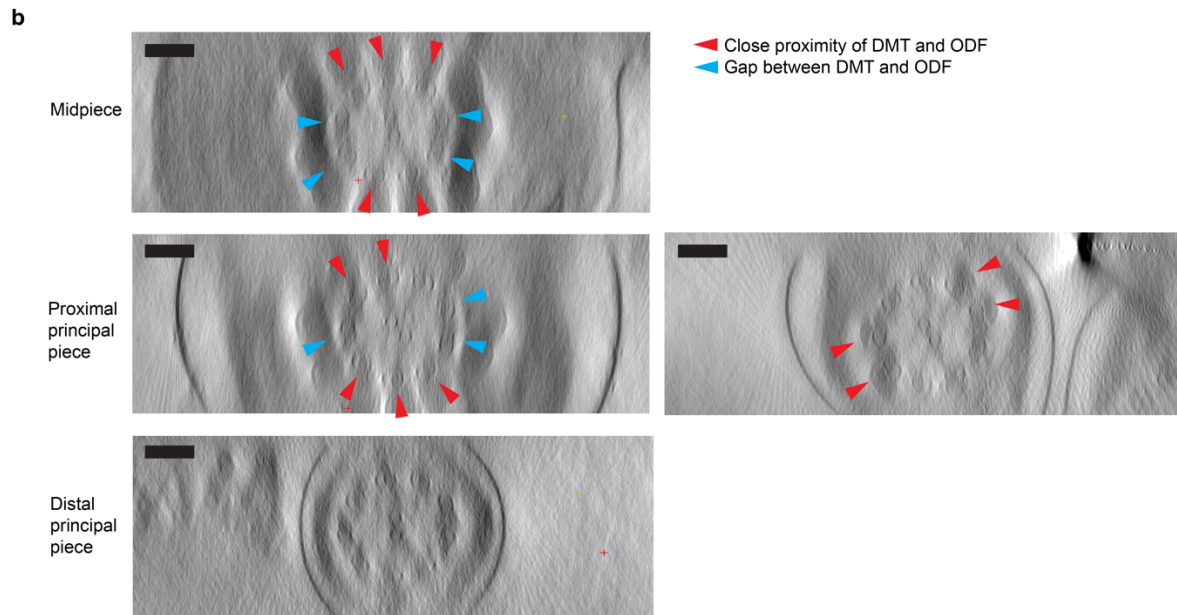
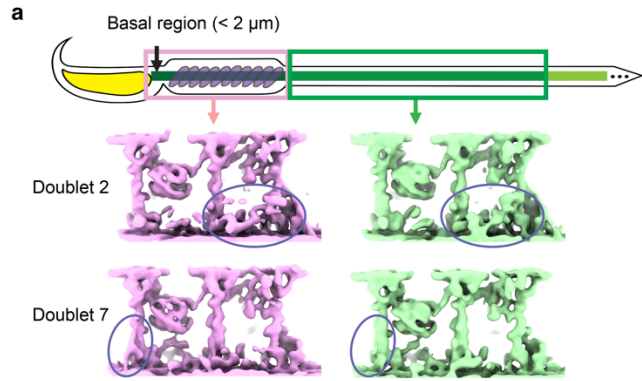
**Extended Data Fig. 6. The 5-6 bridge of mouse sperm axonemes.** **a-d**, Four views of the composite map for 5-6 bridge in mouse sperm axonemes combining maps for local refinement of the doublet 5, doublet 6 and the bridge. The inner arm dyneins, radial spokes, the barrel, N-DRC and extra bridge densities are colored in pink, different shades of cyan, light blue, green and blue, respectively. Note that the radial spokes which repeat every 96 nm on both doublet 5 and doublet 6 are resolved and there appears to be a ~20 nm offset between their longitudinal registers, as indicated in the staggering distance of RS1 and RS2 from doublet 5 and doublet 6 in **d**. **e**, **f**, Two cut-in views of **a** and **c** are shown. Bridge-specific densities are highlighted in blue. These densities extend from the inner arm dyneins towards doublet 6. Direct contacts of the bridge-specific

densities to doublet 6 is indicated by the solid red arrowhead while densities in close proximity of the base of radial spoke 2 in doublet 6 are indicated by the empty red arrowhead. **g, h**, Subvolumes for doublet 1 was aligned and equivalent views of doublet 1 and 2 are shown (as in panel **a** and **b**). The expected positions for dyneins and radial spokes on doublet 2 are circled by dashed and solid red ovals and note they are not resolved even after local refinement, suggesting they do not have a consistent offset. The microtubule from doublet 2 is nevertheless partially resolved since variant longitudinal mismatching would not smear a tube of “continuous densities” compared to “discrete densities” like dyneins and radial spokes through averaging.



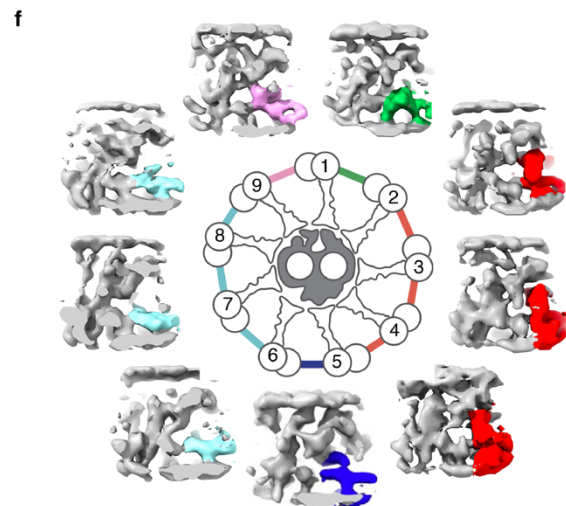
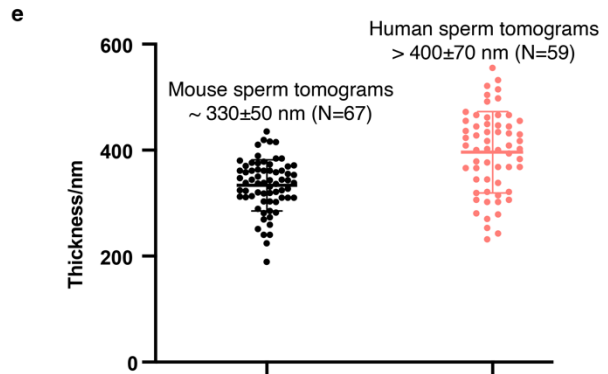
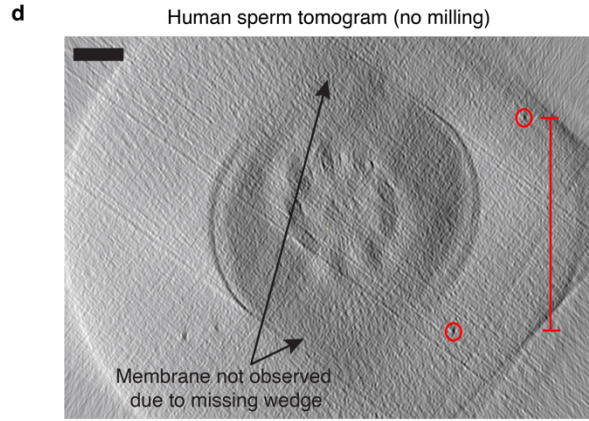
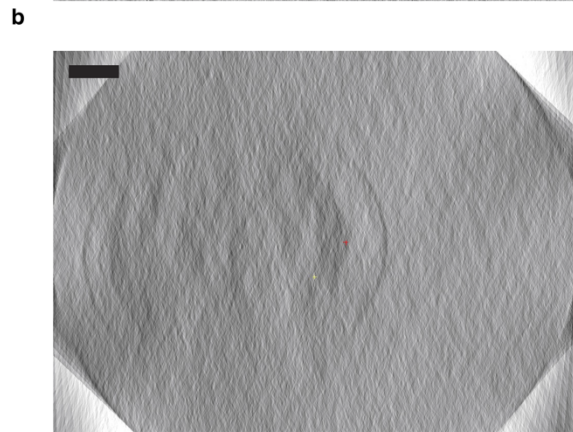
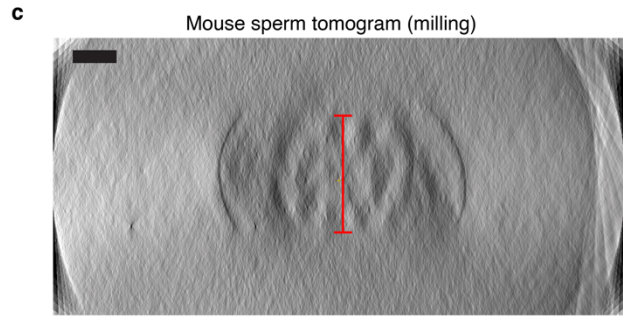
**Extended Data Fig. 7. The inner arm dyneins in doublet 5 and doublet 9 differ from the consensus average in mouse sperm axonemes. a,** An overlay of inner arm dyneins from doublet 5. The assigned inner arm dyneins, N-DRC and 5-6bridge densities from the doublet 5 are colored in pink, green and blue, respectively while the densities for the consensus average are in grey. Different inner arm dyneins are named according to the nomenclature defined by studies of *Chlamydomonas* flagella. The shifted positions of dynein e and dynein g are indicated by the two yellow arrows. **b,** An overlay of inner arm dyneins from doublet 9 and the consensus average were blue and grey, respectively. Note dynein b in doublet 9 is not resolved.



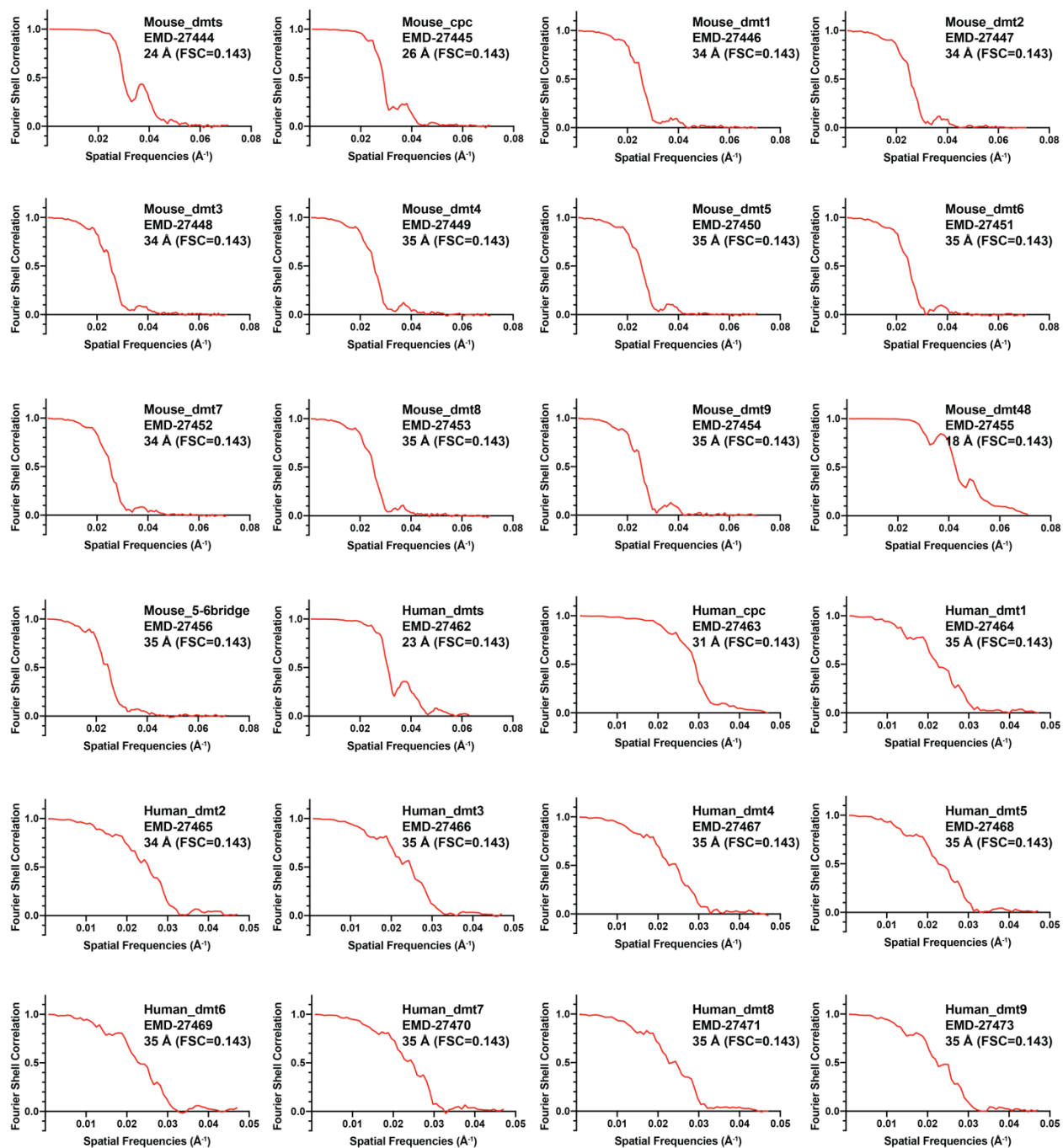


**Extended Data Fig. 8. Longitudinal consistency of doublets in mouse sperm axonemes.** **a**, Schematic of a mouse sperm flagella with the basal region ( $< 2 \mu\text{m}$ ), midpiece and principal piece highlighted in the top panel. Subvolume averages of doublet 2 and doublet 7 from the midpiece and the principal piece are shown. The shapes of densities for the scaffolds at the base of radial spoke 3 appear different in doublet 2 and are circled. Additional densities at the base of radial spoke 1 in the doublet 7 in the midpiece region are observed and circled. **b**, Four xz slices of tomograms in different regions of the mouse sperm flagella are shown. Outer dense fibers that are in close proximity to the doublets and the ones with gaps in between are indicated (red and blue arrowheads, respectively) (scale bars: 100 nm). **c**, Two xy slices of two 3D tomograms of the basal region of mouse sperm axoneme are shown. The singlet microtubules of the central pair complex extend further into the cell bodies and the beginning of the doublet microtubules are indicated by the arrows and arrowheads, respectively (scale bars: 200 nm). **d**, Densities corresponding to different protein complexes from subvolume averages of the basal region (6 tomograms,  $N = 670$  subtomograms) and the consensus average are overlaid and colored in blue and grey, respectively. Note the sperm-specific features in N-DRC and radial spokes exist in the average of doublets in the basal region and are highlighted using empty red arrowheads.



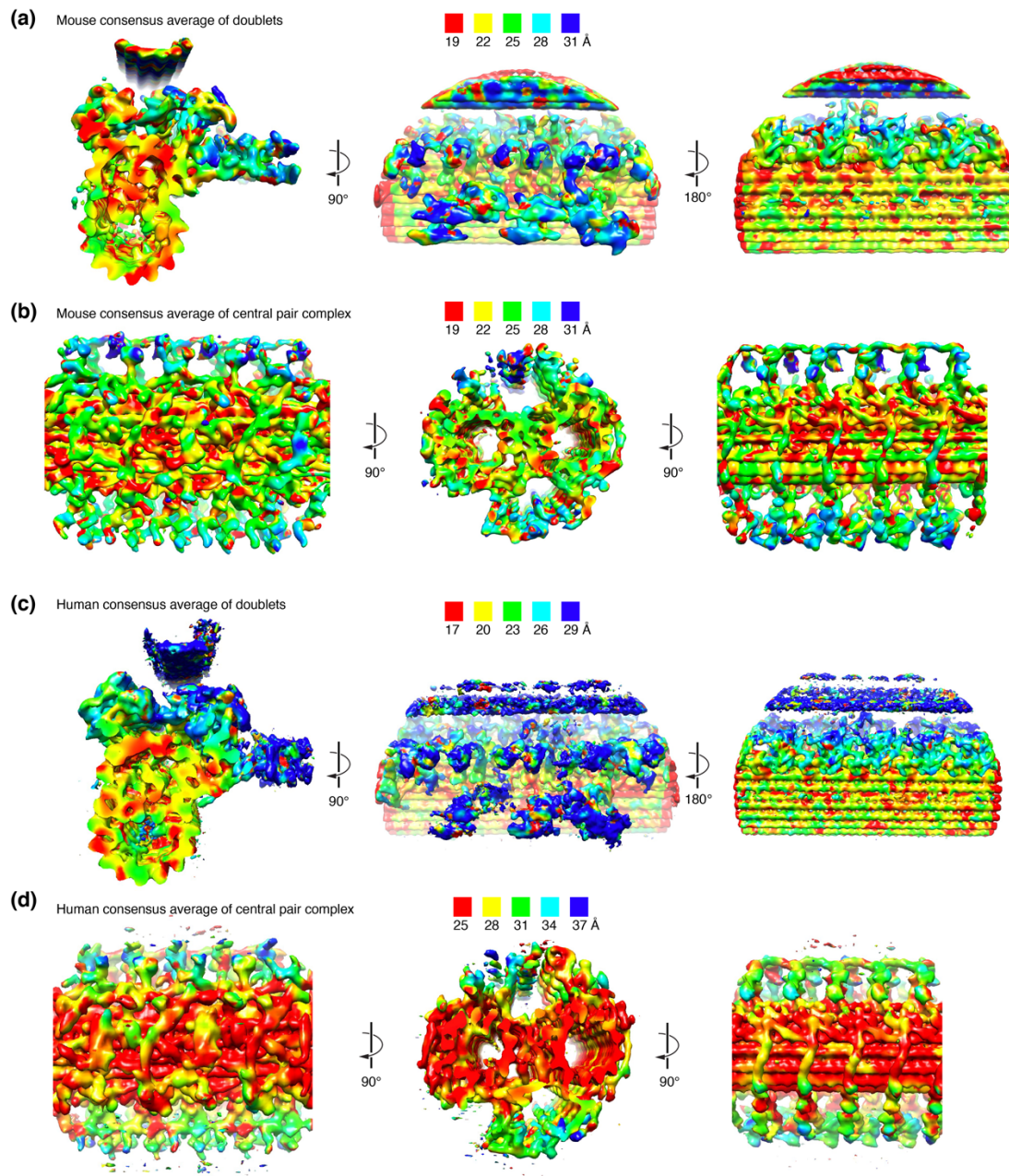


**Extended Data Fig. 9. CryoET data of human sperm without milling and asymmetric distribution of sperm-specific features in N-DRCs in human sperm.** **a**, A representative xy slice of a tomogram of human sperm (bin4, pixel size=10.64 Å, image thickness: 1, displayed in IMOD). Although the A- and B-tubule of the microtubule doublets are discernible, other features like axonemal dyneins and radial spokes are not clear in this slice. This is in contrast to the example of mouse sperm lamella shown in Extended Data Fig. 1h-i (scale bar: 100 nm). **b**, A representative xz slice of the same tomogram of human sperm (bin4, pixel size=10.64 Å, image thickness: 5, displayed in IMOD) (scale bar: 100 nm). **c**, A representative xz slice of a tomogram of mouse sperm lamella (bin4, pixel size=14.12 Å, image thickness: 10, displayed in IMOD). The red bar indicates how we measure the thickness of the lamella ( $330\pm 50$  nm) (scale bar: 100 nm). **d**, A representative xz slice of a tomogram of human sperm (bin4, pixel size=10.64 Å, image thickness: 100, displayed in IMOD). Gold beads on the top and bottom surfaces are circled and the red bar indicates how we measure the thickness of the ice near the cell. Note that the top and bottom membrane of the sperm cells is not resolved due to the missing wedge so the actual thickness is larger than the measured thickness of ice in the vicinity ( $> 400\pm 70$  nm) (scale bar: 100 nm). **e**, A dot plot showing the thickness of lamellae of mouse sperm and ice near human sperm as a lower bound estimate of the actual cells. The means and standard deviations are indicated (for N=67 mouse sperm tomograms and N=59 human sperm tomograms). **f**, Densities corresponding to N-DRC from the nine per-doublet averages are shown around a schematic of a cross-section view of the (9+2)- axonemes. Common features among the N-DRC are colored in grey, while the unique features are highlighted in various colors.



**Supplementary Data 1. Fourier shell correlation (FSC) curves of subvolume averages.** The FSC curves are labeled with the names of the structures, the EMDB deposition numbers, and the resolution estimate based on FSC = 0.143 standard.





**Supplementary Data 2. Local resolution maps of the consensus averages of mouse and human sperm.** The local resolution maps were generated using blocres from the Bsoft package. These local-resolution maps illustrate relative differences in resolution across the maps but the absolute values may not be exact. In general, structural features near the microtubules are better resolved than those that are further away.

## Methods

All chemicals were purchased from Sigma-Aldrich unless otherwise noted.

### Sample preparation

Mouse sperm were collected from 10 to 16-week-old C57Bl/6J mice based on the published protocol<sup>226</sup>. Briefly, the sperm were stripped from vasa deferentia by applying pressure to cauda epididymis in 1 x Krebs buffer (1.2 mM  $\text{KH}_2\text{PO}_4$ , 120 mM NaCl, 1.2 mM  $\text{MgSO}_4 \cdot 7\text{H}_2\text{O}$ , 14 mM dextrose, 1.2 mM  $\text{CaCl}_2 \cdot 2\text{H}_2\text{O}$ , 5 mM KCl, 25 mM  $\text{NaHCO}_3$ ). The sperm were washed and resuspended in ~100  $\mu\text{L}$  Krebs buffer for the following experiments.

Human sperm cells were collected by masturbation from healthy donors and visually inspected for normal morphology and motility before use. Spermatozoa were isolated by the swim-up procedure in HTF or HS solution as previously described<sup>140</sup> and then concentrated by 5-minute centrifugation at 500g. The supernatant was reduced to 100  $\mu\text{L}$  and the cells are resuspended.

All experimental procedures utilizing human-derived samples were approved by the Committee on Human Research at the University of California, Berkeley, IRB protocol number 2013-06-5395.

### Grid preparation

EM grids (Quantifoil R 2/2 Au 200 mesh) were glow discharged to be hydrophilic using an easiGlow system (Pelco). The grid was then loaded onto a Leica GP cryo plunger (pre-equilibrated to 95% relative humidity at 25 °C). The mouse sperm suspension was then mixed with 10-nm gold beads (Electron Microscopy Science, cat #25487) to achieve final concentrations at  $2\text{-}6 \times 10^6$  million cells/mL. For the demembrated mouse sperm, Triton-X 100 was added to 0.1% final concentration in the final suspension. The human sperm suspension was mixed with 10-nm gold beads to achieve final concentrations at  $0.5\text{-}2 \times 10^6$  million cells/mL. Then 3.5  $\mu\text{L}$  sperm mixture was added to each grid, followed by an incubation of 15 sec. The grids were then blotted for 4 sec and plunge-frozen in liquid ethane.

### Cryogenic focused ion beam (cryoFIB) milling

CryoFIB was performed either manually using an Aquilos cryo-FIB/SEM microscope (Thermo Fisher Scientific) or automatically using an Aquilos II cryo-FIB/SEM microscope (Thermo Fisher Scientific). A panorama SEM map of the whole grid was first taken at 377x magnification using an acceleration voltage of 5 kV with a beam current of 13 pA, and a dwell time of 1  $\mu\text{s}$ . Targets with appropriate thickness for milling were picked on the map. A platinum layer (~10 nm) was sputter coated and a gas injection system (GIS) was used to deposit the precursor compound trimethyl(methylcyclopentadienyl) platinum (IV). The stage was tilted to 15-20°, corresponding to a milling angle of 8-13° relative to the plane of grids. FIB milling was performed using stepwise decreasing current as the lamellae became thinner (1.0 nA to 30 pA, final thickness: ~300 nm). The grids were then stored in liquid nitrogen before imaging.

### Image acquisition and tomogram reconstruction

Tilt series of mouse sperm were collected on a 300-kV Titan Krios transmission electron microscope (Thermo Fisher Scientific) equipped with a high brightness field emission gun (xFEG), a spherical aberration corrector, a Bioquantum energy filter (Gatan), and a K3 Summit detector (Gatan). The images were recorded at a nominal magnification of 19,500x in super-resolution counting mode using SerialEM<sup>227</sup>. After binning over 2 x 2 pixels, the calibrated pixel size was 3.53 Å on the specimen level. For each tilt series, images were acquired using a modified dose-symmetric scheme between -48° to 48° relative to the lamella with 3° steps and grouping of two images on either side (0°, 3°, 6°, -3°, -6°, 9°, 12°, -9°, -12°, 15°...). At each tilt angle, the image was recorded as movies divided into eight subframes. The total electron dose applied to a tilt series was 100 e<sup>-</sup>/Å<sup>2</sup>. The defocus target was set to be -4 to -7 μm.

Tilt series of human sperm were recorded at a nominal magnification of 33,000x in super-resolution counting mode. After binning over 2 x 2 pixels, the calibrated pixel size was 2.66 Å on the specimen level. The total electron dose applied to a tilt series was 100 e<sup>-</sup>/Å<sup>2</sup>. For each tilt series, images were acquired using a bidirectional scheme between -48° to 48° relative to the lamella starting from either 0° or 21°, with an incremental step of 3°. The defocus target was set to be 2~5 μm. At each tilt, the image was recorded as movies divided into eight subframes.

All movie frames were corrected with a gain reference collected in the same EM session. Movement between frames was corrected using MotionCor2 without dose weighting<sup>228</sup>. Alignment of the tilt series and tomographic reconstructions were performed using Etomo<sup>229</sup>. The aligned tilt series were then CTF-corrected using TOMOCTF<sup>230</sup> and the tomograms were generated using TOMO3D<sup>231</sup> (bin2, pixel size: 7.06 Å).

In total, we started with 24 milling grids of mouse sperm and obtained 200 lamellae. Tilt series with no crystal ice were kept and further processed. In some cases, a significant part of the (9+2) axoneme was milled away and we only processed the ones with at least 5 doublets and also enough space including the central pair complex for subvolume averaging. In the end, the final reconstructions of the consensus averages were from 70 usable tomograms. For the human sperm cryoET dataset, the final reconstructions of the consensus averages are from 65 tilt series with the flagella orientations within ~30° of the tilt axis. Note the final tomograms used for different reconstructions vary as tomograms may be discarded due to bad alignment or may lack certain doublets.

### **Subvolume averaging**

Subsequent subvolume extraction, classification and refinement were all performed using RELION3<sup>232</sup> (see the schematic workflow in Extended Data Fig. 2a). Briefly, subvolumes from the doublets were manually picked every 24 nm and extracted with a box size large enough to accommodate a complete 96-nm repeating unit (pixel size: 7.06 Å, box size: 180 pixels, dimension: 127.08 nm). Initially, subvolumes were aligned to a map of *Tetrahymena* doublets (EMDB-9023) lowpass filtered to 80 Å and the resulting map was used as the reference for further processing. Manual curation of the data was performed to check the alignment accuracy and data quality for each tomogram. Supervised 3D classification on radial spokes gave rise to four class averages of the 96-nm repeating units at four different registries, staggered from one

another by 24 nm. The Pixel View in IMOD was used to determine the coordinates corresponding to the base of radial spoke 2 in all four class averages and all subvolumes were re-extracted and recentered to the same point. All subvolumes were combined and aligned to one reference and duplicate subvolumes were removed based on minimum distance (< 40 nm). The remaining subvolumes were aligned to yield the consensus average for all nine doublets. These subvolumes were later remapped and sorted to calculate per-doublet averages (the script is also attached below). The MIPs inside microtubule doublets repeat every 48 nm. Subvolumes of the 96-nm repeating units were recentered on MIP features that repeat every 48 nm and refined with a mask focusing on the microtubules only.

To generate an average for the central pair complex, subvolumes were picked and extracted from the central pair complex every 16 nm (pixel size: 7.06 Å, box size: 160 pixels, dimension: 112.96 nm) (Extended Data Fig. 2b). Refinement of all subvolumes to an average of Sea Urchin central pair (EMDB-9385) resulted in a central pair with only 16-nm repeating features. The alignment parameters were modified to reset all translations (x, y, z) to zero and then used for a second round of refinement with local search only. Focused classification was then performed on the microtubule-associated proteins on the C1 microtubule to separate the two populations of subvolumes (~50% each) corresponding to the central pair complex with 32-nm periodicity and an offset of 16 nm between them. The subvolumes were then re-centered and extracted on the same protein features for the two class averages. All subvolumes were aligned to the same reference using local searches. Duplicate subvolumes were removed based on minimum separating distance (< 30 nm). The remaining subvolumes were refined to generate the consensus average for the central pair complex.

Subvolumes large enough to include all nine doublets were re-extracted centering on the aligned subvolumes of the central pair complex (pixel size: 21.18 Å, box size: 160 pixels, dimension: 338.88 nm). These subvolumes were averaged without further alignment and used to re-extract subvolumes corresponding to individual doublets. Subvolumes corresponding to a particular doublet were aligned and re-mapped back to the tomograms in three dimensions. However, these subvolumes do not have the correct alignment for the 96-nm repeating features but the centers of them nevertheless trace the axis of that microtubule doublet accurately when they are remapped in three dimensions (using the attached script below). The 96-nm periodic subvolumes curated above to generate the consensus average of 96-nm repeats were then sorted. The subvolumes corresponding to a particular doublet were then aligned and averaged.

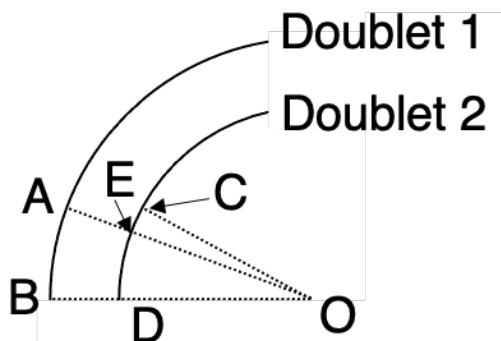
For the multi-body refinement (see the schematic workflow in Extended Data Fig. 2c), the subvolumes corresponding to specific radial spoke-central pair interface were re-extracted based on the subvolumes of 96-nm units of individual doublet microtubules. The particles were recentered at the junction between the head and the stalk of radial spoke 2 to include enough features from both the doublets and central pair complex. The radial spokes were then aligned with a mask. This mask and a mask covering the central pair complex were used for the multibody analysis implemented in RELION3<sup>214</sup>. Briefly, separate refinement of the radial spokes and central pair protrusions provided two sets of alignment parameters: three translational shifts (x,y,z) and three Euler angles required to align one subvolume to each reference. Thus 12 parameters can be used to remap the two references back to each raw subvolume and the spatial

relationship of the two rigid bodies in each subvolume could be determined by these 12 parameters. Principal Component Analyses (PCA) essentially reprojected the original 12-dimensional data in a new 12-dimensional space with 12 new orthogonal eigenvectors. These 12 eigenvectors could be mathematically determined so that they represent decreasing variations of the entire data along the individual eigenvectors. Our analyses suggest the first eigenvector/axis is parallel to the axoneme axis and the variations along this axis account for 40-50% of the total variations. When all subvolumes were divided into 10 groups based on their projection values on the first axis (10% lowest, 10%-20% lowest, ..., 90%-100% highest). Each group was then represented by a snapshot depicting the averaging projection values of the group members and 10 of these snapshots were morphed to generate the animation (Supplementary Movie 1).

The resolutions for maps were estimated based on FSC of two independently refined half datasets (FSC = 0.143). Local resolution maps for the consensus averages of doublets and the central pair complex of both human and mouse sperm were calculated by blocres in Bsoft (Supplementary Data 2). These local-resolution maps represent relative differences in resolution across the maps but the absolute values may not be exact. IMOD was used to visualize the tomographic slices<sup>229</sup>. UCSF Chimera was used to manually segment the maps for various structure features and these maps were colored individually to prepare the figures using UCSF ChimeraX<sup>233-235</sup>.

### Estimation of accumulated offsets in axonemes

The bending curvature of mouse sperm could be as big as  $2 \times 10^5 \text{ m}^{-1}$  or  $0.20 \mu\text{m}^{-1}$  based on literature (OD =  $5 \mu\text{m} = 5000 \text{ nm}$ )<sup>1</sup>. The distance between the neighboring doublets is 72 nm (measured in the average of the axoneme shown in Fig. 2d, OB = 5072 nm). If AB and CD represent one 96-nm repeat from Doublet 1 and Doublet 2, respectively, offset  $\Delta = CE \sim OC \times (\angle COD - \angle AOB) = 5000 \times (96/5000 - 96/5072) = 1.4 \text{ nm}$ .



Note the  $\Delta$  represents the additional offset per 96 nm repeat. In a tomogram that contains an axoneme of  $\sim 2 \mu\text{m}$ , if the offset between the first pair of 96-nm repeats is 0 nm, the offset of the 20<sup>th</sup> pair is 28 nm. Note this initial offset (0 nm) is tomogram-specific depending on how much sliding has happened upstream or downstream of the imaging area and the imaged cell.

### Data Availability

The maps of the following structures are available in the Electron Microscopy Data Bank: EMD-27444, consensus average of 96 nm-repeating structure of mouse doublets; EMD-27445, 32 nm-repeating structure of central pair complex of mouse sperm; EMD-27446, mouse



doublet 1; EMD-27447, mouse doublet 2; EMD-27448, mouse doublet 3; EMD-27449, mouse doublet 4; EMD-27450, mouse doublet 5; EMD-27451, mouse doublet 6; EMD-27452, mouse doublet 7; EMD-27453, mouse doublet 8; EMD-27454, mouse doublet 9; EMD-27455, 48 nm-repeating structure of doublet microtubule of mouse sperm; EMD-27456, 5-6 bridge of mouse sperm; EMD-27462, consensus average of 96 nm-repeating structure of human doublets; EMD-27463, 32 nm-repeating structure of central pair complex of human sperm; EMD-27464, human doublet 1; EMD-27465, human doublet 2; EMD-27466, human doublet 3; EMD-27467, human doublet 4; EMD-27468, human doublet 5; EMD-27469, human doublet 6; EMD-27470, human doublet 7; EMD-27471, human doublet 8; EMD-27473, human doublet 9. The raw tilt series of mouse sperm lamellae and the corresponding tilt angle files are available in the EMPIAR database (EMPIAR-11221).

## Code Availability

### The script to remap coordinates of subvolumes in three dimensions

```
# Take input of x,y,z coordinates (space separated) and output a Chimera markers file (.cmm suffix).
#
# Example use
#
# python3 make_markers.py tomo0112.coords > tomo0112.cmm
#
# Here's documentation on the Chimera marker file format.
#
# https://www.cgl.ucsf.edu/chimera/docs/ContributedSoftware/volumepathtracer/volumepathtracer.html#markerfiles
#

voxel_size = 1.0      # Scale input x,y,z coordinates to get Angstroms
radius = 10          # Radius of marker spheres in Angstroms.

from sys import argv, stdout
input_filename = argv[1]
input_lines = open(input_filename).readlines()
lines = ['<marker_set name="%s">' % input_filename]
for i, line in enumerate(input_lines):
    x,y,z = [voxel_size * float(x) for x in line.split()]
    lines.append('<marker x="%0.2f" y="%0.2f" z="%0.2f" radius="%0.2f" id="%d" />'
                % (x,y,z,radius,i+1))
lines.append('</marker_set>')

stdout.write('\n'.join(lines))
```

## Chapter 6: Conclusion

The studies detailed in preceding chapters represent different efforts to improve our understanding of the physiology and structural biology of human sperm cells, with the intention of laying the scientific foundation that could be used to inform the development of unisex, non-hormonal contraceptives. These diverse projects used very different approaches to investigate critical sperm-specific proteins located on the head, midpiece, and tail of the spermatozoon.

In Chapter 2, we described methods of human sperm isolation and high-speed video microscopy that have been optimized over many years in our lab. These methods should shorten the time it takes for new researchers to begin performing experiments on human sperm, which is critical for growing the field and accelerating the pace of discovery and contraceptive development. Although the techniques described for manual flagellar analysis using high-speed microscopy are labor-intensive and have been mostly supplanted by computer-aided sperm analysis (CASA), they remain important for more detailed analyses of flagellar waveforms than CASA can provide.

Chapter 3 studied the basis of human sperm energy production and the importance of the mitochondrial membrane potential and plasma membrane potential in human sperm functional physiology to investigate whether small-molecule uncouplers might be usable as contraceptives. Interestingly, we observed that while some small-molecule uncouplers (which depolarize membranes and therefore impair oxidative phosphorylation in mitochondria) have a deleterious effect on sperm motility, this effect is not due to a decrease in ATP content, which lends credence to the idea that human sperm are metabolically redundant enough to compensate for a decrease in mitochondrial ATP production by increasing the rate of glycolysis. While this outcome makes the idea of systemically applied sperm-targeted contraceptive uncouplers less viable, the results suggest that it may be possible to use niclosamide, an FDA-approved uncoupler, as an ingredient in spermicide gels. This work will inform future contraceptive development efforts that involve inhibiting aspects of human sperm metabolism.

Chapter 4 investigated the structure and function of TMEM95, a sperm-specific protein involved in the fusion of the sperm head with the egg plasma membrane. In addition to producing the first x-ray crystal structure of the human TMEM95 ectodomain and performing molecular assessments of its ability to bind to various key proteins involved in fertilization, this study proved that TMEM95 has a binding partner on the egg plasma membrane, and that this interaction is involved in sperm-egg membrane fusion but not sperm-egg binding. Future studies will determine the identity of TMEM95's binding partner, and a better understanding of the complex sperm-egg binding and fusion machinery will help determine whether these interactions are able to be targeted for production of a pericoital fertilization-blocking contraceptive.

Chapter 5 focused on the sperm axoneme, which is the central structural feature of the sperm flagellum, and creates the vigorous motility that sperm need to reach and fertilize the egg. The unprecedented resolution of the cryo-electron tomography maps created in this study allowed us to go beyond the well-known "9+2" arrangement of microtubule doublets and recognize several novel protein densities between the microtubule doublets. This study also

recognized several new layers of radial asymmetry, from asymmetrical faces of the central pair microtubules to asymmetrical distributions of the newly recognized connecting proteins between the various microtubule pairs. These asymmetries are likely critical to producing the chiral waveforms that are necessary for sperm motility, hyperactivation, and perhaps even navigation. Future efforts will identify each of these newly-recognized proteins, and allow us to determine whether these critical structural and motor proteins may be tractable targets for motility-inhibiting contraceptives.

Taken together, these studies advance the understanding of multiple aspects of sperm biology and set the stage for further studies which may prove whether the approaches and targets investigated here are viable ways of creating novel unisex, nonhormonal contraception. During the five years that these studies were being conducted, the field of novel contraceptive development advanced significantly, with many new investigators joining the effort, many potential contraceptives making significant progress through the preclinical and clinical development pipeline, multiple new funders committing significant amounts of money towards the goal, the reengagement of pharmaceutical companies (including both startups and major companies), and a structural biology revolution that has vastly accelerated the characterization of sperm-specific proteins. These factors together make it a uniquely exciting time to be part of this field and promise that the long-awaited goal of effective pharmaceutical contraception for people with testes will finally become a reality soon. I feel proud of the role that I and my collaborators have played in creating this inflection point of accelerating momentum, and I look eagerly forward to the future.

## References

1. Lindemann, C. B. & Lesich, K. A. Functional anatomy of the mammalian sperm flagellum. *Cytoskelet. Hoboken NJ* **73**, 652–669 (2016).
2. Kim, C. R. *et al.* PHF7 Modulates BRDT Stability and Histone-to-Protamine Exchange during Spermiogenesis. *Cell Rep.* **32**, 107950 (2020).
3. Suarez, S. S. & Pacey, A. A. Sperm transport in the female reproductive tract. *Hum. Reprod. Update* **12**, 23–37 (2006).
4. Suarez, S. S. Mammalian Sperm Interactions with the Female Reproductive Tract. *Cell Tissue Res.* **363**, 185–194 (2016).
5. Zheng, L.-P., Wang, H.-F., Li, B.-M. & Zeng, X.-H. Sperm-specific ion channels: targets holding the most potential for male contraceptives in development. *Contraception* **88**, 485–491 (2013).
6. Rahman, M. S., Lee, J.-S., Kwon, W.-S. & Pang, M.-G. Sperm Proteomics: Road to Male Fertility and Contraception. *International Journal of Endocrinology* vol. 2013 e360986 <https://www.hindawi.com/journals/ije/2013/360986/> (2013).
7. Cormier, N., McGlone, J. J., Leszyk, J. & Hardy, D. M. Immunocontraceptive target repertoire defined by systematic identification of sperm membrane alloantigens in a single species. *PLOS ONE* **13**, e0190891 (2018).
8. Haden, N. P., Hickox, J. R., Whisnant, C. S. & Hardy, D. M. Systematic characterization of sperm-specific membrane proteins in swine. *Biol. Reprod.* **63**, 1839–1847 (2000).
9. Robertson, M. J. *et al.* Large-scale discovery of male reproductive tract-specific genes through analysis of RNA-seq datasets. *BMC Biol.* **18**, 103 (2020).

10. Lu, Y. & Ikawa, M. Eukaryotic fertilization and gamete fusion at a glance. *J. Cell Sci.* **135**, jcs260296 (2022).
11. Sinha, S. *et al.* Contraceptive and infertility target DataBase (CITDBase): A contraceptive drug development tool for targeting and analysis of human reproductive specific tissues. *Biol. Reprod.* (2021) doi:10.1093/biolre/ioab172.
12. Abbe, C. R., Page, S. T. & Thirumalai, A. Male Contraception. *Yale J. Biol. Med.* **93**, 603–613 (2020).
13. Lishko, P. V. Contraception: Search for an Ideal Unisex Mechanism by Targeting Ion Channels. *Trends Biochem. Sci.* **41**, 816–818 (2016).
14. Sedgh, G., Singh, S. & Hussain, R. Intended and Unintended Pregnancies Worldwide in 2012 and Recent Trends. *Stud. Fam. Plann.* **45**, 301–314 (2014).
15. Finer, L. B. & Zolna, M. R. Declines in Unintended Pregnancy in the United States, 2008–2011. *N. Engl. J. Med.* **374**, 843–852 (2016).
16. Potter, J. E. *et al.* Challenging unintended pregnancy as an indicator of reproductive autonomy. *Contraception* **100**, 1–4 (2019).
17. Kost, K. & Zolna, M. Challenging unintended pregnancy as an indicator of reproductive autonomy: a response. *Contraception* **100**, 5–9 (2019).
18. Sundaram, A. *et al.* Contraceptive Failure in the United States: Estimates from the 2006–2010 National Survey of Family Growth. *Perspect. Sex. Reprod. Health* **49**, 7–16 (2017).
19. Daniels, K. & D., J. J. (Ph. *Contraceptive Methods Women Have Ever Used: United States, 1982-2010*. (U.S. Department of Health and Human Services, Centers for Disease Control and Prevention, National Center for Health Statistics, 2013).

20. Bitzer, J. & Simon, J. A. Current issues and available options in combined hormonal contraception. *Contraception* **84**, 342–356 (2011).
21. McDonald, S. W. Cellular Responses to Vasectomy. *Int. Rev. Cytol.* **199**, 295–339 (2000).
22. Jarow, J. P., Goluboff, E. T., Chang, T. S. & Marshall, F. E. Relationship between antisperm antibodies and testicular histologic changes in humans after vasectomy. *Urology* **43**, 521–524 (1994).
23. Jarow, J. P. *et al.* Quantitative Pathologic Changes in the Human Testis after Vasectomy. *N. Engl. J. Med.* **313**, 1252–1256 (1985).
24. Royle, M. G., Parslow, J. M., Kingscott, M. M. B., Wallace, D. M. A. & Hendry, W. F. Reversal of Vasectomy: The Effects of Sperm Antibodies on Subsequent Fertility. *Br. J. Urol.* **53**, 654–659 (1981).
25. Reynolds-Wright, J. J., Cameron, N. J. & Anderson, R. A. Will Men Use Novel Male Contraceptive Methods and Will Women Trust Them? A Systematic Review. *J. Sex Res.* **58**, 838–849 (2021).
26. Dorman, E. *et al.* Modeling the impact of novel male contraceptive methods on reductions in unintended pregnancies in Nigeria, South Africa, and the United States. *Contraception* **97**, 62–69 (2018).
27. Gipson, J. D., Koenig, M. A. & Hindin, M. J. The Effects of Unintended Pregnancy on Infant, Child, and Parental Health: A Review of the Literature. *Stud. Fam. Plann.* **39**, 18–38 (2008).
28. Herd, P., Higgins, J., Sicinski, K. & Merkurieva, I. The Implications of Unintended Pregnancies for Mental Health in Later Life. *Am. J. Public Health* **106**, 421–429 (2016).

29. Trussell, J. The cost of unintended pregnancy in the United States. *Contraception* **75**, 168–170 (2007).
30. Trussell, J. *et al.* Burden of unintended pregnancy in the United States: potential savings with increased use of long-acting reversible contraception. *Contraception* **87**, 154–161 (2013).
31. Grimes, D. A. *et al.* Unsafe abortion: the preventable pandemic. *The Lancet* **368**, 1908–1919 (2006).
32. World Health Organization. *Trends in maternal mortality 2000 to 2017: estimates by WHO, UNICEF, UNFPA, World Bank Group and the United Nations Population Division.* (World Health Organization, 2019).
33. Ronsmans, C. & Graham, W. J. Maternal mortality: who, when, where, and why. *The Lancet* **368**, 1189–1200 (2006).
34. Nour, N. M. An Introduction to Maternal Mortality. *Rev. Obstet. Gynecol.* **1**, 77–81 (2008).
35. Lu, M. C. Reducing Maternal Mortality in the United States. *JAMA* **320**, 1237–1238 (2018).
36. Hoyert, D. L. Maternal Mortality Rates in the United States, 2020. **5** (2022).
37. MacDorman, M. F., Declercq, E., Cabral, H. & Morton, C. Is the United States Maternal Mortality Rate Increasing? Disentangling trends from measurement issues Short title: U.S. Maternal Mortality Trends. *Obstet. Gynecol.* **128**, 447–455 (2016).
38. Finer, L. B. & Zolna, M. R. Unintended pregnancy in the United States: incidence and disparities, 2006. *Contraception* **84**, 478–485 (2011).
39. Finer, L. B. & Sonfield, A. The evidence mounts on the benefits of preventing unintended pregnancy. *Contraception* **87**, 126–127 (2013).
40. Gebel Berg, E. The Chemistry of the Pill. *ACS Cent. Sci.* **1**, 5–7 (2015).

41. Campelia, G. D., Abbe, C., Nickels, L. M., McElmeel, E. & Amory, J. K. “Shared risk”: Reframing risk analysis in the ethics of novel male contraceptives. *Contraception* **102**, 67–69 (2020).
42. Abbe, C. & Roxby, A. C. Assessing safety in hormonal male contraception: a critical appraisal of adverse events reported in a male contraceptive trial. *BMJ Sex. Reprod. Health* bmjsrh-2018-200206 (2019) doi:10.1136/bmjsrh-2018-200206.
43. Portman, D., Eisenberg, D. L., Cason, P. & Howard, B. Variability in Contraceptive Clinical Trial Design and the Challenges in Making Comparisons Across Trials. *Adv. Ther.* (2021) doi:10.1007/s12325-021-01915-3.
44. Watkins, E. S. How the Pill Became a Lifestyle Drug: The Pharmaceutical Industry and Birth Control in the United States Since 1960. *Am. J. Public Health* **102**, 1462–1472 (2012).
45. Callahan, R. L., Mehta, N. J., Nanda, K. & Kopf, G. S. The new contraceptive revolution: developing innovative products outside of industry†,‡. *Biol. Reprod.* **103**, 157–166 (2020).
46. Cheng, C. Y. & Mruk, D. D. The Blood-Testis Barrier and Its Implications for Male Contraception. *Pharmacol. Rev.* **64**, 16–64 (2012).
47. Drevet, J. R. Epididymal approaches to male contraception. *Basic Clin. Androl.* **28**, 12 (2018).
48. Wang, C., Festin, M. P. R. & Swerdloff, R. S. Male Hormonal Contraception: Where Are We Now? *Curr. Obstet. Gynecol. Rep.* **5**, 38–47 (2016).
49. Waller, D., Bolick, D., Lissner, E., Premanandan, C. & Gamerman, G. Reversibility of Vasalgel™ male contraceptive in a rabbit model. *Basic Clin. Androl.* **27**, (2017).
50. Nickels, L. M., Shane, K. & Vahdat, H. L. Catalyzing momentum in male contraceptive development†. *Biol. Reprod.* ioab208 (2021) doi:10.1093/biolre/ioab208.



51. Vahdat, H. L., Shane, K. & Nickels, L. M. The role of team science in the future of male contraception. *Biol. Reprod.* **103**, 167–175 (2020).
52. Balbach, M. *et al.* Optimization of lead compounds into on-demand, nonhormonal contraceptives: leveraging a public–private drug discovery institute collaboration. *Biol. Reprod.* (2020) doi:10.1093/biolre/ioaa052.
53. Amory, J. K. Male contraception. *Fertil. Steril.* **106**, 1303–1309 (2016).
54. Smith, J. F. *et al.* Disruption of the principal, progesterone-activated sperm Ca<sup>2+</sup> channel in a CatSper2-deficient infertile patient. *Proc. Natl. Acad. Sci.* **110**, 6823–6828 (2013).
55. Mundt, N., Spehr, M. & Lishko, P. V. TRPV4 is the temperature-sensitive ion channel of human sperm. *eLife* <https://elifesciences.org/articles/35853> (2018) doi:10.7554/eLife.35853.
56. Miller, M. R. *et al.* Asymmetrically Positioned Flagellar Control Units Regulate Human Sperm Rotation. *Cell Rep.* **24**, 2606–2613 (2018).
57. Miller, M. R. *et al.* Unconventional endocannabinoid signaling governs sperm activation via the sex hormone progesterone. *Science* **352**, 555–559 (2016).
58. Mannowetz, N., Naidoo, N. M., Choo, S.-A. S., Smith, J. F. & Lishko, P. V. Slo1 is the principal potassium channel of human spermatozoa. *Elife* **2**, e01009 (2013).
59. Lishko, P. V., Botchkina, I. L., Fedorenko, A. & Kirichok, Y. Acid Extrusion from Human Spermatozoa Is Mediated by Flagellar Voltage-Gated Proton Channel. *Cell* **140**, 327–337 (2010).
60. Lishko, P. V., Botchkina, I. L. & Kirichok, Y. Progesterone activates the principal Ca<sup>2+</sup> channel of human sperm. *Nature* **471**, 387–391 (2011).

61. Mallowetz, N., Miller, M. R. & Lishko, P. V. Regulation of the sperm calcium channel CatSper by endogenous steroids and plant triterpenoids. *Proc. Natl. Acad. Sci.* **114**, 5743–5748 (2017).
62. Lishko, P. V. & Kirichok, Y. The role of Hv1 and CatSper channels in sperm activation: Hv1 and CatSper channels in sperm activation. *J. Physiol.* **588**, 4667–4672 (2010).
63. Piotrowska, K., Wang, C., Swerdloff, R. S. & Liu, P. Y. Male hormonal contraception: hope and promise. *Lancet Diabetes Endocrinol.* **5**, 214–223 (2017).
64. Gava, G. & Meriggiola, M. C. Update on male hormonal contraception. *Ther. Adv. Endocrinol. Metab.* **10**, (2019).
65. Behre, H. M. *et al.* Efficacy and Safety of an Injectable Combination Hormonal Contraceptive for Men. *J. Clin. Endocrinol. Metab.* **101**, 4779–4788 (2016).
66. Ilani, N. *et al.* A New Combination of Testosterone and Nestorone Transdermal Gels for Male Hormonal Contraception. *J. Clin. Endocrinol. Metab.* **97**, 3476–3486 (2012).
67. Gu, Y. *et al.* Multicenter Contraceptive Efficacy Trial of Injectable Testosterone Undecanoate in Chinese Men. *J. Clin. Endocrinol. Metab.* **94**, 1910–1915 (2009).
68. Yuen, F., Nguyen, B. T., Swerdloff, R. S. & Wang, C. Continuing the search for a hormonal male contraceptive. *Best Pract. Res. Clin. Obstet. Gynaecol.* **66**, 83–94 (2020).
69. Nguyen, B. T. *et al.* Acceptability of oral dimethandrolone undecanoate in a 28-day placebo-controlled trial of a hormonal male contraceptive prototype. *Contraception* **102**, 52–57 (2020).
70. Nguyen, B. T. *et al.* Acceptability of the oral hormonal male contraceptive prototype, 11 $\beta$ -methyl-19-nortestosterone dodecylcarbonate (11 $\beta$ -MNTDC), in a 28-day placebo-controlled trial. *Contraception* **104**, 531–537 (2021).

71. Page, S. T. & Amory, J. K. Male hormonal contraceptive — are we there yet? *Nat. Rev. Endocrinol.* **14**, 685–686 (2018).
72. Yuen, F. *et al.* Comparison of metabolic effects of the progestational androgens dimethandrolone undecanoate and 11 $\beta$ -MNTDC in healthy men. *Andrology* **9**, 1526–1539 (2021).
73. Page, S. T., Blithe, D. & Wang, C. Hormonal Male Contraception: Getting to Market. *Front. Endocrinol.* **13**, 891589 (2022).
74. Fawcett, D. W. The mammalian spermatozoon. *Dev. Biol.* **44**, 394–436 (1975).
75. Park, S. *et al.* CRISPR/Cas9-mediated genome-edited mice reveal 10 testis-enriched genes are dispensable for male fecundity. *Biol. Reprod.* **103**, 195–204 (2020).
76. Sun, J. *et al.* CRISPR/Cas9-based genome editing in mice uncovers 13 testis- or epididymis-enriched genes individually dispensable for male reproduction. *Biol. Reprod.* **103**, 183–194 (2020).
77. Inoue, N. & Wada, I. Deletion of the initial methionine codon of the Tmem95 gene causes subfertility, but not complete infertility, in male mice. *Biol. Reprod.* **106**, 378–381 (2022).
78. Bourhill, T., Narendran, A. & Johnston, R. N. Enzastaurin: A lesson in drug development. *Crit. Rev. Oncol. Hematol.* **112**, 72–79 (2017).
79. Deras, R. *et al.* PD36-10 THE MAMMALIAN REPRODUCTIVE GENETICS DATABASE, VERSION 2 (MRGDv2). *J. Urol.* **207**, e636 (2022).
80. Cheng, C. Y. & Mruk, D. D. New frontiers in nonhormonal male contraception. *Contraception* **82**, 476–482 (2010).
81. Page, S. T., Amory, J. K. & Bremner, W. J. Advances in Male Contraception. *Endocr. Rev.* **29**, 465–493 (2008).

82. Murdoch, F. E. & Goldberg, E. Male contraception: Another holy grail. *Bioorg. Med. Chem. Lett.* **24**, 419–424 (2014).
83. Saggiorato, G. *et al.* Human sperm steer with second harmonics of the flagellar beat. *Nat. Commun.* **8**, (2017).
84. Turner, R. M. Moving to the beat: a review of mammalian sperm motility regulation. *Reprod. Fertil. Dev.* **18**, 25 (2006).
85. Suarez, S. S. Control of hyperactivation in sperm. *Hum. Reprod. Update* **14**, 647–657 (2008).
86. Austin, C. R. Observations on the penetration of the sperm in the mammalian egg. *Aust. J. Sci. Res. Ser B Biol. Sci.* **4**, 581–596 (1951).
87. Chang, M. C. Fertilizing Capacity of Spermatozoa deposited into the Fallopian Tubes. *Nature* **168**, 697–698 (1951).
88. Suarez, S. S., Varosi, S. M. & Dai, X. Intracellular calcium increases with hyperactivation in intact, moving hamster sperm and oscillates with the flagellar beat cycle. *Proc. Natl. Acad. Sci.* **90**, 4660–4664 (1993).
89. White, D. R. & Aitken, R. J. Relationship between calcium, cyclic AMP, ATP, and intracellular pH and the capacity of hamster spermatozoa to express hyperactivated motility. *Gamete Res.* **22**, 163–177 (1989).
90. Uhler, M. L., Leung, A., Chan, S. Y. W. & Wang, C. Direct effects of progesterone and antiprogesterone on human sperm hyperactivated motility and acrosome reaction\*\*Presented in part at the 39th Annual Meeting of the Society of Gynecologic Investigation, San Antonio, Texas, March 18 to 21, 1992. *Fertil. Steril.* **58**, 1191–1198 (1992).
91. Cooper, T. G. & Yeung, C.-H. Computer-aided evaluation of assessment of “grade a” spermatozoa by experienced technicians. *Fertil. Steril.* **85**, 220–224 (2006).

92. Lu, J. C., Huang, Y. F. & Lü, N. Q. Computer-aided sperm analysis: past, present and future. *Andrologia* **46**, 329–338 (2014).
93. Roan, N. R. *et al.* Peptides Released by Physiological Cleavage of Semen Coagulum Proteins Form Amyloids that Enhance HIV Infection. *Cell Host Microbe* **10**, 541–550 (2011).
94. Roan, N. R. *et al.* Semen amyloids participate in spermatozoa selection and clearance. *eLife* **6**, (2017).
95. Lishko, P., Clapham, D. E., Navarro, B. & Kirichok, Y. Chapter Four - Sperm Patch-Clamp. in *Methods in Enzymology* (ed. Marshall, W. F.) vol. 525 59–83 (Academic Press, 2013).
96. Fredricsson, B., Möller, L., Pousette, A. & Westerholm, R. Human sperm motility is affected by plasticizers and diesel particle extracts. *Pharmacol. Toxicol.* **72**, 128–133 (1993).
97. *WHO laboratory manual for the examination and processing of human semen.* (World Health Organization, 2010).
98. Kruger, T. F. *et al.* New method of evaluating sperm morphology with predictive value for human in vitro fertilization. *Urology* **30**, 248–251 (1987).
99. Wennemuth, G., Babcock, D. F. & Hille, B. Calcium Clearance Mechanisms of Mouse Sperm. *J. Gen. Physiol.* **122**, 115–128 (2003).
100. Burnett, L. A. *et al.* Testicular expression of Adora3i2 in Adora3-knockout mice reveals a Role of mouse A3Ri2 and human A3Ri3 adenosine receptors in sperm. *J. Biol. Chem.* **285**, 33662–33670 (2010).
101. Muschol, M., Wenders, C. & Wennemuth, G. Four-dimensional analysis by high-speed holographic imaging reveals a chiral memory of sperm flagella. *PLOS ONE* **13**, e0199678 (2018).
102. Mortimer, S. T. CASA—Practical Aspects. *J. Androl.* **21**, 515–524 (2000).

103. Vyklicka, L. & Lishko, P. V. Dissecting the signaling pathways involved in the function of sperm flagellum. *Curr. Opin. Cell Biol.* **63**, 154–161 (2020).
104. Molina, L. C. P. *et al.* Membrane Potential Determined by Flow Cytometry Predicts Fertilizing Ability of Human Sperm. *Front. Cell Dev. Biol.* **7**, (2020).
105. Brown, S. G. *et al.* Depolarization of sperm membrane potential is a common feature of men with subfertility and is associated with low fertilization rate at IVF. *Hum. Reprod.* **31**, 1147–1157 (2016).
106. Irigoyen, P. *et al.* Mitochondrial metabolism determines the functional status of human sperm and correlates with semen parameters. *Front. Cell Dev. Biol.* **10**, (2022).
107. Boguenet, M., Bouet, P.-E., Spiers, A., Reynier, P. & May-Panloup, P. Mitochondria: their role in spermatozoa and in male infertility. *Hum. Reprod. Update* (2021) doi:10.1093/humupd/dmab001.
108. Zhang, G. *et al.* Mitochondrial Biomarkers Reflect Semen Quality: Results from the MARCHS Study in Chongqing, China. *PLOS ONE* **11**, e0168823 (2016).
109. Zhang, G. *et al.* Mitochondrial functionality modifies human sperm acrosin activity, acrosome reaction capability and chromatin integrity. *Hum. Reprod.* **34**, 3–11 (2019).
110. Childress, E. S., Alexopoulos, S. J., Hoehn, K. L. & Santos, W. L. Small Molecule Mitochondrial Uncouplers and Their Therapeutic Potential: Miniperspective. *J. Med. Chem.* **61**, 4641–4655 (2018).
111. Bielawski, J., Thompson, T. E. & Lehninger, A. L. The effect of 2,4-dinitrophenol on the electrical resistance of phospholipid bilayer membranes. *Biochem. Biophys. Res. Commun.* **24**, 948–954 (1966).

112. Kenwood, B. M. *et al.* Identification of a novel mitochondrial uncoupler that does not depolarize the plasma membrane. *Mol. Metab.* **3**, 114–123 (2014).
113. Bertholet, A. M. *et al.* Mitochondrial uncouplers induce proton leak by activating AAC and UCP1. *Nature* **606**, 180–187 (2022).
114. Dolce, V., Scarcia, P., Iacopetta, D. & Palmieri, F. A fourth ADP/ATP carrier isoform in man: identification, bacterial expression, functional characterization and tissue distribution. *FEBS Lett.* **579**, 633–637 (2005).
115. Lim, C. H., Brower, J. V., Resnick, J. L., Oh, S. P. & Terada, N. Adenine Nucleotide Translocase 4 Is Expressed Within Embryonic Ovaries and Dispensable During Oogenesis. *Reprod. Sci.* **22**, 250–257 (2015).
116. Brower, J. V. *et al.* Evolutionarily Conserved Mammalian Adenine Nucleotide Translocase 4 Is Essential for Spermatogenesis. *J. Biol. Chem.* **282**, 29658–29666 (2007).
117. Hamazaki, T. *et al.* Functional Expression of Human Adenine Nucleotide Translocase 4 in *Saccharomyces Cerevisiae*. *PLOS ONE* **6**, e19250 (2011).
118. Leung, W.-Y., Hamazaki, T., Ostrov, D. A. & Terada, N. Identification of adenine nucleotide translocase 4 inhibitors by molecular docking. *J. Mol. Graph. Model.* **45**, (2013).
119. Zhang, Y. *et al.* Human Adenine Nucleotide Translocase (ANT) Modulators Identified by High-Throughput Screening of Transgenic Yeast. *J. Biomol. Screen.* **21**, 381–390 (2016).
120. Hereng, T. H. *et al.* Exogenous pyruvate accelerates glycolysis and promotes capacitation in human spermatozoa. *Hum. Reprod.* **26**, 3249–3263 (2011).
121. Gallon, F., Marchetti, C., Jouy, N. & Marchetti, P. The functionality of mitochondria differentiates human spermatozoa with high and low fertilizing capability. *Fertil. Steril.* **86**, 1526–1530 (2006).

122. Paoli, D. *et al.* Mitochondrial membrane potential profile and its correlation with increasing sperm motility. *Fertil. Steril.* **95**, 2315–2319 (2011).
123. Firsov, A. M. *et al.* Protonophoric action of BAM15 on planar bilayers, liposomes, mitochondria, bacteria and neurons. *Bioelectrochemistry* **137**, 107673 (2021).
124. Kadri, H., Lambourne, O. A. & Mehellou, Y. Niclosamide, a Drug with Many (Re)purposes. *ChemMedChem* **13**, 1088–1091 (2018).
125. Jurgait, A. *et al.* Niclosamide Is a Proton Carrier and Targets Acidic Endosomes with Broad Antiviral Effects. *PLoS Pathog.* **8**, (2012).
126. Bertholet, A. M. *et al.* H<sup>+</sup> transport is an integral function of the mitochondrial ADP/ATP carrier. *Nature* **571**, 515 (2019).
127. Levy, S. E., Chen, Y.-S., Graham, B. H. & Wallace, D. C. Expression and sequence analysis of the mouse adenine nucleotide translocase 1 and 2 genes. *Gene* **254**, 57–66 (2000).
128. Kim, Y.-H. *et al.* Compartmentalization of a unique ADP/ATP carrier protein SFEC (Sperm Flagellar Energy Carrier, AAC4) with glycolytic enzymes in the fibrous sheath of the human sperm flagellar principal piece. *Dev. Biol.* **302**, 463–476 (2007).
129. World Health Organization. *WHO laboratory manual for the examination and processing of human semen.* (World Health Organization, 2021).
130. Brucker, C. & Lipford, G. B. The human sperm acrosome reaction: physiology and regulatory mechanisms. An update. *Hum. Reprod. Update* **1**, 51–62 (1995).
131. Hirohashi, N. & Yanagimachi, R. Sperm acrosome reaction: its site and role in fertilization†. *Biol. Reprod.* **99**, 127–133 (2018).
132. Satouh, Y., Inoue, N., Ikawa, M. & Okabe, M. Visualization of the moment of mouse sperm–egg fusion and dynamic localization of IZUMO1. *J. Cell Sci.* **125**, 4985–4990 (2012).



133. Balestrini, P. A. *et al.* Seeing is believing: Current methods to observe sperm acrosomal exocytosis in real time. *Mol. Reprod. Dev.* **87**, 1188–1198 (2020).
134. du Plessis, S. S., Agarwal, A., Mohanty, G. & van der Linde, M. Oxidative phosphorylation versus glycolysis: what fuel do spermatozoa use? *Asian J. Androl.* **17**, 230–235 (2015).
135. Ford, W. C. L. Glycolysis and sperm motility: does a spoonful of sugar help the flagellum go round? *Hum. Reprod. Update* **12**, 269–274 (2006).
136. Storey, B. T. Mammalian sperm metabolism: oxygen and sugar, friend and foe. *Int. J. Dev. Biol.* **52**, 427–437 (2008).
137. Kenwood, B. M., Calderone, J. A., Taddeo, E. P., Hoehn, K. L. & Santos, W. L. Structure–activity relationships of furazano[3,4-b]pyrazines as mitochondrial uncouplers. *Bioorg. Med. Chem. Lett.* **25**, 4858–4861 (2015).
138. Goldberg, E. The Sperm Specific Form of Lactate Dehydrogenase (LDHC4) is Required for Fertility and is an Attractive Target for Male Contraception (A Review). *Biol. Reprod.* (2020) doi:10.1093/biolre/ioaa217.
139. Zhang, X., Zhang, Y., Zhang, T., Zhang, J. & Wu, B. Significantly enhanced bioavailability of niclosamide through submicron lipid emulsions with or without PEG-lipid: a comparative study. *J. Microencapsul.* **32**, 496–502 (2015).
140. Skinner, W. M., Mannowetz, N., Lishko, P. V. & Roan, N. R. Single-cell Motility Analysis of Tethered Human Spermatozoa. *Bio-Protoc.* **9**, (2019).
141. Mortimer, S. T., van der Horst, G. & Mortimer, D. The future of computer-aided sperm analysis. *Asian J. Androl.* **17**, 545–553 (2015).

142. Tang, S. *et al.* Human sperm TMEM95 binds eggs and facilitates membrane fusion. 2022.06.10.495573 Preprint at <https://doi.org/10.1101/2022.06.10.495573> (2022).
143. Liu, B. *et al.* Recording Electrical Currents across the Plasma Membrane of Mammalian Sperm Cells. *JoVE J. Vis. Exp.* e62049 (2021) doi:10.3791/62049.
144. Kirichok, Y. & Lishko, P. V. Rediscovering sperm ion channels with the patch-clamp technique. *MHR Basic Sci. Reprod. Med.* **17**, 478–499 (2011).
145. Rust, M. J., Bates, M. & Zhuang, X. Sub-diffraction-limit imaging by stochastic optical reconstruction microscopy (STORM). *Nat. Methods* **3**, 793–796 (2006).
146. Huang, B., Wang, W., Bates, M. & Zhuang, X. Three-Dimensional Super-Resolution Imaging by Stochastic Optical Reconstruction Microscopy. *Science* **319**, 810–813 (2008).
147. Wojcik, M., Hauser, M., Li, W., Moon, S. & Xu, K. Graphene-enabled electron microscopy and correlated super-resolution microscopy of wet cells. *Nat. Commun.* **6**, 7384 (2015).
148. Inoue, N., Ikawa, M., Isotani, A. & Okabe, M. The immunoglobulin superfamily protein Izumo is required for sperm to fuse with eggs. *Nature* **434**, 234–238 (2005).
149. Bianchi, E., Doe, B., Goulding, D. & Wright, G. J. Juno is the egg Izumo receptor and is essential for mammalian fertilization. *Nature* **508**, 483–487 (2014).
150. Pausch, H. *et al.* A Nonsense Mutation in TMEM95 Encoding a Nondescript Transmembrane Protein Causes Idiopathic Male Subfertility in Cattle. *PLoS Genet.* **10**, e1004044 (2014).
151. Zhang, S. *et al.* Detection of Bovine TMEM95 p.Cys161X Mutation in 13 Chinese Indigenous Cattle Breeds. *Animals* **9**, 444 (2019).

152. Noda, T. *et al.* Sperm proteins SOF1, TMEM95, and SPACA6 are required for sperm–oocyte fusion in mice. *Proc. Natl. Acad. Sci.* **117**, 11493–11502 (2020).
153. Lamas-Toranzo, I. *et al.* TMEM95 is a sperm membrane protein essential for mammalian fertilization. *eLife* **9**, e53913 (2020).
154. Bedford, J. M., Moore, H. D. M. & Franklin, L. E. Significance of the equatorial segment of the acrosome of the spermatozoon in eutherian mammals. *Exp. Cell Res.* **119**, 119–126 (1979).
155. Yanagimachi, R. Mammalian fertilization. in *The Physiology of Reproduction*. (eds. Knobil, E. & Neill, J.) vol. 1 (Raven Press, 1994).
156. Bianchi, E. & Wright, G. J. Cross-species fertilization: the hamster egg receptor, Juno, binds the human sperm ligand, Izumo1. *Philos. Trans. R. Soc. B Biol. Sci.* **370**, 20140101 (2015).
157. Inoue, N., Saito, T. & Wada, I. Unveiling a novel function of CD9 in surface compartmentalization of oocytes. *Development* **147**, dev189985 (2020).
158. Aydin, H., Sultana, A., Li, S., Thavalingam, A. & Lee, J. E. Molecular architecture of the human sperm IZUMO1 and egg JUNO fertilization complex. *Nature* **534**, 562–565 (2016).
159. Ohto, U. *et al.* Structure of IZUMO1–JUNO reveals sperm–oocyte recognition during mammalian fertilization. *Nature* **534**, 566–569 (2016).
160. Vance, T. D. R. *et al.* SPACA6 ectodomain structure reveals a conserved superfamily of gamete fusion-associated proteins. *Commun. Biol.* **5**, 1–14 (2022).
161. Schreiber, G. & Keating, A. E. Protein binding specificity versus promiscuity. *Curr. Opin. Struct. Biol.* **21**, 50–61 (2011).

162. Chen, J., Sawyer, N. & Regan, L. Protein–protein interactions: General trends in the relationship between binding affinity and interfacial buried surface area. *Protein Sci.* **22**, 510–515 (2013).
163. Tang, S. & Kim, P. S. A high-affinity human PD-1/PD-L2 complex informs avenues for small-molecule immune checkpoint drug discovery. *Proc. Natl. Acad. Sci.* **116**, 24500–24506 (2019).
164. Qu, Y., Lu, D., Jiang, H., Chi, X. & Zhang, H. EZH2 is required for mouse oocyte meiotic maturation by interacting with and stabilizing spindle assembly checkpoint protein BubRI. *Nucleic Acids Res.* **44**, 7659–7672 (2016).
165. Inoue, N., Hagihara, Y., Wright, D., Suzuki, T. & Wada, I. Oocyte-triggered dimerization of sperm IZUMO1 promotes sperm–egg fusion in mice. *Nat. Commun.* **6**, 8858 (2015).
166. Inoue, N. & Wada, I. Monitoring dimeric status of IZUMO1 during the acrosome reaction in living spermatozoon. *Cell Cycle* **17**, 1279–1285 (2018).
167. Inoue, N. *et al.* Molecular dissection of IZUMO1, a sperm protein essential for sperm–egg fusion. *Dev. Camb. Engl.* **140**, 3221–3229 (2013).
168. Barbaux, S. *et al.* Sperm SPACA6 protein is required for mammalian Sperm-Egg Adhesion/Fusion. *Sci. Rep.* **10**, 5335 (2020).
169. Inoue, N., Hagihara, Y. & Wada, I. Evolutionarily conserved sperm factors, DCST1 and DCST2, are required for gamete fusion. *eLife* **10**, e66313 (2021).
170. Noda, T. *et al.* Sperm membrane proteins DCST1 and DCST2 are required for sperm–egg interaction in mice and fish. *Commun. Biol.* **5**, 1–11 (2022).
171. Fujihara, Y. *et al.* Spermatozoa lacking Fertilization Influencing Membrane Protein (FIMP) fail to fuse with oocytes in mice. *Proc. Natl. Acad. Sci.* **117**, 9393–9400 (2020).

172. Cafe, S. L., Anderson, A. L. & Nixon, B. In vitro Induction and Detection of Acrosomal Exocytosis in Human Spermatozoa. *Bio-Protoc.* **10**, e3689–e3689 (2020).
173. Tsunoda, Y. & Chang, M. Further studies of antisera on the fertilization of mouse, rat, and hamster eggs in vivo and in vitro. *Int. J. Fertil.* **22**, 129–139 (1977).
174. Vonrhein, C. *et al.* Data processing and analysis with the autoPROC toolbox. *Acta Crystallogr. D Biol. Crystallogr.* **67**, 293–302 (2011).
175. Liebschner, D. *et al.* Macromolecular structure determination using X-rays, neutrons and electrons: recent developments in Phenix. *Acta Crystallogr. Sect. Struct. Biol.* **75**, 861–877 (2019).
176. Emsley, P. & Cowtan, K. Coot: model-building tools for molecular graphics. *Acta Crystallogr. D Biol. Crystallogr.* **60**, 2126–2132 (2004).
177. Ashkenazy, H. *et al.* ConSurf 2016: an improved methodology to estimate and visualize evolutionary conservation in macromolecules. *Nucleic Acids Res.* **44**, W344–W350 (2016).
178. Le Naour, F., Rubinstein, E., Jasmin, C., Prenant, M. & Boucheix, C. Severely Reduced Female Fertility in CD9-Deficient Mice. *Science* **287**, 319–321 (2000).
179. Miyado, K. *et al.* Requirement of CD9 on the Egg Plasma Membrane for Fertilization. *Science* **287**, 321–324 (2000).
180. Kaji, K. *et al.* The gamete fusion process is defective in eggs of Cd9-deficient mice. *Nat. Genet.* **24**, 279–282 (2000).
181. Wallmeier, J. *et al.* Motile ciliopathies. *Nat. Rev. Dis. Primer* **6**, 1–29 (2020).
182. Bayless, B. A., Navarro, F. M. & Winey, M. Motile Cilia: Innovation and Insight From Ciliate Model Organisms. *Front. Cell Dev. Biol.* **7**, (2019).

183. Ishikawa, T. Axoneme Structure from Motile Cilia. *Cold Spring Harb. Perspect. Biol.* **9**, a028076 (2017).
184. Satir, P., Heuser, T. & Sale, W. S. A Structural Basis for How Motile Cilia Beat. *BioScience* **64**, 1073–1083 (2014).
185. Satir, P. STUDIES ON CILIA : III. Further Studies on the Cilium Tip and a ‘Sliding Filament’ Model of Ciliary Motility. *J. Cell Biol.* **39**, 77–94 (1968).
186. Summers, K. E. & Gibbons, I. R. Adenosine Triphosphate-Induced Sliding of Tubules in Trypsin-Treated Flagella of Sea-Urchin Sperm. *Proc. Natl. Acad. Sci. U. S. A.* **68**, 3092–3096 (1971).
187. Lindemann, C. B. & Lesich, K. A. The many modes of flagellar and ciliary beating: Insights from a physical analysis. *Cytoskeleton* **78**, 36–51 (2021).
188. Witman, G. B., Plummer, J. & Sander, G. Chlamydomonas flagellar mutants lacking radial spokes and central tubules. Structure, composition, and function of specific axonemal components. *J. Cell Biol.* **76**, 729–747 (1978).
189. Huang, B., Piperno, G., Ramanis, Z. & Luck, D. J. Radial spokes of Chlamydomonas flagella: genetic analysis of assembly and function. *J. Cell Biol.* **88**, 80–88 (1981).
190. Smith, E. F. & Sale, W. S. Regulation of Dynein-Driven Microtubule Sliding by the Radial Spokes in Flagella. *Science* **257**, 1557–1559 (1992).
191. Bower, R. *et al.* The N-DRC forms a conserved biochemical complex that maintains outer doublet alignment and limits microtubule sliding in motile axonemes. *Mol. Biol. Cell* **24**, 1134–1152 (2013).
192. Grossman-Haham, I. *et al.* Structure of the radial spoke head and insights into its role in mechanoregulation of ciliary beating. *Nat. Struct. Mol. Biol.* **28**, 20–28 (2021).

193. Gui, M. *et al.* Structures of radial spokes and associated complexes important for ciliary motility. *Nat. Struct. Mol. Biol.* **28**, 29–37 (2021).
194. Pigino, G. *et al.* Cryoelectron tomography of radial spokes in cilia and flagella. *J. Cell Biol.* **195**, 673–687 (2011).
195. Bui, K. H., Sakakibara, H., Movassagh, T., Oiwa, K. & Ishikawa, T. Asymmetry of inner dynein arms and inter-doublet links in Chlamydomonas flagella. *J. Cell Biol.* **186**, 437–446 (2009).
196. Bui, K. H., Yagi, T., Yamamoto, R., Kamiya, R. & Ishikawa, T. Polarity and asymmetry in the arrangement of dynein and related structures in the Chlamydomonas axoneme. *J. Cell Biol.* **198**, 913–925 (2012).
197. Lin, J., Heuser, T., Song, K., Fu, X. & Nicastro, D. One of the nine doublet microtubules of eukaryotic flagella exhibits unique and partially conserved structures. *PLoS One* **7**, e46494 (2012).
198. Dutcher, S. K. Asymmetries in the cilia of Chlamydomonas. *Philos. Trans. R. Soc. Lond. B. Biol. Sci.* **375**, 20190153 (2020).
199. Hansen, J. N., Rassmann, S., Jikeli, J. F. & Wachten, D. SpermQ—A Simple Analysis Software to Comprehensively Study Flagellar Beating and Sperm Steering. *Cells* **8**, 10 (2019).
200. Babcock, D. F., Wandernoth, P. M. & Wennemuth, G. Episodic rolling and transient attachments create diversity in sperm swimming behavior. *BMC Biol.* **12**, 67 (2014).
201. Leung, M. R. *et al.* The multi-scale architecture of mammalian sperm flagella and implications for ciliary motility. *EMBO J.* **40**, e107410 (2021).

202. Nicastro, D. *et al.* The Molecular Architecture of Axonemes Revealed by Cryoelectron Tomography. *Science* **313**, 944–948 (2006).
203. Carbajal-González, B. I. *et al.* Conserved structural motifs in the central pair complex of eukaryotic flagella. *Cytoskelet. Hoboken NJ* **70**, 101–120 (2013).
204. Gui, M. *et al.* De novo identification of mammalian ciliary motility proteins using cryo-EM. *Cell* **184**, 5791-5806.e19 (2021).
205. Ma, M. *et al.* Structure of the Decorated Ciliary Doublet Microtubule. *Cell* **179**, 909-922.e12 (2019).
206. Ichikawa, M. *et al.* Subnanometre-resolution structure of the doublet microtubule reveals new classes of microtubule-associated proteins. *Nat. Commun.* **8**, 15035 (2017).
207. Song, K. *et al.* In situ structure determination at nanometer resolution using TYGRESS. *Nat. Methods* **17**, 201–208 (2020).
208. Owa, M. *et al.* Inner lumen proteins stabilize doublet microtubules in cilia and flagella. *Nat. Commun.* **10**, 1143 (2019).
209. Lin, J. *et al.* Cryo-electron tomography reveals ciliary defects underlying human RSPH1 primary ciliary dyskinesia. *Nat. Commun.* **5**, 5727 (2014).
210. Gadadhar, S. *et al.* Tubulin glycylation controls axonemal dynein activity, flagellar beat, and male fertility. *Science* **371**, eabd4914 (2021).
211. Han, L. *et al.* Cryo-EM structure of an active central apparatus. *Nat. Struct. Mol. Biol.* **29**, 472–482 (2022).
212. Gui, M., Wang, X., Dutcher, S. K., Brown, A. & Zhang, R. Ciliary central apparatus structure reveals mechanisms of microtubule patterning. *Nat. Struct. Mol. Biol.* **29**, 483–492 (2022).



213. Hou, Y. *et al.* Chlamydomonas FAP70 is a component of the previously uncharacterized ciliary central apparatus projection C2a. *J. Cell Sci.* **134**, jcs258540 (2021).
214. Nakane, T., Kimanius, D., Lindahl, E. & Scheres, S. H. Characterisation of molecular motions in cryo-EM single-particle data by multi-body refinement in RELION. *eLife* **7**, e36861 (2018).
215. Linck, R. W., Chemes, H. & Albertini, D. F. The axoneme: the propulsive engine of spermatozoa and cilia and associated ciliopathies leading to infertility. *J. Assist. Reprod. Genet.* **33**, 141–156 (2016).
216. Lindemann, C. B. Functional significance of the outer dense fibers of mammalian sperm examined by computer simulations with the geometric clutch model. *Cell Motil. Cytoskeleton* **34**, 258–270 (1996).
217. Kikkawa, M., Ishikawa, T., Nakata, T., Wakabayashi, T. & Hirokawa, N. Direct visualization of the microtubule lattice seam both in vitro and in vivo. *J. Cell Biol.* **127**, 1965–1971 (1994).
218. Zhang, R., Alushin, G. M., Brown, A. & Nogales, E. Mechanistic Origin of Microtubule Dynamic Instability and Its Modulation by EB Proteins. *Cell* **162**, 849–859 (2015).
219. Firat-Karalar, E. N., Sante, J., Elliott, S. & Stearns, T. Proteomic analysis of mammalian sperm cells identifies new components of the centrosome. *J. Cell Sci.* **127**, 4128–4133 (2014).
220. Warner, F. D. & Satir, P. The structural basis of ciliary bend formation. Radial spoke positional changes accompanying microtubule sliding. *J. Cell Biol.* **63**, 35–63 (1974).
221. Mitchell, D. R. & Nakatsugawa, M. Bend propagation drives central pair rotation in *Chlamydomonas reinhardtii* flagella. *J. Cell Biol.* **166**, 709–715 (2004).

222. Gadélha, H., Hernández-Herrera, P., Montoya, F., Darszon, A. & Corkidi, G. Human sperm uses asymmetric and anisotropic flagellar controls to regulate swimming symmetry and cell steering. *Sci. Adv.* **6**, eaba5168 (2020).
223. Lin, J. & Nicastro, D. Targeted dynein inhibition generates flagellar beating. 153254 Preprint at <https://doi.org/10.1101/153254> (2017).
224. Yamaguchi, H., Oda, T., Kikkawa, M. & Takeda, H. Systematic studies of all PIH proteins in zebrafish reveal their distinct roles in axonemal dynein assembly. *eLife* **7**, e36979 (2018).
225. Lin, J. & Nicastro, D. Asymmetric distribution and spatial switching of dynein activity generates ciliary motility. *Science* **360**, eaar1968 (2018).
226. van der Spoel, A. C. *et al.* Reversible infertility in male mice after oral administration of alkylated imino sugars: a nonhormonal approach to male contraception. *Proc. Natl. Acad. Sci. U. S. A.* **99**, 17173–17178 (2002).
227. Mastronarde, D. N. Automated electron microscope tomography using robust prediction of specimen movements. *J. Struct. Biol.* **152**, 36–51 (2005).
228. Zheng, S. Q. *et al.* MotionCor2: anisotropic correction of beam-induced motion for improved cryo-electron microscopy. *Nat. Methods* **14**, 331–332 (2017).
229. Kremer, J. R., Mastronarde, D. N. & McIntosh, J. R. Computer visualization of three-dimensional image data using IMOD. *J. Struct. Biol.* **116**, 71–76 (1996).
230. Fernández, J. J., Li, S. & Crowther, R. A. CTF determination and correction in electron cryotomography. *Ultramicroscopy* **106**, 587–596 (2006).
231. Agulleiro, J.-I. & Fernandez, J.-J. Tomo3D 2.0--exploitation of advanced vector extensions (AVX) for 3D reconstruction. *J. Struct. Biol.* **189**, 147–152 (2015).

232. Bharat, T. A. M. & Scheres, S. H. W. Resolving macromolecular structures from electron cryo-tomography data using subtomogram averaging in RELION. *Nat. Protoc.* **11**, 2054–2065 (2016).
233. Pettersen, E. F. *et al.* UCSF Chimera--a visualization system for exploratory research and analysis. *J. Comput. Chem.* **25**, 1605–1612 (2004).
234. Goddard, T. D. *et al.* UCSF ChimeraX: Meeting modern challenges in visualization and analysis. *Protein Sci. Publ. Protein Soc.* **27**, 14–25 (2018).
235. Pettersen, E. F. *et al.* UCSF ChimeraX: Structure visualization for researchers, educators, and developers. *Protein Sci. Publ. Protein Soc.* **30**, 70–82 (2021).

# Animal Use Protocol Approval Letter

UNIVERSITY OF CALIFORNIA, BERKELEY

BERKELEY • DAVIS • IRVINE • LOS ANGELES • RIVERSIDE • SAN DIEGO • SAN FRANCISCO



SANTA BARBARA • SANTA CRUZ

ANIMAL CARE AND USE COMMITTEE  
OFFICE FOR ANIMAL CARE AND USE  
2150 SHATTUCK AVENUE, SUITE 300  
BERKELEY, CA 94704-5940

(510) 642-8855  
Web Site: <http://acuc.berkeley.edu>  
PHS Assurance: **A.3084-01**  
USDA Registration: **93-R-0432**

## Approval Letter

October 31, 2022

Principal Investigator: Polina Lishko

Department: Molecular & Cell Biology

Protocol # **AUP-2015-07-7742-2**

Protocol Title: The Role of Ion Channels in Reproduction and Aging

Approval date: October 31, 2022

Expiration date: May 31, 2024

Funding: SPO ID: 035853-002, SPO ID: 20202636, SPO ID: 20202797, SPO ID: 050553-001

The University of California, Berkeley's Animal Care and Use Committee (ACUC) has completed its review of your Animal Use Protocol # AUP-2015-07-7742-2 and granted approval. Your approval will expire on May 31, 2024. Reference this Protocol number when ordering animals.

As Principal Investigator, it is your responsibility to ensure that all individuals working with you on the projects described in this protocol are thoroughly familiar with, and adhere to, the approved procedures. Accordingly, please carefully review the protocol with your personnel, and keep a copy of your current protocol in a location where it can be readily consulted by them.

**No changes in personnel, animal numbers, species, or animal use procedures may be made without prior review and approval by the ACUC.** Proposed changes must be submitted in the form of an amendment to your protocol and be approved by the ACUC before being undertaken.

If you have any questions, or require additional assistance, please do not hesitate to contact the Office for Animal Care and Use (OACU) at [acuc@berkeley.edu](mailto:acuc@berkeley.edu) or 510-642-8855.

Sincerely,

Karsten Gronert, CHAIR

# Human Subjects Protocol Approval Letter



Committee for Protection of Human Subjects (CPHS)  
Office for Protection of Human Subjects (OPHS)

1608 Fourth Street, Suite 220  
Berkeley, CA 94710-5940  
510 642-7461  
[ophs@berkeley.edu](mailto:ophs@berkeley.edu)  
[cphs.berkeley.edu](http://cphs.berkeley.edu)  
FWA# 00006252



## NOTICE OF APPROVAL FOR HUMAN RESEARCH

**DATE:** *September 14, 2021*  
**TO:** Polina Lishko  
**CPHS PROTOCOL NUMBER:** 2013-06-5395  
**CPHS PROTOCOL TITLE:** *The role of sperm ion channels in fertilization*  
*SPO ID: 20150304, SPO ID: 20160148, SPO ID: 041022-002, SPO ID: 047481-001, SPO ID: 046800-001, SPO ID: 20201653, Funding Type: Campus Funding, Funding Type: NIH - Misc (erroneously removed from SPO section by I)*  
**FUNDING SOURCE(S):**

A(n) *amendment* application was submitted for the above-referenced protocol. The Committee for Protection of Human Subjects (CPHS) has reviewed and approved the application on an expedited basis, under Category 3 of the federal regulations.

Effective Date: *September 14, 2021*

Expiration Date: *October 30, 2030*

*Continuation/Renewal:* Applications for continuation review should be submitted no later than 6 weeks prior to the expiration date of the current approval. *Note: It is the responsibility of the Principal Investigator to submit for renewed approval in a timely manner. If approval expires, all research activity (including data analysis) must cease until re-approval from CPHS has been received.* See [Renew \(Continue\) an Approved Protocol](#).

*Amendments/Modifications:* Any change in the design, conduct, or key personnel of this research must be approved by the CPHS **prior** to implementation. For more information, see [Amend/Modify an Approved Protocol](#).

*For protocols that have been granted approval for more than one year:* Certain modifications that increase the level of risk or add FDA oversight may require a continuing review application to be submitted and approved in order for the protocol to continue. If one or more of these changes occur, a Continuing Review application must be submitted and approved in order for the protocol to continue.

*Unanticipated Problems and Adverse Events:* If any study subject experiences an unanticipated problem involving risks to subjects or others, and/or a serious adverse event, the CPHS must be informed **promptly**. For more information on definitions and reporting requirements related to this topic, see [Adverse Event and Unanticipated Problem Reporting](#).

This approval is issued under University of California, Berkeley Federalwide Assurance #00006252.

If you have any questions about this matter, please contact the OPHS staff at 642-7461 or email [ophs@berkeley.edu](mailto:ophs@berkeley.edu).

Sincerely,

Committee for Protection of Human Subjects (CPHS)

UC Berkeley